Exploiting data sparsity in parallel magnetic resonance imaging

Bing Wu

Department of Electrical and Computer Engineering

A thesis presented for the degree of
Doctor of Philosophy

University of Canterbury
Christchurch, New Zealand
September 2009

给我的父母：

小时候我一直认为我是个奇迹，直到有一天我明白你们才是真正的奇迹。

Abstract

Magnetic resonance imaging (MRI) is a widely employed imaging modality that allows observation of the interior of human body. Compared to other imaging modalities such as the computed tomography (CT), MRI features a relatively long scan time that gives rise to many potential issues. The advent of parallel MRI, which employs multiple receiver coils, has started a new era in speeding up the scan of MRI by reducing the number of data acquisitions. However, the finally recovered images from under-sampled data sets often suffer degraded image quality.

This thesis explores methods that incorporate prior knowledge of the image to be reconstructed to achieve improved image recovery in parallel MRI, following the philosophy that 'if some prior knowledge of the image to be recovered is known, the image could be recovered better than without'. Specifically, the prior knowledge of image sparsity is utilized. Image sparsity exists in different domains. Image sparsity in the image domain refers to the fact that the imaged object only occupies a portion of the imaging field of view; image sparsity may also exist in a transform domain for which there is a high level of energy concentration in the image transform. The use of both types of sparsity is considered in this thesis.

There are three major contributions in this thesis. The first contribution is the development of 'GUISE'. GUISE employs an adaptive sampling design method that achieves better exploitation of image domain sparsity in parallel MRI. Secondly, the development of 'PBCS' and 'SENSECS'. PBCS achieves better exploitation of transform domain sparsity by incorporating a prior estimate of the image to be recovered. SENSECS is an application of PBCS that achieves better exploitation of transform domain sparsity in parallel MRI. The third contribution is the implementation of GUISE and PBCS in contrast enhanced MR angiography (CE MRA). In their applications in CE MRA, GUISE and PBCS share the common ground of exploiting the high sparsity of the contrast enhanced angiogram.

The above developments are assessed in various ways using both simulated and experimental data. The potential extensions of these methods are also suggested.

Acknowledgements

This is the bit of the thesis that I enjoyed writing the most. There are many people and organisations that helped and supported me to eventually put this thesis together, and I would like to take this opportunity to express my personal appreciation.

Prof. Phil Bones, Dr. Richard Watts and Prof. Rick Millane gave me guidance while I was pursuing my Ph.D. Phil has been way more than just an advisor to me during this time course. His passions about research and outdoor things pushed my work and life forward. Phil also was generous enough to volunteer himself taking injection for conducting the MR experiments, twice. Richard is a guru of MRI, and he knows everything about it. I really enjoyed the late-Friday-night scan sessions in *St George* with Richard, those were the times that I saw my sequence running on the million-dollar scanner. Rick edited many of my scripts and basically taught me how to write academic English.

Special thanks to Dr Julian Maclaren and Dr Antony Butler. I was very lucky to know Dr Julian Maclaren while he was completing his Ph.D. at Canterbury. Not only he helped me for various things such as building the bottle phantom that was used in one of the experiments, he was also a life role model to me. Julian and Jana were also very kind to shelter me while I was in Freiburg, not to mention the guided tour to the beer gardens. I am particularly grateful to Antony for the Friday nights he spent with me in the scan sessions. Part of the thesis work would not be possible without his help.

I gratefully thank for the financial support provided by the FRST, New Zealand and University of Canterbury. Especially the conference allowance in the Top Achiever scholarship allowed me to go to see the world.

To my friends and my cousin: without you folks my completion of Ph.D. would have been faster, but less enjoyable.

Contents

Chapter 1

Introduction

This introductory chapter consists of three sections: an overview of the research and its objectives; a summary of the main contributions; and a guide to the structure of this thesis.

1.1 Overview and objectives

MRI is a non-invasive imaging technique that is widely used in both clinical medicine and research. A limitation in the use of MRI is its relatively long scan time, typically in the range from minutes to tens of minutes for a 3D scan. The long scan time makes MRI suspectable to motion of the imaged object during the scan, which could cause severe artifacts in the final image. Also the long scan time limits dynamic MRI studies in which a temporally varying object is continuously imaged over a time period, such as imaging the blood flow in MR angiography; capture of the desired dynamic information often requires a short image acquisition time.

Many approaches have been taken to reduce the image acquisition time in MRI, and can be classified into two groups: accelerating the data acquisition and reducing the number of data acquisitions. The fast data acquisition approach is fundamentally limited by the intrinsic engineering and physical constraints, and hence research attention has concentrated on reducing the number of data acquisitions. Due to the nature of MRI data acquisition, acquiring less than a full data set results in global artifacts in the recovered images, and hence additional information about the image is required to compensate for the missing data acquisitions to remove the image artifacts.

The introduction of parallel MRI (pMRI) started a new era in accelerating MR scans [BBM+04]. In parallel MRI multiple receiver coils are employed, and multiple copies of the data measurements are received in different coils, each weighted by the spatial coil sensitivity. The

redundancy in the data sets from multiple receiver coils is exploited to compensate for the missing data acquisitions. The level of data acquisition acceleration achievable is determined the number of receiver coils used. However, in practice the recovered images in parallel MRI are often impaired with reconstruction artifacts that limit its usefulness.

The main focus of this thesis is to utilise additional prior knowledge about the underlying image to achieve better image recovery in parallel MRI. The following questions are considered: what types of prior knowledge could be used; how should these items of prior knowledge be used; and what are the effects in the final image reconstruction?

1.2 Thesis contributions

There are three main contributions in this thesis: **development of 'GUISE'**, **development of 'PBCS' and 'SENSECS'** and **implementation of GUISE and PBCS in contrast enhanced MR angiography**. The first two contributions lead to novel image recovery methods and the third contribution considers a case in which applications of the newly developed methods are particularly promising. More details of the contributions are given below:

A general parallel MRI formulation: A generalized Cartesian parallel MRI formulation that accommodates different data sampling strategies is derived. The relationship between this general formulation and other existing pMRI methods are explored in a systematic and intuitive way. It also leads to the development of the formulation for GUISE.

Noise metric: Two new metrics (*IT metric* and *ST metric*) for judging the noise immunity of different sampling patterns are developed. *ST metric* is an alternative of *IT metric* that is much more computationally efficient.

Adaptive sampling pattern design: For the first time, a computationally efficient pMRI sampling pattern design method is developed. It is shown that this method achieves a good compromise between optimality and computational complexity, and leads to better image reconstruction results compared to similar pMRI methods.

Compressed sensing (CS) in pMRI: The implementation of CS in pMRI is presented. Also its intrinsic performance limitation is discussed.

PBCS: PBCS is an elegant approach that allows a prior estimate of the underlying image to be incorporated in the compressed sensing image recovery process. PBCS also modifies the form of the reconstruction artifacts so that they can be more easily reduced.

SENSECS: SENSECS is an application of PBCS in parallel imaging, and achieves better

synergetic exploitation of coil sensitivity encoding and image transform sparsity. It gives better image reconstruction results than using either of the conventional SENSE and CS methods.

GUISE and PBCS in CE MRA: Two Cartesian sliding window methods that are respectively based on GUISE and PBCS are presented. They both exploit the sparsity in contrast enhanced angiogram and allow image prior knowledge to be incorporated. They also allow retrospective selection of acceleration factors at image reconstruction.

3D object support estimation based on MIP images: A computationally efficient method for estimating the 3D object support region based on maximum intensity projection (MIP) images is presented. It is computationally cheap and also has low risk of under-estimating the object support.

Parallel MRI motion correction: A motion correction method based on parallel MRI was developed in collaboration with another Ph.D. student. It is easy to implement and effective, and does not have the drawbacks that beset the conventional motion correction methods.

1.3 Publications

Each of the three major contributions mentioned in previous section led to preparation of a journal paper:

- **B. Wu**, P. Bones, R. Millane, and R. Watts, "Improved matrix inversion in image plane parallel imaging", *Magnetic Resonance Imaging*, 2009; 27: 942-953.
- **B. Wu**, P. Bones, R. Millane, and R. Watts, "Prior estimate based compressed sensing in parallel MRI", *Magnetic Resonance in Medicine*, accepted, under revision.
- **B. Wu**, P. Bones, A. Butler, R. Millane, and R. Watts, "Cartesian sliding window methods with retrospective selection of acceleration factor for contrast enhanced MR angiography", under revision.

The following conference papers have also arisen from the research work:

- **B. Wu**, P. Bones, R. Millane, and R. Watts, "Prior estimate based compressed sensing", *Proceedings of ISMRM 18th Scientific Meeting*, 2010, Stockholm, Sweden.
- **B. Wu**, P. Bones, R. Millane, and R. Watts, "Prior estimate based compressed sensing in CE MRA", *Proceedings of ISMRM 18th Scientific Meeting*, 2010, Stockholm, Sweden.

- B. Vafadar, **B. Wu**, P. Bones, "A new 3D image projection method", *Proceeding Image and Vision Computing New Zealand*, 2009, Wellington.

- P. Bones, **B. Wu**, B. Vafadar, A.P.H. Butler, and R. Watts, "On improved temporal resolution for magnetic resonance angiography", *In Signal Recovery and Synthesis, The Optical Society of America*, 2009, San Jose, USA.

- **B. Wu**, P. Bones, R. Millane, and R. Watts, "Improved compressed sensing in parallel imaging", *Proceedings of ISMRM 17th Scientific Meeting*, 2009, Honolulu.

- **B. Wu**, A. Butler, P. Bones, R. Millane, and R. Watts, "Contrast enhanced MRA with retrospective acceleration factor", *Proceedings of ISMRM 17th Scientific Meeting*, 2009, Honolulu.

- **B. Wu**, P. Bones, R. Millane, and R. Watts, "Exploiting image sparsity in parallel magnetic resonance imaging", *SPIE optics and photonics*, 2008, San Diego.

- **B. Wu**, P. Bones, R. Millane, and R. Watts, "Improved compressed sensing magnetic resonance imaging", *Proceedings of Engineering and Physical Sciences in Medicine and the Australian Biomedical Engineering Conference*, 2008, Christchurch.

- P. Bones, **B. Wu**, R. Millane, and R. Watts, "Towards better temporal resolution in magnetic resonance angiography", *Proceedings of Engineering and Physical Sciences in Medicine and the Australian Biomedical Engineering Conference*, 2008, Christchurch.

- **B. Wu**, P. Bones, R. Millane, and R. Watts, "Applying compressed sensing (CS) in parallel MRI", *Proceedings of ISMRM 16th Scientific Meeting*, 2008, Toronto.

- J. Maclaren, **B. Wu**, P. Bones, R. Millane, and R. Watts, "SENSE motion correction", *Proceedings of ISMRM 16th Scientific Meeting*, 2008, Toronto.

- **B. Wu**, P. Bones, R. Millane, and R. Watts, "Ordered k-space data acquisition in Contrast Enhanced Magnetic Resonance Angiography (CE-MRA)", *Proceeding of SPIE medical imaging*, 2008, San Diego.

- P. Bones, **B. Wu**, R. Millane, and R. Watts, "Support Constraint in 3-D Magnetic Resonance Imaging", *In Signal Recovery and Synthesis, The Optical Society of America*, 2007, Washington DC.

- **B. Wu**, P. Bones, R. Millane, and R. Watts, "Improved 3D image plane parallel magnetic resonance imaging (pMRI) method", *Proceeding Image and Vision Computing New Zealand*, 2007, Hamilton.

1.4 Thesis structure

The thesis consists of two main parts: in Chapter 2-4 the necessary background material is introduced, and Chapter 5, 6 and 7 respectively present the three novel contributions mentioned in the previous section. In more detail, the contribution of each chapter in this thesis is organised as following:

Chapter 2 lays out the mathematical foundation of this thesis. The matrix notations used are introduced as are the specific signal processing tools used.

Chapter 3 gives an overview of the essential knowledge of MRI. Topics including MR physics, signal formation and image formation are covered, and attention is especially paid to the sampling issues in MRI.

Chapter 4 is an overview of parallel MRI. The principles and development history of parallel imaging are given. Several of the commonly used parallel MRI techniques are reviewed. A new parallel imaging based motion correction method is presented to illustrate the practical utility of parallel imaging.

Chapter 5 presents the development of the GUISE method. A generalised formulation of parallel MRI is first given, which leads to the derivation of GUISE formulation. Then an adaptive sampling pattern design method for GUISE is presented. The performance of GUISE is investigated in simulation and in vivo studies.

Chapter 6 presents the development of PBCS and SENSECS. The compressed sensing theory and its implementation in MRI are first reviewed. Then PBCS is presented to overcome the performance limitation of conventional compressed sensing. Next the application of PBCS in parallel MRI is discussed, and SENECS is proposed to achieve better image recovery in parallel MRI comparing to the conventional CS approach. Finally, the performance of PBCS and SENSECS are investigated using experimental data sets.

Chapter 7 presents the implementation of GUISE and PBCS in CE MRA. Firstly, a brief introduction of CE MRA is given and the practical difficulty of capturing the arterial phase contrast is identified. Then new two methods that are respectively based on GUISE and CS methods are proposed to tackle this difficulty. Comparison of the performance of the two methods are made based on the outcome of phantom and volunteer studies using the new methods are presented.

Chapter 8 is a summary of the work presented in this thesis and also provides suggestions for future work.

Chapter 2

Mathematical preliminaries

This chapter provides the mathematical foundation for the work to be presented in the later chapters. Specifically, the following topics are covered : matrix notations, linear transforms and the inverse problem.

2.1 Matrix notations

The majority of the work presented in this thesis is based on linear algebra in the matrix form; a list of matrix notation used in this thesis is given for reference in Table 2.1.

Table 2.1 Summary of notation used in the thesis

symbol	meaning
$\mathbf{f}$	1D vector
$f[\mathbf{n}]$	multi-dimensional vector
$\|\mathbf{f}\|_n$	nth norm of vector $\mathbf{f}$
$\mathbf{f}[i]$	ith element in vector $\mathbf{f}$
$\mathbf{A}$	matrix
$\mathbf{A}^T$	transpose of $\mathbf{A}$
$\mathbf{A}^H$	Hermitian transpose of $\mathbf{A}$
$\mathbf{A}^{-1}$	inverse of $\mathbf{A}$
$\mathbf{A}^+$	Moore-Penrose inverse of $\mathbf{A}$

As often is the case, M-D discrete sequences are stacked into column-wise vectors for the convenience of matrix operations. The convention used for stacking sequences into their vector forms is the same as that used in MATLAB®: an M-D discrete sequence, $f[\mathbf{n}]$ of size $\mathbf{N}$, where $\mathbf{n} = [n_1, n_2, n_3, ..., n_M]^T$ and $\mathbf{N} = [N_1, N_2, N_3, ..., N_M]^T$, is stacked along the coordinate governed by dimensions N_1, then N_2, N_3, and so on. i.e. $\mathbf{f}[l] = f[\mathbf{n}]$, where the relationship between l and $\mathbf{n}$ is given by:

$$l = n_1 + n_2 N_1 + n_3 N_1 N_2 + \cdots + n_M N_1 N_2 \cdots N_{M-1} \tag{2.1}$$

where

$$\mathbf{n} = \begin{pmatrix} n_1 \\ n_2 \\ n_3 \\ \vdots \\ n_M \end{pmatrix} = \begin{pmatrix} l \bmod N_1 \\ \lfloor l/N_1 \rfloor \bmod N_2 \\ \lfloor l/(N_1 N_2) \rfloor \bmod N_3 \\ \vdots \\ \lfloor l/(N_1 N_2 \cdots N_{M-1}) \rfloor \bmod N_M \end{pmatrix}. \tag{2.2}$$

2.2 Linear transforms

Linear transforms generically refer to functions that map a vector from one space to another, and they are essential components in many science branches. There exist numerous linear transforms and they have the common nature of providing alternative ways of representing signals. Usually linear transforms can be employed to obtain further information which is not readily available in the raw signal format. Nowadays, the computational power of digital computers allows vastly improved efficiency in applying discrete transforms to sampled and digitised signals. Three transforms that have a close relation to this thesis work are reviewed here: discrete Fourier transform (DFT), discrete cosine transform (DCT) and discrete wavelet transform (DWT). The DFT forms the foundation of MRI, whereas DCT and DWT are common tools in image compression that serve important roles in later chapters.

2.2.1 Discrete Fourier transform

The Fourier transform is one form of the general Fourier analysis [SW71], which decomposes a signal into a series of sinusoidal functions at different frequencies. Specifically, the Fourier transform represents the signal in terms of complex exponentials, and the outcome provide frequency domain information of the signal. It is widely used in general signal processing studies and especially is the mathematical principle that modern MRI is based

on. The Fourier transform of an M-dimensional (M-D) signal $f(\mathbf{x})$ is given as:

$$F(\mathbf{u}) = \int_{-\infty}^{\infty} \cdots \int_{-\infty}^{\infty} f(\mathbf{x}) \exp(-i2\pi \mathbf{u}^T \mathbf{x}) d\mathbf{x}, \tag{2.3}$$

where $\mathbf{x} = [x_1, x_2, \ldots, x_M]^T \in \mathbb{R}^M$ and $\mathbf{u} = [u_1, u_2, \ldots, u_M]^T \in \mathbb{R}^M$, which respectively represent the location in the raw signal domain and the frequency domain. $F(\mathbf{u})$ is then the frequency component of $\exp(-i2\pi \mathbf{u}^T)$ present in the entire duration of the signal $f(\mathbf{x})$. Consequently, the inverse Fourier transform is given by

$$f(\mathbf{x}) = \int_{-\infty}^{\infty} \cdots \int_{-\infty}^{\infty} F(\mathbf{u}) \exp(i2\pi \mathbf{u}^T \mathbf{x}) d\mathbf{u}, \tag{2.4}$$

in the general M-D case.

In the analytical form of the continuous Fourier transform above, the signal is assumed to be defined over an infinite domain. However, usually only a finite portion of the signal that is of practical interest is discretely sampled and stored, which allows the discrete version of the Fourier transform to be conveniently applied:

$$F[\mathbf{k}] = \sum_{n_1=0}^{N_1-1} \cdots \sum_{n_M=0}^{N_M-1} f[\mathbf{n}] \exp\left[-i2\pi \mathbf{k}^T (\mathbf{n} \circ^{-1} \mathbf{N})\right], \tag{2.5}$$

where $\circ^{-1}$ denotes the element-wise division, and hence $\mathbf{n} \circ^{-1} \mathbf{N} = [n_1/N_1, n_2/N_2, \ldots, n_M/N_M]^T$; $\mathbf{n} = [n_1, n_2, \ldots, n_M]^T$ and $\mathbf{k} = [k_1, k_2, \ldots, k_M]^T$ are respectively the discrete analogy of $\mathbf{x}$ and $\mathbf{u}$ in the continuous case. The inverse DFT (IDFT) is then

$$f[\mathbf{n}] = \frac{1}{N_1 N_2 \ldots N_M} \sum_{k_1=0}^{N_1-1} \cdots \sum_{k_M=0}^{N_M-1} F[\mathbf{k}] \exp\left[i2\pi \mathbf{k}^T (\mathbf{n}/\mathbf{N})\right]. \tag{2.6}$$

By restricting the range of the signal for the transform to be that of $\mathbf{N} = [N_1, N_2, \cdots, N_M]^T$, applying a DFT implicitly implies a periodic extension of the signal $f[\mathbf{n}]$ outside the range with a period of $\mathbf{N}$. Thus:

$$\begin{aligned} f[\mathbf{n+N}] &= \sum_{k_1=0}^{N_1-1} \cdots \sum_{k_M=0}^{N_M-1} F[\mathbf{k}] \exp\left[i2\pi \mathbf{k}^T \{(\mathbf{n} + \mathbf{N}) \circ^{-1} \mathbf{N}\}\right] \\ &= \sum_{k_1=0}^{N_1-1} \cdots \sum_{k_M=0}^{N_M-1} F[\mathbf{k}] \exp\left[i2\pi \mathbf{k}^T (\mathbf{n} \circ^{-1} \mathbf{N}) + i2\pi \mathbf{k}^T\right] \\ &= f[\mathbf{n}] \end{aligned} \tag{2.7}$$

The DFT can be conveniently represented in matrix form as:

$$\mathbf{F} = \mathbf{W_N}\,\mathbf{f}, \tag{2.8}$$

where $\mathbf{f}$ is a column vector obtained by stacking the M-D signal $f_{\mathbf{n}}$ using the convention described in Section 2.1. The Fourier matrix $\mathbf{W_N}$ is obtained by taking the Kronecker product of 1D Fourier matrices corresponding to sizes $N_1, N_2 \cdots N_M$:

$$\mathbf{W_N} = \mathbf{W}_{N_M} \otimes \mathbf{W}_{N_{M-1}} \otimes \cdots \otimes W_{N_1}, \tag{2.9}$$

and the 1D Fourier matrix for a signal of length N is defined as:

$$(\mathbf{W}_N)_{kl} = \exp(-i2\pi kl/N), \tag{2.10}$$

where $k, l = 1, \ldots, N$.

2.2.2 Discrete cosine transform

The cosine transform is another form of Fourier analysis. As indicated by its name, only cosine functions are used as the basis functions compared to the complex exponentials of the Fourier transform. The difference in the basis functions used is due to the different assumptions made on the nature of the signal. In the cosine transform, the signal is assumed to be an even function over the infinite domain, therefore the odd terms vanish when taking the integral. The Fourier transform can be decomposed as two parts as:

$$\begin{aligned} F(\mathbf{u}) &= \int_{-\infty}^{\infty} \cdots \int_{-\infty}^{\infty} f(\mathbf{x}) \exp(-i2\pi \mathbf{u}^T\mathbf{x}) d\mathbf{x} \\ &= \int_{-\infty}^{\infty} \cdots \int_{-\infty}^{\infty} f(\mathbf{x}) \cos(2\pi \mathbf{u}^T\mathbf{x}) d\mathbf{x} - i \int_{-\infty}^{\infty} \cdots \int_{-\infty}^{\infty} f(\mathbf{x}) \sin(2\pi \mathbf{u}^T\mathbf{x}) d\mathbf{x} \end{aligned}. \tag{2.11}$$

Since $f(\mathbf{x})$ is assumed to be an even function, and so is the $f(\mathbf{x})\cos(2\pi \mathbf{u}^T\mathbf{x})$, whereas $f(\mathbf{x})(\sin(2\pi \mathbf{u}^T\mathbf{x})$ is an odd function. Thus:

$$F(\mathbf{u}) = \int_{-\infty}^{\infty} \cdots \int_{-\infty}^{\infty} f(\mathbf{x}) \cos(2\pi \mathbf{u}^T\mathbf{x}) d\mathbf{x} \tag{2.12}$$

In the discrete cosine transform (DCT), the use of cosine functions as the basis functions implies an even signal extension outside the boundaries within which the original signal is defined. However, such an assumption gives rise to two decisions to be made on the extensions over the signal boundaries: firstly, should an even extension of the signal be made on both sides of the signal or just on one side; secondly about where in the signal the even extension is made, i.e. for a discrete sequence [1,2,3], should the even extension be [3,2,1,1,2,3] or [3,2,1,2,3]. The ambiguities in the decisions give rise to different forms of

DCT [OSB99], and the signal extensions assumed by 4 commonly encountered forms are illustrated in Fig. 2.1 along with that of the DFT.

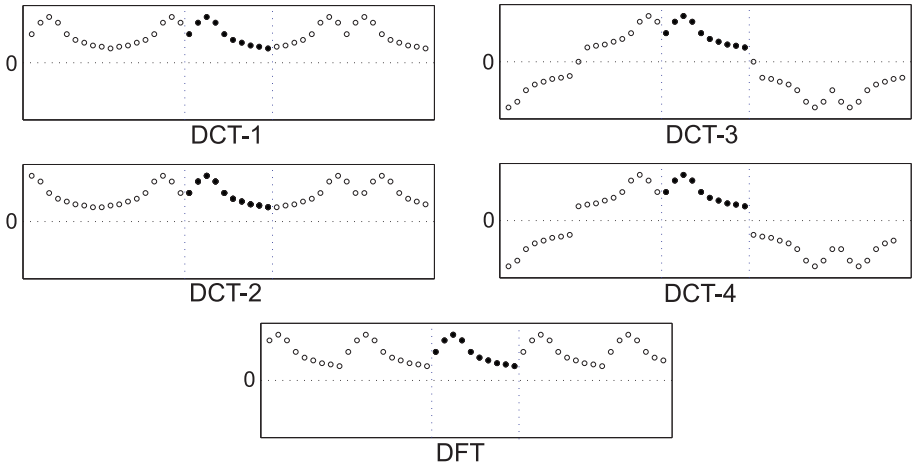

Figure 2.1 Discrete signal extensions over boundaries as implied by different forms of DCT and DFT. The 1D signal used for illustration consists of 10 discrete points that are filled, and the extensions of the signal made are empty. DCT-1 and DCT-2 imply the signal has even extensions over both sides of the boundaries, whereas DCT-3 and DCT-4 only assume the signal has even extension over the left boundary. DCT-1 and DCT-3 assumes the signal is even about the boundary points, whereas DCT-2 and DCT-4 assumes the signal is even about half point beyond the boundary points. DFT simply assumes the signal is periodic.

Comparing the different forms of signal extensions in Fig. 2.1, it is seen that the periodic extension as implied by the DFT tends to result in a high level of discontinuity at the boundaries, whose representation naturally requires a lot of sinusoidal functions. On the other hand, even extension as implied by DCT transforms increase the smoothness at boundaries and thus allow them to be employed in data compressions. DCT-2 is the most commonly used form as it is most likely to result in smooth signal extensions; it is therefore often simply referred as the DCT and so is the case in this thesis. For an M-D sequence, the DCT-2 is defined as:

$$F[\mathbf{k}] = \sum_{n_1=0}^{N_1-1} \cdots \sum_{n_M=0}^{N_M-1} f[\mathbf{n}] \; \{\cos(\pi/N_1(n_1+\frac{1}{2})k_1)\cos(\pi/N_2(n_2+\frac{1}{2})k_2))\cdots + \cos(\pi/N_M(n_M+\frac{1}{2})k_M)\}, \tag{2.13}$$

and the inverse transform is given as:

$$f[\mathbf{n}] = \frac{1}{2}F[1] + \sum_{n_1=0}^{N_1-1} \cdots \sum_{n_M=0}^{N_M-1} F[\mathbf{k}] \; \{\cos(\pi/N_1(k_1+\frac{1}{2})n_1)\cos(\pi/N_2(k_2+\frac{1}{2})n_2))\cdots + \cos(\pi/N_M(k_M+\frac{1}{2})n_M)\}, \tag{2.14}$$

where the first term arises from the boundary assumption made. Similarly to DFT, DCT

can also be performed in the matrix form and the M-D cosine matrix could can be obtained by taking the Kronecker products of 1D cosine matrices, which are defined as for a length N sequence as:

$$(W_N)_{kl} = \cos(\pi/N(k + \frac{1}{2})l)), \tag{2.15}$$

where $k, l = 0, 1, \ldots, N - 1$.

2.2.3 Discrete wavelet transform

Although Fourier series analysis provides frequency analysis of a signal, it does not distinguish between different locations for a particular frequency component within the raw signal. Consider the two signals shown in Fig. 2.2. The first signal consists of a unit amplitude sinusoid of varying frequency in different time periods: 10Hz over 0∼0.5 s, 20Hz over 0.5∼1 s, 30Hz over 1∼1.5 s and 40 Hz over 1.5∼2 s; the second signal is all the same but the frequency varies in the opposite time order. It is seen that these two clearly distinct signals have exactly the same discrete Fourier transform and they cannot be distinguished based on the Fourier analysis [1]. Thus the Fourier transform is only suited in dealing with stationary signals whose frequency components doe not change over time or space. However, realistic signals of interest tend to be dynamic signals who convey different frequency component at different time or space.

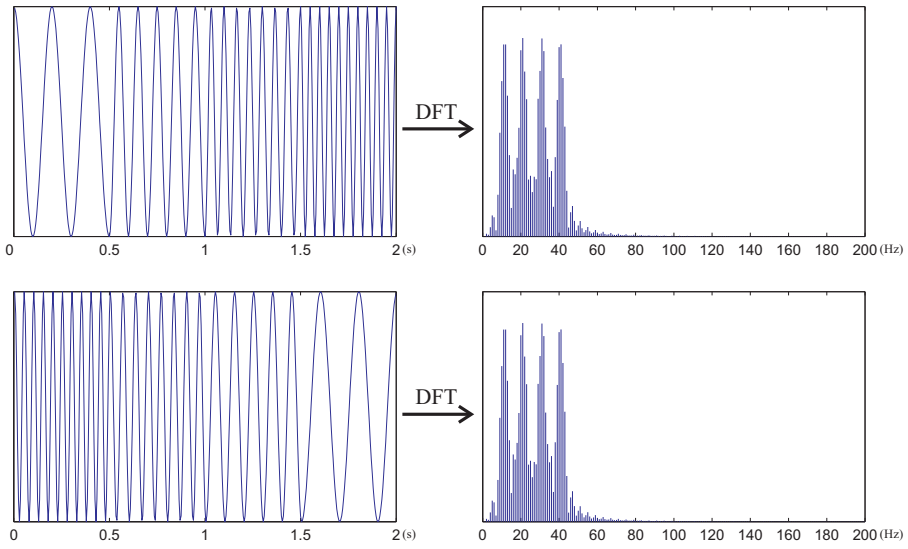

Figure 2.2 Comparing the Fourier transform of two dynamic signals that have the same frequency components but exist in different time order.

An obvious approach to overcome the above issue is to divide the raw signals into segments and apply Fourier analysis to each of the individual segments so that we could have both information of the frequency components and their locations, and this is exactly what

[1] Fourier transforms of the two signal do have different phases

short term Fourier transform (STFT) does. However, the puzzling question is, what sizes the segments should be? A small segment size will give good time resolution but bad frequency resolution, whereas a big segment size will give a good frequency resolution but a bad time resolution. Such trade-off agrees with the the Heisenberg's quantum mechanics uncertainty principle, which states that signal cannot be known exactly at both frequency and time. To overcome this issue, the wavelet transform performs a multi-resolution analysis: spectra are calculated using different segment sizes, which gives us a big collection of time-frequency (for convenience, time-frequency is used for now but it is equally applicable for the space-frequency domain) representation of the signal at different resolutions.

In the discrete wavelet transform (DWT), the desired multiresolution analysis is achieved by passing the signal through a series of digital filters. The signal is first passed through a half band low pass filter and a half band high pass filter (in which either the lower or higher half of the frequency band is maintained) that are characterized by their impulse response of g and h respectively. The filtering operation can be seen as convolution of the signal with their impulse responses:

$$\begin{aligned} y_{\text{low}} &= \sum_{k=1}^{k=N} x[k]g[N-k] \\ y_{\text{high}} &= \sum_{k=1}^{k=N} x[k]h[N-k] \end{aligned} \tag{2.16}$$

The filter outputs y_{low} and y_{high} now each contain half of the frequency range of the original signal x. As stated by Nyquist sampling law, the sampling rate in the outputs can be reduced by a factor of 2 without any loss of information, a process is that is known as down-sampling which discards every second sample. Such filtering and down-sampling is illustrated in Fig. 2.3. As the result of down-sampling, the time resolution is halved as

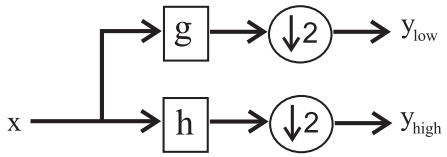

Figure 2.3 Passing a signal through half band filters decomposes its frequency band into two sections, each only requires half of the original sampling rate.

only half the number of samples are used to characterize the signal whereas the frequency resolution is doubled as the outputs only contain half of the frequency range of the input. Such a filtering process can be repeated by passing the low frequency output y_{low} into another set of down-sampling filters to further reduce the time resolution and improve the frequency resolution as shown in Fig. 2.4.

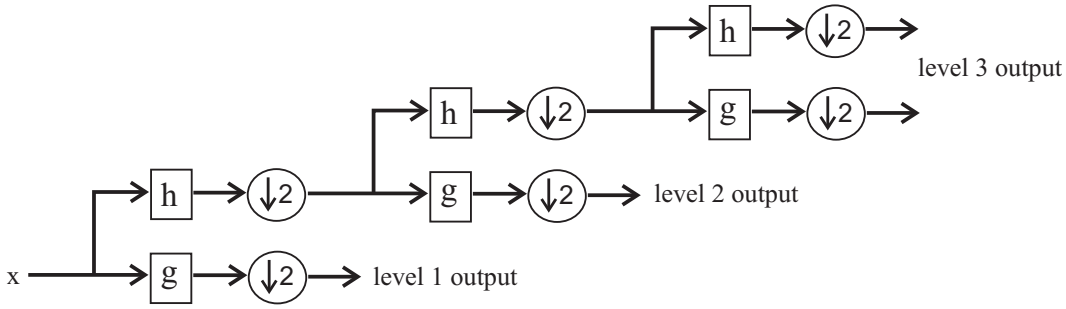

Figure 2.4 Passing a signal through a half band filter bank that consists of achieves multiple levels of frequency decomposition, outputs at different filter levels represent different levels of trade off between time resolution and frequency resolution.

The outputs at the the filter bank are a range of time-frequency signal representations that have good time resolution and poor frequency resolution at high frequencies and good frequency resolution and poor time resolution at low frequencies. The trade-off between the time and frequency resolution in the outputs is determined by the number of levels in the filter bank. For many natural signals, most energy tends to be concentrated within certain time-frequency bands, and thus other time-frequency representations can be discarded with little loss of signal information. This property makes DWT suitable for signal compression.

2.3 Inverse problem

The inverse problem can be broadly defined as the process of finding the underlying parameters given a set of observations that are derived from the set the parameters. For example, find x such that

$$y = W(x) \tag{2.17}$$

where y is the observation made, and W is the observation process assumed. In cases where W is a linear operator, Eq. (2.17) can be put into a matrix form:

$$\mathbf{y} = \mathbf{W}\mathbf{x} \tag{2.18}$$

where the $\mathbf{x}$ and $\mathbf{y}$ are respectively the vectors containing the parameters sought and the observations made, and matrix $\mathbf{W}$ denotes the linear observation process.

Image recovery in MRI is a linear inverse problem, in which the observation process $\mathbf{W}$ is the sample acquisition in the Fourier space and observations $\mathbf{F}$ are the Fourier transform

coefficients measured, and the parameter $\mathbf{f}$ to be sought is the underlying image, so that:

$$\mathbf{F} = \mathbf{W}\mathbf{f} \tag{2.19}$$

Often an unique solution does not exist for Eq. (2.19) due to the imperfection in knowledge about the observation process, such as the presence of noise, the incomplete data measurements, etc. An approximate solution is sought instead, and solving for an approximate solution can be seen as an optimization process for a given set of optimization criteria. With the presence of noise, least squares is a commonly used optimization technique and is given by:

$$\check{\mathbf{f}} = \arg\min_{\mathbf{f}} \frac{1}{2} \sum_{i=1}^{i=M} (\mathbf{F}[i] - \tilde{\mathbf{F}}[i])^2, \quad \tilde{\mathbf{F}} = \mathbf{W}\mathbf{f}, \tag{2.20}$$

where $\check{\mathbf{f}}$ is an estimate of the underlying image $\mathbf{f}$ that is of length M. Hence Eq. (2.20) measures the sum of the squares of the difference between the actual measurements and the measurements derived from the estimation $\check{\mathbf{f}}$. In linear algebra form, the optimization can be written as:

$$\check{\mathbf{f}} = \arg\min_{\mathbf{f}} (||\mathbf{F} - \mathbf{W}\mathbf{f}||_2) \tag{2.21}$$

where $||\cdot||_n$ denotes the n-th Euclidean norm, and is defined as $||\mathbf{x}||_n = \sum_{i=1}^{i=M} \sqrt[n]{\mathbf{x}[i]^n}$.

Many techniques have been developed to solve Eq. (2.21), and they can be classified as either direct methods or iterative methods. In direct methods, the Moore-Penrose inverse (also known as pseudo-inverse) of the known matrix $\mathbf{W}$ is taken to gain an optimal estimation of $\mathbf{f}$ in the least squares sense. Iterative methods may also be employed to solve Eq. (2.21). In contrast to the direct approach, the iterative methods attempt to solve the inverse problem by finding successive approximations to the solution starting from an initial guess. Commonly encountered iterative methods are steepest gradient descent [Sny05], the projection onto convex sets (POCS) [YW82] and conjugate gradients [HS52]. Compared to the direct matrix inversion, iterative methods are often much less computationally demanding, and hence are favored in cases when the size of the matrix is large. However the drawback of the the iterative methods is their slow convergence, and the analysis of the number of iterations to gain the approximation with a desired level of accuracy is usually difficult.

Often, the inverse problem is ill-conditioned, which makes solving Eq. (2.21) particularly difficult. Other prior knowledge of the underlying image may be incorporated as addi-

tional constraints in Eq. (2.21) to aid the image recovery:

$$\check{\mathbf{f}} = \arg\min_{\mathbf{f}} \ ||\mathbf{F} - \mathbf{W}\mathbf{f}||_2, \quad \text{subject to} \ \ g(\mathbf{f}) \tag{2.22}$$

where $g(\mathbf{f})$ represents prior knowledge of the image $\mathbf{f}$ to be used. A significant portion of the work in this thesis focuses on image recovery with various types of image constraints used, and addresses the following questions:

1. What types of prior knowledge can be used?
2. How should the prior knowledge be used?
3. What are the consequences of using a specific type of prior knowledge?

Chapter 3

Magnetic resonance imaging

In this chapter, the background of magnetic resonance imaging is provided for readers with little knowledge of the subject. Subjects including the nuclear magnetic resonance physics, the molecule excitation and image formation are covered. However it is intended to be comprehensive but non-detailed. For a more thorough and systematic description of MRI, readers are encouraged to refer to [McR03, Nis96].

3.1 Nuclear magnetic resonance

Nuclear magnetic resonance (NMR) refers to the phenomenon that atoms with an odd number of protons and/or neutrons possess a 'spin' property, which can be described as the nuclear angular moment at the quantum mechanic level. A commonly used analogy to the spin of an individual atom is a spinning top spinning around its own axis. The most relevant atom in biology is the hydrogen atoms (^1H) due to their abundance in water. It is the spinning properties of these hydrogen atoms make the MR imaging feasible.

Without the presence of an external magnetic field, all the spins of the hydrogen atoms are randomly orientated (Fig. 3.1(a)) due to thermal noise, and as the result the overall net magnetic momentum is zero. However, when an external magnetic field B_0 is applied, all the spins will be aligned with field and will adopt either the field direction or the anti field direction. However, there will be slightly more atoms adopting the field direction due to its lower energy state, which gives rise to a non-zero magnetic spin moment in the field direction (Fig. 3.1.(b)). A single spin in the field direction is used to represent this net magnetic moment in the following text for ease of illustration.

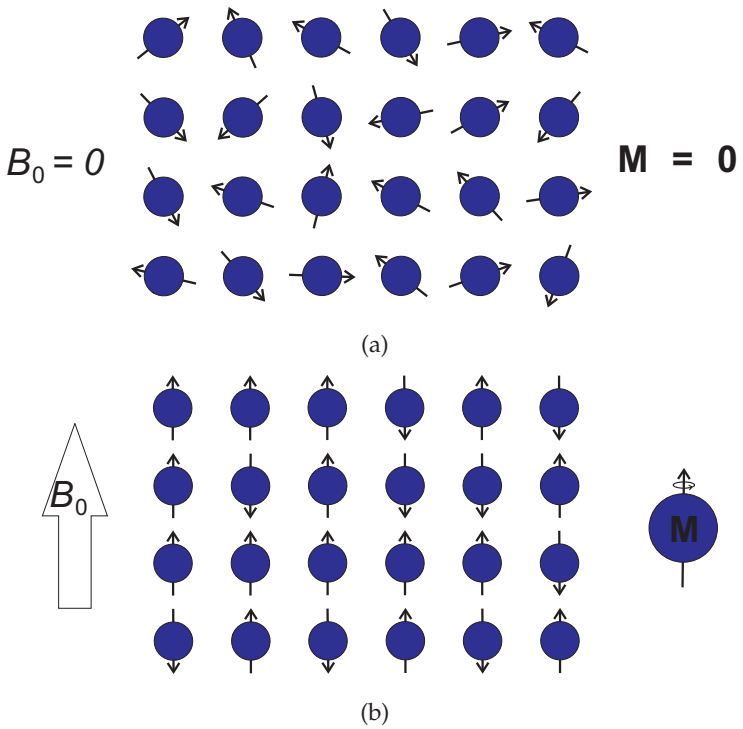

Figure 3.1 Depiction of the behavior of bulk atom spins. Atoms are represented by solid circles, with the arrows indicating their spin orientations. (a) Without the presence of an external magnetic field, spins are randomly orientated due to thermal noise, thus the overall magnetization is zero. (b) when an external magnetic field is applied, spins align up with the field and a greater number of spins adopt the field direction, giving rise to a non-zero net magnetization moment in the field direction.

A very important physical phenomenon which takes place with the presence of an external field is that the spinning atoms exhibit a Larmor resonance frequency ω_0 that is determined by the field strength B_0:

$$\omega_0 = \gamma B_0, \tag{3.1}$$

where γ is the so-called gyromagnetic ratio [Nis96]. Different types of atoms have different gyromagnetic ratio constants and that of hydrogen atoms (^1H) is 42.58MHz/T. Thus at the commonly used field strengths used by commercial scanners at 1.5T and 3.0T the $Larmor$ frequencies of hydrogen atoms are respectively 63.87Mhz and 127.74Mhz.

3.2 Signal generation

In the presence of a constant magnetic field B_0, the spins are at their equilibrium in the field direction (Fig. 3.2(a)). The field direction is referred as the z-axis, and the $x-y$ plane which the field direction is perpendicular to is referred as the transverse plane. When

a radio frequency (RF) magnetic field at the Larmor frequency is applied, the spins are excited and pushed away from their equilibrium at z-axis towards the transverse plane, and start precessing about the z axis. The trajectory towards the transverse plane can be depicted in the 'laboratory frame' [Nis96] as shown in Fig. 3.2.(b). Classically, it can be represented by a vector that is tipped away from the main axis by an angle α (Fig. 3.2.(c)), which is known as the flip angle. The size of the flip angle is determined by the amplitude of the RF magnetic field applied and is an important parameter in MR pulse design. This tipped magnetization vector gives rise to a transverse plane component M_{xy}. According to Faraday's law of induction, this transverse plane component can be detected by a RF receiver coil that is oriented with axis perpendicular to the magnetic field direction.

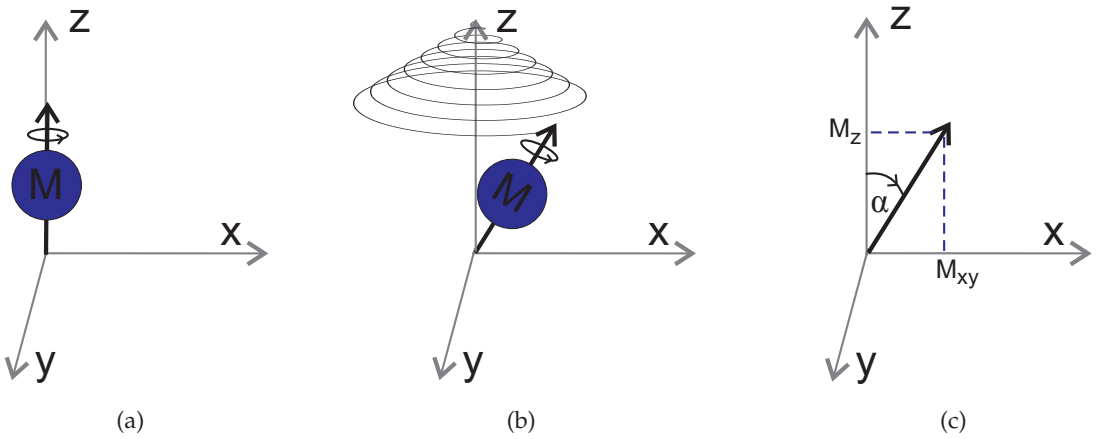

Figure 3.2 Excitation of the spin with the application of a RF pulse. (a) The spin is at the its equilibrium on the z axis, (b) the laboratory frame depicting its path towards the transverse plane after excitation, (c) the excitation can be equivalently represented by a vector rotation by the flip angle α from the z axis, and results in non-zero projection on the $x - y$ plane.

After the RF magnetic field is removed, the spins start returning to the equilibrium in the field direction while keep on precessing at the Larmor frequency about the z axis. As the result, the z axis projection M_z (or equivalently the longitudinal magnitisation) gradually increases, and T_1 is the time constant (also known as the longitudinal or spin-lattice relaxation time) that describes the rate at which net magnetisation in the longitudinal direction returns to its equilibrium level as shown in Fig. 3.3.(a). Simultaneously, but independently, the transverse plane projection M_{xy} (or equivalently the transversal magnitisation) will gradually decrease, and T_2 is the time constant (also known as the transverse or spin-spin relaxation time) that describes the rate at which net magnetisation in the transverse plane decays as shown in Fig. 3.3.(b). Different body tissues are featured with distinctive T_1 and T_2 values, which allow good tissue contrast to be achieved in T_1 or T_2 weighted images. A third commonly used contrast mechanism is the proton density, which measures the num-

ber of protons per unit tissue that contribute to the detected signal when the T_1 and T_2 effects are minimized. The ability of being able to choose different contrast mechanisms gives MRI great imaging flexibility over other imaging techniques.

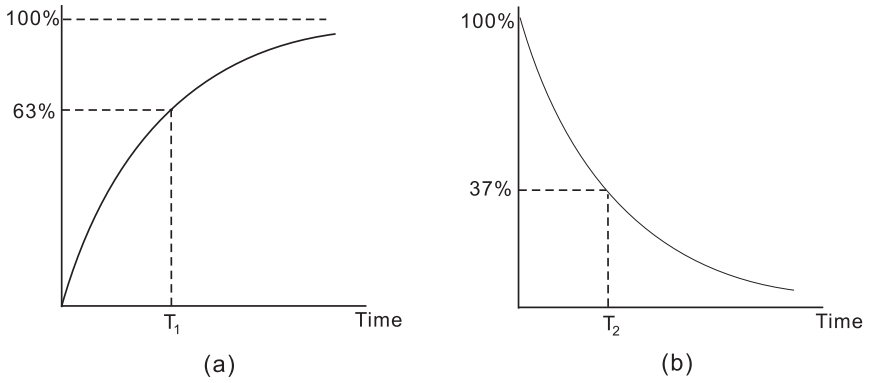

Figure 3.3 After the removal of RF magnetic field, increase and decay of the longitudinal and transversal magnetisation take place, and follow an exponential trajectory towards equilibrium. (a) T_1 and (b) T_2 are the time constants that depict how rapidly each process occurs.

3.3 Image formation

Although the principle of nuclear magnetic resonance has long been applied in chemical analysis, MRI was not born until late 1970s [Lau73] as the direct measurement of NMR signal contains no spatial information. Consider the case where a patient is placed within an uniform magnetic field B_0 (Fig. 3.4(a)). As determined by Eq. (3.1), all the hydrogen molecules throughout the body have the same larmor frequency. An RF field applied at this frequency will simultaneously excite all the molecules and give an output that is the sum of those of all these spins, which does not provide any spatial information. In MRI, the localization of the spin excitations is achieved by three gradient coils that generate additional gradient fields with linearly varying field strengths in x, y, z direction respectively. The linear gradients are thus defined as:

$$G_x = \frac{\partial B_z}{\partial x} , \qquad G_y = \frac{\partial B_z}{\partial y} , \qquad G_z = \frac{\partial B_z}{\partial z} .$$

3.3.1 Selective excitation

The first step in spatial encoding is selective excitation. With the application of gradient field(s), the resulting overall field strength is made to vary linearly along a certain direction, and consequently are the Larmor frequencies of the spins. For instance if a gradient field is applied in the z axis (Fig. 3.4(b)), a RF pulse with designated frequency band can be applied so that only molecules that are within a narrow range of z locations are excited.

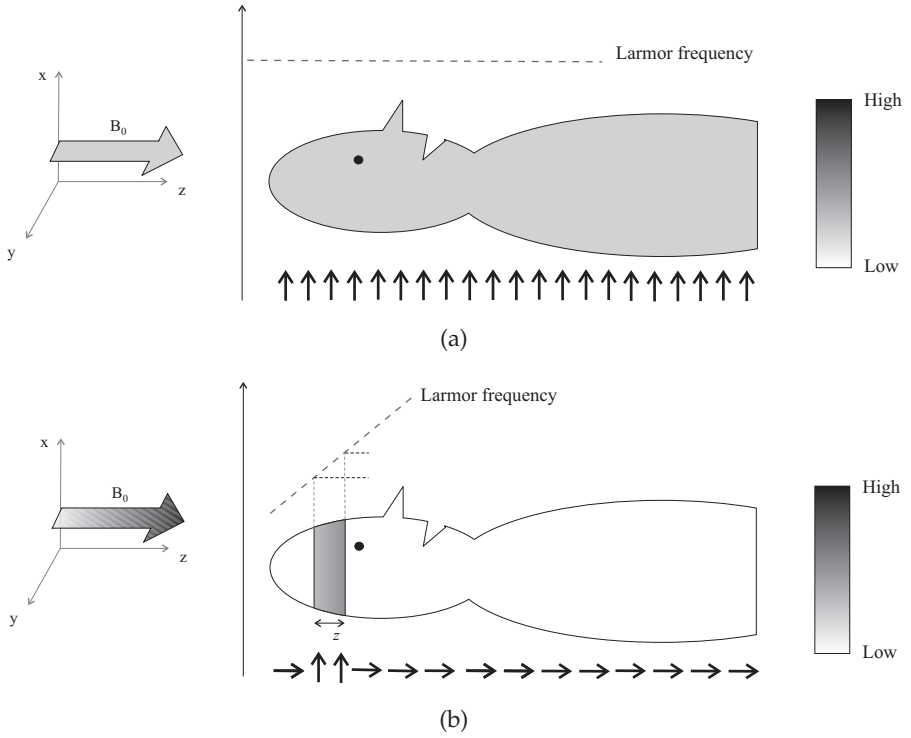

Figure 3.4 Selective excitation by applying a linear gradient field. (a) when the patient is under an uniform magnetic field B_0 (as indicated by the uniform color band), all the spins along the z axis (field direction) will be simultaneously excited at the same Larmor frequency. (b) with the application of a linearly varying field (as indicated by the linearly varying color band), it is possible to only excite molecules within a narrow range of z locations by applying a RF pulse sequence with a certain frequency band.

3.3.2 Imaging plane

As mentioned above, it is possible to obtain a linear gradient field in any direction using a combination of the gradient coils, and thus so is the selective excitation. To avoid the ambiguities that would arise in using directions x, y, z to describe image orientations, anatomical directions are used in defining the image orientations: left to right (L-R), anterior to posterior (A-P) and superior to inferior (S-I). The three commonly used orthogonal imaging planes are defined by these directions as illustrated in Fig. 3.5 below, and any other imaging planes at other angles are referred as the oblique planes.

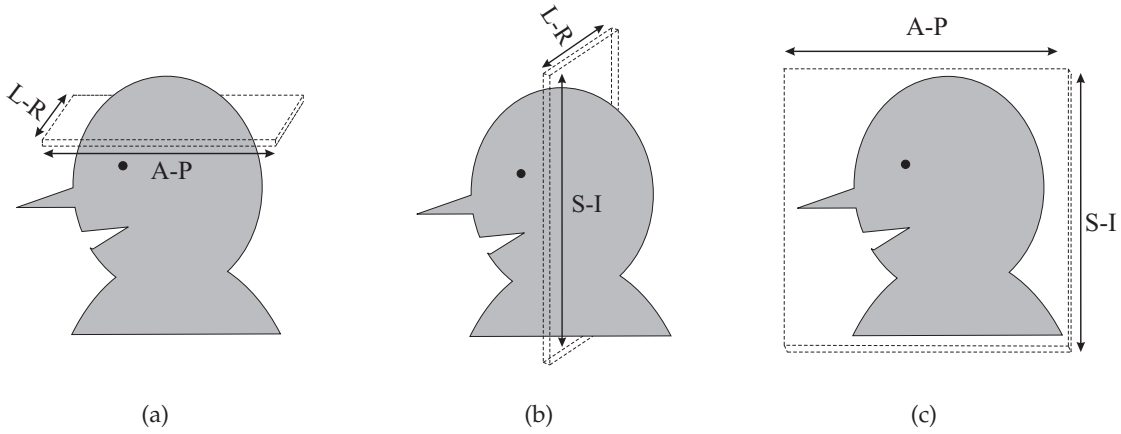

Figure 3.5 Commonly used imaging planes: (a) axial, (b) coronal, (c) sagittal. The orthogonal planes are defined by the anatomical directions : left-right (L-R), anterior-posterior (A-P), superior-inferior (S-I) as indicated.

3.3.3 Fourier imaging

Given that the region to be imaged has been selectively excited, it is then the objective to know each $M(x, y)$ (or $M(x, y, z)$ depending on whether it is 2D or 3D excitation) within that excited region so that a contrast map of different tissues can be formed within the excited region. Instead of measuring each spin individually, which is practically infeasible, we measure the Fourier coefficients of the overall magnetization. Then image reconstructions are made based on the Fourier coefficients collected. Fourier space is also commonly known as 'k-space' in MR community, and will be referred to in this way in the rest of this thesis. There are different imaging methods depending on the data trajectory in k-space, i.e. the order in which the Fourier coefficients are measured. The most commonly utilized method is Cartesian Fourier (2D or 3D) imaging, in which Fourier coefficients are taken on the Cartesian grids in a line-by-line fashion. In the following sections, the Fourier encoding of the magnetization spins are discussed in both cases of 2D imaging and 3D imaging, assuming that the field direction is at the S-I direction (z-axis) as depicted in Fig. 3.5.

2D Fourier imaging

In this case, the excited region is thin enough to be treated as a 2D plane. The desired 2D Fourier encodings are achieved by successive application of two field gradients (for example, G_x and G_y for x-y plane), which respectively act as either frequency encoding (FE) or phase encoding (PE). The key difference between PE and FE is that PE 'presets' the spins for measurement, whereas measurements are continuously taken in the duration of FE. In Fig. 3.6, the interaction of the gradient coils and the overall spin magnetization

is illustrated, and the corresponding k-space data measurements are shown. With respect to Fig. 3.6, the following is a description of the different phases in 2D Fourier imaging sequence:

1. **Time point 1**
   Immediately after a 90° selective pulse, all the spins are in phase immediately after the selective excitation [1]. At this point, the 2D spin plane is essentially weighted with a unity plane, thus the measurement gained is simply the sum of all the spins and which is equivalent to the DC term in the Fourier space.

2. **During time point 1 to 2**
   The PE is applied in the y direction. Application of a y field gradient gradient (G_y) makes the field strength increase linearly along the y axis and also does the precessing frequency. There is an increasing phase variation of the spins along the y axis, changing linearly with time.

3. **Time point 2** The PE is switched off, the FE is switched on by applying G_x. At this time instant, all the spins along the y axis again precess at the same frequency, however they have a linear phase variation. Effectively, the overall magnetization is weighted by a complex exponential function $exp(-i2\pi y)$, and thus the measurement which is the sum of all the magnitisations corresponds to a point along the k_y axis in the k-space.

4. **During time point 2 to 3** While FE (G_x) is applied, there is a linear increase in precession frequency in the x direction. If a snap shot is taken at one time instant, there is a linear phase variation in the precessions that can be seen as a weighting function of $exp(-i2\pi x)$ (such as that in diagram 3), and this corresponds to a point $< k_x, k_y >$ in the k-space plane where k_y is determined by the previous PE applied. As time goes by, the phase variation increases and effectively it is moving along the k_x axis at a specific k_y in the k-space. The output signal is sampled throughout this time interval.

5. **Time point 3** The FE is switched off. By now a line has been acquired in the k_x direction.

6. **During time point 3 to 4** A delay occurs to allow the spins to return to their z axis equilibrium before the application of the next excitation pulse. The total time between two successive excitation pulses are referred as the repetition time and is a determining factor in the total scan time.

[1] To simplify the task, we assume that all the excited spins in the transverse plane are initially in phase. In practice, an additional refocusing RF pulse is required to bring all the spins in phase.

7. **During time point 4 to 6** The same process is repeated however with different PE encoding to acquire a line in the k_x direction at a different k_y.

In this way the 2D k-space is populated in a line-by-line fashion, and the inverse Fourier transform of the complete k-space gives an image of the underlying magnetization.

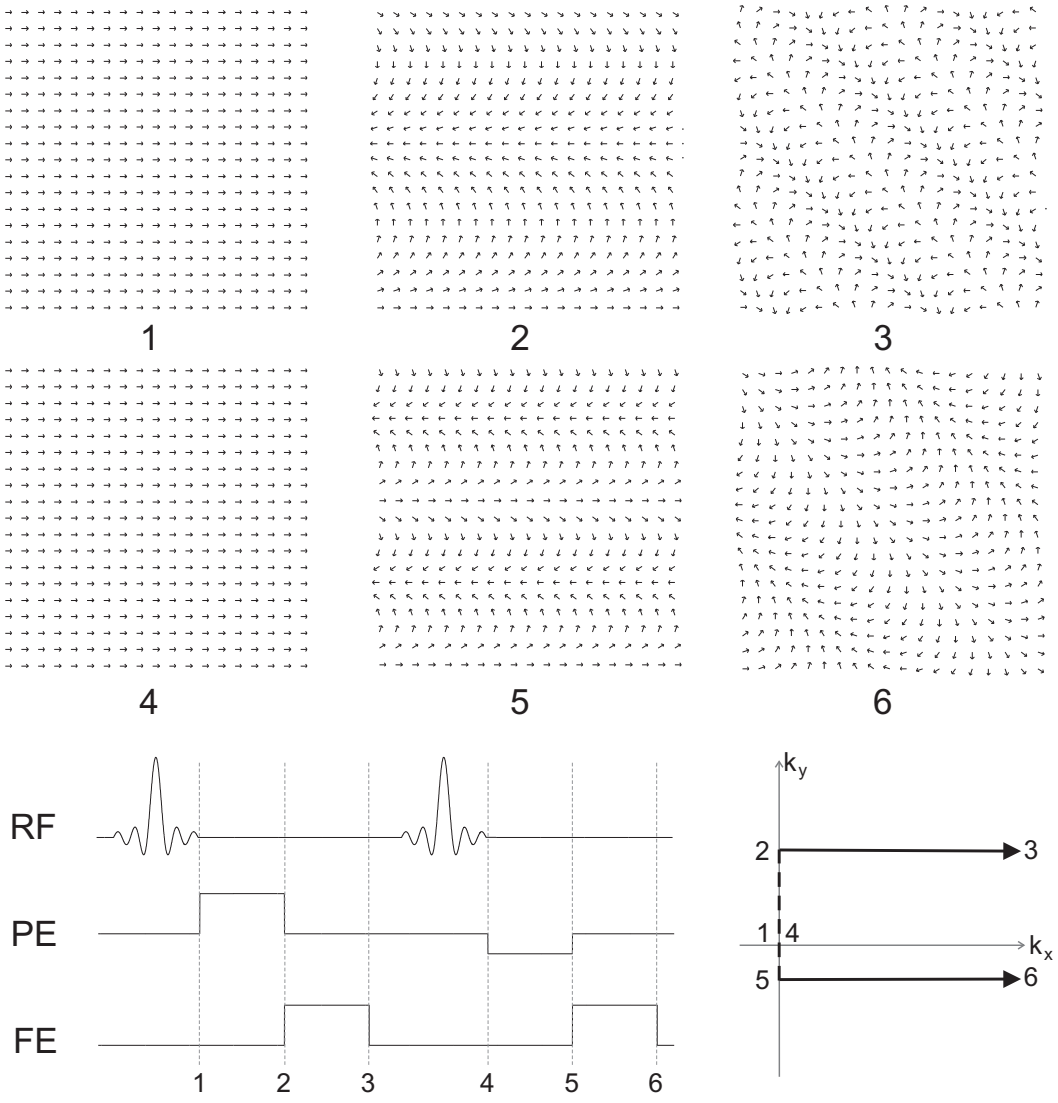

Figure 3.6 Illustration of Fourier encoding of the excited spins within a 2D plane. The top diagrams (numbered as 1 to 6) depict the spin distributions that result from the application of gradient field at different time points (bottom left), and the corresponding k-space data acquisition (bottom right).

3D Fourier imaging

In this case, the excited region is treated as a 3D object. Consequently, the Fourier encoding of the overall excited magnitisation require the employment of all the 3 field gradients, out

of which two will act as PE and one will be the FE. The same excitation strategy as depicted in Fig. 3.6 is applied, however two field gradients (G_x, G_y)are simultaneously applied, giving increments in precessing frequency along both axes. Having left both gradients on for a while, a movement from the k-space origin to a k_x, k_y in the transverse plane is achieved. Application of a G_z gradient then results in a read-out line along the k_z axis with the specific $< k_x, k_y >$. This process is repeated until the entire 3D k-space volume is sampled. A 3D inverse Fourier transform then leads to an image of the underlying magnetization volume.

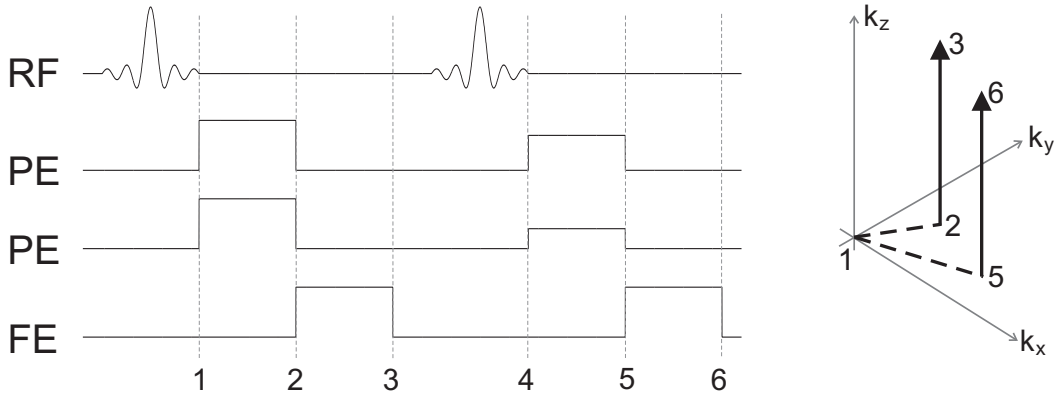

Figure 3.7 Illustration of the application of gradient fields and the corresponding data acquisitions in 3D k-space. Two PE gradients (G_x, G_y) and one FE gradient (G_z) are used. During time point 1 to time point 6, two read-out lines in the k_z directions are made.

3.4 Data acquisition considerations

In Fourier imaging, there are two decisions on sampling to be made in order to achieve a proper image recovery: the data sampling rates and data set size, which respectively determine the field of view (FOV) and image spatial resolution.

3.4.1 Sampling rate

Sampling in the signal domain causes the periodic repetition of the signal's representation in the Fourier domain, and vise versa. In order to avoid aliasing artifacts, which refers to the overlapping of the repetitions, the sampling rate needs to satisfy the Nyquist sampling limit [Sha49]. Thus the sampling rate of a temporally (or spatially) varying signal needs to be the twice its highest frequency component. As illustrated in Fig. 3.8, in case of sampling a 1D k-space, the sample spacing (Δk) needs to be selected so that $\frac{1}{\Delta k}$ is at least as large as the support of the signal.

In MRI, sampling is made of the signal's Fourier representation in 2D or 3D k-space, and

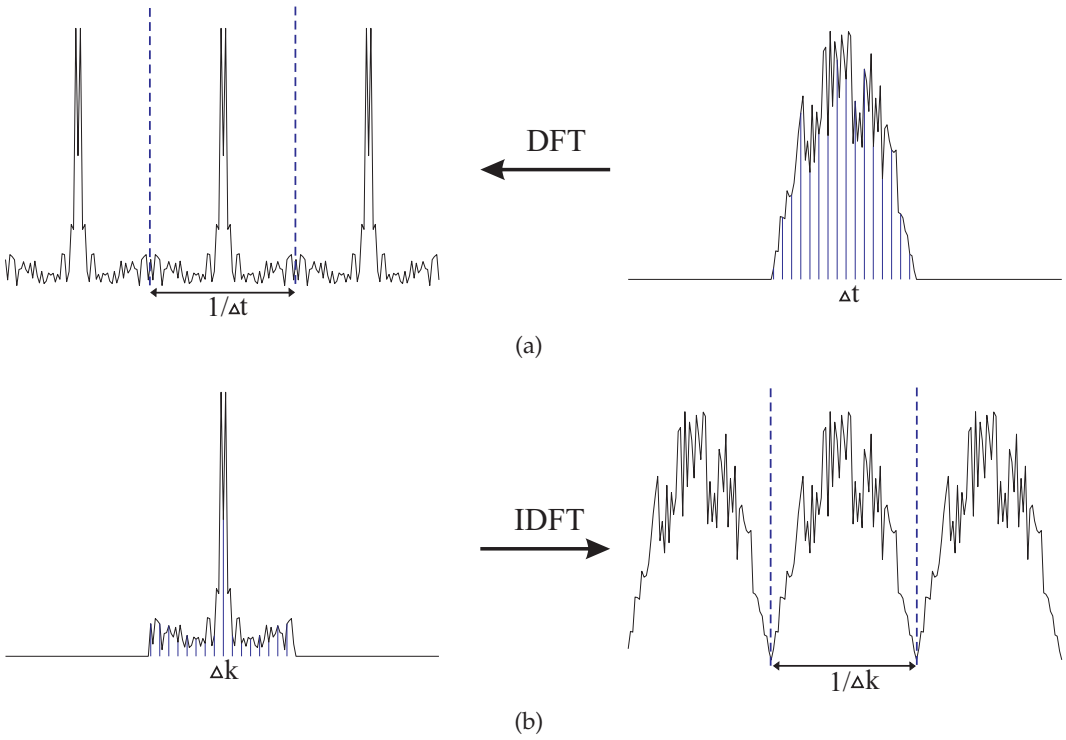

Figure 3.8 Sampling a 1D signal at the Nyquist sampling limit: (a) sampling the spatial signal with a sample gap Δt results in periodic repetition of its Fourier transform each $\frac{1}{\Delta t}$ along the frequency axis; (b) sampling its Fourier transform at the rate of Δk results in repetition of the spatial signal each $\frac{1}{\Delta k}$ along the x axis.

image recovery is made in the corresponding 2D or 3D spatial domain. Thus the gap between neighboring k-space samples is related to the field of view (FOV, the image's spatial domain extent) in each direction as:

$$\begin{aligned} \Delta k_x &= \frac{1}{FOV_x} \\ \Delta k_y &= \frac{1}{FOV_y} \end{aligned} \tag{3.2}$$

Hence to avoid aliasing artifacts, the object imaged should not have spatial extents exceeding $\frac{1}{\Delta k_x}$ and $\frac{1}{\Delta k_y}$ in the x and y direction.

3.4.2 Data acquisition size

The data acquisition size refers to the number of samples to be measured in each direction for a given sample spacing and thus determines the area of k-space coverage. As illustrated in Fig. 3.9, when it transfers to the image domain, the data acquisition size determines the

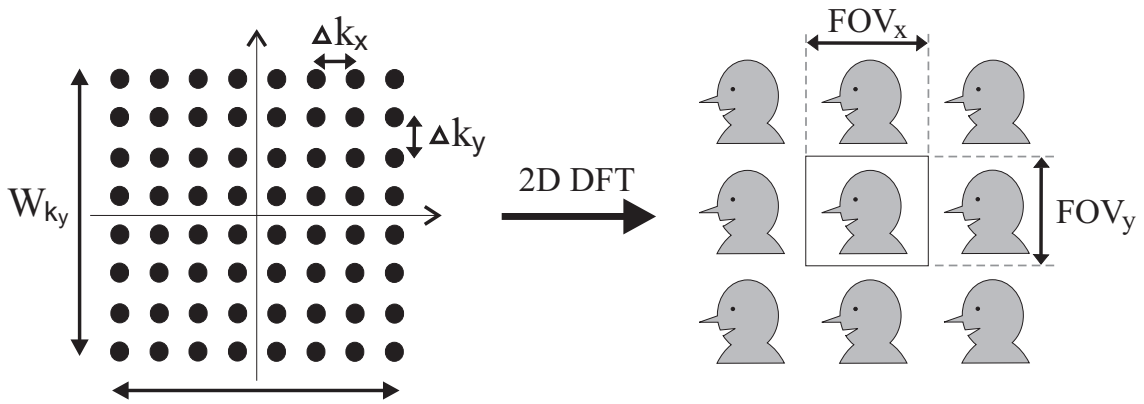

Figure 3.9 Sampling in the 2D k-space results in periodic repetition of the image in both directions. On the left, samples in the 2D k-space are represented by dots on Cartesian grids. The spacing between the samples in each direction determines the respective size of FOV.

spatial resolution of the image.

$$\Delta x = \frac{FOV_x}{N_x} = \frac{1}{\Delta k_x N_x} = \frac{1}{W_{k_x}} \tag{3.3}$$

$$\Delta y = \frac{FOV_y}{N_y} = \frac{1}{\Delta k_y N_y} = \frac{1}{W_{k_y}} \tag{3.4}$$

A high spatial resolution image is usually desirable to reveal fine features in the image, however comes at the cost of a long data acquisition time (increased amount of data acquisition). This trade-off between spatial resolution and scan time will be investigated throughout the rest of this thesis.

3.5 Scan time reduction

The line-by-line data acquisition used in conventional Fourier MRI gives rise to an intrinsically long scan time. With the employment of fast data acquisition sequences, data acquisition for a single 2D slice can be completed within tens of seconds, however the coverage of a 3D volume (either by acquiring consecutive 2D slices or direct 3D Fourier imaging) may still take up to 15 to 20 minutes. A long scan time gives rise to several potential problems, and the most severe issue is motion during data acquisition. Since the data acquisition takes place in the Fourier space, motion of the imaged object in the scan duration causes data inconsistency which will appear as ghosting artifacts in the recovered image. Fig. 3.10 shows a recovered image from a scan in which the patient's (a baby in this case) motion took place.

Apart from the bulk motion effects caused by patient's movement, other types of natural motion are often encountered in various types of imaging situation, such as respira-

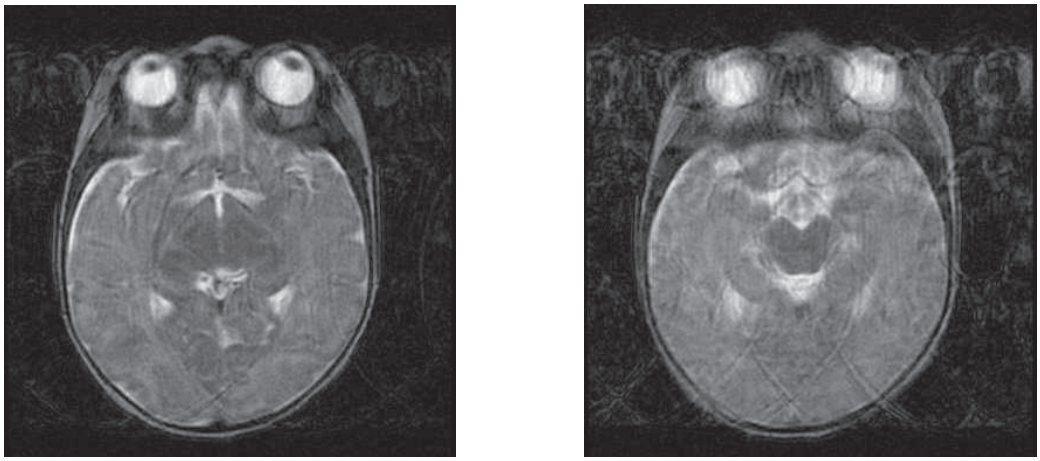

(a) (b)

Figure 3.10 The effects of patient motion during data acquisition. The axial brain image slice is corrupted by (a) mild,(b) severe motion artifacts. (Originally from Lianne Woodward, Child Development Research Group, University of Canterbury, adopted from Julian Maclaren's doctoral thesis [Mac07]).

tional motion, cardiac motion and blood flow. Various approaches have been taken to either attempt to prevent the motion during the scan or compensate the motion artifacts in the post-processing [ATPA05, MBMW07, LBB+85, FSPC97], and different levels of success have been achieved.

Another more fundamental approach to reduce the motion artifacts is to reduce the necessary scan time. In general, fast scans come in two flavors: either employing a faster imaging sequence or reduce the amount of data acquisition.

3.5.1 Fast imaging sequences

In the conventional Fourier data acquisition as illustrated in Section 3.3.3, the total scan time is roughly given by $TR \times N$, where N is the number of the PE steps and TR is the repetition time that is taken for each individual acquisition. One approach to achieve an overall faster data acquisition is to acquire multiple k-space lines within a single repetition time interval, and this is what echo planar imaging (EPI) [Man77] and Fast spin echo (FSE) [HNF86] attempt to achieve. As illustrated in Fig. 3.11, multiple read-outs are made and lead to a trajectory that covers multiple lines in k-space in a single excitation or single shot. Thus a rectangular k-space can be covered in a single or several shot(s), allowing significant scan time reduction. However, practical implementation of EPI has several severe limitations, such as the demanding requirement on gradient field switching, and therefore is prone to various types of artifacts [HBV99].

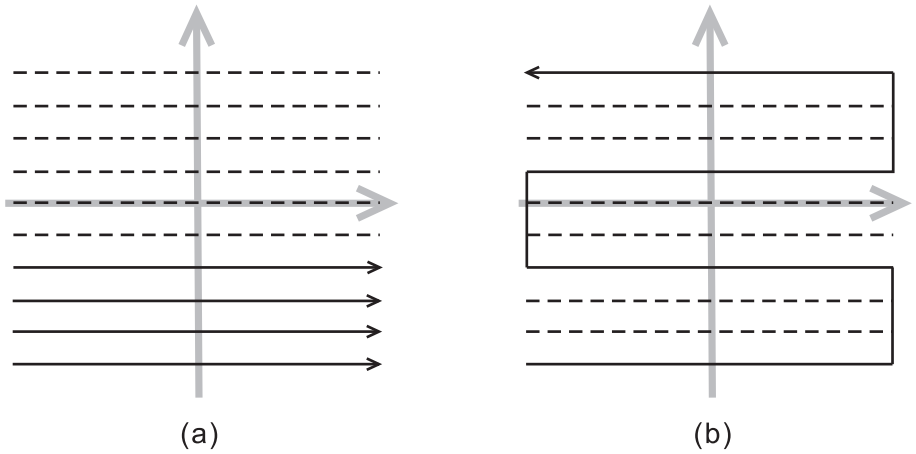

Figure 3.11 Data readout in conventional Fourier imaging and fast spin echo. In (a) conventional Fourier imaging, one single read-out is made per excitation that gives one line in k-space, and the number of excitations equals to the number of k-space lines. In (b) fast spin echo, one excitation is followed by several read-outs that transverses several lines in k-space, hence the entire k-space can be covered by using much smaller number of excitations.

3.5.2 Data under-sampling

Since fast acquisition sequences are intrinsically constrained by the engineering and physical limits, other approaches seek to shorten the scan time by intentionally skipping k-space samples. As discussed previously, either reducing the sampling rate or the data sample size has adverse effects in the image reconstruction if a Fourier transform is directly performed on the incomplete data set. However, prior knowledge of the image can be exploited in the post-processing to compensate for the missing Fourier coefficients. For instance, in the so called half Fourier imaging, as the imaged object is always real in practice, its Fourier transform is featured with Hermitian symmetry. Thus in principal only half of the symmetrical k-space needs to be actually measured, and the other half can be generated as the complex conjugates of the measured samples. Parallel imaging to be discussed in Chapter 4 is another example. In general, based on the image prior knowledge various types of constraints can be imposed on the image reconstruction process to achieve image recovery from incomplete measurements, which is the topic that is discussed throughout this thesis.

Chapter 4

Parallel MR imaging

Parallel magnetic resonance imaging (pMRI) was developed in response to the desire to further reduce the necessary scan time without sacrificing spatial resolution. In short, pMRI employs multiple RF receiver coils that have different sensitivities to the magnetization signal (commonly referred to as coil sensitivity) within the FOV, then a reduced number of phase encoding (PE) steps are performed to achieve scan time reduction. In post processing, the simultaneously acquired partial k-space data sets are combined to form a final image. In this chapter, an overview of the pMRI techniques is provided. Firstly, the difference between conventional single coil MR imaging and parallel MR imaging is discussed. Then history of pMRI technique development is given, followed by an overview of the different pMRI methods currently in use. Lastly, a new motion correction method based on pMRI is proposed.

4.1 An idealistic example

Sampling density reduction using multiple receiver coils can be illustrated in a simple example in Fig. 4.1, where two rectangular coils are placed in series along the PE direction to cover a complete rectangular FOV. Assume each RF coil is only sensitive to $\frac{1}{2}$ of the FOV as labeled and features with uniform coil sensitivity within the designated FOV, each receiver coil only sees half of the FOV. Then essentially the imaging FOV for each receiver coil is halved, which means the sample spacing can be doubled without causing aliasing artifacts in the image as discussed in Section 3.4.1. As shown in Fig. 4.1, only $\frac{1}{2}$ of total number of phase encoding steps are acquired at doubled sample spacing, while maintaining the same k-space coverage and consequently the spatial resolution. In post-processing, images of individual partition of the FOV can be simply cascaded to form a complete FOV image.

However in Fig. 4.1, the assumption of the sharp coil sensitivity cut-off across the FOV

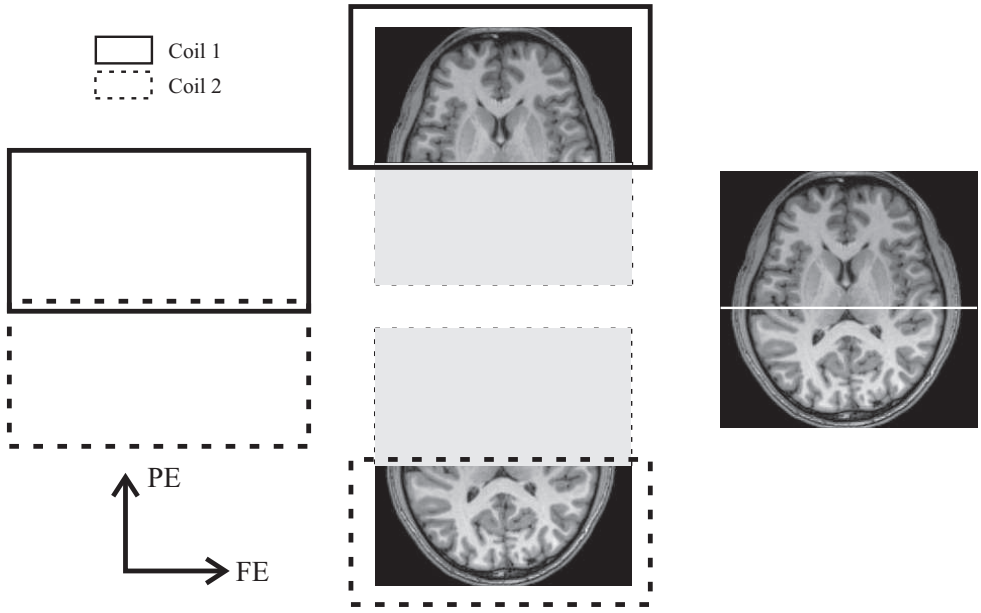

Figure 4.1 An idealistic model of multi-coil imaging. Each of the two coil covers half of the desired FOV with an uniform signal reception sensitivity profile along the PE direction. Then doubling the sample spacing along the PE direction results in aliasing-free images with halved FOV due to limited spatial sensitivity extent. At the reconstruction, the two half FOVs can simply be cascaded to form a complete image.

boundaries is rather unrealistic as the spatial coil sensitivity profile in reality has a smoothly varying nature, which means the effective FOV for individual coil cannot be just $\frac{1}{2}$ of the FOV. In practice, the FOVs covered by individual receiver coil overlap, and different receiver coils feature varying coil sensitivity profile over the image FOV. As the result, the simultaneously required k-space data sets in multiple receiver coils contains redundancy. This redundancy is then exploited using the knowledge of the coil sensitivity profile of the receiver coils to compensate for the missing k-space measurement to form an aliasing-free image.

4.2 RF receiver coils

The core difference between conventional MR imaging and parallel MR imaging is the receiver coil device employed. Conventional MR imaging can be performed using either a single receiver coil or a coil array, however the coil array is a crucial ingredient in parallel imaging. In the following sections, the characteristics of single receiver coils and coil arrays are briefly discussed.

4.2.1 Single receiver coil

In cases where a single receiver coil is used, it is desirable for the receiver coil to have a high sensitivity profile as well as an uniform sensitivity profile. The former is necessary in maintaining a high SNR level whereas the latter allows an image with an uniform background to be formed. In practice, trade-off between high sensitivity profile and uniform sensitivity profile is often to be made due to the limited size of the coils in practice. The actual characteristics of the receiver coils (the coils sensitivity profiles) are largely dependent on their geometries which can be classified as either volume coils or surface coils.

Volume coils surrounds the volume of imaging interest, such as the head or a limb. The usually used volume receiver coils are the birdcage coils, one of which is illustrated in Fig. 4.2.(a). They feature homogeneous signal reception sensitivity over the enveloped imaging volume. Surface coils have simpler structures than the volume coil and can be seen as a loop of wires [HBV99]. They are designed to image localized regions where the coil can be placed closely to the region of imaging interest. Compared to volume coils, surface coil ((Fig. 4.2.(b)) have better signal reception sensitivity (hence better SNR) in regions that are in close proximity to the coil centre. However the signal reception sensitivity tends to drop with the distance away from the coil centre (Fig. 4.2.(d)), hence high SNR can only be achieved within a limited FOV. Also the images obtained using a single surface coil require background correction due to the non-uniform sensitivity profile over the FOV. A common application of surface coils is spinal imaging, where a surface coil is placed directly underneath the spine region to be imaged.

4.2.2 Coil arrays

Coil arrays consist of several individual receiver coil elements arranged to cover the desired FOV to be imaged. In practice, coil arrays usually consist of multiple surface coil elements to provide high SNR over a large FOV. The specific geometrical arrangements of the coil elements are application dependent. Shown in Fig. 4.3 are two commonly encountered coil array setups. In pMRI, the coil arrays used are phased coil arrays [REH$^+$90]. The term phase refers to the fact that the received signal is polarized with respect to differently orientated receiver coils and the phase information is retained. Phased coil arrays are decoupled coil arrays which means the signal reception in different receiver coils contains distinctive information of the imaged object (to be further discussed in detail later on). [1] Individual coil elements in coil arrays are characterized by their distinctive spatial coil sensitivity profiles over the FOV, which is discussed in the following sections.

[1] Mutually coupled coil arrays in which mutual inductance exists between neighboring coil elements are also in use. Due to the coupling effects, the coupled array coils lead to lower SNR level [REH$^+$90] and also they are not suitable for parallel imaging. The main advantage of coupled coil array is the low design complexity.

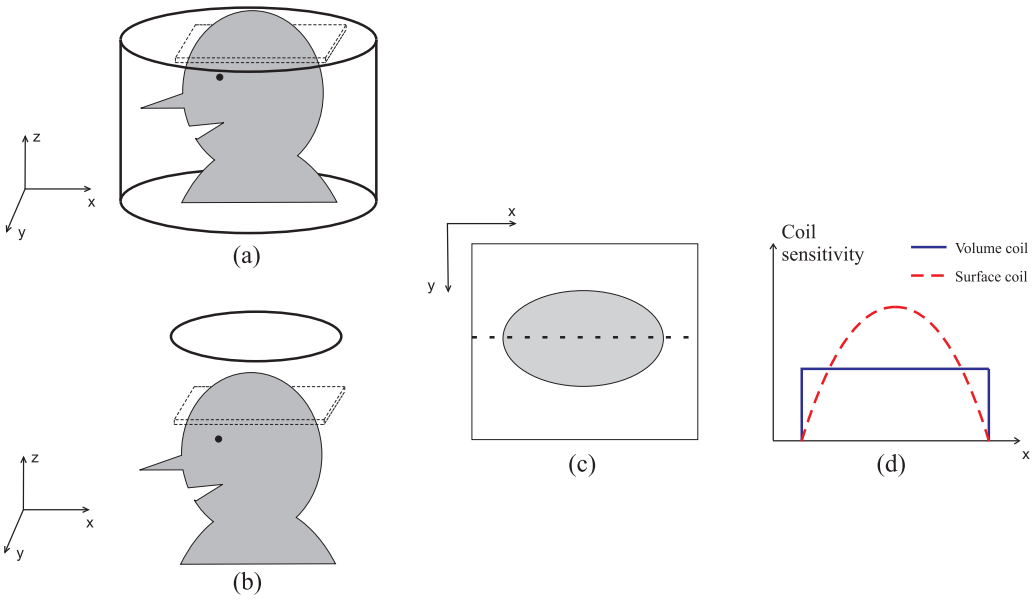

Figure 4.2 Imaging an axial plane brain slice using (a) volume coil and (b) surface coil. Simplistic models of coil sensitivity profile across the FOV (dashed line in (c)) of the two types of coils are shown in (d): a volume coil has a relatively constant coil sensitivity and a surface coil has a spatially varying coil sensitivity profile.

Coil sensitivity profiles

The image received in the individual receiver coil can be seen as the underlying magnetization weighted by the receiver coil sensitivity profile. Mathematically, the image received in the mth coil f_m can be written as:

$$f_m = c_m \circ f \tag{4.1}$$

where f, c_m is the image magnetization and the coil sensitivity profile of the mth coil respectively; and $\circ$ denotes the element-by-element product.

The coil sensitivity profile at a given spatial location of a coil element is function of both the distance and relative orientation of the spatial location to the coil, and hence is a complex function in which the distance and orientation respectively determine the magnitude and phase. Following the electromagnetic principle of reciprocity, which states that the relationship between an oscillating current and the resulting electric field is unchanged if one interchanges the points where the current is placed and where the field is measured, the coil sensitivities of a given image field of view (FOV) can be modeled using Maxwell's electromagnetic law or less accurately by the Biot-Savart law [MVN95]. Shown in Fig. 4.4 are the magnitude of simulated coil sensitivity profiles of 4 coil elements in an 8-channel head coil array in Fig. 4.3, actual images obtained from the corresponding receiver coil shown in the lower row.

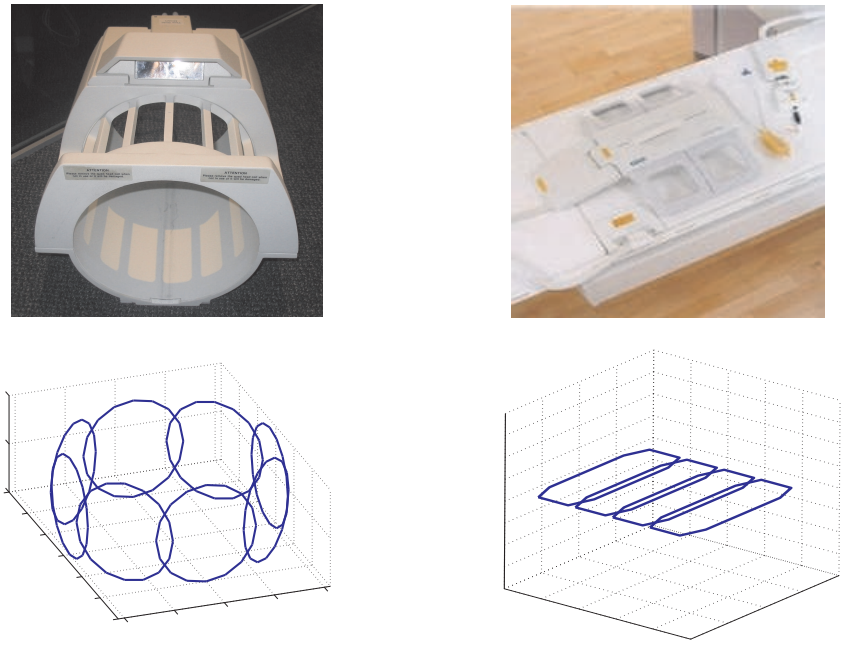

(a) (b)

Figure 4.3 Two representative sets of coil arrays: (a) an 8-channel head coil array, (b) a 4-channel spine coil array. On the upper row are the pictures of the typical coil sets used in a MRI suite; the lower row shows the corresponding simulated coil array models that give more insight of their signal reception properties.

Image formation from multi-coil receiver data sets

Surface array coils were initially designed to overcome the trade off between high image SNR and image uniformity that exists in cases of single receiver coils, hence it is important to be able to combine the local coil sensitivity weighted images to form an overall high SNR image without sensitivity modulation. Combination of the measurements from individual receiver coils that produces optimal SNR by phase shifting of the received signals has been proposed in [REH+90]. That however requires precise knowledge of the magnitudes as well as relative phases of different receiver coils, which are often impractical or too time consuming to obtain. A much more straightforward method is to take the sum-of-squares combination of the individual receiver coil images:

$$\hat{f} = \sqrt{\sum_{m=1}^{M} f_m^2} \tag{4.2}$$

where the final estimation of the pixel $\hat{f}$ is the RMS of the images from all the M coil elements. Sum-of-square combination eliminates the need for knowledge of coil sensitivity profile, at the cost of degraded SNR and increased sensitivity to image artifacts [REH+90].

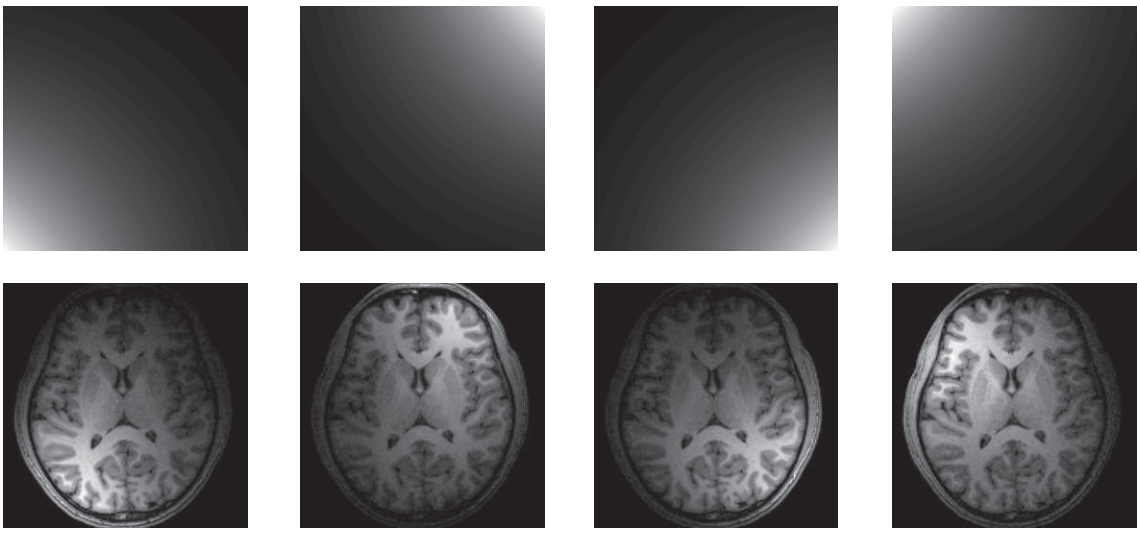

Figure 4.4 Magnitude of simulated coil sensitivity profiles using the Biot-Savart law for 4 symmetrically placed coils in an 8-channel head coil, and also the corresponding sensitivity-weighted images.

4.3 History of pMRI

The advancement of rapid data acquisition could not fully address the need for scan time reduction, especially in the area of dynamic imaging. From the late 1980s, attempts have been made to reduce the number of PE steps by the employment of multiple receiver coils. In 1988, the first attempt by Hutchinson *et al.* [HU88], and then subsequently also by Kwiat *et al.* [KEN91] in 1991, was to employ the same number of coil elements as the number of pixels in the image, so that the need of phase encoding steps can be completely eliminated (their approach can be seen as a somewhat extreme exaggeration of the example in Fig. 4.1). Apparently, their approach was infeasible in any practical sense.

The next attempt by Carlson and Minemura in 1991 [KMW89] and then 1993 [CM93] involved the use of two receiver coils: one coil had a homogenous coil sensitivity over the FOV while the other had with a linear varying sensitivity over the FOV. Their approach was to acquire partial k-space data sets simultaneously in each coil, and in the post processing the missing k-space lines were generated by combination the acquired k-space lines based on the known coil sensitivity profiles. This method is considered to be the first parallel MR method that achieved scan acceleration using the knowledge of coil sensitivity map, and it is a preliminary form of the first clinical pMRI method simultaneous acquisition of spatial harmonics (SMASH) [SW97] later on. However, its requirement for linear sensitivity profile made this approach impractical.

The next published attempt to use multiple receiver coil to reduce data acquisition was by Ra and Rim [RR91], in which the knowledge of the distinctive coil sensitivity profiles were

used to remove the aliasing artifacts caused by under-sampled k-space data sets. This was the closest form of method to the modern pMRI methods, and in fact forms the basis of the later sensitivity encoding (SENSE). But Ra only demonstrated results in with phantom study and the no further development into clinical implementation was made.

The first clinical study using pMRI was introduced by Sodickson *et al.* in 1997, termed as the simultaneous acquisition of spatial harmonics (SMASH) [SW97]. The spatial coil sensitivity functions are combined to compensate for the skipped PE steps. Although the initial implementation of SMASH was subject to many further improvements and optimizations, Sodickson was first to obtain clinical images from accelerated scanning.

In 1999, Pruessmann introduced the method named sensitivity encoding (SENSE) [PWSB99], which explicitly relies on the knowledge of coil sensitivity weighting to remove the aliasing artifacts. As mentioned previously, SENSE shares the similar concept as the early development by Ra and Rim, although a much more in-depth derivation of the method was presented along with a more practical method for developing the coil sensitivity estimations [LPS05]. SENSE since then has greatly advanced the clinical application of pMRI due to its implementation simplicity and high image reconstruction fidelity.

The main distinction between SMASH and SENSE is the domain in which final image reconstruction is carried out. In SMASH, complete k-space data sets are first generated which are then combined to generate a final image. In SENSE, aliased images from individual coil receivers are directly combined to form the final image. As a result, they are also respectively referred to as k-space methods and image plane pMRI methods, by which modern pMRI methods can be classified. Each type of pMRI method has its own advantages and shortcomings (more fully discussed in Chapter 5), and both have been implemented in clinical use. Later investigation of pMRI has gone into the effort to optimize the existing methods, extension to non-Cartesian sampling patterns has also been made to exploit the associated benefits.

4.4 Modern pMRI methods

In this section, representative pMRI methods and their variations are reviewed that give background for the next chapter where a generalized pMRI formation is presented. To distinguish the pMRI implementation in 2D and 3D imaging where under-sampling takes place in a single or both PE directions, the names of 3D pMRI methods are prefixed with '2D'. Notice that by convention the name of the pMRI method has one less dimension than the image it forms. For instance, SENSE and 2D SENSE respectively refer to the SENSE method in 2D imaging and 3D imaging.

As the FE direction is always fully sampled in practice, image reconstructions can be decomposed into a series of lower dimension problems, i.e. reconstructing a 2D image is equivalent to reconstructing a series of 1D lines perpendicular to the FE direction and reconstructing a 3D image is equivalent to reconstructing a series of 2D planes perpendicular to the FE direction. Thus it suffices to only consider reconstructing a line along the PE direction in case of 2D imaging, and a plane defined by two PE directions in case of 3D imaging. Consequently, the under-sampling strategy in 2D and 3D imaging can be respectively represented by a 1D and 2D sampling mask.

As mentioned previously, pMRI methods can be classified as either k-space methods or image plane methods determined by the space in which data reconstruction is carried out. In the following sections, a representative k-space method (SMASH) and image plane method (SENSE) and also their evolved versions are reviewed.

4.4.1 k-space pMRI methods

Simultaneous acquisition of spatial harmonics: SMASH

As the first demonstrated in vivo pMRI method, simultaneous acquisition of spatial harmonics (SMASH), conveys a high level of elegance: the spatially varying coil sensitivity profiles are combined to synthesize the harmonic modulation that is normally achieved by the application of a gradient field, so that skipped PE steps can be generated in post-processing. Specifically, the known coil sensitivity functions C_m from all the M coils are combined to give a composite coil sensitivity $\tilde{C}$ function that approximates an exponential harmonic function $e^{-i(n\Delta k_y y)}$, assuming y is the PE direction:

$$\sum_{m=1}^{M} a_m C_m = \tilde{C} \approx e^{-i(n\Delta k_y y)} \tag{4.3}$$

where a_m is the weighting coefficients used for combining the coil sensitivity function of the mth coil. Then at reconstruction the acquired partial data sets are combined using the same weighting coefficients. The resulting data set represents a shift of $n\Delta k_y$ relative to the measured sample positions:

$$\begin{aligned} \sum_{m=1}^{M} a_m F_m(k_y) &= \int \sum_{m=1}^{M} a_m C_m(y) f(y) e^{-ik_x y} dy \\ &= \int f(y) e^{-ik_x y} \sum_{m=1}^{M} a_m C_m(y) dy \\ &= \int f(y) e^{-ik_x y} e^{-i(n\Delta k_y y)} dy \\ &= \tilde{F}(k_y + n\Delta k_y) \end{aligned} \tag{4.4}$$

In order to form a composite data set at acceleration factor of R, R sets of fitting coefficients $a^0, a^1 ... a^{R-1}$ are needed to synthesize harmonic up to the $R-1$th order. An example of fitting the sensitivity profiles an 8-channel receiver coil to zeroth and first harmonic is shown in Fig. 4.5. With the knowledge of these fitting coefficients, composite data set can be formed with under-sampled data sets at acceleration factor of 2 as illustrated Fig. 4.6.

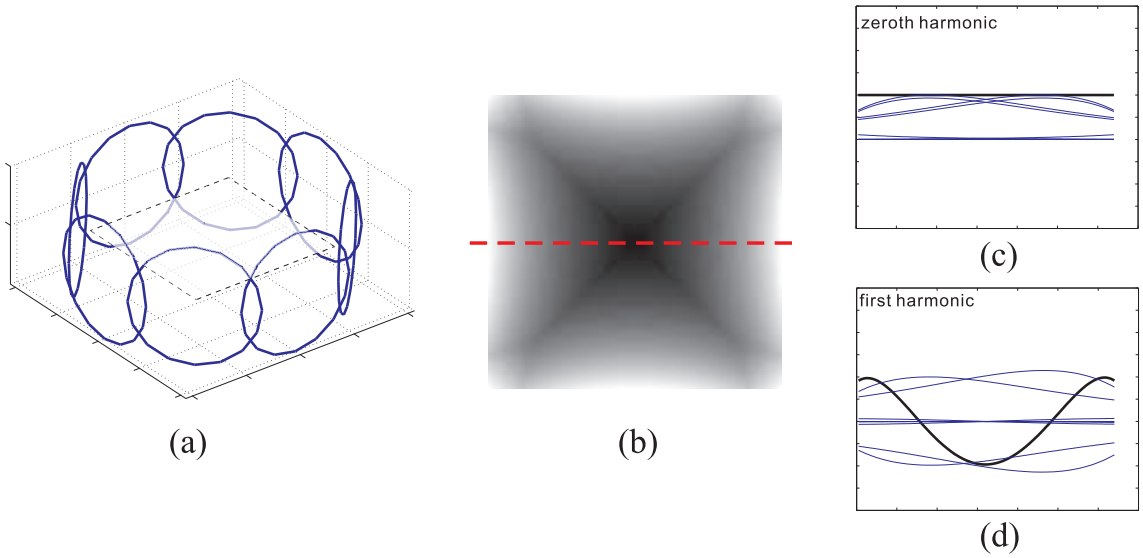

Figure 4.5 Fitting the simulated axial plane coil sensitivity functions of an 8-channel head coil (a) to a zeroth harmonic and a first harmonic. In (b) the composite coil sensitivity profile consisting of all the individual coil sensitivity profiles is shown. Fitting a line across the axial plane (b) to a zeroth harmonic and a first harmonic are shown in (c) and (d) respectively, in which the light grey lines represent the coefficient-weighted coil sensitivity profiles and the dark line represents the fitted line.

One difficulty in implementing SMASH is that accurate estimation of the coil sensitivity profiles is required. This makes SMASH prone to reconstruction errors in practice. Auto-SMASH [JGES98] was developed to bypass the need for explicit coil sensitivity profile estimation. In addition to the regularly acquired partial measurements, $R-1$ auto calibration scan (ACS) lines are acquired for an acceleration factor of R. In the reconstruction, composite calibration scan (CCS) lines are first formed by combining the actually measured ACS lines from individual coils and then the combination coefficients which would otherwise be estimated by fitting the coil sensitivity profiles are instead obtained by fitting the neighboring lines to the ACS lines as shown in Fig. 4.7. Then the gained fitting coefficients can be used in the SMASH construction as illustrated in Fig. 4.6.

Generalized Auto-calibrating Partially Parallel Acquisitions (GRAPPA)

In Generalized Auto-calibrating Partially Parallel Acquisitions (GRAPPA, [GJH+02]), several improvements were made over the auto-SMASH approach. The operation of GRAPPA reconstruction is illustrated in Fig. 4.8. Firstly, instead of forming composite ACSs which may suffer from SNR loss due to phase offsets of different receiver coils as in auto-SMASH,

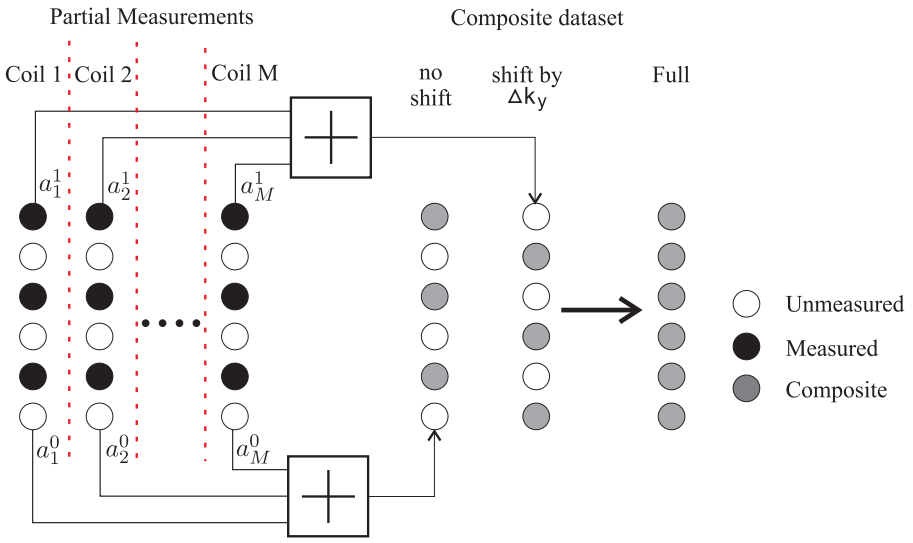

Figure 4.6 Diagram illustrating the SMASH reconstruction at acceleration factor of 2. Two halves of composite data set at different relative shifts to the k-space measurements are first formed using weighting coefficients gained from the coil sensitivity fitting illustrated in Fig. 4.5, they are then combined to form a complete composite data set. Each circle represents a PE line with the FE direction orthogonal to the plane of the page.

the ACSs acquired in each individual receiver coil are directly used as the targets for fitting. Then complete composite data sets for each receiver coil are first formed, which can then be by sun of squares to achieve more optimal SNR. Secondly, rather than using a single line to fit to the ACSs, data fitting has been extended to include a few neighboring lines to improve the reconstruction fidelity (as illustrated by the boxed region in Fig. 4.8). In addition, a sliding-block reconstruction approach can be used, which allows an unacquired line to be reconstructed in several different ways (such as illustrated in Fig. 4.8), and then the final data estimation is made based on a weighted average of all the possible reconstructions. Significantly improved image reconstructions comparing to those obtained the SMASH method are received as reported in [GJH+02].

One question that naturally arises is: how many neighboring points should be included for reconstruct a target point in GRAPPA? As reported in [GJH+02], data reconstruction fidelity improves as more measurements are included. However, at the same time the computational complexity and numerical instability increases. The latter causes a degraded SNR, which often offsets the gain in data reconstruction fidelity. Such behavior has been further investigated in [YMOS05], in which the concept of k-space locality was introduced: the correlation among neighboring k-space samples in multiple receiver coils is determined by the Fourier domain representation of the spatial coil sensitivity functions; since the coil sensitivity functions are smoothly varying, the correlation among neighbouring k-space samples decrease rapidly as the distance increases. Hence in practice a moderate number of neighbouring points should be used in the presence of noise, and the optimal sample

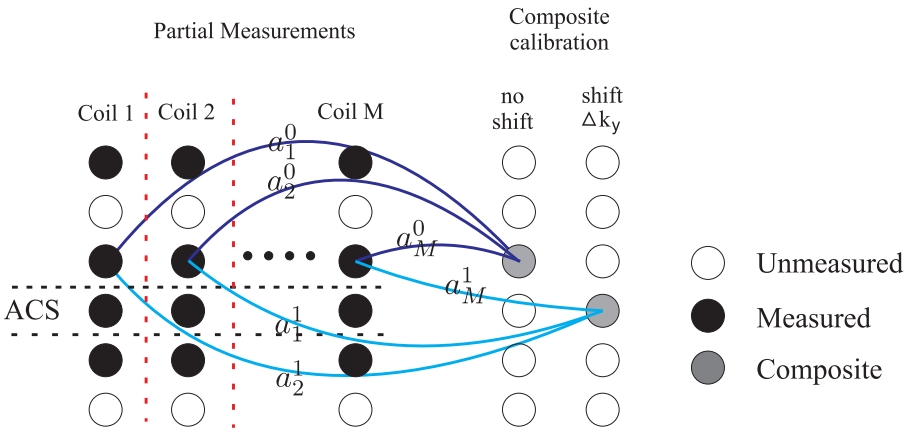

Figure 4.7 In auto-SMASH, weighting coefficients for achieving a k-space shift of Δk_y required for data combination are obtained by fitting acquired data to composite calibration scan (CCS) line that are Δk_y away. In the diagram, the coefficients for SMASH image reconstruction at acceleration factor of 2 are obtained by fitting the acquired partial data sets to the composite calibration lines that are at the same position and at Δk_y away.

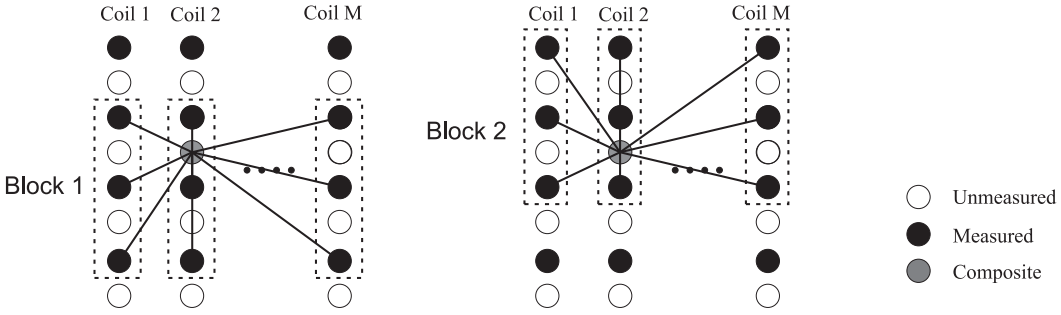

Figure 4.8 Diagram illustrating the GRAPPA reconstruction at acceleration factor of 2. Multiple measured lines are used to estimate a missing k-space line for each individual receiver coil. Hence there often exist multiple ways of producing a target data point as illustrated by the block 1 and block 2.

set to be used for data estimation should be determined from the knowledge of the coil sensitivity functions.

2D GRAPPA

The nature of k-space pMRI methods allow their straightforward extensions to 3D, in which sample lines are combined to form composite data lines in both PE directions. 2D GRAPPA has received the most attention due to the high performance of GRAPPA-like reconstruction approaches. In [BBM+06a], Blaimer *et al.* proposed and compared two types of GRAPPA implementation in 3D pMRI. The first type is a natural extension of the 1D GRAPPA operation, where measured data in both directions are simultaneously combined to produce the missing k-space lines. In the alternative approach, which they termed the 2D-GRAPPA-operator, estimation of the same k-space data is split into two consecutive 1D

GRAPPA reconstructions, i.e. reconstruction is first made in first PE direction and then the estimated data are also used to produce composite data in the other PE direction. It was reported that the second approach produces better reconstruction as each individual 1D GRAPPA fitting is numerically more stable [BBM+06a], at the cost of an increased level of computation.

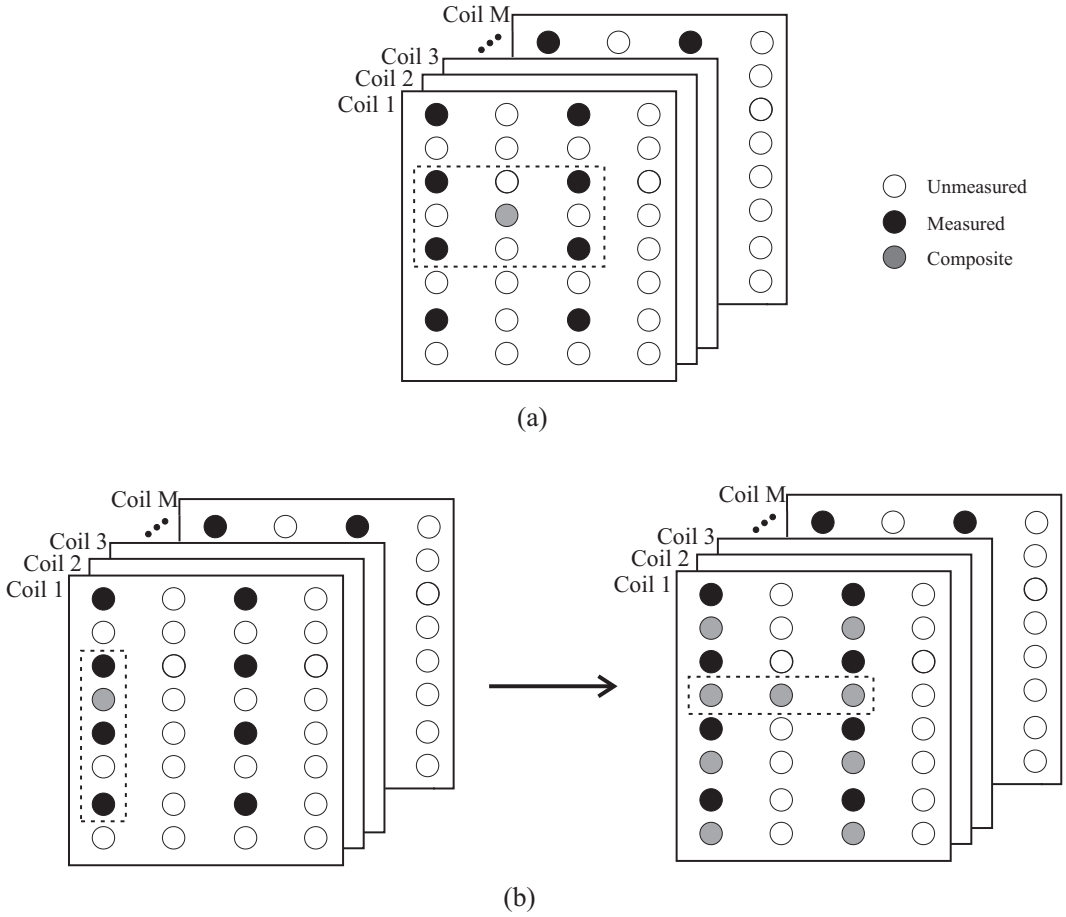

Figure 4.9 Diagram illustrating the 2D GRAPPA operation at an acceleration factor of 4,which is evenly spread in two PE directions. The missing data can either be reconstructed directly using a 2D block reconstruction as shown in (a), or a two-step 1D block reconstruction can be performed to achieve the same goal as shown in (b).

4.4.2 Image plane pMRI methods

Sensitivity encoding (SENSE)

The same sampling strategy as in SMASH is employed in the sensitivity encoding (SENSE) method: $R-1$ phase encoding (PE) lines are skipped out of each R lines in a regular manner to achieve an acceleration factor of R. Effectively, the sample spacing in k-space has been increased by a factor of R, and the effective FOV along the PE direction (denoted as FOV_{PE}) in the image plane has been reduced by a factor of R.

The same FOV folding mechanism takes place in different receiver coils, however the folded pixels are differently weighted by the local spatial coil sensitivity profile of each individual coil. In the example illustrated in Fig. 4.10, increasing the k-space sample spacing by a factor of 2 causes pixels that are $FOV_y/2$ apart to be aliased together. Taking a pair of pixels f_a and f_b, and denoting their superimposition in two different receiver coils as $\tilde{f}_1$ and $\tilde{f}_2$, a linear system that represents the folding process can be written:

$$\begin{bmatrix} \tilde{f}_1 \\ \tilde{f}_2 \end{bmatrix} = \begin{bmatrix} c_{1,a} & c_{1,b} \\ c_{2,a} & c_{2,b} \end{bmatrix} \begin{bmatrix} f_a \\ f_b \end{bmatrix}, \tag{4.5}$$

where $c_{m,a}$ and $c_{m,b}, m = 1, 2$, are the coil sensitivity weighings at the original positions of the folded pixels in the two receiver coils. The encoding matrix is commonly referred as the sensitivity encoding matrix, direct inversion of which allows an estimation of the underlying pixels to be obtained.

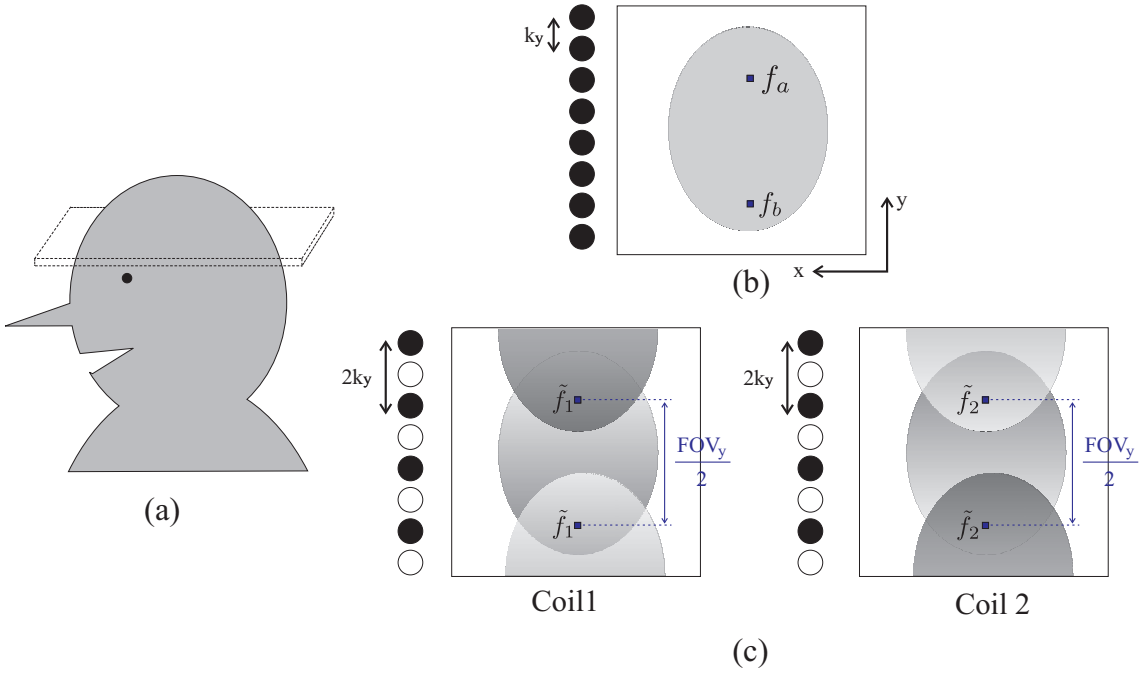

Figure 4.10 SENSE: Under-sampling by regularly skipping PE lines (each dot represents a PE line going into the page) results in an images with reduced FOV in the PE direction. In imaging an axial brain slice shown in (a), sampling at Nyquist rate using a single receiver coil results in a complete, uniform image shown in (b). In case two receiver coils are used, sampling at half of the Nyquist rate along the k_y direction results in images with halved FOV in both receiver coils, as seen in (c). Note that the spatially varying coil sensitivity weighting in the two receiver coils are represented by the varying image backgrounds.

In a more general case, an acceleration factor of R leads to a reduction factor of R of in the FOV_{PE} direction. Define $L = \frac{N}{R}$, there are L unique pixels in the aliased image each is a superimposition of R pixels in the FOV_{PE} direction. Similarly, knowledge of the coil sen-

sitivity profiles allows the following linear system to be formed for the lth superimposed pixel from all the M receiver coils:

$$\begin{bmatrix} \tilde{f}_1 \\ \tilde{f}_2 \\ \cdots \\ \tilde{f}_M \end{bmatrix} = \begin{bmatrix} c_{1,1} & c_{1,2} & \cdots & c_{1,R} \\ c_{2,1} & c_{2,2} & \cdots & c_{2,R} \\ \cdots & \cdots & \cdots & \cdots \\ c_{M,1} & c_{M,2} & \cdots & c_{M,R} \end{bmatrix} \begin{bmatrix} f_1 \\ f_2 \\ \cdots \\ f_R \end{bmatrix}, \quad \tilde{\mathbf{f}}_l = \mathbf{C}_l \mathbf{f} \tag{4.6}$$

where $\tilde{\mathbf{f}}_l$, $\mathbf{f}$ and $\mathbf{C}$ respectively represent the lth aliased pixel, the lth group of pixels that are aliased together and the corresponding sensitivity matrix. Formulation in Eq. (4.6) allows a least-square estimate $\check{\mathbf{f}}_l$ of the underlying pixels to be obtained by taking the pseudo-inverse of the sensitivity matrix $\mathbf{C}_l$:

$$\check{\mathbf{f}}_l = \mathbf{C}_l^{+} \tilde{\mathbf{f}}_l = (\mathbf{C}_l^H \mathbf{C}_l)^{-1} \mathbf{C}_l^H \tilde{\mathbf{f}}_l \tag{4.7}$$

By the simple rules of linear algebra, it is possible to unfold up to M pixels for a total number of M independent receiver coils, i.e. an acceleration factor up to M is allowed.

In practice, SENSE reconstructions are impaired by reconstruction noise. Comparing to the case of full data acquisition, the increased noise level in SENSE reconstruction comes from two sources: firstly, due to the less number of samples measured, the intrinsic noise power is increased by a factor of R for an acceleration factor of R, or equivalently the SNR drops by a factor of $\sqrt{R}$; secondly, the intrinsic data noise is amplified through the reconstruction process, as the encoding matrix is no longer orthonormal as is the case for full data acquisition [BBM$^+$04]. The second noise source is dominant at high acceleration factors, and much research attention has been directed to minimizing this additional noise amplification. A closer look at this additional noise amplification process is taken in the following, it shares a same nature as was initially presented in [PWSB99], however this approach is much simpler.

Let the lth group of pixels be impaired with zero mean, white Gaussian noise $\mathbf{n}_l$ ($\mathbf{n}_l$ is used for notation consistency, although the noise statistics should not differ among different groups), so that the noise-corrupted and folded pixels, $\tilde{\mathbf{e}}_l$, is given by

$$\tilde{\mathbf{e}}_l \;=\; \mathbf{C}_l \mathbf{f}_l + \mathbf{n}_l. \tag{4.8}$$

Attempting a solution using the pseudo-inverse of the sensitivity matrix results in a noise term of $\check{\mathbf{n}}_l = \mathbf{C}_l^{+} \mathbf{n}_l$, i.e.

$$\check{\mathbf{f}}_l^{+} = \mathbf{C}_l^{+} \tilde{\mathbf{e}}_l = \mathbf{f}_l + \mathbf{C}_l^{+} \mathbf{n}_l. \tag{4.9}$$

Then a noise matrix $\mathbf{X}_l$ can be constructed for the lth group of reconstructed pixels using the noise term $\check{\mathbf{n}}_l$:

$$\mathbf{X}_l = \mathbf{E}[\check{\mathbf{n}}_l \check{\mathbf{n}}_l^H] = \mathbf{E}[(\mathbf{C}_l^+ \mathbf{n}_l)(\mathbf{C}_l^+ \mathbf{n}_l)^H] = \mathbf{C}_l^+ \mathbf{E}[\mathbf{n}_l \mathbf{n}_l^H](\mathbf{C}_l^+)^H = \mathbf{C}_l^+ \mathbf{\Phi}_l (\mathbf{C}_l^+)^H \tag{4.10}$$

where $\mathbf{\Phi}_l$ is a covariance matrix representing the intrinsic noise in the data measurement. The p-th diagonal element is the noise variance for the p-th pixel in the lth group and off diagonal elements are the correlations of noise from different pixels. Given the assumed white noise source with a variance of δ^2, $\mathbf{\Phi}_l$ becomes a diagonal matrix with δ^2 on the main diagonal and zero elsewhere, hence we have:

$$\mathbf{X}_l = \delta^2 \mathbf{C}_l^+ (\mathbf{C}_l^+)^H = \delta^2 (\mathbf{C}^H \mathbf{C})^{-1}. \tag{4.11}$$

Similarly the p-th element on the main diagonal of X_l represents the noise power in the p-th pixel in the lth pixel group in the reconstructed image. Then the ratio of the noise power in reconstruction to that of full data acquisition to measure the loss of SNR in SENSE reconstruction:

$$\frac{[X_{SENSE}]_{p,p}}{[X_{Full}]_{p,p}} = \frac{\sqrt{\delta^2_{SENSE}}\sqrt{(C^H_{SENSE} C_{SENSE})^{-1}_{p,p}}}{\sqrt{\delta^2_{Full}}\sqrt{(C^H_{Full} C_{Full})^{-1}_{p,p}}} = \sqrt{R}\sqrt{\frac{(C^H_{SENSE} C_{SENSE})^{-1}_{p,p}}{(C^H_{Full} C_{Full})^{-1}_{p,p}}} \tag{4.12}$$

where $\sqrt{R}$ accounts for the intrinsic noise loss due to under-sampling, and $(C)_{p,p}$ represents the noise level at the pth pixel in the reconstructed image with a particular method. At full data acquisition, there is no folding takes place and hence C_{Full} is a diagonal matrix with pth element on the diagonal $[C_{Full}]_{p,p} = [C_{SENSE}]_{p,p}$ and zeros elsewhere. Hence Eq. (4.12) can be rewritten as:

$$\frac{[X_{SENSE}]_{p,p}}{[X_{Full}]_{p,p}} = \sqrt{R}\sqrt{(C^H_{SENSE} C_{SENSE})^{-1}_{p,p} (C^H_{SENSE} C_{SENSE})_{p,p}} \tag{4.13}$$

The additional noise amplification factor $\sqrt{(C^H_{SENSE} C_{SENSE})^{-1}_{p,p} (C^H_{SENSE} C_{SENSE})_{p,p}}$ is determined by the local coil sensitivity weighting, which is in turn determined by the receiver coil geometry. Hence it was named as the geometry factor (g-factor) and used as a measure for the noise level in the SENSE reconstructions.

In k-space pMRI methods (except the original SMASH approach [SW97]) knowledge of the coil sensitivity profile is implicitly derived from the use of the auto-calibration lines, however in SENSE knowledge of the coil sensitivity profile is explicitly involved in the image reconstruction as seen in Eq. (4.6). Therefore accurate knowledge of coil sensitivity profiles is required in SENSE reconstructions. In principle, coil sensitivity profile for a

given set of coil arrays is independent of the scan subject[2], hence a look-up-table approach is possible: the coil sensitivity profile for a 3D image volume can be obtained and stored, and then the coil sensitivity weighting for a particular point in the 3D space can be directly looked up by its spatial location. However, in practice it is difficult to precisely calibrate the spatial location of a imaging plane given the time constraint in conducting a MRI scan.

In the SENSE approach [PWSB99], it was proposed to obtain an estimation of the coil sensitivity profiles as a by-product from a low resolution calibration scan as illustrated in Fig. 4.11. Firstly, low resolution images are obtained from all the receiver coils as shown in Fig. 4.11.(a). Then each of these images is divided by a homogenous background image (Fig. 4.11.(b)) that can be obtained by either taking the sum-of-square of the individual coil images as discussed in Section 4.2.2, or it can be obtained by employing a separate body coil as proposed in [PWSB99]. The resulting division is a raw map of coil sensitivity weighting as seen in Fig. 4.11.(c), which in practice is impaired with noises and possibly slight residual object feature modulations. Due to the intrinsically smooth nature of the coil sensitivity profiles, image processing techniques can be employed to eliminate the rapid variations such as shown in Fig. 4.11.(d). The role of a calibration scan can be replaced by a sampling pattern with a fully sampled k-space centre such as that shown in Fig. 4.7, and then the low resolution images can then be produced from the fully sampled k-space centers. Such a process is known as an in-vivo calibration. The advantage of in-vivo calibration over a separate calibration scan is to eliminate the potential risk of patient motion between the calibration scan and the actual scan, and the apparent drawback is the need for extra data acquisitions that undermines the utility of scan time reduction offered by parallel imaging.

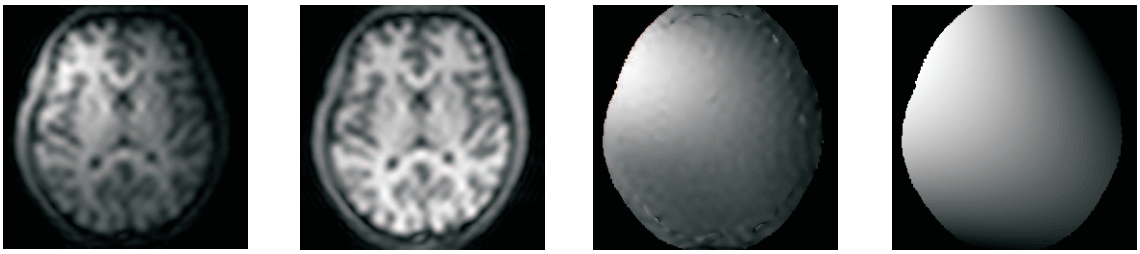

Figure 4.11 Estimating the coil sensitivity profiles from a low resolution data set: (a) low resolution image from a single coil reconstructed from a k-space centre (32×32 out of 256×256); (b) the sum-of-square of low resolution images from all the receiver coils; (c) raw sensitivity map obtained by dividing (a) by (b); and (d) refined coil sensitivity map after applying a low order polynomial fit to (c).

[2]In practice, some coupling may exist between the coil and the object being imaged.

Controlled aliasing in volumetric parallel imaging (CAIPIRINHA)

The distinctiveness of the coil sensitivity weighting at the locations of the pixels which become folded determines the ease of solving for the folded pixels, and hence the quality of SENSE image reconstructions [BBHM05]. In practice, the coil sensitivity profiles are fixed for a given set of the receiver coils which constrains the practical application of SENSE. Controlled Aliasing in volumetric parallel imaging (CAIPINRINA, [BBHM05]) is an elegant approach to enhance the coil sensitivity variation of the folded pixels in multi-slice imaging. Specifically, image aliasing is made to take place cross different image slices rather than being limited to within a single 2D slice. As illustrated in Fig. 4.12.(a), a volumetric sequence is used to excite two slices that are spatially separated. In the case of full data acquisition (acquiring twice the number of PE steps as a single slice excitation), two slices can be recovered with a double FOV along the PE direction as shown in Fig. 4.12.(b). To achieve an acceleration factor of 2, alternating lines in the k-space are skipped as for SENSE. As the result, superimposition of the two image slices takes place as shown in Fig. 4.12.(c).

In principle, knowledge of sensitivity encoding can be used to separate the superimposed slices in Fig. 4.12.(c). However attempting such a solution will typically result in a high g-factor since there is little difference in the coil sensitivity weighting at same pixel in near-by slices. In CAIPIRINHA [BBHM05], Breuer proposed to use a modified slice superimposition in which one slice is shifted with respect to the other as illustrated in Fig. 4.12.(d). In this way, the coil sensitivity variation of the superimposed pixels is increased compared to the conventional SENSE approach since the additional coil sensitivity difference across different slices is exploited. Considerable in-vivo reconstruction improvements compared to in-plane SENSE using this strategy have been reported.

2D SENSE and 2D CAIPIRINHA

In 2D SENSE, uniform under-sampling is extended to both PE directions: to achieve an overall acceleration factor of R, $R_1 - 1$ and $R_2 - 1$ k-space lines are skipped in a regular manner in each PE direction, where $R = R_1 \times R_2$. As illustrated in Fig. 4.13, the same aliasing mechanism applies, R_1 and R_2 evenly spaced voxels from each PE direction are folded onto a single voxel in the image plane. The separation of the folded voxels along the two PE directions of dimension N_1 and N_2 are $L_1 = N_1/R_1$ and $L_2 = N_2/R_2$. Given the knowledge of the originating voxels and the coil sensitivity profiles, the same sensitivity encoding system as Eq. (4.6) can be formed to solve for each group of aliased voxels.

In 3D imaging, modifying the aliasing appearance can be easily achieved by adjusting the sampling strategy. The regular folding pattern in 2D SENSE is modified by shifting the

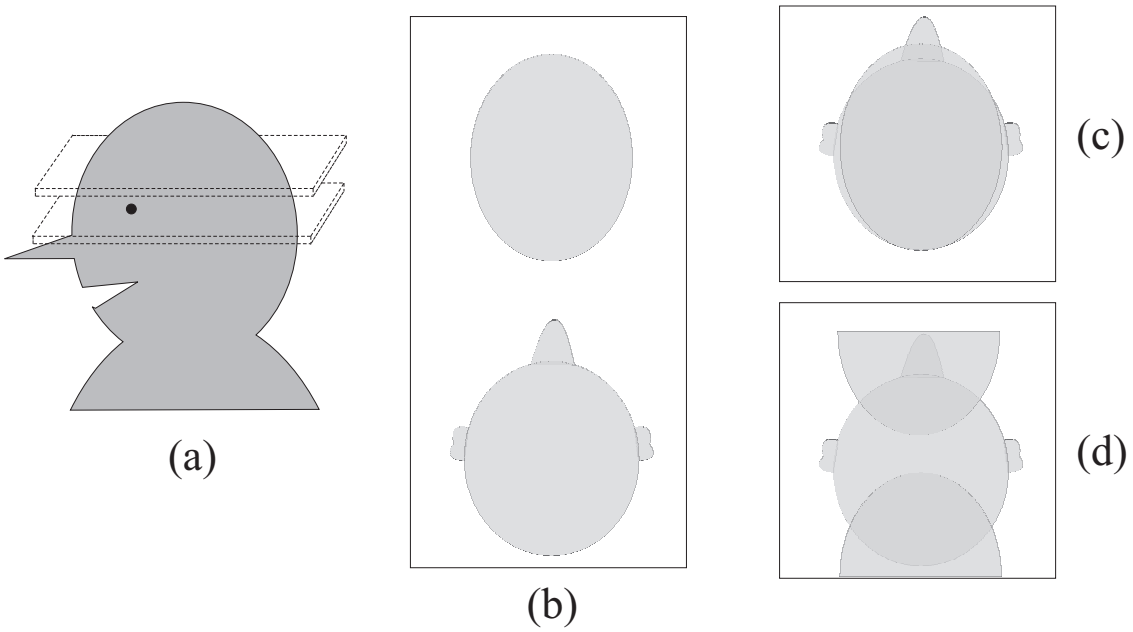

Figure 4.12 CAIPIRINHA improves the efficiency of coil sensivity encoding in multiple slice imaging. In (a), two slices are simultaneously excited using a volumetric sequence. Full data acquisition results in a doubled FOV along the PE direction as seen in (b). Under-sampling at an acceleration factor of 2 results in superimposition of the two slices onto each other, however such folding pattern in (c) is ineffective in terms of sensitivity encoding. Shifting an image slice with respect to the other by applying a phase modulation to the volumetric sequence [BBHM05] enhances the coil sensitivity weighting distinctiveness of the folded pixels as shown in (d), and hence achieves more effective sensitivity encoding than the case of conventional single slice SENSE approach.

regular sample position in two PE directions by different amounts. In Fig. 4.13, it is seen that the regular under-sampling strategy in 2D SENSE leads to a regular folding pattern, whereas non-regularly spaced voxels are folded together in 2D CAIPIRINHA as a result of the modified under-sampling strategy used.

As suggested by Breuer in [BBM$^+$06b], sampling patterns in 2D CAIPIRINHA can be seen to be consisted of grids of size $R \times R$ for an acceleration factor of R. As acceleration factors go up, the number of possible CAIPIRINHA patterns increases. For an acceleration factor R, there exist $\frac{R^2!}{(R^2-R)!}$ possible sampling patterns. Breuer [BBM$^+$06b] then proposed to judge the sampling patterns by examining their corresponding point spread functions (PSF), those which feature the largest minimal separation (referred as d_{min}) between the non-zero elements in their PSF are considered to be favorable, such as shown in Fig. 4.13.(b) and (c). The large separation of the non-zero elements in their PSFs leads to folding patterns that cause voxels that are spatially further apart to be folded together comparing to the case of 2D SENSE, and hence achieves more effective sensitivity encoding. However, one problem of 2D CAIPIRINHA in practice is that there often exist multiple candidates with the same d_{min} at a given acceleration factor such as the case in Fig. 4.13 (b) and (c). In [BBM$^+$06b], the authors suggested a trial-and-error approaches in performing several

pre-scans to select the most suitable sampling pattern.

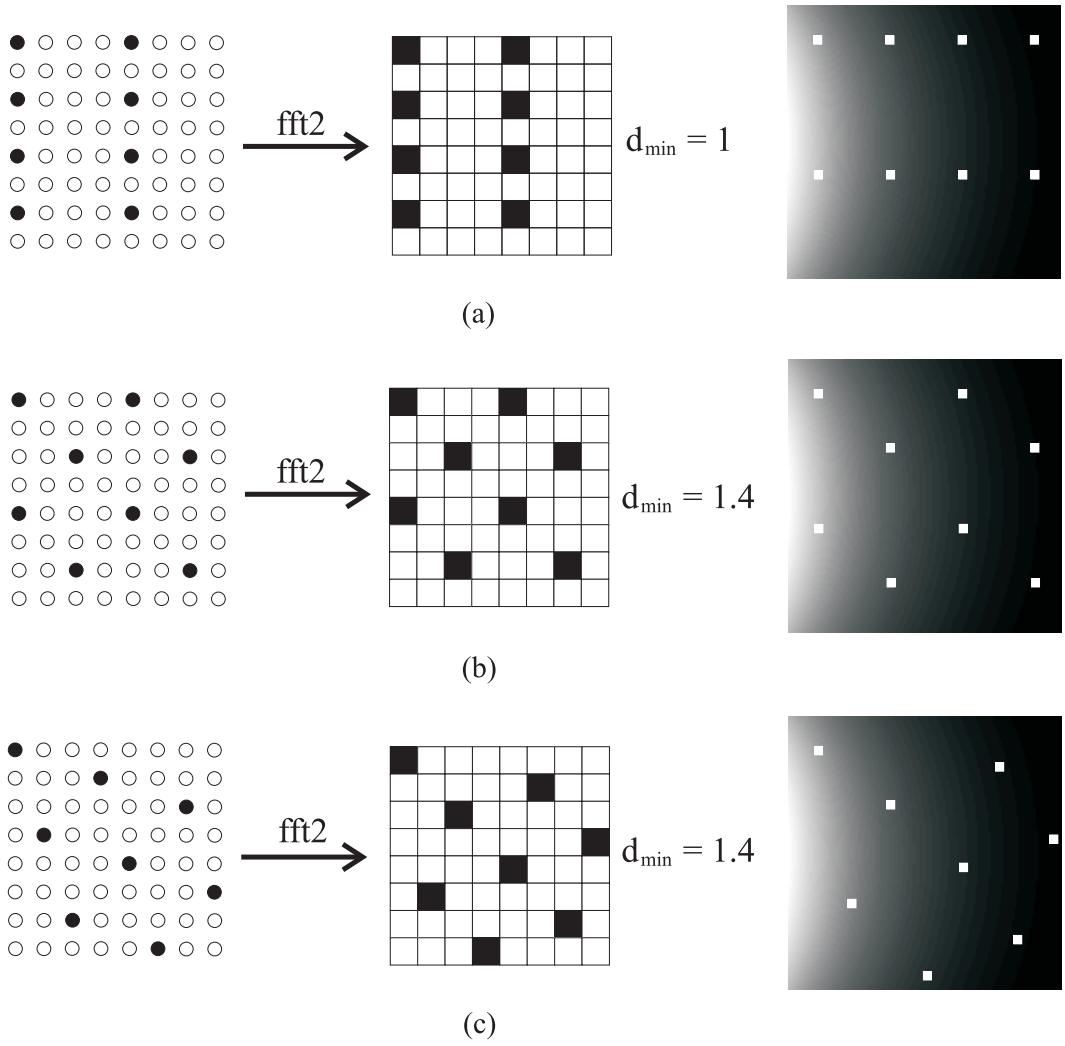

Figure 4.13 Comparing the under-sampling strategies used by 2D SENSE and 2D CAIPIRINHA. At an acceleration factor of 8, sampling patterns consist of shearing grids of size 8×8 are considered (filled and empty circle represents the acquired and skipped sample position), and they are judged by the PSF (filled and empty square represents the zero and non-zero element in the PSF) of the shearing grids. In (a), a 2D SENSE regular sampling pattern has a regular PSF that causes voxels that are regularly spaced to be folded together. In (b) and (c), modified sampling patterns used in 2D CAIPIRINHA feature larger minimal spacing d_{min} in their PSFs, which cause voxels that are further apart in the spatial domain to be folded together.

4.4.3 k-space or image plane pMRI, which is better ?

k-space and image plane pMRI methods tackle the image reconstructions differently, and each type of method has its own advantages and shortcomings. At the present, GRAPPA and SENSE, as the representative k-space and image space pMRI methods, have received the most research attention and are available on commercial scanners for clinical use. In the following, image reconstructions using GRAPPA and SENSE in 2D imaging and 3D imaging are compared. The data used in reconstruction was an axial plane brain slice (256×256) obtained using a 3T GE scanner[3]. Under-sampling was performed either in one direction or both directions to simulate the scenarios of 2D or 3D imaging. For a thorough comparison, reconstructions were performed at both moderate and high acceleration factors. A central k-space region of size 32×256 and 32×32 are retained in 1D and 2D GRAPPA for auto calibration; and the same data are used for extracting coil sensitivity profile for 1D and 2D SENSE reconstructions respectively.

The reconstruction results are shown in Fig. 4.14. Firstly, it is seen that extending the under-sampling to both directions as in 3D imaging results in significantly improved reconstruction results comparing to those gained in 2D imaging in both cases of SENSE can CAIPIRINHA (comparing the reconstruction outcome at acceleration factor of 4 in both cases). Secondly, it is seen that the reconstruction results using the two methods have distinctive features: SENSE reconstructions are impaired with reconstruction noise, whereas GRAPPA reconstructions contain residual aliasing artifacts and blurred image details. Such difference arises from the distinctive nature of k-space and image plane methods, which will be more fully discussed in Chapter 5. As suggested by [HB06], the features of SENSE and GRAPPA complements each other, and methods that incorporate both GRAPPA and SENSE in reconstruction were proposed to take the advantages of both methods. In addition, it is observed that SENSE reconstruction in both 2D imaging and 3D imaging result in better image details and SNR than GRAPPA at moderate acceleration factors (AF at 2 in 2D imaging and AF at 4 in 3D imaging). However at high acceleration factors (AF at 4 in 2D imaging and AF at 8 in 3D imaging), SENSE reconstructions suffer from severe SNR deterioration and GRAPPA tends offer relatively more stable outcomes. This observation agrees with that was reported in [HB06]. Overall, as discussed in [BBM$^+$04, JJS07], both types of methods performed well in clinical studies, and the optimal choice of a pMRI method depends on the specific application.

[3]The data set used is from the Parallel imaging Utilizing Localized Surface-coil Acquisition and Reconstruction (PULSAR) [JJS07], website *http://www.ece.tamu.edu/ mrsl/JIMJI_TAMU/pulsarweb/downloads.htm*

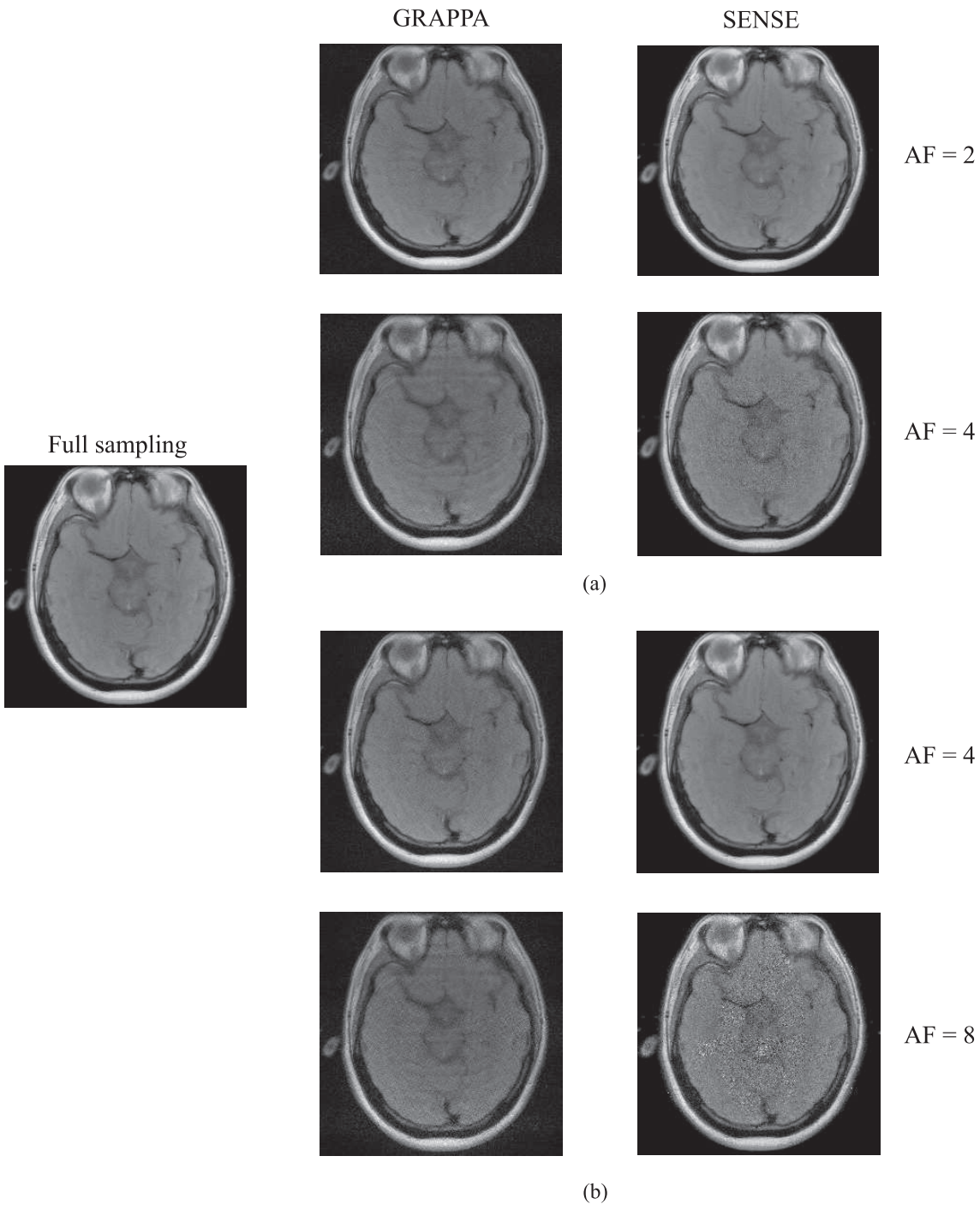

Figure 4.14 Comparisons of GRAPPA and SENSE reconstructions in (a) 2D imaging and (b) 3D imaging. Acceleration factors of 2 and 4 are used in 2D imaging, whereas acceleration factors of 4 and 8 were used in 3D imaging. In 2D imaging, under-sampling is restricted in a single dimension; in 3D imaging, under-sampling takes places in both dimensions. Image reconstruction with full data acquisition is shown on the left for comparison.

4.5 Motion correction with pMRI

The development of modern pMRI methods started a new era in MRI, almost every area of clinical MRI could potentially benefit from the use of pMRI. Correcting for patient motion during the scan is an especially interesting topic as pMRI offers intrinsically fast imaging. In the following, a new motion correction method based on the SENSE method is presented. This work was completed with Dr Julian Maclaren when he was performing research for his Ph.D. in University of Canterbury, New Zealand [Mac07].

This proposed method has a simple nature and is illustrated in Fig. 4.15. The overall process can be decomposed into three steps. Firstly, fast spin echo (FSE) (introduced in Section 3.5.1), is employed to acquire the entire k-space using FSE in multiple shots, each of which consists of evenly spaced PE lines and can be used to perform a SENSE reconstruction. Due to the rapid completion of a single shot, typically it can be assumed that data collected within each shot is motion free, however data collected between different shots may not be consistent due to patient motion. Next, SENSE reconstruction is performed using data obtained in each of the shots which leads to a set of motion-free images. However, the reconstructed images themselves may not be consistent due to the motion, as illustrated in Fig. 4.15. Lastly, the reconstructed images are registered and combined to give a final image. As each individual image features degraded SNR due to under-sampling, combining these images leads to improved SNR in the final image.

In-vivo experiments were carried out using a GE 1.5T scanner equipped with an 8-channel brain coil, axial brain slices of matrix size 128×256 were obtained. FSE with echo train length 32 was used, i.e. in each shot 32 FE lines were acquired. Three scans were performed with a volunteer who was instructed to stay still, move slightly and move continuously in each scan respectively. Image reconstructions were performed using the above method and using direct inverse fourier transform for comparison. In the implementation of SENSE, the required knowledge of coil sensitivity profiles were extracted from a low resolution scan (32×256). Image registration was performed by Julian Maclaren as in [Mac07]: the relative motion between different images was estimated and corresponding corrections were made in k-space, then the corrected k-space data sets were combined to give a composite data set, which is then Fourier transformed to give the final image.

The results are shown in Fig. 4.16. It is seen that the new method produced alias-free images in both experiments where motion took place. In contrast, motion corrupted images were produced by direct transforms. However, one imperfection of this method is the loss of SNR, which can be clearly seen by comparing the outcomes in the motion-free case. As discussed in Section 4.4.2, there are two sources of SNR loss: firstly, an intrinsic SNR loss of $\sqrt{R}$ due to under-sampling at acceleration factor of R; secondly, SENSE reconstructions

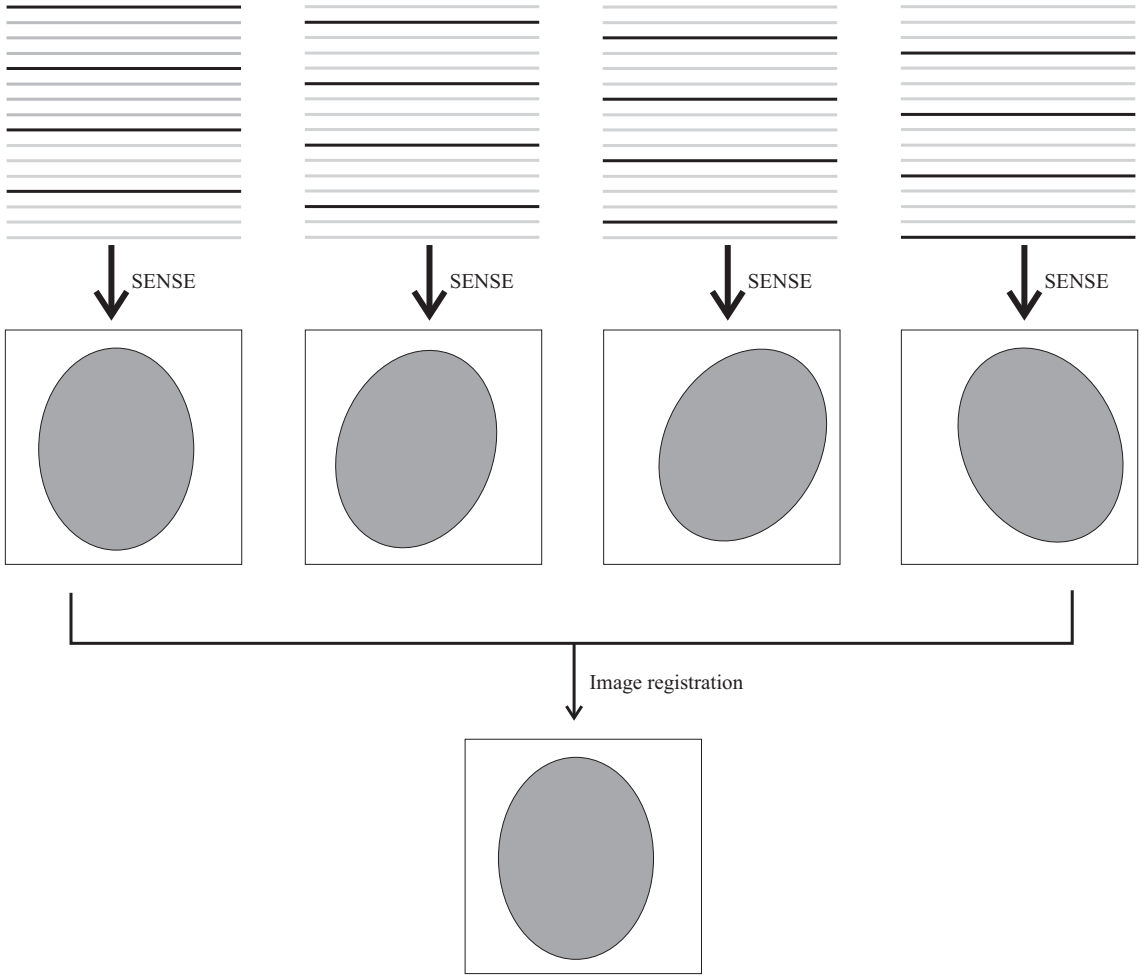

Figure 4.15 Diagram illustrating motion correction method based on FSE sequence and SENSE reconstructions. Each shot in FSE allows one motion free image to be reconstructed, and combining the images from multiple FSE shots compensate for the SNR loss due to reduced number of data acquisitions.

are subject to additional SNR loss that can be characterised by the 'g-factor'. Combining R individual reconstructions compensate for the SNR loss due to first cause, however the SNR loss due to imperfect SENSE reconstructions (g-factor) propagates to the final reconstructed the image. A reduction of the SNR loss is possible by carrying out image reconstructions using multiple motion-free shots in cases where motion may only exist in between some but not all FSE shots, so that noise amplifications in SENSE reconstructions are minimised.

Although only preliminary results for this new pMRI based motion correction method were obtained, and no quantitative comparisons have been made with existing motion correction methods such as Periodically Rotated Overlapping ParallEL Lines with Enhanced Reconstruction (PROPELLER, [Pip99]) and Translation and Rotation Estimation using Linear Least squares and Interleaved Strips (TRELLIS, [MBMW07]), potential advantages of this method can be seen. In either PROPELLER or TRELLIS, motion correction is performed in k-space and requires k-space data extrapolation which makes the reconstruction process computationally heavy. In this method here, the computational requirements are relatively modest. Another advantage is the fact that the method can produce both the original image and the motion-corrected image using a standard data acquisition sequence with no extra k-space measurements; in the fore-mentioned methods, the entire k-space is essentially measured twice which makes the scan more vulnerable to motion.

In general, motion correction employing pMRI methods is very promising and has the potential to outperform conventional motion correction methods. The growing popularity of multiple receiver coil sets is likely to increase interest in performing the motion correction with pMRI methods.

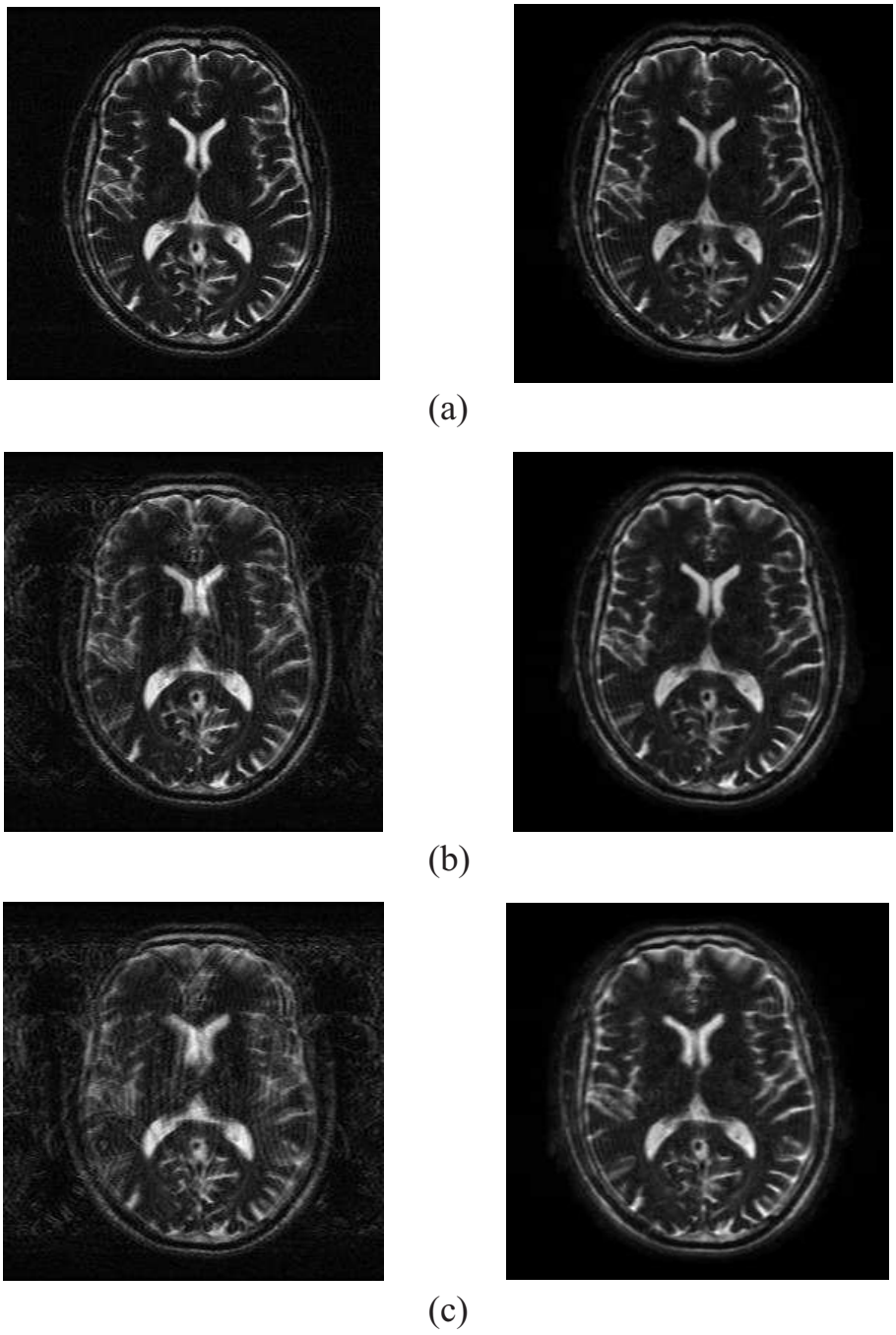

Figure 4.16 Results of *in vivo* experiments in case of (a) no motion, (b) slight motion, (c) continuous motion. Direct inverse Fourier transform reconstructions using complete data set are shown on the left and motion corrected images using the new method are shown on the right.

Chapter 5

Generalized UnalIasing using Support and sensitivity Encoding (GUISE)

In this chapter, a generalized parallel MRI formulation is presented, and the acronym GUISE (Generalized UnalIasing using Support and sensitivity Encoding) has been adopted for this formulation. The relationship between this general formulation and other existing pMRI methods that are reviewed in Chapter 4 is explored. Attention is then paid in inverting the encoding matrix in minimizing the reconstruction artifacts in a least-square sense. A novel sampling strategy design method is developed in conditioning the encoding matrix inversion. Special attention is given to the computational efficiency of the sampling strategy method so that application in clinical imaging is feasible. The object region of support (ROS) is identified as an intrinsic constraint and is incorporated in the reconstruction process. In the application of 3D MR imaging, the performance of this sampling strategy is compared with that of other similar formulations including 2D SENSE and 2D CAIPIRINHA. The incorporation of other image constraints are also discussed.

5.1 A general formation of pMRI

K-space data from the mth coil represents the multi-dimensional Fourier transform of the coil sensitivity weighted object magnetization:

$$F_m[\mathbf{k}] = \sum_{n_1=0}^{N_1-1} \cdots \sum_{n_D=1}^{N_D-1} (c_m[\mathbf{n}] \circ f[\mathbf{n}]) \exp\left[-i2\pi \mathbf{k}^T (\mathbf{n} \circ^{-1} \mathbf{N})\right], \tag{5.1}$$

where D is 2 or 3 for 2D or 3D imaging respectively; $c_m[\mathbf{n}]$, $F_m[\mathbf{n}]$ and $f[\mathbf{n}]$ are respectively the discrete sequence of coil sensitivity profile, the k-space measurement in the mth coil and object magnetization. Following the convention given in Section 2.1, the system can be represented conveniently in the matrix form as

$$\mathbf{F}_m \;=\; \mathbf{W}\,\mathrm{diag}(\mathbf{c}_m)\,\mathbf{f}\,, \tag{5.2}$$

where $\mathbf{F}_m$, $\mathbf{c}_m$, and $\mathbf{f}$ are respectively the stacked column vectors respectively formed from the multi-dimensional quantities $c_m[\mathbf{n}]$, $F_m[\mathbf{n}]$ and $f[\mathbf{n}]$. $\mathrm{diag}(\mathbf{x})$ is a diagonal matrix with the elements of vector $\mathbf{x}$ on the diagonal and zero elsewhere, and hence elements on the main diagonal of $\mathrm{diag}(\mathbf{c}_m)\,\mathbf{f}$ are the sensitivity weighted image elements in the mth coil. $\mathbf{W}$ is the multi-dimensional Fourier matrix as introduced in Section 2.2.1, left multiplication by which performs the DFT with appropriate dimensions.

At the Nyquist sampling rate, data sets from multiple receiver coils contain redundancy, which can be exploited to receive an improved SNR in the combined data set as discussed in Section 4.2.2. In pMRI, this redundancy is utilized to compensate for the samples that are intentionally skipped to reduce scan time. Under-sampling in k-space is equivalent to deleting the corresponding entries in $\mathbf{F}_m$ to skipped phase encoding, which can be expressed as

$$\mathrm{diag}(\mathbf{h})\,\mathbf{F}_m \;=\; \mathrm{diag}(\mathbf{h})\,\mathbf{W}\,\mathrm{diag}(\mathbf{c}_m)\,\mathbf{f}\,, \tag{5.3}$$

where $\mathbf{h}$ is a binary sampling mask with 1 and 0 corresponding to measured and skipped sample positions respectively. As the FE direction is always fully sampled in practice, under-sampling is only applied to PE direction(s). Without loss of generality, overall 2D or 3D k-space can be decomposed into lines or planes consisting of PE direction(s) as discussed in Section 5.2, then each decomposed line or plane can be treated separately using the above formulation. For instance, in 3D imaging Eq. (5.3) applies to a 2D plane consisted of two PE directions, and all the quantities are 2D functions.

In Eq. (5.3) above, it is infeasible to invert the encoding matrix to estimate the underlying image due to its rank deficiency, i.e. there are more unknowns than the number of independent equations. Stacking the encoding matrix as well as the measurements corresponding to different receiver coils forms a hybrid encoding system $\mathbf{E}^{\mathrm{G}}$:

$$\mathbf{F}^{\mathrm{P}} \;=\; \mathbf{E}^{\mathrm{G}}\,\mathbf{f}\,,\;\; \mathbf{E}^{\mathrm{G}} \;=\; \begin{bmatrix} \mathrm{diag}(\mathbf{h})\,\mathbf{W}\,\mathrm{diag}(\mathbf{c}_1) \\ \mathrm{diag}(\mathbf{h})\,\mathbf{W}\,\mathrm{diag}(\mathbf{c}_2) \\ \cdots \\ \mathrm{diag}(\mathbf{h})\,\mathbf{W}\,\mathrm{diag}(\mathbf{c}_M) \end{bmatrix},\;\; \mathbf{F}^{\mathrm{P}} \;=\; \begin{bmatrix} \mathrm{diag}(\mathbf{h})\,\mathbf{F}_1 \\ \mathrm{diag}(\mathbf{h})\,\mathbf{F}_2 \\ \cdots \\ \mathrm{diag}(\mathbf{h})\,\mathbf{F}_M \end{bmatrix}, \tag{5.4}$$

where $\mathbf{F}^{\mathrm{P}}$ denotes the collective partial data sets from all the receiver coils. The hybrid matrix $\mathbf{E}^{\mathrm{G}}$ ('G' for general) is the general pMRI encoding matrix, which maps the underlying object magnetization to the Fourier transform of an image weighted by the local coil sensitivity profile. The input to the encoding process is in image plane and the output is in the k-space. This feature is important in distinguishing with other types of pMRI methods that are discussed in the following sections.

Due to the distinct coil spatial sensitivity weighting in different coils, the simultaneously acquired samples in different coils contains distinctive information and the row rank of the hybrid encoding matrix $\mathbf{E}^{\mathrm{G}}$ increases by the number of phase encoding steps for every coil used. Fig. 5.1 illustrates the structure (magnitude of the elements) of a hybrid encoding matrix constructed from the coil sensitivity profile of an 8-channel receiver coil. The effects of distinctive coil sensitivity weighting are seen as the varying modulations in the matrix rows corresponding to different receiver coils (Fig. 5.1.(b)). Under-sampling in k-space effectively remove rows from the matrix $\mathbf{E}^{\mathrm{G}}$. Applying a regular under-sampling strategy at acceleration factor of 2, every second row in the encoding matrix is removed as shown in Fig. 5.1.(c). The matrix in Fig. 5.1.(c) is in the coil-basis form, in which rows that correspond to the same coil are grouped together. In the gradient-based form that is shown in Fig. 5.1.(d), rows correspond to the same gradient encoding steps are grouped together, and hence the difference of the same encoding step in different receiver coils due to the distinctive coil sensitivity weighting can be seen (as zoomed in Fig. 5.1.(d)). The gradient-based form is very useful in relating this general encoding matrix to those of different pMRI methods.

The known encoding matrix $\mathbf{E}^{\mathrm{G}}$ can be inverted to estimate the underlying object magnetization as long as it has full rank. However its size in practice often prohibits the direct matrix inversion. For instance, in 2D imaging with an 8-channel receiver coil the matrix to be inverted is typically of size $(128 \times 8) \times 128$ when 128 PE steps are taken and the matrix size will increase dramatically to $(128^2 \times 8) \times 128^2$ if 128 PE steps are taken in both PE directions in 3D imaging.

5.2 Relation with existing pMRI methods

All pMRI methods discussed previously are special variants of the general pMRI formulation, in which different simplifications are made to the general encoding matrix $\mathbf{E}^{G}$ in Eq. (5.4) to achieve the necessary computational efficiency. In the following sections, the relations of the general encoding matrix to those of the k-space methods and image plane methods are explored.

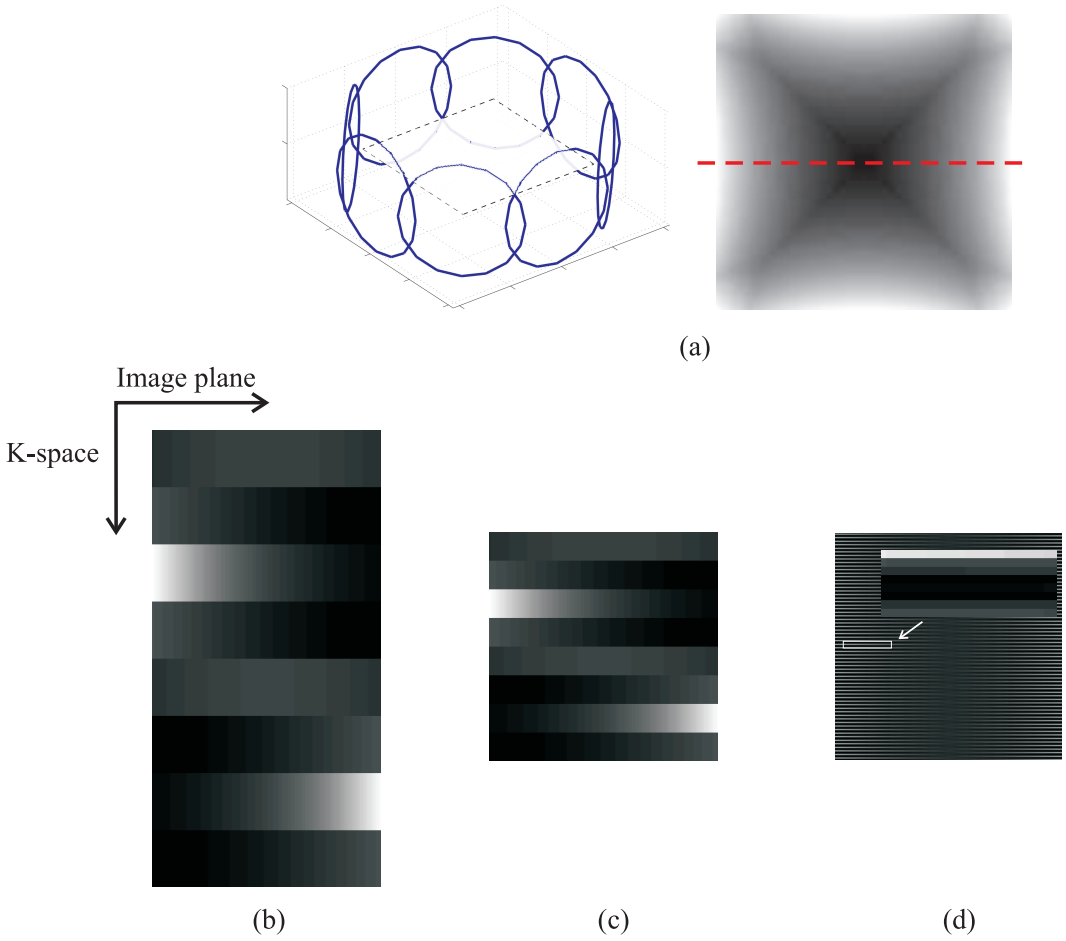

Figure 5.1 Simulated general pMRI encoding matrix using a cross-section coil sensitivity profile from an 8-channel receiver coil (a). In (b) the magnitudes of the elements in the general encoding matrix $\mathbf{E}^{G}$ are plotted, and the eight sections (with distinctive background modulation) in the matrix rows respectively correspond to the 8 receiver coils used. The rows and columns in the general encoding matrix correspond to quantities in image plane and k-space respectively. Under-sampling at an acceleration factor of 2 with regular sampling pattern removes half of the matrix rows as shown in (c). The matrix can be put into the gradient-based form by rearranging the rows, so that the 8 neighboring rows correspond to one Fourier encoding in different receiver coils, as seen in the enlarged region in (d).

5.2.1 k-space methods

In k-space methods, both the input and output of the reconstruction process are in k-space. Hence a Fourier transform should be inserted in the input of the general encoding matrix for transition from the general pMRI formation in Eq. (5.3) to that of k-space method, i.e. (note $\mathbf{W}^{\mathrm{H}}\mathbf{W} = \mathbf{I}$):

$$\begin{aligned} \mathbf{F}_m &= \mathbf{W}\,\mathrm{diag}(\mathbf{c}_m)\,\mathbf{W}^{\mathrm{H}}\mathbf{W}\,\mathbf{f} \\ &= \mathbf{W}\,\mathrm{diag}(\mathbf{c}_m)\,\mathbf{W}^{\mathrm{H}}\mathbf{F} \end{aligned} \tag{5.5}$$

Similarly, stacking the data and encoding matrices for multiple receiver coils forms the overall hybrid encoding matrix:

$$\mathbf{F}^{\mathrm{P}} = \mathbf{E}^{\mathrm{K}}\,\mathbf{F}\,,\quad \mathbf{E}^{\mathrm{K}} = \begin{bmatrix} \mathrm{diag}(\mathbf{h})\,\mathbf{W}\,\mathrm{diag}(\mathbf{c}_1)\,\mathbf{W}^{\mathrm{H}} \\ \mathrm{diag}(\mathbf{h})\,\mathbf{W}\,\mathrm{diag}(\mathbf{c}_2)\,\mathbf{W}^{\mathrm{H}} \\ \cdots \\ \mathrm{diag}(\mathbf{h})\,\mathbf{W}\,\mathrm{diag}(\mathbf{c}_M)\,\mathbf{W}^{\mathrm{H}} \end{bmatrix},\quad \mathbf{F}^{\mathrm{P}} = \begin{bmatrix} \mathrm{diag}(\mathbf{h})\,\mathbf{F}_1 \\ \mathrm{diag}(\mathbf{h})\,\mathbf{F}_2 \\ \cdots \\ \mathrm{diag}(\mathbf{h})\,\mathbf{F}_M \end{bmatrix}. \tag{5.6}$$

where the hybrid encoding matrix $\mathbf{E}^{\mathrm{K}}$ ('K' stands for K-space) maps the Fourier representation of the object magnetization $\mathbf{F}$ to $\mathbf{F}^{\mathrm{P}}$ that consists of Fourier representations coil sensitivity weighted object magnetization in different receiver coils with a sampling pattern $\mathbf{h}$ applied.

Fig. 5.2 illustrates the structure (magnitudes of the elements in the matrix) of a k-space encoding matrix that is constructed using the same coil sensitivity profiles that were used in Fig. 5.1. An obvious feature of the k-space matrix (Fig. 5.2.(a)) is its sparseness, it is seen that the elements around the matrix diagonals are much more significant compared to the other elements. The sparseness of the encoding matrix is due to the smoothly varying coil sensitivity profiles. By the rule of convolution, multiplying the object magnetization with the coil sensitivity profile in spatial domain is equivalent to convolving the Fourier transform of the object magnetization with that of the coil sensitivity profile. The smoothly varying coil sensitivity profiles have sparse Fourier transforms, that lead to sparse k-space point spread functions (PSF) as represented by different rows in the encoding matrix. As the result of the convolution, k-space data in each receiver coils are correlated, however the level of correlation among neighboring k-space points drops rapidly as the k-space separation increases, which leads to the sparsity in Fig. 5.2.(a).

Under-sampling is equivalent to removing rows that correspond to skipped k-space samples. In Fig. 5.2.(b) the under-sampled k-space matrix is formed with a regular under-sampling strategy at an acceleration factor of 2 used. Similar to the gradient-based matrix

Figure 5.2 Simulated k-space encoding matrices using the same coil sensitivity profiles as in Fig. 5.1. At Nyquisit sampling rate, the encoding matrix (a) shows the correlation among the neighbouring samples. Under-sampling removes the rows that correspond to skipped samples as seen in (b). It is seen that the measurement-based encoding matrix is approximately block diagonal, thus its inversion to estimate the missing k-space measurements can be approximately achieved by inverting a series of much smaller matrices on the diagonal.

in Fig. 5.1.(c), measurement-based matrix can be formed by performing a row permutation so that the rows corresponding to the same k-space measurement from different receiver coils are grouped together as shown in Fig. 5.2.(c), and this illustrates the nature of the k-space reconstructions.

It is seen that the permuted k-space encoding matrix (Fig. 5.2.(c)) is approximately block diagonal. Different k-space methods use different levels of truncation in approximating the k-space encoding matrix as block diagonal, so that matrix inversion can be achieved by inverting a series of much smaller sub-matrices along the diagonal. The size of the sub-matrices to be inverted is determined by the number of measurements involved in estimating the missing k-space data. In SMASH, only one k-space sample is incorporated in the reconstruction at a time, hence the sub-matrices to be inverted only have one single column; whereas several k-space samples are used in GRAPPA, this improves reconstruction fidelity in exchange for increased computational complexity. The dropping correlation among neighbouring samples as shown by the block-diagonal encoding matrix illustrates the k-space locality principle utilized by PARS [YMOS05]: as samples that are more distant from the sample to be estimated are incorporated in the reconstruction, the gain of reconstruction fidelity drops as the samples are less correlated.

5.2.2 Image plane methods

In image plane pMRI methods, both the input and output to the reconstruction process are in the spatial domain. Hence an inverse Fourier transform should be inserted at the output of the general encoding matrix for transition from the general pMRI formation in Eq. (5.3), i.e.:

$$\begin{aligned} \tilde{\mathbf{f}}_m &= \mathbf{W}^{\mathrm{H}} \operatorname{diag}(\mathbf{h})\, \mathrm{F}_m \\ &= \mathbf{W}^{\mathrm{H}} \operatorname{diag}(\mathbf{h})\, \mathbf{W} \operatorname{diag}(\mathbf{c}_m)\, \mathbf{f} \end{aligned} \tag{5.7}$$

where $\tilde{\mathbf{f}}_m$ is the image formed with aliasing artifacts by direct inversion of under-sampled data from the mth receiver coil. Following the same stacking procedure as in the previous cases, a hybrid system of Fourier encoding and sensitivity encoding is formed:

$$\tilde{\mathbf{f}} = \mathbf{E}^{\mathrm{I}}\, \mathbf{f}\,, \quad \mathbf{E}^{\mathrm{I}} = \begin{bmatrix} \mathbf{W}^{\mathrm{H}} \operatorname{diag}(\mathbf{h})\, \mathbf{W} \operatorname{diag}(\mathbf{c}_1) \\ \mathbf{W}^{\mathrm{H}} \operatorname{diag}(\mathbf{h})\, \mathbf{W} \operatorname{diag}(\mathbf{c}_2) \\ \cdots \\ \mathbf{W}^{\mathrm{H}} \operatorname{diag}(\mathbf{h})\, \mathbf{W} \operatorname{diag}(\mathbf{c}_M) \end{bmatrix}, \quad \tilde{\mathbf{f}} = \begin{bmatrix} \tilde{\mathbf{f}}_1 \\ \tilde{\mathbf{f}}_2 \\ \cdots \\ \tilde{\mathbf{f}}_M \end{bmatrix}, \tag{5.8}$$

where $\mathbf{E}^{\mathrm{I}}$ ('I' for image) is the image plane encoding matrix that maps the underlying object magnetization to coil sensitivity weighted aliased images in different receiver coils.

Fig. 5.3 illustrates the structure (magnitudes of the elements in the matrix) of a image plane encoding matrix that is constructed using the same coil sensitivity profiles that were used in Fig. 5.1. At Nyquist sampling rates, the image plane encoding matrix maps the image to coil sensitivity weighted images in different receiver coil, hence its diagonals consist of the coil sensitivity profiles of different receiver coils as (Fig. 5.3.(a)). For the encoding matrix of each individual receiver coil, there is a one-to-one mapping of the image elements to their coil sensitivity weighted versions.

Fig. 5.3.(b) shows the encoding matrix with a regular under-sampling strategy at acceleration factor of 2 (a SENSE sampling pattern). Recall that in SENSE under-sampling leads to reduced FOV, and this can be seen as the halved number of rows in Fig. 5.3.(b). As a result of the under-sampling, the mapping between the input and output of the encoding process is no longer one-to-one: two image elements separated by half of FOV are now mapped onto one image element at the output. The encoding process can be better illustrated by the encoding matrix in the image-element-based form (Fig. 5.3.(c)), which is achieved by grouping the rows corresponding to the same folded image element in different receiver coils together. It is seen that the resulting encoding matrix is block diagonal, hence inversion the encoding matrix can be equivalently achieved by inverting a series of much

Figure 5.3 Simulated image plane encoding matrix using the same coil sensitivity profiles as in Fig. 5.1. At Nyquist sampling rate, the encoding matrix in (a) consists of coil sensitivity profiles on its diagonals and maps the image to coil sensitivity weighted images in different receiver coils. At acceleration factor of 2 with regular sampling pattern, the number of rows is halved as shown (b). The image-element-based matrix (c) illustrates the nature of SENSE reconstruction in which sub-matrices are individually inverted to invert the block diagonal encoding matrix; the non-zero regions in one of the sub-matrices are labeled and enlarged.

smaller matrices each of which represents the folding of a small group of image elements. The non-zero regions in one of the sub-matrices are zoomed and shown in Fig. 5.3.(c).

5.2.3 Comparison of k-space and image plane pMRI methods

The difference in the reconstruction outcomes of image plane and k-space methods can be explained by the nature of their approach of inverting the encoding matrix. It is seen in Fig. 5.2 and Fig. 5.3 that both types of methods exploit the sparsity of the encoding matrix and attempt to invert the overall encoding matrix by inverting a series of much smaller matrices for computational efficiency. K-space methods approximate the encoding matrix as block diagonal by truncating elements that are less significant, hence the inexact matrix inversions lead to residual artifacts in reconstructions. Image plane methods (such as SENSE and CAIPIRINHA) employ special under-sampling strategies to achieve block diagonal encoding matrices, hence inversion of the encoding matrix can be equivalently achieved by inverting sub-matrices. However, the SENSE encoding matrices at high acceleration factors may be ill-conditioned, inversion of which will result in high levels of reconstruction noise. Mathematically, this is caused by the small singular values of the encoding matrix, as is more fully explained later. K-space methods are in fact equivalent to the image space methods if all the measured k-space samples are incorporated in estimat-

ing the unmeasured ones [BLH01]. However practical k-space methods only incorporate a small number of neighboring samples that are most relevant in the reconstruction. Thereby by approximating the overall matrix inversion by inverting a series of small matrices effectively truncates the small singular values in the encoding matrices, hence the k-space reconstructions are generally more noise stable. Overall, image plane methods provide optimal data estimation whereas k-space methods allow a trade-off between reconstruction fidelity and stability to be made.

Image plane methods have a key advantage over k-space methods: they allow much greater freedom in incorporating additional constraints or prior knowledge in the reconstruction to improve the reconstructions. In contrast, little success for such approaches has been reported for k-space methods. In the next section a new image plane method that utilizes an adaptive sampling strategy and incorporates other image constraints is presented.

5.3 GUISE - formulation

The new pMRI method is termed as Generalized UnalIasing using Support and sensitivity Encoding (GUISE) to emphasize the fact that both knowledge of coil sensitivity weighting and object support are incorporated in inverting the encoding matrix. Compared to other existing image plane pMRI methods, GUISE has the key advantage of allowing the freedom of employing a sampling pattern which that is adaptively designed for each scan to improve the image reconstruction. The formulation of this method can be seen as a variation of the general image plane encoding matrix as given in Eq. (5.8), with the incorporation of knowledge of object ROS.

Objects are often only supported (non-zero) on a particular region or regions in the spatial domain. In practice, the FOV, in the form of a rectangular parallelepiped, is determined by the k-space sampling density along each different direction. Since the natural shape of the imaged object is unlikely to coincide with FOV, the resulting object image generally only has a limited extent within the FOV. Due to the gaps between the object support and the frame of FOV, sampling at the Nyquisit rate in the frequency domain results in gaps in the object spatial domain replications (Fig. 5.4). As shown in [Mar86, CM90], when such gaps exist, the k-space samples are linearly dependent, meaning that a sample set obtained at the Nyquisit rate contains redundancy. As another evidence of the sampling redundancy, the fundamental minimal sampling density [Lan67] is shown to be dependent on the measure of object support.

The region of support (ROS) constraint can be seen as a binary mask S, elements of which

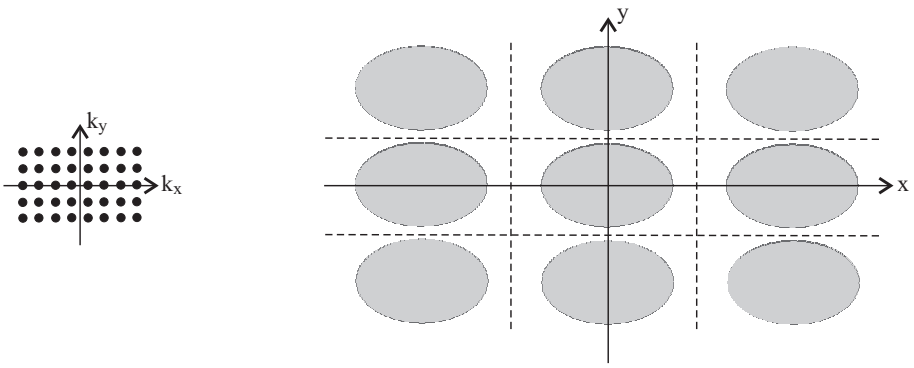

Figure 5.4 Sampling the Fourier transform of an object with limited ROS within the FOV at Nyquisit rate results in gaps in between the replications, which suggests data set sampled at Nyquisit rate contains redundancy.

are 1 if thy are within the object, and 0 otherwise, thus:

$$S(\mathbf{n}) = \begin{cases} 1 & f(\mathbf{n}) \neq 0 \\ 0 & f(\mathbf{n}) = 0 \end{cases} \tag{5.9}$$

The knowledge of the object support constraint can be straightforwardly incorporated in the Fourier encoding in MRI as:

$$\mathbf{F} = \mathbf{W}(\mathbf{s} \circ \mathbf{f}) \tag{5.10}$$

where $\mathbf{s}$ is a column vector obtained by stacking the ROS mask S. Another view of the linear dependency of the k-space samples is that the k-space data are now effectively the result of convolving the Fourier transform of the object with that of the binary support mask, hence they are no longer independent. Alternatively, Eq. (5.10) can be rewritten in a form in which the zero elements outside the object support are removed as well as the corresponding columns in the encoding matrix to form

$$\mathbf{F} = \mathbf{W}[\rho]\mathbf{f}[\rho], \tag{5.11}$$

where ρ denotes the subset that correspond to the elements within the object support region. By the rules of linear algebra, the number of independent rows in $\mathbf{W}$ just needs to be as large as the size of the set ρ for $\mathbf{W}$ to be inverted, i.e. less than full set of samples measured at Nyquisit density are required to recover for $\mathbf{f}[\rho]$. Hence in theory knowledge of object support constraint allows full object recovery from an incomplete measurement set with an acceleration factor up to $\alpha = 1/\phi$, where ϕ denotes the ratio of the ROS area to the total FOV area. The recovery problem has been investigated in [BBMR03, Lan67, GR00].

Similarly the object support constraint can be incorporated in the image plane pMRI en-

coding matrix, which leads to the GUISE formulation as:

$$\mathbf{F} = \mathbf{E}[\rho]\mathbf{f}[\rho] \tag{5.12}$$

Since the analysis is concentrated on the image plane encoding matrix, for brevity, $\mathbf{E}$ is to denote the encoding matrix in GUISE instead of $\mathbf{E}^{\mathrm{I}}$ from henceforth. In pMRI, employment of M receiver coils allows an acceleration factor up to M, with the incorporation of the ROS the maximum possible acceleration factor is improved to $\alpha = M/\phi$.

5.4 GUISE - analysis

In this section, two important aspects of image recovery methods are considered for GUISE: the reconstruction error and reconstruction efficiency.

5.4.1 Reconstruction error

In general, the unaliasing process in image plane pMRI is subject to noise amplification, since coil sensitivity encoding cannot fully compensate for the missing k-space measurements. From the linear algebraic point of view, the encoding matrix is no longer orthogonal, rather its decreasing singular values cause the matrix inversion to be unstable. As seen in reconstruction error analysis of SENSE, which is a special variant of the general image plane pMRI, image unfolding is subject to additional local noise amplification.

In SENSE, the geometry factor (g-factor) is used as a metric for measuring the reconstruction noise amplification level as discussed in Section 4.4.2. However the g-factor is not a suitable metric for the general image unaliasing process as the general encoding matrix incorporates the coil sensitivity encoding as well as the Fourier encoding. As the result, image elements are aliased together with an additional Fourier modulation rather than simply superimposed. Also the g-factor does not give a measure of the overall noise level, which is required in judging the performance of a sampling pattern. In the following, a noise metric based on the singular value decomposition (SVD) is derived to serve as a more suitable measure of the overall noise level.

Denote the aliased and noise-corrupted image from the mth receiver coil as $\tilde{\mathbf{e}}_m$:

$$\tilde{\mathbf{e}}_m \ = \mathbf{W}^{-1}\,\mathrm{diag}(\mathbf{h})\,\mathbf{W}\,\mathrm{diag}(\mathbf{c}_m)\,\mathbf{f} + \mathbf{n}_m \ , \tag{5.13}$$

Collecting measurements from M coils, the encoding matrix with noise corruption can be

written as:

$$\tilde{\mathbf{e}} \;=\; \mathbf{E}\,\mathbf{f} + \mathbf{n},\;\; \tilde{\mathbf{e}} \;=\; \begin{bmatrix} \tilde{\mathbf{e}}_1 \\ \tilde{\mathbf{e}}_2 \\ \cdots \\ \tilde{\mathbf{e}}_M \end{bmatrix},\;\; \mathbf{n} \;=\; \begin{bmatrix} \mathbf{n}_1 \\ \mathbf{n}_2 \\ \cdots \\ \mathbf{n}_M \end{bmatrix}. \tag{5.14}$$

By taking the pseudo-inverse of $\mathbf{E}$, denoted $\mathbf{E}^{+}$, the estimate $\check{\mathbf{f}}$ obtained in a least squares sense is impaired with a noise term $\check{\mathbf{n}} = \mathbf{E}^{+}\mathbf{n}$, i.e.

$$\check{\mathbf{f}} = \mathbf{E}^{+}\tilde{\mathbf{e}} = \mathbf{f} + \mathbf{E}^{+}\mathbf{n}\,. \tag{5.15}$$

The expected value of the noise power is given by:

$$E\left[(\check{\mathbf{n}})^2\right] \;=\; E\left[\check{\mathbf{n}}^H\check{\mathbf{n}}\right] \;=\; E\left[(\mathbf{E}^{+}\mathbf{n})^H(\mathbf{E}^{+}\mathbf{n})\right] \;=\; E\left[\mathbf{n}^H(\mathbf{E}\mathbf{E}^H)^{+}\mathbf{n}\right]. \tag{5.16}$$

Since $(\mathbf{E}\mathbf{E}^H)^{+}$ is Hermitian, it is unitarily diagonalizable [Str88] and can be written as $\mathbf{V}\Lambda\mathbf{V}^H$ where $\mathbf{V}$ is a unitary matrix and Λ is a diagonal matrix of the eigenvalues of $(\mathbf{E}\mathbf{E}^H)^{+}$. Thus:

$$E\left[\check{\mathbf{n}}^2\right] = E\left[\mathbf{n}^H\mathbf{V}\Lambda\mathbf{V}^H\mathbf{n}\right] = E\left[(\mathbf{V}^H\mathbf{n})^H\Lambda(\mathbf{V}^H\mathbf{n})\right]. \tag{5.17}$$

Since $\mathbf{V}$ is unitary, $\mathbf{V}^H\mathbf{n}$ has the same statistics as $\mathbf{n}$. Let the elements of this new vector be u_1, u_2, …, u_N, and the elements of the diagonal matrix Λ be λ_1,λ_2 ,…,λ_N, where N is the column rank of $\mathbf{E}$, or the total number of image elements within the FOV.

$$\begin{aligned} E\left[\check{\mathbf{n}}^2\right] &= E\left[\bar{u}_1\lambda_1u_1 + \bar{u}_2\lambda_2u_2 + \ldots + \bar{u}_N\lambda_Nu_N\right] \\ &= E\left[\lambda_1\left|u_1\right|^2 + \lambda_2\left|u_2\right|^2 + \ldots + \lambda_N\left|u_N\right|^2\right] \\ &= \delta^2\sum_{i=1}^{N}\lambda_i\,, \end{aligned} \tag{5.18}$$

where δ^2 is the power of the added white noise. Since the sum of the eigenvalues of a square matrix is equal to its trace [Str88], and each eigenvalue of $(\mathbf{E}^H\mathbf{E})^{-1}$ is the inverse of a squared singular value $\mathbf{E}$:

$$E\left[(\check{\mathbf{n}})^2\right] = \delta^2\sum_{i=1}^{N}\frac{1}{\sigma_i^2} = \delta^2\mathrm{trace}(\mathbf{E}^H\mathbf{E})^{-1} \tag{5.19}$$

Hence the the sum of the inverse of the squared singular values gives a measure of the overall noise level amplification. For brevity, it is referred as the IT (inverse trace) metric.

The IT metric is a better measure in judging the least squares error than the usual condition number (the ratio of the largest to the smallest singular value), as the latter often gives an incomplete description of the matrix inversion in the presence of noise. Furthermore, the IT metric is completely determined by the encoding matrix itself rather than the actual signal, hence it serves as a useful measure of the performance of different sampling patterns.

In the case where the object has a known ROS, in which only P elements lie within the ROS, the above term can be written as:

$$E\left[(\check{\mathbf{n}})^2\right] = \delta^2 \sum_{i=1}^{P} \frac{1}{\sigma_i^2} = \mathrm{trace}(\mathbf{E}[\rho]^H \mathbf{E}[\rho])^{-1} \tag{5.20}$$

It is seen that reducing the number of image elements to be recovered reduces the number of singular values and hence leads to a smaller IT metric ([BACB01]). Thus incorporating the object support constraint in image reconstruction by excluding pixels outside the ROS reduces the reconstruction noise level within the object ROS.

5.4.2 Reconstruction efficiency

As shown previously, image recovery from under-sampled data sets involves inversion of the known encoding matrix in Eq. (5.4). However direct inversion of the general encoding matrix is often computationally intractable due to its size. In this section, decomposition of the overall encoding matrix by using a periodic under-sampling pattern is discussed, so that inversion of the overall encoding matrix can be equivalently achieved by inverting a series of much smaller sub-matrices to achieve reconstruction efficiency.

Consider a sampling pattern H of size $\mathbf{N}$ that is periodic, and it consists of a repeated block G of size $\mathbf{C}$. As shown in [BACB01], its PSF h can be written as:

$$h[\mathbf{n}] = \begin{cases} \sqrt{L}\, g[\mathbf{n} \circ^{-1} \mathbf{L}] & \mathbf{n} = \mathbf{m} \circ \mathbf{L},\ \mathbf{m} \in \mathbb{Z}^M \\ 0 & \text{elsewhere.} \end{cases} \tag{5.21}$$

where g is the PSF of the repeated pattern G, and $\mathbf{L} = \mathbf{N} \circ^{-1} \mathbf{C}$, where $\circ^{-1}$ denotes element wise division. In other words, periodicity cause the sequence to have a sparse PSF with non-zero elements regularly separated by zero elements. This property of periodic sampling patterns is exploited to allow computational efficiency in image reconstruction.

In 3D MR imaging, under-sampling in k-space can be considered as applying a 2D binary mask to the plane defined by the two PE directions. From Eq. (5.21), if the sampling mask is chosen to consist of a 2D repeated block of size $C_1 \times C_2$, then its PSF only has non-zero elements separated by $L_1 = N_1/C_1$ and $L_2 = N_2/C_2$ in each direction. By the rule of

convolution, applying a sampling mask $\mathbf{H}$ in the k-space is equivalent to convolving the the point spread function h of the mask with the image f ,i.e.:

$$\tilde{f} = f \odot h \tag{5.22}$$

As the result of periodic sampling, aliasing takes place in a well controlled manner, as depicted in Fig. 5.5: only image elements that are separated by integer multiples of L_1 and L_2 in each direction respectively are aliased together, forming what is referred to as a sub-sequence. Image elements within each such aliased sub-sequence are independent from image elements in all other sub-sequences. Thus the overall system is decomposed into $L = L_1 \times L_2$ independent sub-sequences, and a sub-system matrix can be set up for the lth sub-sequence:

$$\tilde{\mathbf{e}}_l = \mathbf{E}_l[\rho_l]\,\mathbf{f}_l[\rho_l] + \mathbf{n}_l, \quad \mathbf{E}_l[\rho_l] = \begin{bmatrix} \mathbf{W}^{-1}\,\mathrm{diag}(\mathbf{g})\,\mathbf{W}\,\mathrm{diag}(\mathbf{c}_{l,1}) \\ \mathbf{W}^{-1}\,\mathrm{diag}(\mathbf{g})\,\mathbf{W}\,\mathrm{diag}(\mathbf{c}_{l,2}) \\ \cdots \\ \mathbf{W}^{-1}\,\mathrm{diag}(\mathbf{g})\,\mathbf{W}\,\mathrm{diag}(\mathbf{c}_{l,M}) \end{bmatrix}, \quad \tilde{\mathbf{f}}_l = \begin{bmatrix} \tilde{\mathbf{f}}_{l,1} \\ \tilde{\mathbf{f}}_{l,2} \\ \cdots \\ \tilde{\mathbf{f}}_{l,M} \end{bmatrix}, \tag{5.23}$$

where subscript l is used to denote quantities related to the lth sub-sequence only. The symbol $\mathbf{n}_l$ is used for notational consistency for the noise in the lth sub-sequence; however the noise statistics should not differ in different sub-sequences.

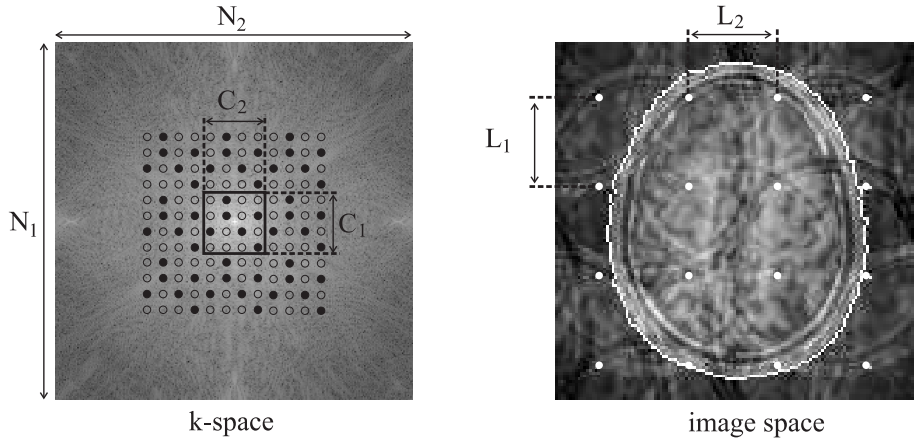

Figure 5.5 A periodic k-space sampling pattern leads to decomposition of the image plane system. On the left, the central region of the k-space under-sampling pattern ($N_1 \times N_2$), consisting of a ($C_1 \times C_2$) repeating block, is shown (dark and bright dots represent acquired and skipped samples, respectively). Aliasing in the resulting image plane is then limited to occur within sub-sequences of image elements, one of which is depicted on the right as a regular set of white dots. There are in total $L_1 \times L_2$ independent sub-sequences and elements in each sub-sequence are separated by L_1 and L_2 as depicted. For each such sub-sequence only those image elements which fall within the ROS region (outlined in white) need to be recovered. The final 2D image is reconstructed by assembling all the recovered sub-sequences.

As reviewed in the previous chapter, SENSE and CAIPIRINHA also employ regular sampling patterns to restrict the folding to image elements from known positions. In their algorithms, the regularity of the sampling patterns (also known as lattice structures, see [TBP03]) causes only a fraction of elements within a sub-sequence to be folded together (see their PSFs in Fig. 5.4.2(a) and (b)) forming a smaller sub-sequence. In the more general formulation above, samples within the repeated blocks are allowed in arbitrary positions; as a result all the elements from the sub-sequence are to be aliased together with a modulation (weighting of different image elements) determined by the PSF of the sampling patterns. In the former case, employing such patterns minimize the number of image elements to be aliased together and is a heuristic attempt to improve the efficiency of sensitivity encoding. However the more general formulation above allows the sampling pattern to be designed for a particular imaging situation to achieve better image reconstruction as is discussed in the next section.

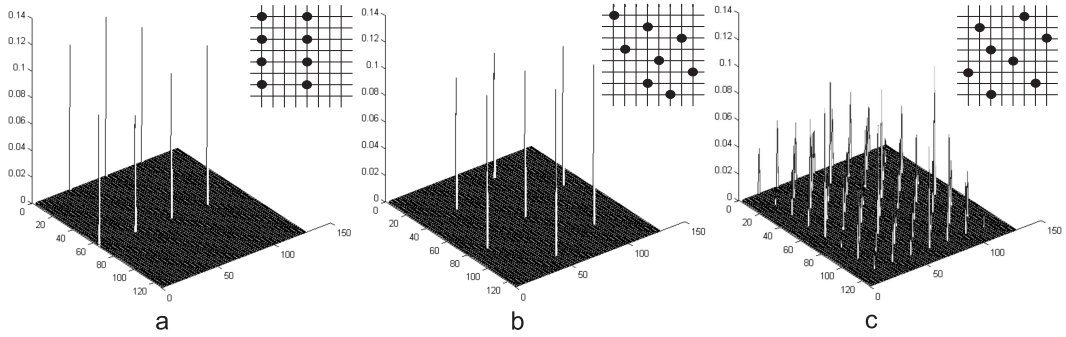

Figure 5.6 Point spread functions (PSF) of different sampling patterns at acceleration factor of 8: (a) 2D SENSE, (b) 2D CAIPIRINHA, (C) a periodic (8×8) non-uniform sampling pattern in GUISE. The repeated block patterns of 8×8 are shown on the top corner in each case. The PSFs indicate how aliasing will take place. It is seen that in (a) and (b), image elements within the sub-sequences will be aliased with uniform weighting whereas aliasing in (c) involves an additional modulation that is determined by the PSF of the sampling pattern.

5.5 GUISE - Sampling pattern design

The image reconstruction quality is determined by the encoding matrix, which is in turn dependent on three factors: 1) the sensitivity functions of the receiver coils, 2) the k-space sampling locations of the measured data, and 3) the object support. In clinical scans, the coil sensitivity profiles and the ROS of the imaged object are both predetermined according to the choice of coil system and the choice of FOV respectively. However the sampling strategy can be adaptively designed based on the knowledge of coil sensitivity profiles and object ROS to optimize the image reconstruction. Despite this possibility, little attention has been paid to the problem of sampling pattern design so far.

As introduced previously, early stage pMRI methods SMASH [SW97] and SENSE [PWSB99] both employ uniform under-sampling patterns. In SMASH, the uniform sampling pattern

allows a uniform coverage of k-space to be achieved, so that the unmeasured k-space data can be estimated from the nearest possible data. In SENSE, the uniform sampling pattern leads to enlarged k-space sample spacing and hence reduced FOV in the image domain. Later variations of these methods including GRAPPA [GJH$^+$02] and SPACE RIP [KLK00] both incorporate a densely sampled k-space centre and uniformly sampled k-space peripheral region for the purpose of achieving auto-calibration and to exploit the high energy concentration level in the central k-space region. CAIPIRINHA [BBHM05] intentionally modifies the regular SENSE sampling pattern to achieve a modified aliasing pattern so that the efficiency of sensitivity encoding is improved. All the above approaches have employed heuristic sampling patterns. A more rigorous approach has been reported by Aggarwal and Bresler in [AB04], in which the sampling pattern is adaptively designed based on an optimizing criteria. Later on, this idea was also extended by the same group (Sharif and Bresler) to dynamic imaging [SB06, SB07], in which sampling pattern design takes place in the temporal-Fourier domain. However, these approaches are generally based on knowledge of the statistical model of the imaging process, which reduces their practical utility.

Adaptive sampling strategy design in the case of single receiver coil MRI has been investigated in [RH95, GR00, GR01, BACB01, BBMR03], in which the knowledge of object ROS is incorporated to allow for under-sampling to take place. In [RH95], Reeves *et al.* set up the problem formulation as Eq. (5.11), and they considered two sample selection methods based on the IT metric in minimizing the least square errors: branch and bound, and sequential backward selection (SBS) to avoid exhaustive search through all the possible sampling patterns. The former approach systemically considers all the possible candidates in the combinatorial sample selection process, and hence is optimal. The latter proceeds by sequentially removing the sample that gives the least reduction to the metric until the desired number of samples are left. SBS offers a trade-off among computational efficiency and optimality. In [GR00], Gao *et al.* considered sequential forward selection (SFS) in which the sample that gives the least increment to the IT metric is selected until the desired number of samples are obtained. SFS was shown to be more computational efficient than SBS. However, the sampling pattern design is still restricted to fairly small size images due to the large matrix inversion involved in computing the IT metric. In [GR01], Gao et al. restricted the possible sampling patterns to be periodic and together with the previously developed SFS, sampling pattern design for a medium-sized image (128×128) can be completed within a minute. In [BACB01] and [BBMR03], Blakeley et al. followed a similar approach in employing periodic sampling sampling patterns and SFS sample selection, and proposed new metrics for the sample selection process. Instead of directly computing the computationally heavy IT metric, these new metrics are based on the distances in between the k-space samples and those of the image elements within the ROS, and hence a much accelerated sampling pattern design process is achieved.

In pMRI, the encoding matrix is further complicated by the different sensitivity encoding in each receiver coil, and the placement of one k-space sample corresponds to several measurements from all the receiver coils. Hence the necessary computational complexity is much increased compared to the case of single receiver MRI. However in practice it is necessary to be able to complete the sampling pattern design process in a time frame within a fraction of the actual scan time, otherwise the long sampling pattern design process would defeat the purpose of under-sampling. Due to the reconstruction efficiency, the sampling patterns are restricted those consisted of repeated blocks, although the method is equivalently applicable to designing general non-periodic sampling patterns. In order to facilitate the sampling pattern design task, it is split into two steps: choosing appropriate sampling block sizes, and then select samples within the block to be measured.

5.5.1 Choosing the repeated block size

The size of the repeated block in k-space determines the size and spatial location of the sub-systems in the image plane as related in Eq. (5.21). It determines which image elements are to be aliased together. Consequently, it sets the coil sensitivity weighting and support constraint for each resulting sub-system. Recall that the block has dimensions $C_1 \times C_2$ that are respectively factors of N_1 and N_2. For commonly used data sizes such as 128 and 256, there exists considerable freedom in choosing the block size. If a specific acceleration factor α is to be achieved, appropriate block sizes are restricted to those which make $C_1 \times C_2$ an integer multiple of α. Appropriate decision of block sizes can be made by considering the block parameters, first in terms of shape, then in terms of overall size.

The shape of the repeating blocks determines which dimension there are more image elements to be aliased, i.e. it is either wide, tall or square. The effects of different repeating block shapes is dependent on the actual coil sensitivity profile and the object support. In terms of the coil sensitivity weighting, it is more beneficial to choose the larger of C_1 or C_2 to correspond to the direction in which there is a greater variation in coil sensitivity. In terms of the object support, it is more advantageous to choose the larger of C_1 or C_2 to correspond to the direction for which the out-of-support region is larger (i.e., for which the distance from the edge of the frame to the support is greater). This is intuitively satisfying since aliasing the free air region onto the object is better than aliasing the object region onto itself.

Assuming that the constraints above have been satisfied, now consider the effects of extending the block size in each dimension. Such effects are illustrated in Fig. 5.7: assuming a circular object support region, and the use of sampling patterns with repeated block dimensions of (2×4) and (8×8) are compared. In the top row, the spatial locations of sub-sequences resulting from the two different sampling patterns are compared. In the

bottom row, the histograms of the sub-support ratio ϕ_l (the ratio of the image elements within the ROS to the total number of image elements in the lth sub-sequence) of all the sub-sequences are compared. Based on the observations in Fig. 5.7, it is postulated that the use of large block sizes has the following influence in exploiting the coil sensitivity and object support constraint:

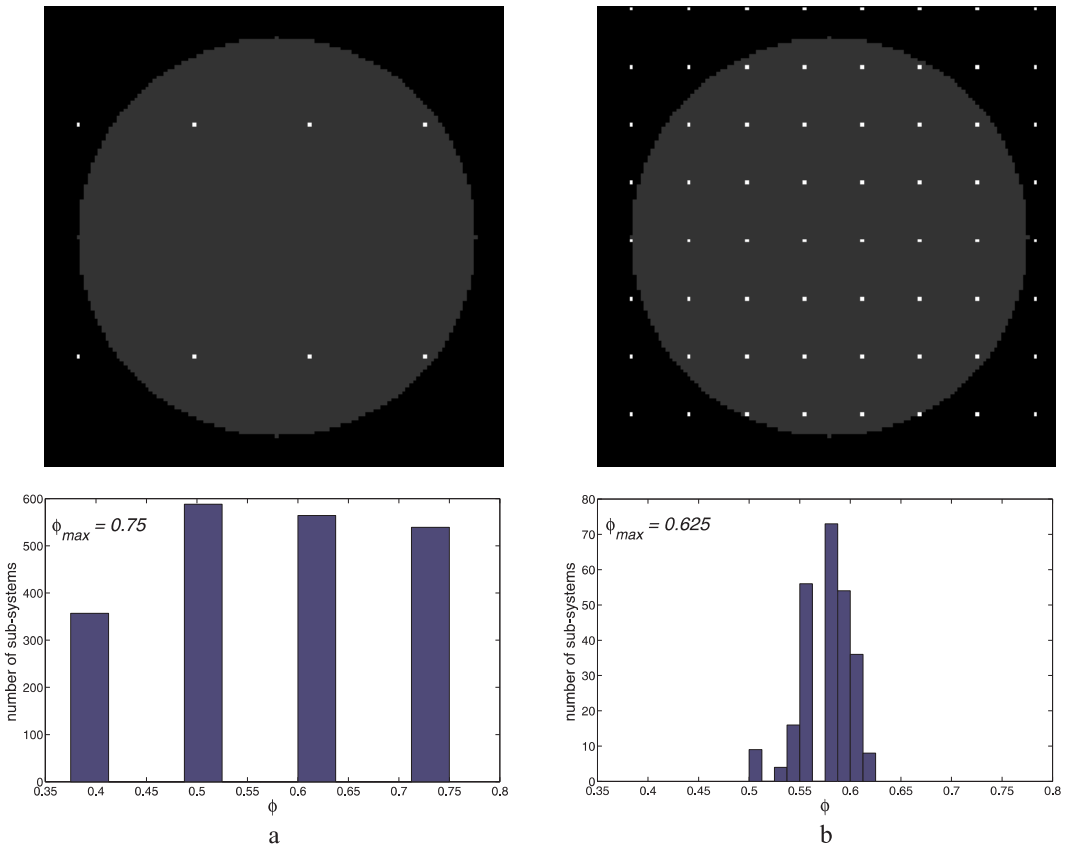

Figure 5.7 An image plane of size 128 $\times$ 128 and sub-systems corresponding to k-space block sizes of (a) 2 $\times$ 4, (b) 8 $\times$ 8. The histogram of all the ϕ_l values indicates that using larger block size leads to a more even distribution of the image elements within the support region (the central circular region as shaded) and also a lower $\phi_{\max}$. Thus expanding the k-space block size promotes the maximum acceleration factor achievable.

Coil sensitivity weighting As the physical coil sensitivity profiles are smoothly varying, the spatial separations of the image elements determine the distinctiveness of their coil sensitivity weighting. In Fig. 5.7, it is seen that a larger block dimension (8×8) leads to increased spatial extent of each sub-sequence (larger coverage within the FOV) and decreased spatial separation between neighboring elements. Enlarged spatial extent of the sub-sequences means the coil sensitivity variation within each sub-system is enhanced; at the same time, because the spatial separation of the neighbouring elements within the sub-sequences is reduced, the minimum variation of coil sensitivity weighting of the image elements within the sub-sequences is reduced. The former factor associated with appropriate sampling patterns can lead to improved efficiency of coil sensitivity encoding as observed

in the improvement from 2D SENSE to 2D CAIPIRINHA. However, the finer sensitivity variation within the sub-sequences means an inappropriate sampling pattern would lead to worse results, since image elements with little difference in sensitivity encoding are to be aliased together.

Region of support (ROS) As in general the object support is contiguous, with an enlarged repeated block size, image elements within the ROS (vice versa free air region outside the ROS) are more evenly distributed among the resulting sub-sequences, i.e. ϕ_l values are distributed over a narrower range as seen in Fig. 5.7.(b). This is a favorable condition for reducing the overall IT metric. Intuitively, it is better to have image elements containing object signal aliased with image elements are known to contain no signal rather than with themselves, as the in the former case the image elements outside the ROS can be eliminated from reconstruction resulting better matrix conditioning for recovering image elements within the ROS. However, the argument at the beginning might not be strikingly clear as the overall ratio of ROS to FOV is fixed. Consider an extreme case where a small block size (thus a small sub-sequence size) is used: some sub-sequences may reside entirely outside the ROS. This effectively means that overall there is a higher degree of aliasing compared to the cases where all the free air regions have been aliased with object region. By exaggerating this argument, in the interest of an overall better conditioned problem, it is better to have all the sub-sequences with a similar degree of aliasing than to have an uneven aliasing profile. Numerically, the IT metric grows rapidly with a decreasing row rank of the encoding matrix, so the sum of all the IT metrics will be smaller if all the sub-systems have similar row rank.

From the above it is indicated that a block dimension as large as possible is suggested for achieving the optimal noise level at reconstruction (support for this conclusion arises from the simulation results presented later in Section 5.7.1). However, not only does the use of large block sizes present difficulties at reconstruction, but it is also a very challenging task to design sampling patterns for large blocks.

5.5.2 Sample selection

The actual repeated block pattern in the sampling pattern determines the PSF of the sampling pattern, and hence the aliasing pattern. For achieving the necessary computational efficiency in sampling pattern design, sequential backward selection (SBS) and sequential forward selection (SFS) are considered. Investigation of the two methods in [RZ99] showed that both SFS and SBS perform consistently well and SBS has a tighter performance upper bound (potentially being more robust). However, SFS is considered to be more suitable for implementation in pMRI taking prior consideration of the necessary computational load:

- With an acceleration factor greater than 2 (the usual case in pMRI), SBS requires more sequential steps to be performed. For instance, at an acceleration factor of 8, completion of SFS requires sequential selections of $\frac{1}{8}$ of all the samples, whereas SBS requires sequential eliminations of $\frac{7}{8}$ of all the samples that has higher level of computational complexity.
- SBS starts with matrix inversion with near full ranks, which is computationally heavier than the case of SFS which starts with inversion of low rank matrices.
- SFS allows data acquisition to take place as soon as the first sample is selected, whereas SBS needs to wait for the entire sample elimination process to be completed before data acquisition.

In addition, the sequentially acquired samples in SFS embed temporal information that can be exploited in dynamic imaging as is investigated in Chapter 7.

An alternative metric

The IT metric itself involves inefficient matrix inversions, which leads to long processing time. Instead consider the sum of the singular values raised to the fourth power, given by $\mathrm{trace}([\mathbf{E}^H\mathbf{E}])^2$. Since the sum of the square of the singular values ($\sum_{i=1}^{i=N}\lambda_i^2$)is a constant term (see *Lemma 1*), the two terms ($\sum_{i=1}^{i=N}\lambda_i^{-2}$ and $\sum_{i=1}^{i=N}\lambda_i^4$) have similar general behavior under minimization: both terms are minimized when all the singular values are equal; both terms raise as the the variance of the singular values increases. The correlation between the two terms is plotted in Fig. 5.8, which shows that there is a monotonically raising relationship between the two terms. Hence the squared trace (ST) metric can be used as a substitute term to be minimized in the sample selection process.

Lemma 1: $\sum_{i=1}^{i=P}\lambda_i^2 = \mathrm{trace}(\mathbf{E}^H\mathbf{E})$ is a constant term.

Firstly,

$$\mathbf{E}^H\mathbf{E} = \frac{1}{N^2}\sum_{m=1}^{M}\mathrm{diag}(\bar{C}_m)\mathbf{A}^H\mathbf{A}\mathrm{diag}(C_m)$$

where $\mathbf{A} = \mathbf{W}^{-1}\,\mathrm{diag}(\mathbf{h})\,\mathbf{W}$ and M is the total number of receiver coils used, and N is the total number of the image elements to be recovered. Then

$$(\mathbf{E}^H\mathbf{E})_{kl} = \sum_{m=1}^{M}\sum_{i=1}^{Q} e^{\frac{-2\pi}{N}\alpha_i(\beta_k-\beta_l)}\bar{c}_{m,k}c_{m,l}$$

where Q is the total number of k-space samples acquired, $\alpha_i, i = 1, 2...Q$ and $\beta_i, i = 1, 2...N$

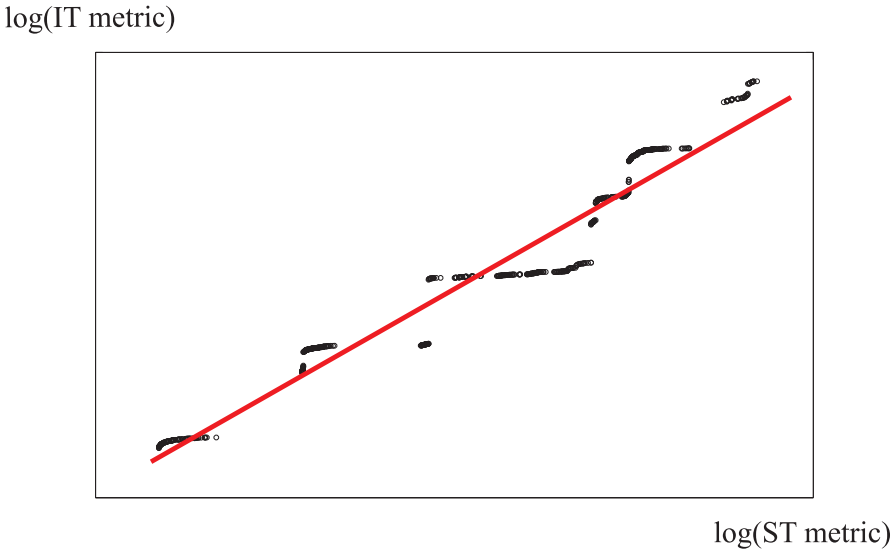

Figure 5.8 Correlation of the ST metric terms and IT metric terms of a simulated system (shown as the circles). A pMRI system is first simulated using the coil sensitivity profiles of an 8-channel receiver coil. Then an under-sampling pattern consisted of a repeated block size of 8×8 at acceleration factor of 4 is applied, which gives rise to independent sub-systems of size 8×8. The IT metric and ST metric terms of all the resulting sub-systems are sorted and plotted against each other. It is seen that there exists a monotonically raising correlation among the two terms (see the line of best fit).

denote for the positions of the acquired samples in k-space and the image elements in spatial domain respectively.

$$\begin{aligned} \text{trace}(\mathbf{E}^H\mathbf{E}) &= \sum_{m=1}^{M}\sum_{k=1}^{P}\sum_{i=1}^{Q} e^{\frac{-2\pi}{N}\alpha_i(\beta_k-\beta_k)}\bar{c}_{m,k}c_{m,k} \\ &= \sum_{m=1}^{M}\sum_{k=1}^{P}\bar{c}_{m,k}c_{m,k} \end{aligned} \tag{5.24}$$

hence the above term equates to a constant term whose value is determined by the coil sensitivity profile and the number of image elements to be recovered within the spatial domain.

Although the ST metric appears to be computationally expensive, its mathematic nature allows very efficient sequential forward selection (SFS) calculation to be carried out. As shown in the *Lemma 2*, the overall ST metric of a sampling pattern is completely determined by the distances among the acquired k-space samples and distances among image elements to be recovered. In another words, it depends on the relative separations among the k-space samples rather than their actual locations. Hence a look up table (LUT) with entries that correspond to all the possible separations among samples in the entire k-space can be first created, and then the overall ST metric for a particular sampling pattern can be gained

by summing up the entries that correspond to the sample separations in that sampling pattern. Such approach allows much computational efficiency in the SFS approach as the change of the overall cost function (ST metric) as a result of introducing an additional sample can be readily obtained by examining the additional sample separations between this new sample and the other pre-selected samples.

Lemma 2: $\mathrm{trace}(\mathbf{E}^H\mathbf{E}\mathbf{E}^H\mathbf{E})$ is determined by the distances of the acquired k-space samples and distances of image elements to be recovered.

$$\begin{aligned}
\mathrm{trace}(\mathbf{E}^H\mathbf{E}\mathbf{E}^H\mathbf{E}) &= \frac{1}{N^4}\sum_{m=1}^{M}\mathrm{diag}(\bar{C}_m)\mathbf{A}^H\mathbf{A}\mathrm{diag}(C_m)\sum_{n=1}^{M}\mathrm{diag}(\bar{C}_n)\mathbf{A}^H\mathbf{A}\mathrm{diag}(C_n) \\
&= \frac{1}{N^4}\sum_{m=1}^{M}\sum_{n=1}^{M}\mathrm{diag}(\bar{C}_m)\mathbf{A}^H\mathbf{A}\mathrm{diag}(C_m)\mathrm{diag}(\bar{C}_n)\mathbf{A}^H\mathbf{A}\mathrm{diag}(C_n) \\
&= \frac{1}{N^4}\sum_{m=1}^{M}\sum_{n=1}^{M}\mathrm{trace}(\mathrm{diag}(\bar{C}_m)\mathbf{A}^H\mathbf{A}\mathrm{diag}(C_m)\mathrm{diag}(\bar{C}_n)\mathbf{A}^H\mathbf{A}\mathrm{diag}(C_n)) \\
&= \frac{1}{N^4}\sum_{m=1}^{M}\sum_{n=1}^{M}\sum_{x=1}^{N}\sum_{y=1}^{N}\bar{c}_{m,x}c_{m,y}\bar{c}_{n,x}c_{n,y}\sum_{i=1}^{Q}\sum_{j=1}^{Q}e^{-\frac{2\pi}{N}(\alpha_i-\alpha_j)(\beta_x-\beta_y)}
\end{aligned}$$

Hence the value of the ST metric is determined by the terms of $(\alpha_i-\alpha_j)(\beta_x-\alpha_y)$, which are the separations of all the sample and the image elements. As the separations of the image elements are determined by the FOV and the object ROS and are thus fixed, the overall ST metric is then completely determined by the separations of the k-space samples in a particular sampling pattern.

5.6 GUISE - use of additional prior knowledge

As GUISE is a generalized version of SENSE, it is thus possible to incorporate the other prior knowledge or constraints that have been suggested for SENSE, such as those in [KA00, HMK+06, JW05, BR05, LKBW04, LWA+05]. The partial Fourier technique exploits the inherent redundancy in k-space measurement, and has been combined with SENSE [KA00, HMK+06, JW05, BR05] for achieving higher acceleration factors. It is either possible to take a sequential approach where conjugate symmetric counterpart of samples are intentionally skipped as in [KA00, HMK+06], or a more convenient form as been suggested in [JW05, BR05]. Based on the assumption that the imaged object is real (the image phase term due to field inhomogeneity can be obtained from a small region in k-space centre and included in the coil sensitivity profile), the system for recovering the lth sub-sequence can

be written as:

$$\begin{bmatrix} \mathrm{Re}\{\tilde{\mathbf{f}}\} \\ \mathrm{Im}\{\tilde{\mathbf{f}}\} \\ 0 \end{bmatrix} = \begin{bmatrix} \mathrm{Re}\{\mathbf{E}[\rho]\} & \mathrm{Re}\{-\mathbf{E}[\rho]\} \\ \mathrm{Im}\{\mathbf{E}[\rho]\} & \mathrm{Re}\{\mathbf{E}[\rho]\} \\ 0 & \lambda\mathbf{I} \end{bmatrix} \begin{bmatrix} \mathrm{Re}\{\mathbf{f}[\rho]\} \\ \mathrm{Im}\{\mathbf{f}[\rho]\} \end{bmatrix}, \tag{5.25}$$

where Re{} and Im{} denotes the real and imaginary part respectively, $\mathbf{I}$ is an identity matrix, and λ is a scalar controlling the weighting of the constraint. Lin *et al.* have also proposed incorporation of an initial estimate $\mathbf{f}_i$ at reconstruction using Tikhonov regularization [LKBW04, LWA+05], which can be written in a similar form:

$$\begin{bmatrix} \tilde{\mathbf{f}} \\ \lambda\mathbf{f}_i[\rho] \end{bmatrix} = \begin{bmatrix} \mathbf{E}[\rho] \\ \lambda\mathbf{I} \end{bmatrix} \mathbf{f}[\rho], \tag{5.26}$$

where $\mathbf{I}$ and λ are the same as in the previous case. In both cases, the row rank of the matrix to be inverted is increased and thus allows a higher acceleration factor and (or) better SNR optimization. However, there exist potential problems in incorporating the above constraints. Firstly, good knowledge of the constraints (which could be sometimes difficult to obtain in practice) are crucial for success; secondly, choosing the appropriate weighting factor λ is important in avoiding the introduction of additional artifacts and presents considerable computational complexity. In the above cases, incorporating the above constraints effectively modifies the objective function to:

$$||\tilde{\mathbf{f}} - \mathbf{E}[\rho_l]\mathbf{f}[\rho]||_2 + \lambda^2||\Theta||_2, \tag{5.27}$$

where $||\cdot||_2$ denotes the 2-norm. Assuming a fixed weighting coefficient λ, the additional objective term Θ has no dependence on the encoding matrix $\mathbf{E}[\rho]$ (hence independent of the sampling pattern used) in the above cases, the adaptive sampling pattern design in GUISE is still valid and leads better conditioned inverse problem. Simultaneous selection of the weighting coefficient and the sampling pattern may be possible by reformatting the above as a bi-variable non-linear optimization.

5.7 Performance of GUISE

The main difference between GUISE and other image plane methods (SENSE and CAIPIRINHA) is the sampling patterns employed in image reconstruction. In the following sections, the performance of the adaptive sampling patterns used in GUISE is investigated using both simulated data and in-vivo data. Image reconstructions with image additional constraint (Tikhonov regularization) in the three different methods are also made and compared.

5.7.1 Simulation

The noise immunity of the sampling pattern employed by SENSE and CAIPIRINHA are compared with those obtained from an adaptive sampling pattern design. In the latter case, the following sample selection methods are used with various block sizes: (a) SFS based on the IT metric; (b) SFS based on the ST metric; and (c) exhaustive search for the pattern that gives the smallest IT metric are tested for various repeated block sizes. The effects of using different repeated block sizes are investigated by performing exhaustive searches for all the associated sampling patterns of a particular block size. Due to the demanding computational requirement, exhaustive searches are limited to relatively small block sizes at high acceleration factors.

The IT metric is fully determined by the knowledge of coil sensitivity weighting and object support and is independent of the actual k-space data. In the simulation, a binary 2D phantom 128×128 with perfectly centered circular ROS was used, along with the axial plane coil sensitivity profile extracted from a simulated 8-channel head coil array that has been employed so far. The IT metric associated with different sampling patterns are compared in two situations: (a) knowledge of ROS is not available; and (b) ROS is known. In the former case, the entire FOV(128×128) is to be recovered, whereas the perfect knowledge of the circular ROS is applied the latter case.

The simulation results of the IT metrics of different sampling patterns are presented in Fig. 5.9 and Fig. 5.10. In Fig. 5.9, the logarithm of the IT metric of all the sampling patterns associated with different block sizes are presented in box-whisker plots. In Fig. 5.10, the logarithm of the IT metric of the sampling pattern given by different sampling strategy design methods are plotted. For 2D CAIPIRINHA, there are several possible candidates, and the one that resulted in the lowest IT metric was selected.

Effects of using different block sizes

Since the actual block sampling pattern determines the conditioning of the system, the effects of different block sizes are determined by comparing with the range of the IT metric of their associated sampling patterns. It is seen in Fig. 5.9 that extending the block size broadens the range of IT metrics in both cases without and with the knowledge of ROS: the worst case IT metric deteriorates and the best case IT metric improves. In the case of recovering the entire FOV, the improvement of best case conditioning is solely dependent on the enhancement of coil sensitivity weighting among the aliased image elements, as a result of the greater spatial extension of sub-sequences associated with larger block sizes. In the latter case, where regions outside the object are eliminated from the reconstruction, the coil sensitivity variation range is restricted to be within the object region. Consequently,

the enhancement of coil sensitivity distinctness offered by larger block sizes is less pronounced. However, the more even distribution of the image elements within the support region among all the sub-systems makes a contribution towards reduced the overall noise level, and is a favorable condition independent of the actual sampling pattern used.

Sample selection

The results derived by an exhaustive search provide the best sampling pattern to which those derived by the practical SFS methods can be compared. Comparing the results of SFS and the exhaustive search shows a good trade-off between efficiency and optimality. For the block sizes for which an exhaustive search is computationally feasible, all the possible sampling patterns are ranked by their resulting IT metrics, and the sampling patterns designed by SFS were found to be always among the best 15%. Also, the outcome of using the IT and ST metrics in SFS are quite similar. The computational time for selecting 4 samples out of 32 elements using exhaustive search, SFS based on the IT metric, and SFS based on the ST metric was approximately 20 hours, 30 minutes, and 0.5 minute, respectively. The PC used was equipped with an Intel Duo Core 2 2.13GHz processor and 2GB RAM. Another benefit of using the ST metric is that the computational complexity increases little as the block size increases, whereas it has direct impact on the computation of IT metric. A moderate block size combined with SFS appears to give a good compromise.

Comparing the results of using different sampling pattern design methods presented in Fig. 5.10, it is seen that the 2D SENSE pattern leads to the highest noise amplification level in both scenarios, since neither the coil sensitivity nor the support constraint is sufficiently exploited for separating the aliased image elements. Comparing the result of using SFS with a block size of 8×8 to 2D CAIPIRINHA, it is seen that the latter offers comparatively better results in the case with no ROS constraint, but gave less favorable results when the ROS constraint is incorporated. This supports the argument advanced earlier that the CAIPIRINHA approach focuses on enhancing the coil sensitivity variation of the aliased image elements according to their spatial locations, which becomes less important when the ROS constraint is incorporated.

5.7.2 In-vivo experiments

A 3D brain scan of a healthy adult volunteer was performed on a GE 1.5T scanner using an 8-channel head coil. Informed consent (Ethical approval was obtained from Upper South A Regional Ethics Committee, New Zealand) from the volunteer was obtained prior to the study. The two PE directions were set to left-right (LR) and anterior-posterior (AP), which correspond to the two directions with significant coil sensitivity variation, and FE is set to the superior-inferior (SI) direction. T_1 weighted 3D Spoiled Gradient Recalled (SPGR)

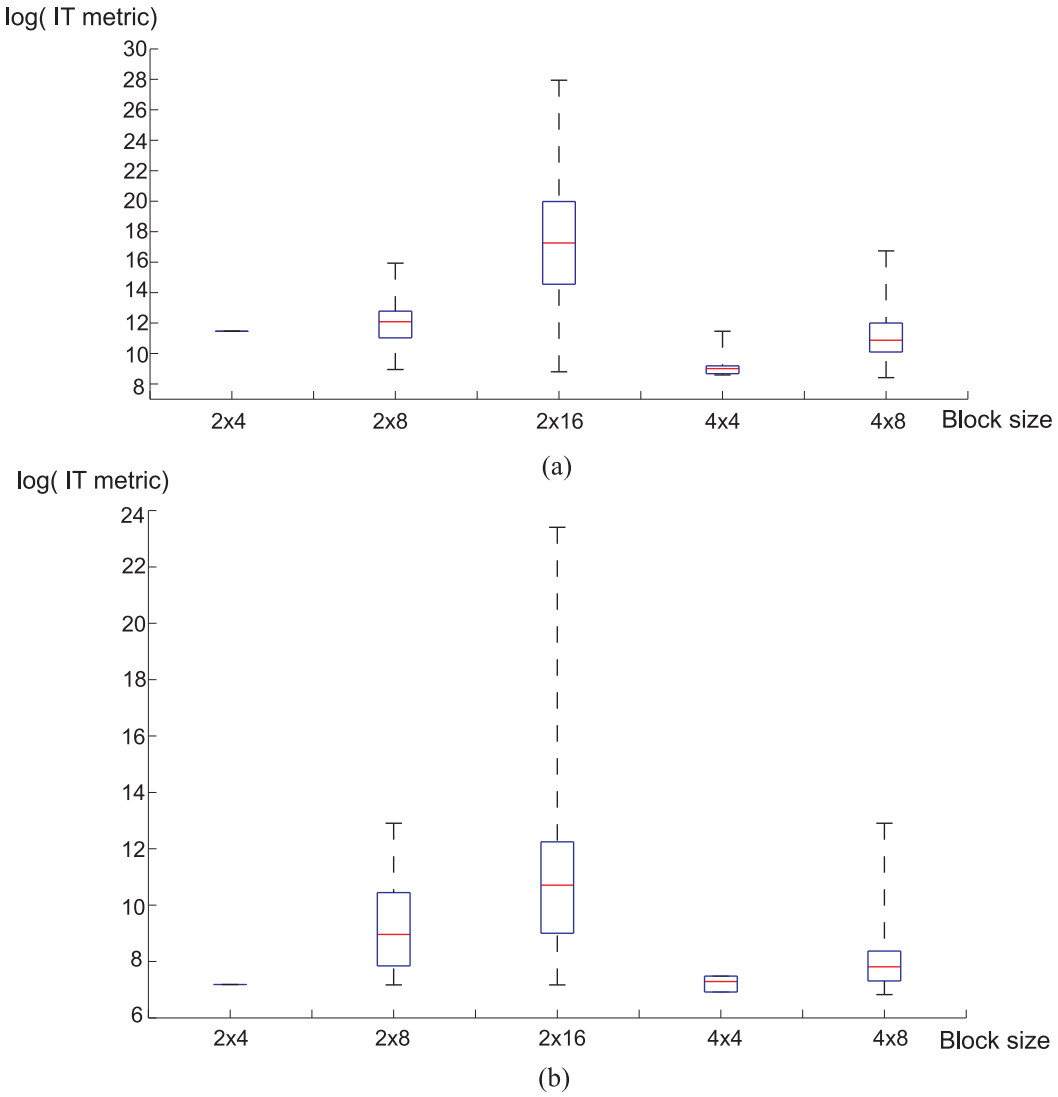

Figure 5.9 Performance of k-space sampling patterns (at acceleration factor of 8) with different sizes of repeated blocks in recovering the simulated phantom : (a) no ROS knowledge is used; (b) perfect knowledge of ROS of the phantom is incorporated in the image recovery. Log(IT metric) of all the possible sampling patterns with given periodicity are obtained and presented in box-whisker plots. It is observed that as the size of the repeated block increases, the performance range of the different sampling patterns broadens, i.e. the upper boundary is higher and the lower boundary is lower. The use of ROS in (b) leads to generally improved performance compared to that presented in (a), when the entire FOV is recovered.

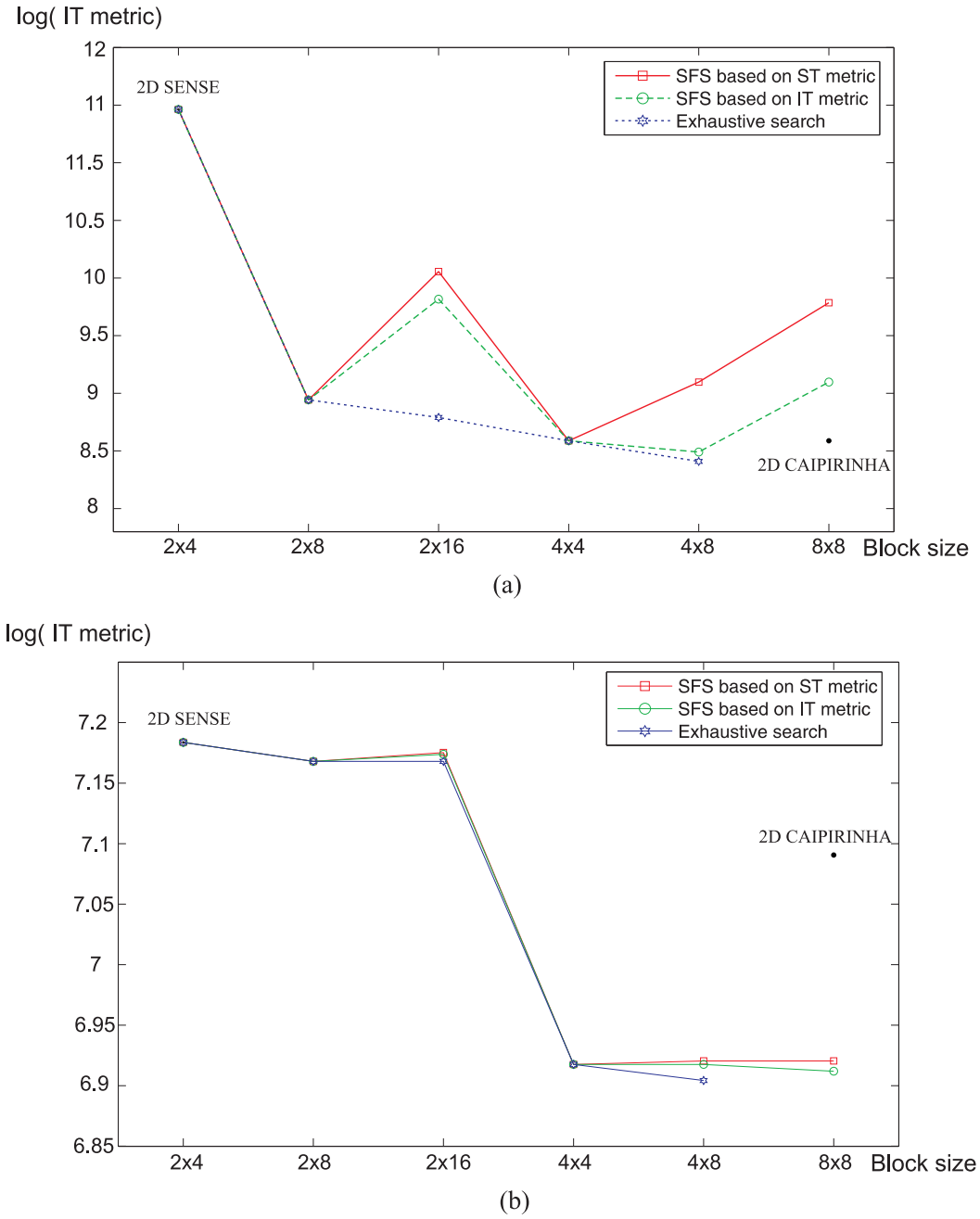

Figure 5.10 Comparing the IT metrics resulting of the proposed SFS sample selections with varying repeated block sizes to those of the fixed sampling patterns employed by 2D SENSE and 2D CAIPIRINHA: (a) no ROS knowledge is used; (b) perfect knowledge of ROS of the phantom is incorporated in the image recovery. The exhaustive search method provides performance bounds for the more practical SFS design methods with each different block sizes. The results for 2D SENSE and the best 2D CAIPIRINHA pattern are as labeled. It is seen that as the sizes of the repeated block increases, the best case performance improves (same as that presented in Fig. 5.9. 2D SENSE leads to the worst IT metric in both (a) and (b). 2D CAIPIRINHA is more advantageous than GUISE when no ROS is used; GUISE outperform 2D CAIPIRINHA when correct ROS knowledge is incorporated in image reconstruction.

was used with the following sequence parameters: TR = 23ms, TE = 10ms, flip angle = 15°, matrix = $128 \times 256 \times 128$, resolution = $1.5\text{mm} \times 0.75\text{mm} \times 1.5\text{mm}$. A full coronal plane data set was acquired to allow reconstructions with different sampling patterns to be performed in post-processing and the inverse DFT was performed along the FE direction prior to further reconstruction of individual axial slices.

To best illustrate the impacts of under-sampling strategies on image reconstruction, 3D images reconstructed using different sampling strategies at a high acceleration factor of 8 (at low acceleration factor of 4, all the three methods give almost perfect image reconstructions; SENSE and CAIPIRINHA do not allow acceleration factor of 6 to be achieved due to the constraint on their sampling pattern design). Coil sensitivity maps and object ROS were both estimated using only the k-space center (32×32). Low order polynomial fitting after sum of square division [PWSB99] was performed to estimate the coil sensitivity maps. For GUISE, asymmetrical block sizes with a LR dimension greater than the AP dimension were chosen to reflect the larger non-object margin in the LR direction, and samples were sequentially selected based on minimizing the ST metric over the 3D brain region shown bounded by solid horizontal lines in Fig. 5.11.(a). A reference image of a single axial slice (indicated by the dash line in Fig. 5.11.(a)), calculated from fully sampled data, is shown in Fig. 5.11.(b). Reconstructions of this axial slice at acceleration factor of 8 using different sampling methods are shown in Fig. 5.11.(c-e). The differences between each respective reconstruction in Fig. 5.11.(c-e) and the reference image are shown in Fig. 5.11.(f-h). The root mean square (RMS) value for each of the latter difference images is shown in the respective figures.

It is seen that GUISE with block size of 8×8 gives a lower overall noise level and a more uniform noise profile compared to other sampling methods as expected. To further justify the utility of adaptive sample selection, the noise level in the reconstructed 3D image volume (specified in Fig. 5.11.(a)) using the normalized root mean squared distance (NRMS) is measured, defined by

$$\text{NRMS} = \sqrt{\frac{\sum_{i=1}^{P}(|f_i^{\text{reference}}| - |f_i^{\text{reconstructed}}|)^2}{\sum_{i=1}^{P}|f_i^{\text{reference}}|^2}}, \tag{5.28}$$

where P denotes the number of voxels recovered within the 3D brain volume (Fig. 5.11.(a)). The predicted noise amplification level (logarithm of overall IT metric) and the NRMS of the reconstructed 3D images at $\alpha = 8$ are listed in Table 6.1. The performance pattern is similar to the simulation results: GUISE-type patterns with appropriate k-space block sizes are superior to the others in terms of giving lower overall noise levels. The consistency between the IT metric and NRMS indicates the IT metric is indeed a good gauge of the noise performance. The maximum achievable acceleration factor for each block size in GUISE-type patterns is also shown in Table 6.1. Although the theoretical upper bound for

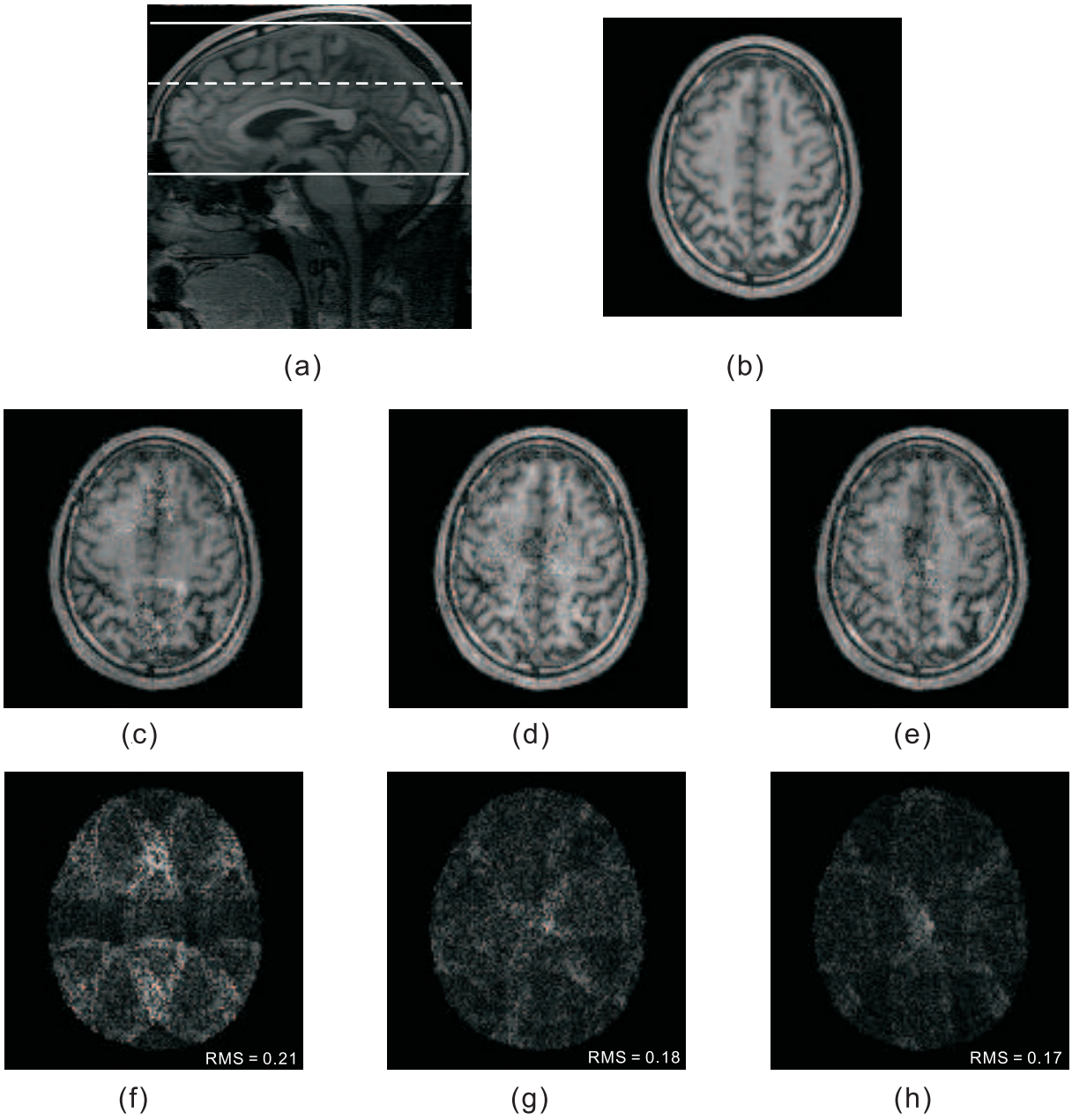

Figure 5.11 Image reconstructions using in-vivo data sets. (a) A sagittal slice reconstructed from the full data acquisition. The solid lines bound the region over which the cost function was minimized for SFS sampling pattern design and the dashed line shows the position of the axial slice compared. (b) The axial slice reconstructed from the full data set and used as a reference image. (c-e) Reconstructed images using 2D SENSE (block size 2×4), 2D CAIPIRINHA (8×8), and GUISE (8×8), respectively; and (f-h) the corresponding noise profiles (difference between the reconstructions and the reference image) with the RMS value of the reconstruction noise shown.

the acceleration factor is $M/\phi_{\max}$, the achievable acceleration factor for a particular block size is often lower since fractional sampling is not possible.

Table 5.1 Comparing the use of different sampling patterns in reconstructing a 3D volume. The first column and second column shows the actual and expected reconstruction noise level at $\alpha = 8$ respectively. The maximum sub-support ratio $\phi_{\max}$ for each sampling pattern is shown in the third column which determines the maximum achievable acceleration factor $\alpha_{\max}$ displayed in the fourth column.

Sampling strategy	NRMS	$log_{10}(IT\,metric)$	$\phi_{\max}$	$\alpha_{\max}$
2D SENSE	0.64	8.43	0.75	8.0
[a]CAI_1	0.57	8.33	0.53	8.0
CAI_2	0.59	8.38	0.53	8.0
CAI_3	0.58	8.32	0.53	8.0
GUISE 2×8	0.69	8.52	0.63	8.0
GUISE 2×16	0.58	8.37	0.63	10.7
GUISE 4×4	0.55	8.31	0.63	8.0
GUISE 4×8	0.54	8.30	0.56	10.7
GUISE 8×8	0.53	8.28	0.53	12.8

[a] There are 3 candidiates for 2D CAIPIRINHA with $\alpha = 8$.

In practice, a low resolution image approximation is often readily available from the calibration scan process, and it is also required for obtaining the estimates of object ROS and coil sensitivity profiles. Hence incorporating the low resolution approximation as a prior knowledge in the image reconstruction has great practical utility.

In Fig. 5.12, a low resolution image approximation constructed using only the 32×32 k-space centre is used as an initial estimate for the Tikhonov regularization in each type of image reconstruction (Eq. (5.26)). A weighting coefficient for the Tikhonov regularization term of 0.05 was used in all the three cases. For the ease of comparison, NRMS for the reconstructions with and without Tikhonov regularization are calculated. Firstly, it is seen that Tikhonov regularization has greatly reduced the amount of reconstruction noise in all the three cases: in each of the reconstruction, a lower NRMS is received when a Tikhonov regularization term is included. It is also noticeable that the non-uniform noise profiles in the reconstruction led to a non-uniform level of artifacts in the regularized reconstructions (as indicated by the arrows). Secondly, it is seen that the relative quality among the regularized reconstructions as assessed by the NRMS is similar to that among the non-regularized reconstructions: GUISE outperformed CAIPIRINHA and SENSE, and SENSE reconstruction was the worst among the three. Hence it is evidenced that image reconstructions with additional image constraints also benefit from the adaptive sampling design.

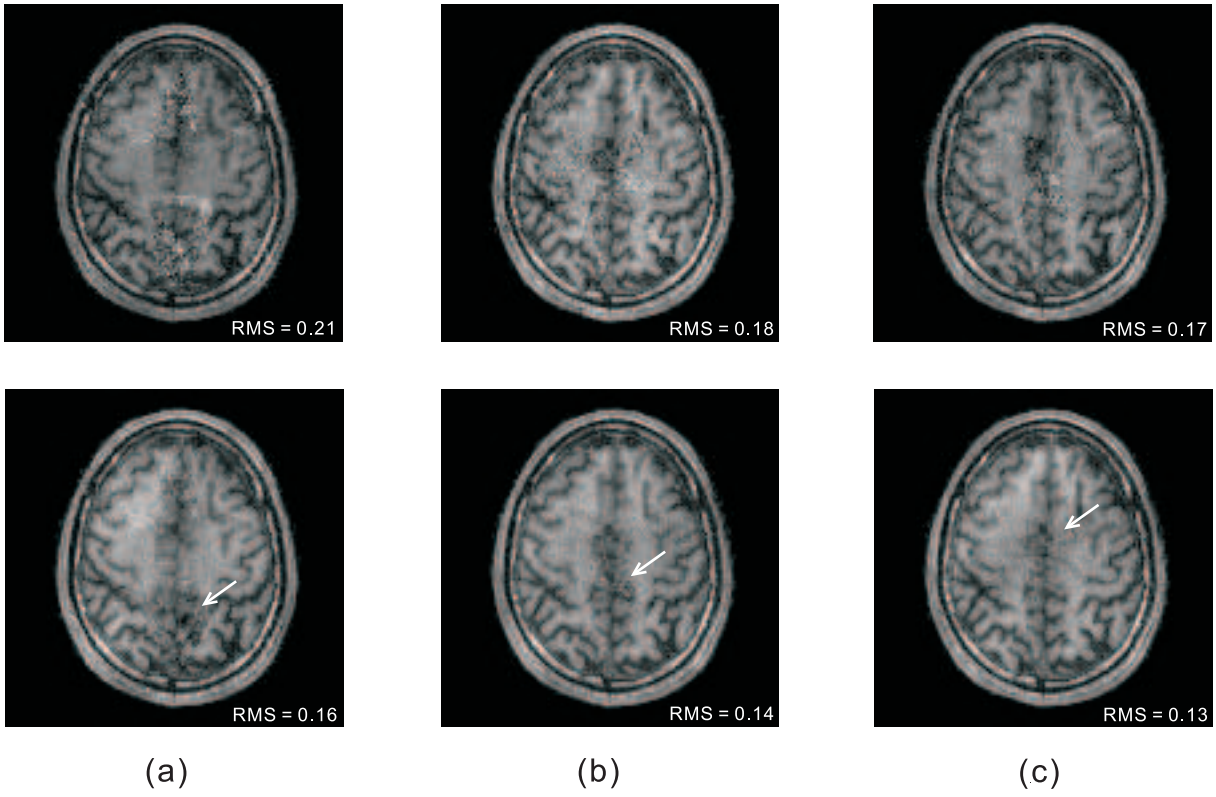

Figure 5.12 Image reconstructions with additional Tikhonov regularization. In the upper row, image reconstructions using (a) SENSE, (b) CAIPIRINHA, (c) GUISE at acceleration factor of 8 are shown (same as those in Fig. 5.11). In the lower row, image reconstruction in each case is made with an additional Tikhonov regularization term. The NRMS for each reconstruction is shown on the bottom right corner, using the image constructed from the full data set as that used in Fig. 5.11. It is seen that Tikhonov regularization is effective in reducing the reconstruction noise, and GUISE outperformed the other two methods in both cases of with and without additional regularization used. The arrows point the residual artifacts in each case.

5.8 Discussion

A new MRI formulation GUISE that incorporates multiple receiver coil and knowledge of object ROS has been presented, and its application in 3D MRI has been considered. It treats the process of aliasing due to under-sampling in k-space as convolving the image with the point spread function of the sampling pattern, and the original image can be recovered if the lack of Fourier encoding can be compensated by distinctive sensitivity encoding and knowledge of object ROS. Combining image support knowledge with coil sensitivity encoding allows an acceleration factor greater than the number of coils and consequently a faster dataset acquisition. However, as image reconstruction becomes unstable at high acceleration factors due to poor conditioning, careful sampling pattern design is required to precondition the image reconstruction.

To achieve efficiency in the reconstruction, k-space sampling patterns are restricted to consist of repeated blocks, leading to the decomposition of the image plane system. Using larger block sizes and consequently larger image plane sub-sequences offers potential benefits of more efficient exploitation of coil sensitivity weighting and ROS, which could lead to more stable matrix inversions. However, only an optimal block sampling pattern can fully exploit these benefits and seeking for such pattern is generally an intractable combinatorial problem. It has been demonstrated that using a sub-optimal SFS design method coupled with moderate block sizes achieves a good trade-off between optimality and computational efficiency. Comparison with similar methods (2D SENSE and 2D CAIPIRINHA) shows that this approach is indeed superior in providing a lower overall noise level. 2D SENSE minimizes the sampling design effort while usually resulting in the highest noise level. 2D CAIPIRINHA heuristically improves the exploitation of coil sensitivity weighting but could not efficiently utilize the knowledge of ROS. Although simulation results show that 2D CAIPIRINHA could be advantageous when the entire FOV is to be recovered, in practice there generally are free air regions of varying sizes in different slices in 3D MRI. In addition, 2D CAIPIRINHA requires trials to be made to find the appropriate pattern among several possible candidates, which is not efficient enough for real-time imaging.

In this treatment so far it has been assumed that the only source for error at image reconstruction is noise, however error in assumed knowledge of coil sensitivity profile and ROS can produce severe artifacts at reconstruction. The effects of incorrect estimation of coil sensitivity profile can be modeled as [XYL04]:

$$\check{\mathbf{f}}' \;=\; (\mathbf{E}+\boldsymbol{\Delta}\mathbf{E})^{+}\tilde{\mathbf{f}},\; \boldsymbol{\Delta}\mathbf{E} \;=\; \begin{bmatrix} \mathbf{W}^{-1}\,\mathrm{diag}(\mathbf{h})\,\mathbf{W}\,\mathrm{diag}(\Delta\mathbf{c}_1) \\ \mathbf{W}^{-1}\,\mathrm{diag}(\mathbf{h})\,\mathbf{W}\,\mathrm{diag}(\Delta\mathbf{c}_2) \\ \cdots \\ \mathbf{W}^{-1}\,\mathrm{diag}(\mathbf{h})\,\mathbf{W}\,\mathrm{diag}(\Delta\mathbf{c}_M) \end{bmatrix}, \tag{5.29}$$

where $\Delta\mathbf{c}_m$ represents error in sensitivity profile estimation in the mth coil. Consequently inversion of $(\mathbf{E} + \Delta\mathbf{E})$ will not give the correct result. The presence of noise is a general cause of inaccurate coil sensitivity estimation from the low resolution data set, especially in regions with low proton density. However, the smoothly varying nature of coil sensitivity functions allow standard signal processing techniques such as a low order polynomial fitting to be used to reduce the noise level, and other methods have also been suggested in [GJH+02, LKC+01]. Using the knowledge of ROS during reconstruction essentially wraps the excluded area into the reconstructed area; it will thus result in aliasing artifacts in the recovered image if a region containing signal has been mistakenly excluded. On the other hand, inclusion of non-object region in the reconstruction only degrades the final SNR, thus a slightly loose ROS constraint is desirable. It is also possible to estimate a tighter ROS from the initial reconstruction and reiterate the reconstruction process.

Aliasing artifacts arising from arbitrary sampling patterns are global and removal of such by matrix inversion is limited by the present computational capacity. In GUISE and its fore-mentioned special variants (SENSE and CAIPIRINHA), periodic sampling patterns on Cartesian grids are employed bypass this issue. They also allow 2-norm optimal estimates (with and without additional objective functions) to be made. On the other hand, iterative approaches have been taken to tackle the problem [PWBB01, LPC+07, SKPJ04]. Computationally cheap algorithms such as conjugate gradient (CG) and projection onto convex sets (POCS) are used to iteratively restore the final image instead of a direct inversion; they allow arbitrary Cartesian and non-Cartesian k-space sampling patterns to be used. Iterative methods also have great flexibility in incorporating linear and non-linear constraints for conditioning the problem, such as these discussed in [LPC+07, SKPJ04]. The newly emerged compressed sensing (CS) technique [LDP07, WBMW08a] (CS in parallel MRI is discussed in Chapter 6) further generalizes the concept of image support to various transform domains, and an explicit mask is not required to recover signal within the transform domain support. Initial attempts to combine CS and pMRI have led to some attractive results [WBMW08a]. However, non-convergence is a potential problem with all iterative approaches, which results in relatively long computational time and compromises between signal to noise ratio (SNR) and residual aliasing [QZZ+05]. The effects of different sampling patterns (Cartesian or non-Cartesian) on the success of iterative methods have not been fully investigated, and is an interesting field for carrying out future work.

The parallelism embedded in the SFS sample selection can be exploited to allow for the use of IT metric to achieve better results. The range of potential applications of GUISE with SFS is broad. It could particularly be of benefit in cases with intrinsically high SNR and (or) small object support regions relative to the FOV. Also the sequential sample selection allows a flexible acceleration factor for temporal studies as presented in Chapter 7.

Chapter 6

Prior estimate Based Compressed Sensing (PBCS)

The focus of this chapter is the implementation of the recently developed information recovery theory compressed sensing (CS) in parallel MRI. Two new methods that are termed as Prior estimate Based Compressed Sensing (PBCS) and SENSECS are proposed. PBCS is an extension of the conventional CS method that allows a prior estimate of the underlying image to be incorporated in the CS recovery via a prior data sorting process. SENSECS is an application of PBCS in parallel imaging in which the SENSE reconstruction is used as the prior estimate in the next stage PBCS reconstruction. The organization of this chapter is given as the following. Firstly, the CS recovery theory is briefly reviewed, followed by the CS implementation in MRI. As the success of conventional CS recovery is limited by the inherent sparsity of the underlying signal to be recovered, PBCS is then introduced to allow the signal to be recovered in an alternative form that features a higher level of sparsity and hence allows better signal recovery. Next, the direct extension of CS recovery in parallel MRI presented, and its intrinsic limitation is discussed. To achieve better synergistic exploitation of pMRI and CS recovery, SENSECS is proposed to exploit complementary properties of SENSE and CS to achieve better reconstructions than using SENSE or CS alone. Experiments using in-vivo data sets were carried out to verify the performance of PBCS and SENSECS.

6.1 Compressed sensing (CS)

Often, the information embedded in a signal can be described using many fewer coefficients than that defined by the Nyquist sampling rate. For instance, raw digital images or videos would normally go through a lossy compression process prior to storage or trans-

mission, which will otherwise be much less affordable due to their sizes. In the conventional process, an analogue signal is first fully acquired (sampled at Nyquist rate) and then the obtained digital signal undergoes a transform; among all the transform coefficients only a small number of the most significant ones are retained. To retrieve the signal, only the retained coefficients are involved in the inverse transform and give an approximate signal representation that is often very good. This is a rather wasteful process, as much of the acquired information ends up being thrown away again. Would it be possible to only measure the information that will be retained at the end? Compressed sensing is a tool to do this, it allows the signal to be measured (sensed) in a compressed form directly. The conventional process of the image sensing and compression and that of compressed sensing are compared in Fig. 6.1. Compressed sensing contains three crucial ingredients: signal sparsity, non-coherent measurements and non-linear recovery. These factors are now discussed in details.

6.1.1 Signal sparsity

In a signal that is sparse, all but a small percentage of the signal components are zeros. Mathematically, in the vector $\mathbf{f} \in \mathbb{R}^N$, there only exists K non-zero elements out of the total N components, where $K \ll N$. The signal can be referred as K-sparse. Since the information of the signal is only contained in the K non-zero elements, there is no need to know the rest of the components. Hence signal sparsity inherently allows incomplete sampling of the signal without loss of information – the very fact exploited by the use of object region of support (ROS) in the previous chapter. In practice, many signals only demonstrate approximate sparsity, in which a large portion of signal coefficients are negligibly small rather than being exactly zeros. For example, if coefficients in a signal decay rapidly according to a power law [Can06]. Such signals may also be referred to as K-sparse, if all but the K most significant are neglected – as it is known to be safe to do so. This is the fact exploited by the current lossy compression algorithms, best known of which is the JPEG family. Overall the signal sparsity is the core of compressed sensing, as it allows the signal to be represented by a much smaller set than its actual size.

6.1.2 Data acquisition

Given that it is known *a priori* that the signal $\mathbf{f}$ to be acquired has a sparse nature – prior knowledge that is not taken into account the Nyquist sampling theorem, the CS theory states that it is possible to recover the K most significant coefficients from M incoherent linear combinations of all the coefficients in $\mathbf{f}$, given that M is in the linear order of K. Mathematically, the measurement $\mathbf{y}$ is obtained by:

$$\mathbf{y}(m) = \langle \psi_m, \mathbf{f} \rangle, \quad m = 1, \ldots, M. \tag{6.1}$$

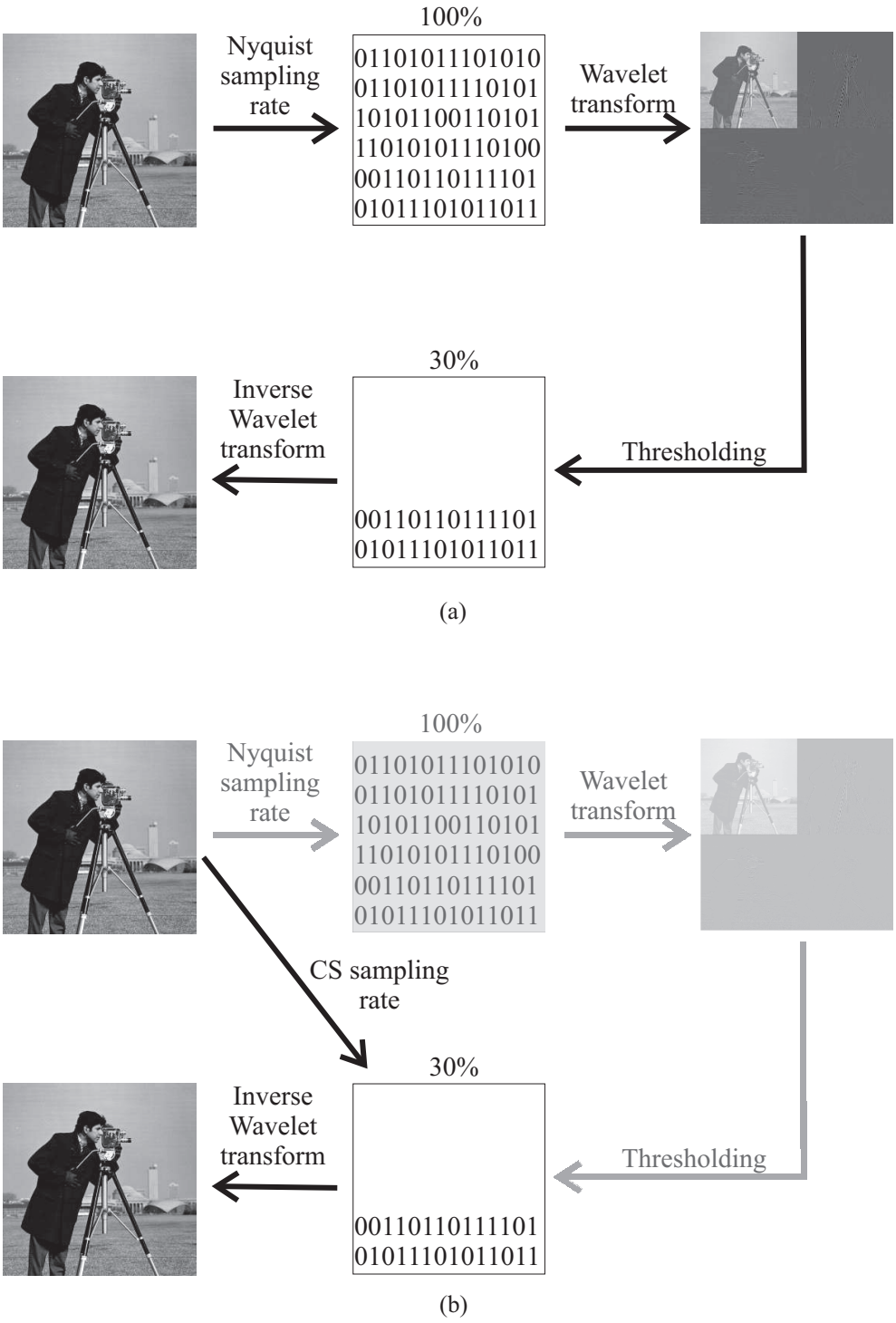

Figure 6.1 Comparing the traditional image sensing and compression process (a) to that of compressed sensing (b). In the former case, pixel-wise samples of the image are first acquired at Nyquist sampling rate and stored. Then all the insignificant coefficients in its Wavelet transform of the image are discarded to reduce the size of the signal. In compressed sensing, it is aimed to directly recover the significant coefficients of the Wavelet transform from samples obtained at a much lower sampling rate.

where ψ_m represents the linear basis function used, and $\langle \mathbf{a}, \mathbf{b} \rangle$ denotes the inner products of vectors $\mathbf{a}$ and $\mathbf{b}$. In the matrix form, the linear measurements about $\mathbf{f}$ with measurement system $\mathbf{\Psi}$ may be written as:

$$\mathbf{y} = \mathbf{\Psi}\mathbf{f} \tag{6.2}$$

where the number of rows and columns of $\mathbf{\Psi}$ are M and N respectively, and thus the Eq. (6.2) is a very under-determined system.

Incoherent linear combinations of the coefficients in $\mathbf{f}$ are crucial for the success of CS recovery. As $\mathbf{f}$ is sparse, most of its coefficients are zeros or very small. Without knowledge of the location of the K significant coefficients, collecting point-wise measurements in $\mathbf{f}$ will very likely to result in many trivial measurements. On the other hand, linear combinations of the coefficients in $\mathbf{f}$ are global descriptions of $\mathbf{f}$, each new measurement contains some new information about $\mathbf{f}$. The incoherence of the linear measurement system further ensures the globalness of the measurements made. In short, it is required that the representation of the sparse signal $\mathbf{f}$ must be spread over the entire linear space of $\mathbf{\Psi}$ (the space spread by the basis of the transform $\mathbf{\Psi}$), so that measurement at any location in the linear space will be non-trivial. An incoherent measurement system is shown to inherently satisfy the restricted isometry property (RIP) [CRT06], which is a sufficient condition for the sparse signal to be recovered from the small set of linear measurements (for the under-determined $\mathbf{\Psi}$ to be invertible). An example of the incoherent measurement matrix is a random matrix [Bar07], which is constructed by randomly drawing entries from a certain distribution. Overall, correlations of the signal with a incoherent linear sensing system ensures the recoverability of the sparse signal from a small set of the resulting linear measurements.

6.1.3 Signal recovery

Given it is assured that sufficient amount of information of the signal $\mathbf{f}$ is contained in the small linear measurements set obtained, a non-linear recovery process is required to decode the sparse signal. In Eq. (6.2), there exists an infinite number of possible solutions and the differences between them and the true solution live in the null space of the rectangular matrix $\mathbf{\Psi}$, hence it is infeasible to identify the underlying signal by solely relying on Eq. (6.2). However, the prior knowledge of signal sparsity can be exploited. To enforce sparsity of in the recovered signal, a constrained optimization can be set as:

$$\min_{\mathbf{f}} \|\mathbf{f}\|_0 \quad \text{subject to } \mathbf{y} = \mathbf{\Psi}\mathbf{f} \tag{6.3}$$

where the 0-norm $\|\mathbf{f}\|_0$ basically counts the number of non-zero entries in the vector $\mathbf{f}$, and hence Eq. (6.3) searches for the sparest solution that is consistent with the measure-

ments obtained. Although this has been demonstrated to be powerful in certain situations [Don06], Eq. (6.3) is practically a combinatorial problem, the solution of which is often computationally prohibitive. Furthermore, the signals of practical interest often contain small coefficients rather than exact zeros. In these cases, the 0-norm would fail to succeed.

In order to achieve the computational efficiency and deal with the cases where the signals are only weakly sparse, the 1-norm is proposed to be used instead in imposing the sparsity constraint [Don06]:

$$\min_{\mathbf{f}} \|\mathbf{f}\|_1 \quad \text{subject to } \mathbf{y} = \mathbf{\Psi f} \tag{6.4}$$

where $\|\mathbf{f}\|_1 = \Sigma_{i=1}^{N} |\mathbf{f}_i|$. Hence instead of measuring the size of the signal support as in the 0-norm case, the sum of its component magnitudes is used. The above is also known the basis pursuit approach [CDS99]. It is shown in [Don06] that in certain special circumstances in which the measurement matrices $\mathbf{\Psi}$ are well conditioned (satisfying the restricted isometry property), Eq. (6.3) and Eq. (6.4) share common solutions. Computational efficiency in solving Eq. (6.4) is achieved by recasting it as a linear optimization, which can be solved using many types of modern techniques [Don06][1].

The geometric interpretation [Bar07] of the 1-norm minimization shown in Fig. 6.2 illustrates why the 1-norm promotes sparsity in the recovered signal, whereas the conventional 2-norm does not. Suppose $\mathbf{f} \in \mathbb{R}^3$, and it is 1-sparse (there is only one non-zero component in $\mathbf{f}$). A single measurement of the linear correlation of components in $\mathbf{f}$ restricts all the possible solutions in Eq. (6.2) to lie in a 2D hyper-plane that is randomly orientated. The 1-norm constrained optimization Eq. (6.4) promotes picking the one with the minimum 1-norm among all the possible solutions. Geometrically, this is equivalent to picking the point of intersection of the 1-norm ball with the hyper-plane (see Fig. 6.2.(b)). Due to the pointy appearance of the 1-norm ball, the intersection is very likely to be around the axis, which is indeed the place all 1-sparse signals live. In contrast, taking the minimization of the conventional 2-norm ball is equivalent to seeking for the intersection of the 2-norm ball with the hyper-plane (see Fig. 6.2.(c)). However, due to the rather isotropic shape of the 2-norm ball, the intersection is likely to be away from the axis, and hence the resulting solutions are not sparse at all.

Overall, the compressed sensing (CS) approach to reconstruct a sparse signal consists of measurements of the linear correlation of the components in the signal, and a reconstruction process that enforces the sparsity in signal recovered.

[1] As the CS recovery basically seeks for the sparsest solution, fractional norms $0 < p < 1$ can also be used [DG09, FL09]. However, their employment significantly reduces the computational efficiency.

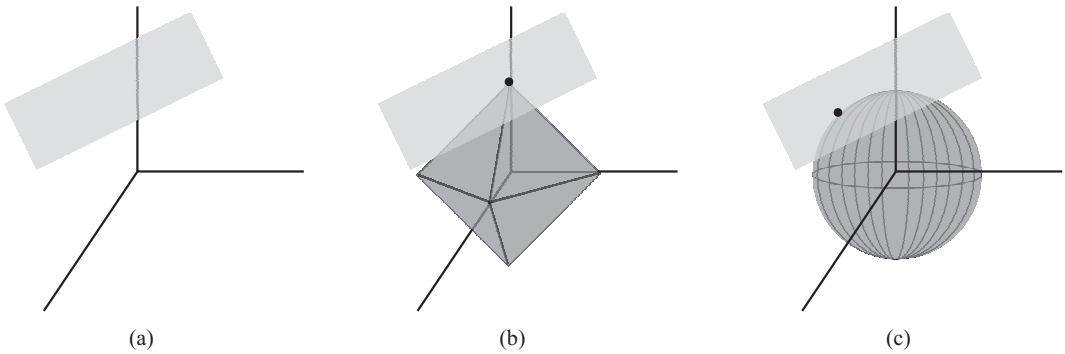

Figure 6.2 Geometrical interpretation of recovering of a 1-sparse signal in $\mathbb{R}^3$ space signal using 1-norm and 2-norm minimization. In (a), one measurement restricts all the possible solutions to a 2D plane. Geometrically, 1-norm and 2-norm minimization correspond to constructing a pointy ball (b) and a round ball (c) respectively in the 3D space. In (b), the intersection of the 1-norm ball with the hyperplane leads to identification of sparse signal around the axis. In (c), the intersection of the 2-norm ball with the hyperplane leads to non-sparse signal away from the axis.

6.2 Compressed sensing (CS) in MRI

The development of CS theory has rapidly attracted the interests of researchers seeking practical applications. MRI is recognized as a particularly promising field of application of CS, as 1) the Fourier space samples are natural linear encodings of the MR images, and 2) there is a strong desire to reduce the number of data measurements in MRI. Implementation of the CS theory in MRI was initiated by Lustig *et al.* in 2007 [LDP07]. In the following subsections, the three crucial factors in applying CS reconstruction to MRI are discussed in the same order as in Section 6.1.

6.2.1 MR image Sparsity

Most MR images are not inherently sparse; the spatial domain sparsity as defined by the object region of support (ROS) is often rather limited except in special cases such as angiography (as discussed in Chapter 7). However MR images generally feature implicit sparsity, which means they have concise representations when expressed in terms of suitable basis functions. Given a set of N orthonormal linear basis functions $\mathbf{\Phi}$, the coefficient sequence $\mathbf{f}_T$ obtained by taking the inner products of the image $\mathbf{f}$ and the basis functions ϕ in $\mathbf{\Phi}$, written as

$$\mathbf{f}_T(n) = \langle \phi_n, \mathbf{f} \rangle, \quad n = 1, \ldots, N, \tag{6.5}$$

may contain only a few significant components, i.e. it may demonstrate weak sparsity. Such sparsity is exploited by various lossy image compression tools such as the JPEG family [TM02], which can also be equivalently applied to medical images [KS06]. Fig. 6.3 demonstrates the compressibility of the MR images by using the DCT and wavelet trans-

forms (as employed by the JPEG and JPEG-2000 compression methods respectively). It is seen that only a very small percentage of the Wavelet/DCT transform coefficients are needed to maintain the perceptual information of the MR images. Hence the Wavelet/DCT transforms of MR images are very sparse and allow many small coefficients to be safely discarded, which allows compressed sensing recovery to be used in reconstructing MR images.

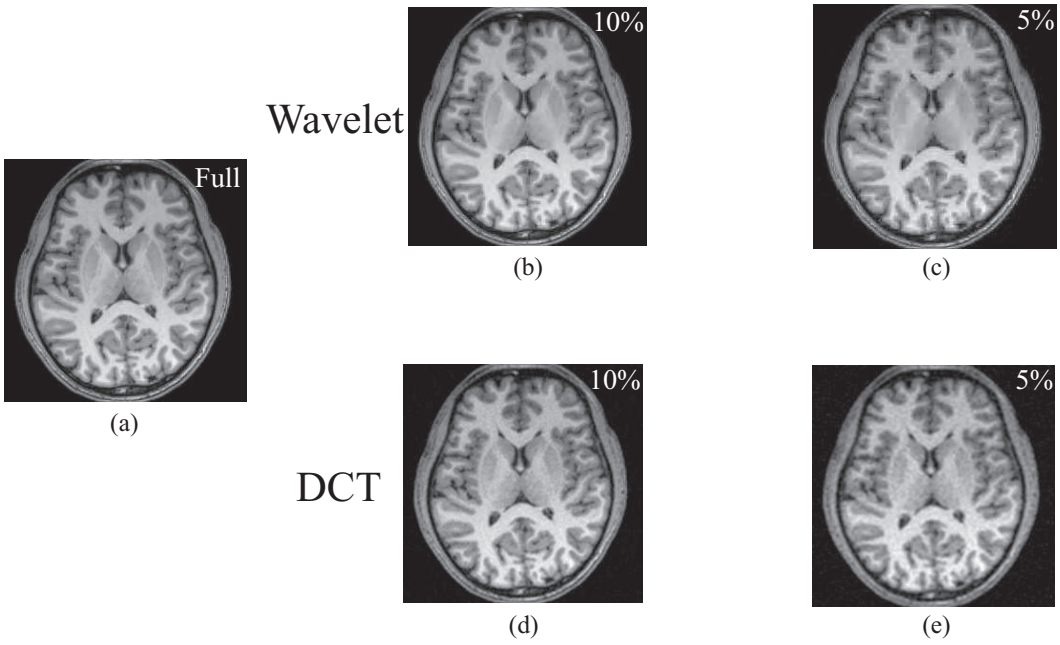

Figure 6.3 Compressibility of a MR brain slice. The wavelet and DCT approximations of the MR brain slice (a) using only 10% and 5% of the most significant coefficients in the transform are shown in (b-e). There appears to be little perceptual loss under such high levels of image compression.

6.2.2 CS Data acquisitions in MRI

As discussed previously, the sparsity of MR images exists under an additional transform $\mathbf{\Phi}$. For an image $\mathbf{f}$ and writing the image sparse representation as $\mathbf{f}_T = \mathbf{\Phi f}$, (assuming $\mathbf{\Phi}$ is orthonormal) the Fourier measurement system can be written as:

$$\mathbf{F} = \mathrm{diag}(\mathbf{h})\,\mathbf{W}\mathbf{\Phi}^{\mathrm{H}}\mathbf{f}_T, \quad \mathbf{f} = \mathbf{\Phi}^{\mathrm{H}}\mathbf{f}_T, \tag{6.6}$$

where $\mathbf{W}$ represents the Fourier matrix, $\mathbf{h}$ is the under-sampling mask, vector $\mathbf{F}$ contains the Fourier measurements made and $^{\mathrm{H}}$ denotes the Hermitian transpose. To ensure the recoverability of the sparse signal $\mathbf{f}_T$ from the partial measurement $\mathbf{F}$, the overall measurement matrix $(\mathrm{diag}(\mathbf{h})\mathbf{W}\mathbf{\Phi}^{\mathrm{H}})$ has to satisfy the RIP, or be incoherent. Lustig *et al.* [LDP07] suggest that the key to achieve an incoherent measurement system is to employ a pseudo-random under-sampling strategy (i.e., the distribution of 1s in $\mathbf{h}$ is pseudo-random), if a wavelet or DCT transform is used as $\mathbf{\Phi}$.

Since the point spread function (PSF) of the sampling mask $\mathbf{h}$ determines how the Fourier measurements are formed, the suitability of different sampling masks can be assessed by comparing their PSFs. Fig. 6.4 compares the PSF of a regular sampling pattern and that of a pseudo-random pattern. It is seen that the sparse PSF corresponding to a regular sampling pattern indicates that only a small portion of the signal contributes to the resulting measurements, which are then not global descriptions of the signal. On the other hand, the dense PSF of a pseudo-random sampling pattern suggests that all the components in the signal will likely to contribute to the resulting measurements; also the appearance of the PSF suggests that incoherent combinations of the signal are likely to be received which is required by the CS recovery principle.

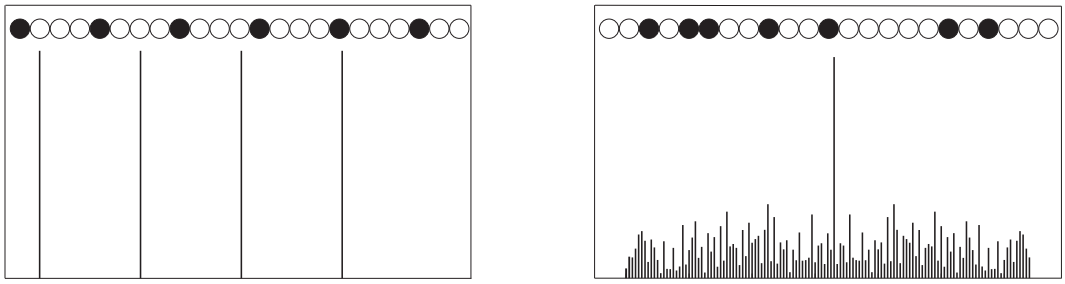

Figure 6.4 The point spread functions (PSF) of a (a) regular (b) pseudo-random sampling patterns in a 1-D example. At the top of each plot, filled and empty circles represent acquired and skipped k-space samples in the sampling mask respectively; the spikes in the diagrams represent the magnitude of the coefficients in the PSFs. From the appearance of their PSFs, it is seen that measurements obtained using a regular Fourier sampling pattern (a) only contains information of a small portion of the signal due to the sparse PSF; pseudo-random sampling strategy ensures that measurements are incoherent combinations of all the components in the signal due to the dense and incoherent PSF.

Lustig *et al.* [LDP07] further proposed the transform point spread function (TPSF), given as:

$$TPSF(i;j) = \mathbf{e}_j^{\mathrm{H}}\, \mathbf{\Phi}\, \mathbf{W}^{\mathrm{H}}\, \mathrm{diag}(\mathbf{h})\, \mathbf{W}\, \mathbf{\Phi}^{\mathrm{H}}\, \mathbf{e}_i \tag{6.7}$$

where $\mathbf{e}_i$ denotes a vector having '1' at ith position and zeros elsewhere, to measure the influence of the ith component on the jth component in the transform domain as the result of under-sampling according to a specific pattern $\mathbf{h}$ in the Fourier domain. The TPSF can be used as a measure of the incoherence level of the resulting measurement system, and hence judges the suitability of different sampling patterns in allowing the best CS recovery for a sparsifying transform $\mathbf{\Phi}$ used.

The TPSFs of a 1D and a 2D sampling strategy that are designed by the 'sparse MRI' tool box [LDP07] [2] are shown in Fig. 6.5. As discussed before, the sampling masks (shown

[2] By Lustig M. , available at http://www.stanford.edu/∼mlustig/.

on the right top corner) have non-uniform probability density functions (PDF) (shown on the left top corner) to accommodate for the fact that there is a much higher level of energy concentration at the centre of the k-space. The TPSFs of the sampling masks reveal the nature of the measurement system in terms of the wavelet coefficients: in case of a 1D under-sampling is used (Fig. 6.5.(a)), only the wavelet coefficients along the same direction contribute to the resulting measurements; in case where a 2D sampling mask is used (Fig. 6.5.(b)), the non-zero coefficients are spread across the entire 2D wavelet domain, and hence the resulting measurements are more global descriptions of the wavelet coefficients. Thus under-sampling in both PE directions better satisfies the CS recovery requirements.

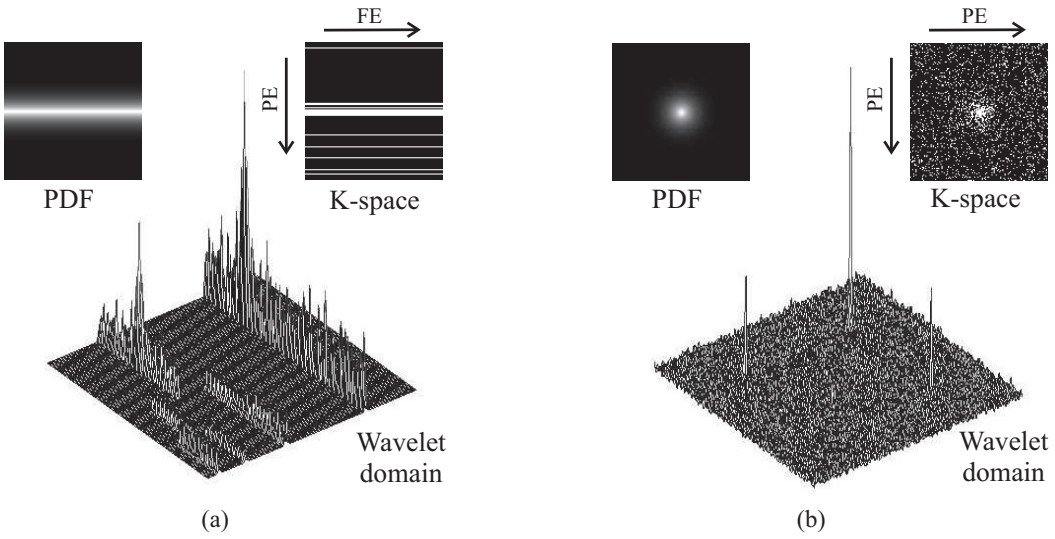

Figure 6.5 TPSFs of (a) 1D and (b) 2D under-sampling masks (at acceleration factor of 8) designed by Lustig's method [LDP07] with a Daubechies 4-level wavelet transform used. The non-uniform sampling density and the corresponding sampling masks are shown on the left and right top corner respectively. From the TPSFs, it is seen that the interference of the wavelet coefficients as a result of under-sampling is restricted to a single direction when under-sampling is restricted to a single PE direction; whereas the interference is spread across the entire 2D wavelet domain if under-sampling takes place in both PE directions.

6.2.3 CS recovery in MRI

As discussed in the previous sections, the intrinsic properties of the MR systems allow the compressed sensing recovery theory to be applied. The CS recovery can be posed as

$$\min_{\mathbf{f}_\mathrm{T}} \ \|\mathbf{f}_\mathrm{T}\|_1 \quad \text{subject to} \ \ \mathbf{F} = \mathrm{diag}(\mathbf{h})\,\mathbf{W}\mathbf{\Phi}^\mathrm{H}\mathbf{f}_\mathrm{T} \tag{6.8}$$

or equivalently as

$$\min_{\mathbf{f}} \ \|\mathbf{\Phi f}\|_1 \quad \text{subject to} \ \ \mathbf{F} = \mathrm{diag}(\mathbf{h})\,\mathbf{W}\mathbf{f} \tag{6.9}$$

where the 1-norm is used to promote signal sparsity in the transform domain, and $\mathbf{\Phi}$ denotes the sparsifying transform involved. Eq. (6.9) can be converted into an unconstrained optimization as:

$$\hat{\mathbf{f}} = \arg\min_{\mathbf{f}} \ (\|\mathbf{F} - \mathrm{diag}(\mathbf{h})\,\mathbf{W}\mathbf{f}\|_2 + \alpha\|\mathbf{\Phi}\mathbf{f}\|_1 + \beta\Xi(\mathbf{f})) \tag{6.10}$$

where α is a weighting coefficient that controls the trade-off between measurement consistency and the sparsity of the recovered image. $\Xi(\mathbf{f})$ represents the additional image constraints that can be incorporated in the reconstruction process, with a corresponding weighting coefficient β. The constraint(s) can either be an object-specific prior knowledge such as the object ROS, a phase constraint or an image prior estimate; alternatively it could be other forms of more generic constraint such as the total variation (TV) [ROF92, LDP07].

Total variation (TV)

For a given discrete function $\mathbf{f}$ of length N, total variation (TV) [ROF92] measures the total absolute variations in the function, and can be written as:

$$TV(\mathbf{f}) = \sum_{n=2}^{N} |(f_n - f_{n-1})| \tag{6.11}$$

where $TV(\mathbf{f})$ denotes the TV operator. In this form, it is equivalent to a finite-difference measure of the function, and hence the use of total variation in Eq. (6.10) can be viewed as an additional sparsifying transform in the finite-differences domain [LDP07]. The TV constraint has been employed in both denoising and image restoration and is known to suppress additive noise while preserving iamge edges [ROF92]. In compressed sensing image reconstruction, since the noise often takes place in another transform domain, the TV constraint is often useful to mitigate the potential high-frequency oscillatory artifacts in CS reconstructions [LDP07]. It is especially useful in the Prior estimate Based Compressed Sensing (PBCS) which is proposed below, in which reconstruction artifacts often have a lot of rapid variations.

6.3 Prior estimate Based Compressed Sensing (PBCS)

The success of CS recovery is determined by the sparsity level of the underlying signal. However, the signal sparsity (or the signal sparsity for a given sparsifying transform) is determined by the natural appearance of the signal and the performance of CS recovery is intrinsically limited [Don06]. In the following, a new method named as Prior estimate Based Compressed Sensing (PBCS) is proposed to overcome this limitation. In PBCS, a prior estimate of the signal is incorporated in the reconstruction to allow the underlying

signal to be recovered in a form that has a higher sparsity level, and hence to achieve an improved signal reconstruction. In the following, PBCS is introduced based on a 1D signal (extracted from a brain cross-sectional slice) for clarity of illustration, although the same principle applies for multi-dimensional signals.

6.3.1 Enhanced signal sparsity by data sorting

With reference to Fig. 6.6, consider representing a signal using a DCT for the purpose of signal compression. In Fig. 6.6.(a), the conventional image compression process is depicted, i.e. the signal's DCT transform is thresholded to maintain only 5% of the most significant coefficients and then an inverse DCT transform is performed to achieve an approximation. In Fig. 6.6.(b), the signal is first sorted using a sorting order R to resemble a monotonic variation, which then goes through the signal compression process. The compressed monotonic signal then undergoes an unsorting process (denoted as R^{-1}) to restore the original order to give the final compressed signal.

It is seen that due to the varying spatial details, the signal's DCT transform contains a range of frequency components (Fig. 6.6.(a)) and hence has limited level of sparsity. As a result, the compression outcome features a lack of the high frequency information. In comparison, the DCT transform of the monotonically varying signal has a much higher level of sparsity, and hence a high signal fidelity is maintained after compression. Then after signal unsorting there is only little amount of information loss in the final compression outcome. For brevity, the sorting and unsorting with sorting order of R are denoted as:

$$\begin{aligned} \mathbf{f} &\xrightarrow{R} \mathbf{g}, \\ \mathbf{g} &\xrightarrow{R^{-1}} \mathbf{f} \end{aligned} \tag{6.12}$$

where $\mathbf{f}$ and $\mathbf{g}$ respectively denote the original and sorted signal.

6.3.2 PBCS formulation

In PBCS, the data sorting strategy is applied to the CS recovery process. Hence instead of attempting to gain an estimate of the underlying signal $\mathbf{f}$, an attempt to recover the sorted signal $\mathbf{g}$ is made instead, where $\mathbf{f} \xrightarrow{R} \mathbf{g}$. The reconstruction outcome is unsorted with R^{-1} to form an estimate of the original signal. As data sorting changes the original form of the signal, the corresponding sensing process should also to be adapted to accommodate such a change in the reconstruction process. In the application of MRI, sorting the image elements require the Fourier encoding process to be altered. Mathematically, the columns in the Fourier matrix $\mathbf{W}$ are rearranged to reflect the change of image element positions in the underlying image and $\mathbf{W}_R$ is used to denote the column-changed Fourier encoding

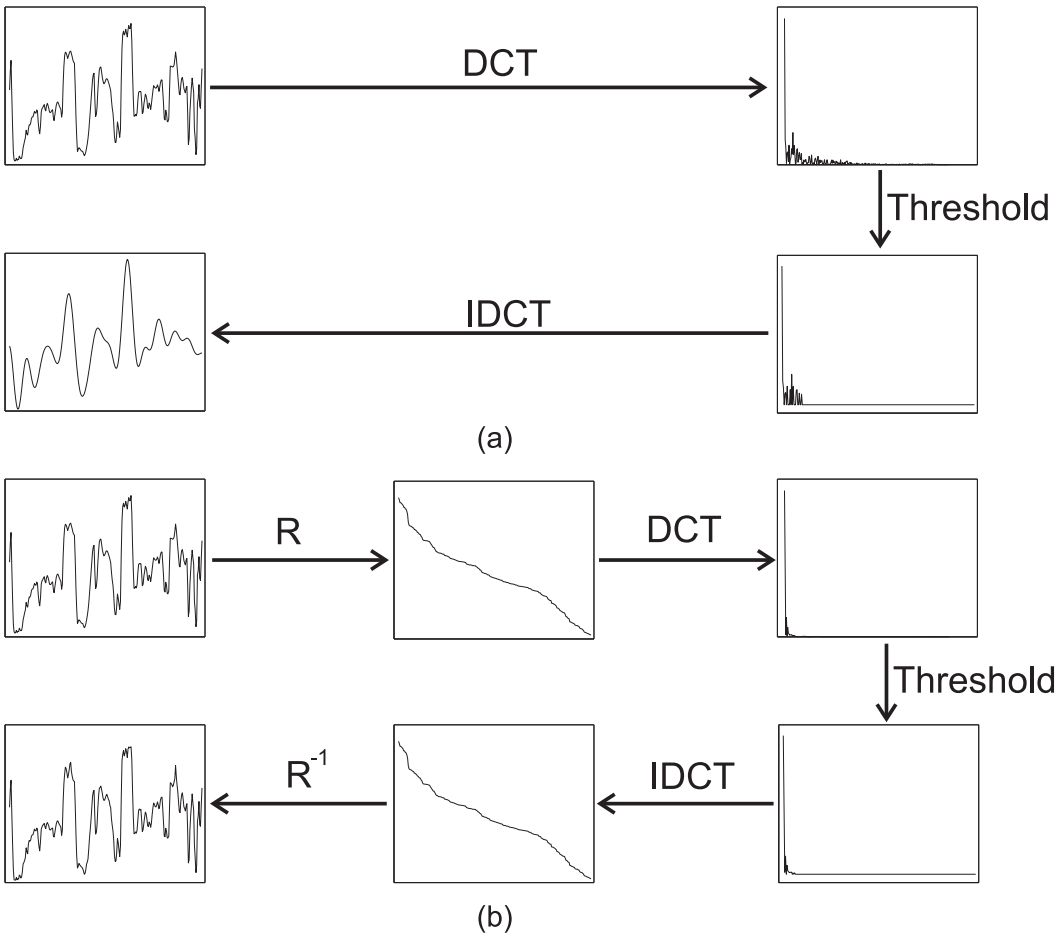

Figure 6.6 Data sorting improves signal sparsity. In (a), conventional signal compression that uses only 5% of the most significant DCT transform coefficients leads to loss of signal information. In (b), a data sorting is incorporated in the compression process. At the same data compression level, much better signal fidelity is maintained in the compression outcome.

matrix for brevity, and the PBCS signal recovery can be written as:

$$\hat{\mathbf{g}} = \arg\min_{\mathbf{g}} \ (\|\mathbf{F} - \mathrm{diag}(\mathbf{h})\,\mathbf{W}_R\,\mathbf{g}\|_2 + \alpha\|\Phi\mathbf{g}\|_1), \quad \hat{\mathbf{g}} \xrightarrow{R^{-1}} \hat{\mathbf{f}} \tag{6.13}$$

where $\hat{\mathbf{g}}$ is an estimate of the sorted signal under sorting order R and $\hat{\mathbf{f}}$ is the final estimate of the underlying signal.

The merit of data sorting in PBCS is to allow the underlying signal to be recovered in an alternative form that can be made to possess higher level of sparsity, which generally promises a better signal recovery. In the simulation in Fig. 6.7, reconstructions of a spatial signal from its under-sampled Fourier domain data using conventional CS and PBCS are compared. It is seen that signal recovery from the under-sampled Fourier domain data using conventional CS recovery scheme in this case leads to an unsuccessful reconstruction. On the other hand, with the knowledge of the appropriate sorting order R, PBCS recovery

of the monotonically varying signal is highly accurate due to its high sparsity level under the DCT transform. Then after applying the unsorting process R^{-1}, a final reconstruction with high fidelity is received.

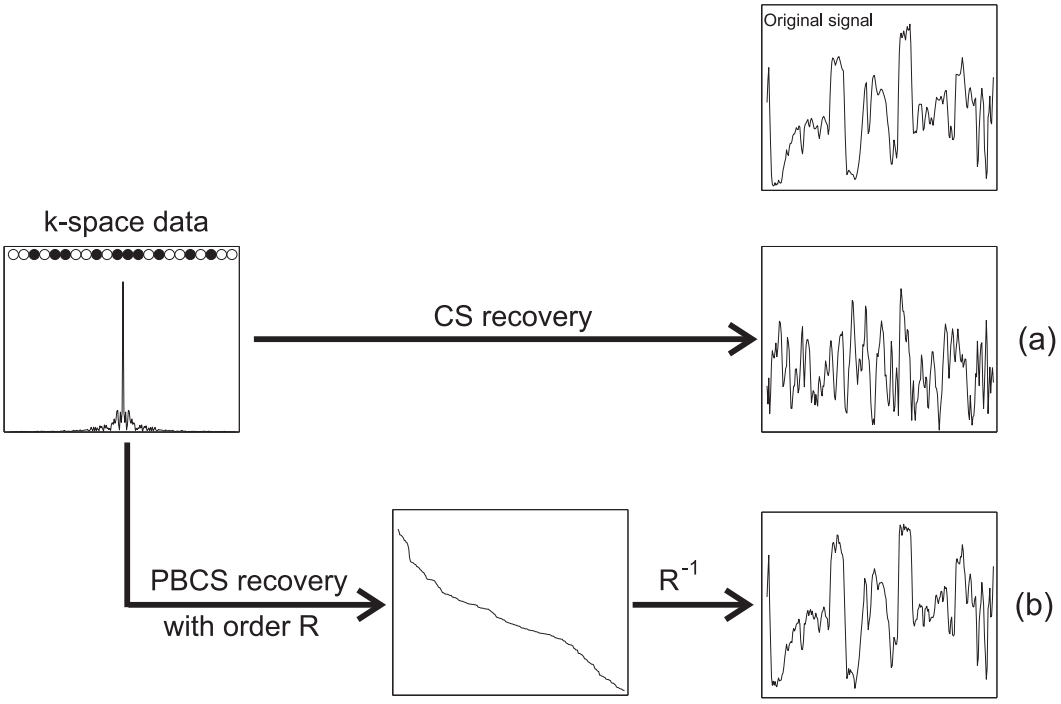

Figure 6.7 Comparing the signal reconstructions from under-sampled Fourier data set using conventional CS and PBCS. The spatial signal's Fourier transform is under-sampled at an acceleration factor of 3. The filled and blank dot respectively represent the acquired and skipped k-space samples, and more samples are acquired in the high energy level k-space region. As illustrated in the diagrams, either a CS recovery or a PBCS recovery is made. In the latter case, the signal is reconstructed in a monotonically varying form which then undergoes an unsorting process. The original signal is shown on the top of the reconstruction outcome for comparison. It is seen that the PBCS recovery leads to much improved reconstruction fidelity.

6.3.3 Using an approximate sorting order in PBCS

In practice, knowledge of the relative magnitudes of the elements in the signal is usually not available as the signal is yet to be recovered. Hence neither is the sorting order R available. Rather an approximate sorting order R' can be obtained from various types of signal prior estimate and the PBCS signal recovery is then written as:

$$\hat{\mathbf{g}} = \arg\min_{\mathbf{g}} \ (\|\mathbf{F} - \mathrm{diag}(\mathbf{h})\,\mathbf{W}_{R'}\,\mathbf{g}\|_2 + \alpha\|\Phi\mathbf{g}\|_1), \quad \hat{\mathbf{g}} \xrightarrow{R'^{-1}} \hat{\mathbf{f}} \tag{6.14}$$

Applying an approximate sorting order to the signal usually results in an imperfectly sorted signal. However, applying a data sorting in the PBCS reconstruction has two interesting consequences: (1) it allows a prior signal estimate to be incorporated; (2) data sorting modifies the form of the reconstruction artifacts. These two consequences are dis-

cussed in details in the following sections.

Applying a sorting order incorporates a prior estimate

In Fig. 6.8, the effects of applying an approximate sorting order that is obtained from a low resolution approximation of the signal are illustrated. In Fig. 6.8.(b), a low resolution approximation of a spatial signal is obtained by low pass filtering the original signal. Then a sorting order R' is obtained by sorting this low resolution approximation to form a monotonically varying signal. In Fig. 6.8.(a), this sorting order R' is used to sort the original signal, the outcome as seen is imperfectly sorted and exhibits discrepancies from a monotonically varying signal. As a result of imperfect sorting, its DCT transform (Fig. 6.8.(a)) contains a range of high frequency components and has a lower level of signal sparsity comparing to that of a perfectly sorted signal (Fig. 6.8.(b)). Now in the process of PBCS recovery when the sorting order R' is used, it is the transform of the approximately sorted signal as shown in Fig. 6.8.(a) that is attempted to be recovered.

The spatial signal in Fig. 6.8.(a) consists of two parts: the prior estimate and the discrepancies between the prior estimate and the actual signal. Likewise, the DCT transform of the approximately sorted signal is also consisted of the DCT transform of the sorted prior estimate (Fig. 6.8.(b)) and the sorted discrepancies (Fig. 6.8.(c)) under sorting order R'. Consider the transform of the sorted prior estimate, as the prior estimate is perfectly sorted under R', its transform (Fig. 6.8.(b)) is extremely sparse and has high level of energy concentration (in this case of a DCT transform, signal energy is highly concentrated in the low frequency components). On the other hand, the transform of the sorted discrepancies demonstrates low sparsity and low level of energy concentration. Thus the DCT transform to be recovered can be decomposed into two parts: strong components that are attributed to the prior estimate and the much weaker components that are attributed to the discrepancies. As promised by the compressed sensing recovery theory, the strong components would be recovered with high fidelity, which means the prior estimate is intrinsically embedded in the reconstruction result. In another word, the use of an sorting order obtained from a prior estimate allows the prior estimate to be incorporated in the PBCS reconstruction.

As a signal can always be decomposed into a prior estimate and the discrepancies between the estimate and the actual signal, the same principle as employed above holds regardless of the type of signal estimate used. The utility of a data sorting on the prior signal estimate is to concisely represent the prior estimate for a specific transform, so that such concise representation can be preserved in the PBCS reconstruction due to its likely large magnitude (concise representation means high level of energy concentration which is likely to have large magnitude). However, the relative magnitude of the representation of the prior

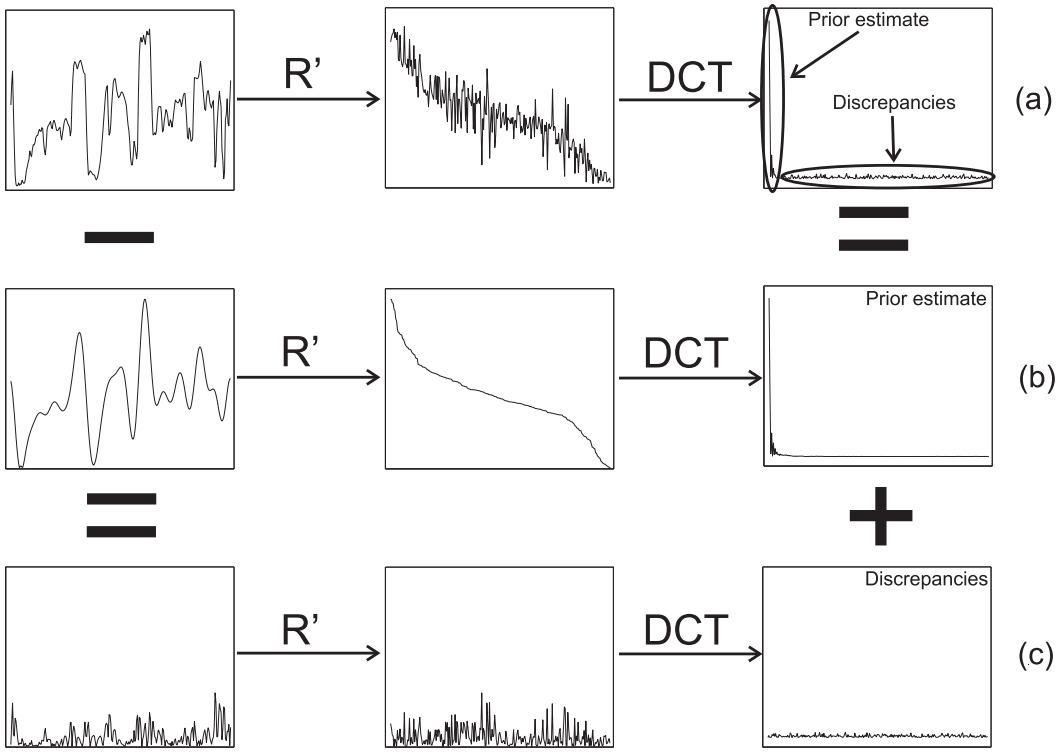

Figure 6.8 Applying an approximate sorting order that is obtained from a prior estimate of the signal in the PBCS recovery incorporates the signal prior estimate. In (b), a sorting order R' is first obtained by sorting a low resolution approximation of the signal shown in (a). Then this sorting order is used to sort the actual signal, which results in an imperfect signal. As a result, the DCT transform of the imperfectly sorted signal (a) has lower level of sparsity comparing to the case of a perfectly sorted signal. The discrepancies between the signal and its approximation is the difference between the two as depicted in (c). Likewise the DCT transform of the signal can be decomposed into two parts respectively attributed to the prior estimate and the discrepancies, as labeled in (a). In this case, the components corresponding to the prior estimate in the DCT transform as seen to be much stronger than that of the discrepancies, hence they will be easily recovered in a CS reconstruction. Thus the prior estimate (b) is essentially embedded in the reconstruction outcome when this approximately sorted signal (a) is recovered using CS recovery.

estimate to thatof the discrepancies in the signal to be recovered (such as in Fig. 6.8.(a)) depends on the accuracy of the estimate. The closer the prior estimate is to the actual signal, the stronger the representation of the prior estimate is with respect to those of the discrepancies, and vice versa. In another words, the more accurate the prior estimate is, the sparser is the transform of the sorted signal to be recovered, and hence the more successful the PBCS recovery is likely to be; however if the prior estimate contains little information about the underlying signal, the transform of the sorted signal is then not likely to be sparse at all, and hence PBCS is not likely to be more advantageous than conventional CS approach.

Data sorting modifies the reconstruction artifacts

As discussed previously, a prior estimate can be incorporated in the PBCS reconstruction by using a sorting order that is obtained from the prior estimate. It is then the objective to recover the discrepancies between the prior estimate and the actual signal so that a more accurate estimate than the known prior estimate can be gained. Unfortunately, usually a sorting order that achieves a concise representation for the prior estimate often leads to a non-concise (non-sparse) representation for the discrepancies, such as in the case observed in Fig. 6.8.(c). By the nature of CS recovery, the non-sparse representation of the discrepancies in the transform domain make it difficult for them to be accurately recovered.

Fortunately, another benefit brought by the data sorting is the modification of the form of the reconstruction artifacts that arise due to inaccurate estimate of the signal transform coefficients. The new form of the artifacts (that are due to imperfect recovery of the discrepancies) make them to be more easily compensated for, and hence aids the recovery of the discrepancies. In the conventional CS recovery, error in the recovered signal transform coefficients lead to structured artifacts that are dependent on the specific transform used. In case of a DCT or wavelet transform, such artifacts are usually seen as loss of signal contrast or blurring artifacts [Don06, LDP07]. These artifacts are difficult to mitigate as they are related to the specific signal/image features. When a sorting order is applied, the structured artifacts are present in the sorted signal/image domain. After undergoing the process of an reverse sorting process, the structured artifacts are likely to be become unstructured in the actual signal/image domain. Unstructured artifacts usually feature high frequency variations, and have a noise-like appearance. Assuming the underlying signal/image has a intrinsically smooth nature, those artifacts can be much easily tackled, such as by using a total variation (TV) constraint in the reconstruction.

The modification of the transform basis functions with respect to the actual signal due to data sorting is illustrated in Fig. 6.9, where a DCT transform is used as the sparsifying transform. Suppose there is an error in recovering a specific DCT coefficient, the corre-

sponding basis function of which is a continuous cosine function (Fig. 6.9.(a)). In the conventional CS reconstruction, such an error will lead to a continuous cosine function with certain magnitude and phase in the recovered signal. If a sorting order R' (the same sorting order as used in Fig. 6.8) is used in the PBCS reconstruction, the continuous cosine modulation is then present in the reconstruction in a sorted signal form. After undergoing the unsorting process, the error in the final reconstructed signal becomes unstructured and has a lot of rapid variations as seen in Fig. 6.9.(b).

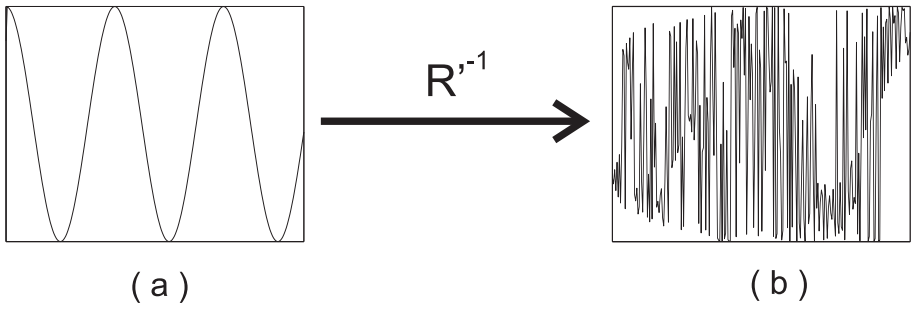

Figure 6.9 Applying a sorting order in CS reconstruction leads to modified form of the transform basis functions with respect to the signal to be recovered. In case of conventional CS recovery, error in recovering a specific DCT coefficient leads to a cosine modulation in the reconstruction as illustrated in (a). In case a sorting order R' is used in the CS reconstruction, a reverse sorting R'^{-1} is then made to restore the reconstruction to the original signal form, the error thereafter will be an 'unsorted' cosine curve, which loses its original structure as shown in (b) and likely features a lot of rapid variations.

In actual PBCS reconstructions, errors will be present in many transform coefficients rather than in a single coefficient. Since the strong coefficients are usually much better recovered than the weak coefficients [Don06], reconstruction artifacts in compressed sensing can be simulated by setting some of the weakest coefficients to zeros (same as a signal compression). Fig. 6.10 compares the outcome of compressing the signal shown in Fig. 6.10.(a) with and without a data sorting applied. In Fig. 6.10.(b), a conventional signal compression as demonstrated in Fig. 6.6.(a) is made to maintain 5% of the most significant DCT coefficients. In Fig. 6.10.(c), a data sorting was involved in the signal compression process as demonstrated in Fig. 6.6.(b), however only an approximate sorting order obtained using a low resolution approximation (same as the sorting order used in Fig. 6.8) was used. Comparing the outcome of the two types of signal compressions, it is seen that the conventional signal compression (Fig. 6.10.(b)) leads to loss of image details. However, in Fig. 6.10.(c), the image details are maintained but are impaired with additional rapid variations (see regions that are indicated by the arrows). In the process of signal reconstruction, the lost image details in Fig. 6.10.(b) are difficult to restore, however the rapid local variations in Fig. 6.10.(c) can be relatively easily removed by utilizing the intrinsic smoothness of the signal. In practice, the smoothness in a 2D image is usually much higher than the 1D case shown here.

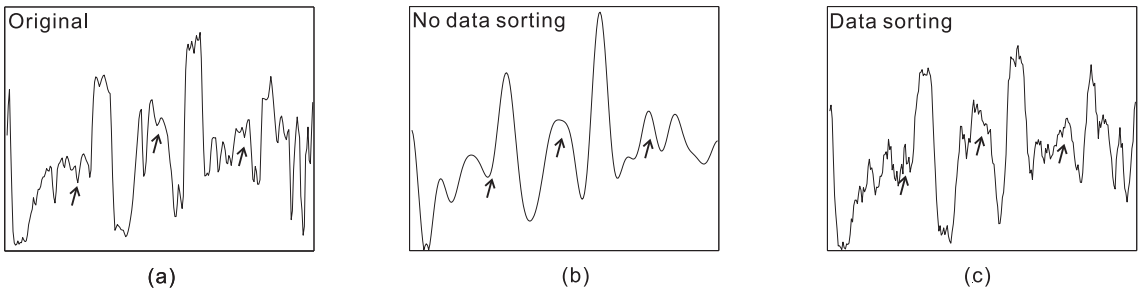

Figure 6.10 Comparing the outcome of signal compression with and without data sorting: (a) original signal to be compressed; (b) conventional signal compression as illustrated in Fig. 6.6.(a); (c) Signal compression with a prior data sorting applied as illustrated in Fig. 6.6.(b), the sorting order is obtained from a low resolution approximation of the signal. It is seen that the artifacts due to signal compression have different forms in (b) and (c). There is a lack of image details in some regions in (b), whereas in (c) the image details are better preserved but are impaired with additional local variations.

6.4 PBCS in parallel MRI

CS image reconstruction in conventional MRI exploits the image sparsity, whereas applying CS image recovery in parallel MRI (pMRI) receives the additional benefits of the distinctive coil sensitivity encoding in different receiver coils. In the following sections, the direct extension of CS formulation to accommodate multiple receiver measurements is presented. However such formulation has an intrinsic limitation. To synergistically exploit coil sensitivity encoding and image sparsity, a new method named SENSECS based on the previously introduced prior estimate based compressed sensing (PBCS) is proposed.

6.4.1 Direct combination of pMRI and CS

Recall that a pMRI measurement system with a sampling mask $\mathbf{h}$ can be written as:

$$\mathbf{F} = \mathbf{E}\mathbf{f}, \;\; \mathbf{E} = \begin{bmatrix} \mathrm{diag}(\mathbf{h})\,\mathbf{W}\,\mathrm{diag}(\mathbf{c}_1) \\ \mathrm{diag}(\mathbf{h})\,\mathbf{W}\,\mathrm{diag}(\mathbf{c}_2) \\ \cdots \\ \mathrm{diag}(\mathbf{h})\,\mathbf{W}\,\mathrm{diag}(\mathbf{c}_M) \end{bmatrix}, \;\; \mathbf{F} = \begin{bmatrix} \mathrm{diag}(\mathbf{h})\,\mathbf{F}_1 \\ \mathrm{diag}(\mathbf{h})\,\mathbf{F}_2 \\ \cdots \\ \mathrm{diag}(\mathbf{h})\,\mathbf{F}_M \end{bmatrix}, \tag{6.15}$$

where $\mathbf{E}$ is the pMRI encoding matrix, and $\mathbf{F}$ represents the the collective partial measurements from all the receiver coils. To utilize multiple coil measurements in CS recovery, the Fourier encoding matrix in Eq. (6.10) is replaced with the pMRI encoding matrix $\mathbf{E}$, giving:

$$\hat{\mathbf{f}} = \arg\min_{\mathbf{f}} \; (\|\mathbf{F} - \mathbf{E}\mathbf{f}\|_2 + \alpha \|\mathbf{\Phi}\mathbf{f}\|_1), \tag{6.16}$$

where $\mathbf{\Phi}$ represents the sparsifying transform used. Essentially, Eq. (6.16) exploits the mutual sparse representation of $\mathbf{f}$ underlying in the coil sensitivity encoded measurements in

multiple receiver coils. Due to the distinctive coil sensitivity weighting in different coils, the k-space measurements received in different coils are distinctive linear combinations of the coefficients of the sparse signal transform. Hence employing measurements from multiple receiver coils allows a better CS recovery compared to the case in conventional single coil MRI.

6.4.2 Limitation of direct combination

As has also been discussed in [LAV+09], direct combination of pMRI and CS recovery as in Eq. (6.16) has an intrinsic limitation that is imposed by the conflicting sampling requirement of pMRI and CS. As discussed previously, the under-sampling strategy or the sampling pattern has large impacts on the reconstruction outcome in both cases of conventional pMRI and CS recovery. In CS, the key sampling requirement is to achieve incoherent aliasing artifacts in the transform domain in which the sparse signal is to be recovered. In cases where a DCT or wavelet transform is used as the sparsifying transform, this is equivalent to having a pseudo-random sampling pattern. On the other hand, from the pMRI aspect it is preferable to have image elements that are spatially far apart to be aliased together (a sparse aliasing pattern) in order to improve the effectiveness of sensitivity encoding, which requires a regular sampling pattern. Thus direct combination of pMRI and CS as in Eq. (6.16) gives rises to a dilemma in terms of sampling pattern design: the sampling pattern that is favored by CS reduces the effectiveness of pMRI, whereas a sampling pattern that could sufficiently exploit sensitivity encoding in pMRI is unsuitable for the CS recovery. Using either type of sampling pattern intuitively reduces the effectiveness of reconstruction in Eq. (6.16).

6.4.3 SENSECS

As coil sensitivity modulation can not fully compensate for the lack of Fourier encoding, reconstruction using partial data sets from different receiver coils leads to imperfect image estimates. The reconstruction outcome using SENSE method and CS recovery have distinctively different characteristics. In SENSE-like methods, direct inversion of the measurement matrix offers a 2nd norm optimal image estimate; however it often leads to reconstruction noise amplification. In the CS recovery, the use of a signal sparsity constraint as well as other constraints such as the TV constraint achieves a low noise level in the reconstructions, however it also leads to loss of image details and contrast in the reconstruction [LDP07]. In short, SENSE-like methods give accurate image estimates that are corrupted by noise, whereas CS reconstructions have a low noise level but are often inaccurate. Hence the pros and cons of the two types of method complement each other. There is clearly an advantage if the merit of one method can be used to compensate for the shortcomings of the other, and the PBCS-based SENSECS method is developed to achieve this.

The flow chart in Fig. 6.11 illustrates the operation of SENSECS in constructing a 2D image. Firstly, as shown on the top, a SENSE reconstruction is made that gives an image estimate that is corrupted by reconstruction noise. Then a sorting order R' is obtained by sorting this reconstruction into a 2D monotonical function [3]. Either a 2D wavelet or DCT transform is used as the sparsifying transform so that the monotonical function has a sparse representation. With this sorting order, a PBCS reconstruction using the same k-space measurements is performed, followed by an unsorting process to form a final reconstruction outcome. As discussed previously, the use of a sorting order obtained from a prior estimate in PBCS allows the prior estimate to be incorporated in the reconstruction. Hence in SENSECS, the noise corrupted SENSE reconstruction is used as the prior estimate and the objective of the second stage PBCS recovery is to preserve the image details from in the SENSE reconstruction and to remove the reconstruction noise. Although the reconstruction noise in SENSE reconstruction often features a non-uniform profile, the data sorting process disrupts its original structure and hence allows it to be reduced by imposing a TV constraint. Notice in Fig. 6.11, the reconstructed 2D curve using PBCS features lots of rapid variations that are attributed to the discrepancies between the SENSE reconstruction and the actual underlying image.

As discussed previously, there is a conflict in choosing a sampling pattern to exploit coil sensitivity encoding and CS recovery conjointly. In SENSECS, the utilities of sensitivity encoding and signal sparsity are respectively exploited in the SENSE reconstruction and PBCS reconstruction stage. To cater for reconstructions in both stages, a hybrid sampling pattern is proposed: a SENSE-like regular sampling pattern is first created, then a small number of additional acquisitions at the k-space centre are included. An example of this hybrid pattern is illustrated in Fig. 6.11. The overall sampling pattern features an approximately sparse PSF that allows efficient use of coil sensitivity encoding [LAV+09]. The additional sample acquisitions at the k-space centre capture the high energy k-space components and aid the PBCS.

[3] Sorting in 2D is the same as the case in 1D that rearrange the pixels according to their relative intensities and those pixels in a 2D model.

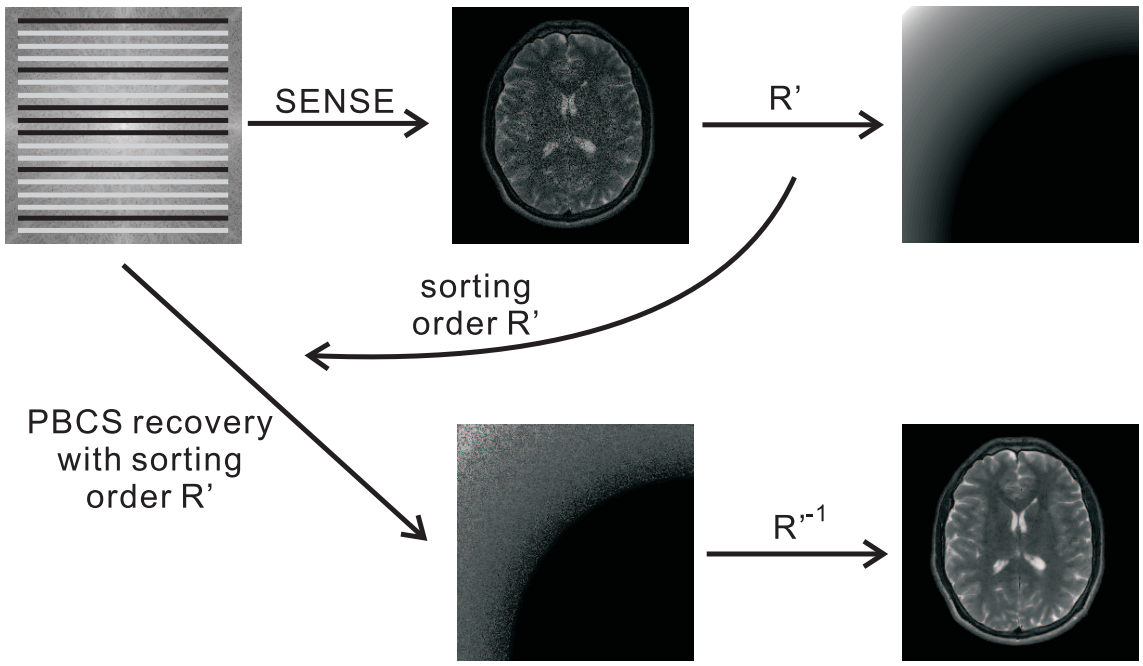

Figure 6.11 Diagram illustrating the operation of SENSECS in constructing a 2D image slice. A SENSE reconstruction is first performed. Then a sorting order R' is gained by sorting the SENSE reconstruction into a 2D monotonical function. This sorting order R' is then used in a PBCS reconstruction that gives an estimate of the image in the sorted form. A final unsorting process gives the final reconstruction. The hybrid sampling pattern as shown (dark and bright lines represent acquired and skipped k-space lines respectively) is a regular sampling pattern with a small number of fully sampled lines at k-space centre.

6.5 Methods

As the performance of CS-like methods is affected by the spatial features of the image to be recovered, the performance of the newly proposed PBCS and SENSECS methods is evaluated based on in vivo experimental data sets. The data used was obtained using a 1.5T GE scanner equipped with a 8-channel head coil. A 2D T2-weighted axial brain slice of a healthy adult volunteer was obtained with the following parameters: FOV = 22 cm, matrix size = 256×256, TR/T2 = 85/20 ms. Phase encoding and frequency encoding are set to be posterior-anterior and left-right respectively. Consent from the volunteer was obtained prior to the scan. A full k-space data set was first obtained, then various forms of sampling patterns were applied to simulate the under-sampling required. Three objectives have been set:

1. To investigate prior image estimate incorporation in PBCS.
2. To assess the significance of the sorting order in PBCS.
3. To assess the performance of SENSECS.

The details for the three series of simulations are given in the following sections.

Unless otherwise stated, the sparsifying transform used in CS-like reconstruction is a 2D wavelet transform (4-level Daubechies). Conjugate gradient descent modified from its initial form in Lustig's *sparseMRI* toolbox [LDP07] was used in the iterative reconstruction, and 40 iterations were performed for each reconstruction to achieve approximate convergence based on experience. To keep consistency among the different simulations, the weighting coefficients of the sparsity term used was set to be $\alpha = 0.02$ and that of the TV term was set to be $\beta = 0.02$ if a TV constraint was incorporated. No particular tuning of the weighting coefficients was made for their optimality, although the magnitudes of the weighting coefficients do have significant influence on the reconstruction outcome [LDP07].

6.5.1 Prior estimate incorporation in PBCS

The objective in this simulation is to verify that PBCS actually allows a prior estimate to be incorporated into the reconstruction. A pseudo-random sampling pattern (at an acceleration factor of 4) based on a uniform probability density function (PDF) was designed and used for the CS reconstructions. A low resolution approximation of the image was obtained using only the fully sampled k-space central regions (32×256) from multiple coil data sets. Then a sorting order was obtained by sorting this low resolution approximation into a 2D monotonical form, and this sorting order was then used in the PBCS reconstructions.

To investigate the utility of prior estimate in PBCS, four types of image reconstruction were made and compared: (1) CS reconstruction with the uniform density sampling pattern; (2) CS reconstruction with the same sampling pattern but with the central 32 k-space lines fully sampled; (3) PBCS reconstruction using the sorting order obtained from the low resolution approximation; (4) CS reconstruction with a uniform density sampling pattern, but with an additional penalty term enforcing the similarity between the reconstruction and the low resolution approximation, i.e.

$$\hat{\mathbf{f}} = \arg\min_{\mathbf{f}} \ (\|\mathbf{F} - \mathrm{E}\,\mathbf{f}\|_2 + \alpha\|\mathbf{\Phi}\mathbf{f}\|_1 + \gamma\|\mathbf{f} - \mathbf{g}\|_2) \tag{6.17}$$

where $\mathbf{g}$ is the low resolution approximation, and γ is the associated weighting coefficient and was set to 0.04.

The first method of reconstruction (number (1) above) is unlikely to lead to a successful CS recovery due the uniform sampling density used, as it is necessary to over-sample the k-space centre to capture the high energy k-space components (see Section 6.2.2). In the other three types of reconstructions (numbers (2), (3), (4) above), the missing low frequency

information is incorporated into the reconstruction process in different ways. In method (2), the low frequency components in k-space are directly included in the reconstruction. In (3), the low frequency information is incorporated via the process of data sorting in PBCS. In (4), the low frequency information is used as a regularizing term in the reconstruction.

6.5.2 Significance of the sorting order in PBCS

The objective of this series of simulations is to investigate the effects of applying different sorting orders in PBCS reconstruction. PBCS reconstructions with the use of the following types of sorting orders were made: (1) no sorting order used; (2) a sorting order that was obtained by sorting a low resolution image approximation (same as used in Section 6.5.1); (3) a sorting order that was obtained by sorting a full resolution image that is formed using full k-space data sets; (4) a randomized sorting order, which was obtained from a random number generator. In each of the PBCS reconstructions, the uniform density sampling pattern at an acceleration factor of 4 (same as that used in Section 6.5.1) was used. To investigate the effects of data sorting on reconstruction artifacts, each reconstruction was made with and without a TV constraint applied.

6.5.3 SENSECS

In order to investigate the performance of SENSECS, image reconstructions using CS, SENSE and SENSECS at various acceleration factors were made and compared. In CS reconstructions, the CS-favored sampling patterns were used and designed using Lustig's *sparseMRI* toolbox [LDP07]. In both SENSE and SENSECS, the hybrid sampling patterns as discussed in Section 6.4.3 were used. At each level of under-sampling, a conventional regular SENSE sampling pattern was first created, then 4 additional lines at the k-space centre were included. For instance, at an acceleration factor of 6, after fully sampling the central 4 lines in the SENSE-like regular sampling pattern, the effective acceleration factor became 5.7. The same number of samples were included in the sampling patterns (varying sample density) used for the CS reconstructions. Also, in order to illustrate that the second PBCS reconstruction phase in SENSECS is not a simple filtering process, a wavelet shrinkage [DRT95] denoising process was applied to the SENSE reconstructions for comparison. Wavelet shrinkage essentially has a similar nature to wavelet compression: all the small coefficients in the wavelet domain are discarded to remove any rapid fluctuations in the image. To quantitatively evaluate the performance of the different reconstruction methods, the normalized mean square errors (NMSE) between the reconstructed and image reconstructed from full data set were calculated, defined by:

$$\mathrm{NRMS} = \sqrt{\frac{\sum_{i=1}^{P}(|I_i^{\mathrm{reference}}| - |I_i^{\mathrm{reconstructed}}|)^2}{\sum_{i=1}^{P}|I_i^{\mathrm{reference}}|^2}}, \tag{6.18}$$

where P denotes the number of pixels within the region of interest, and $I^{\text{reconstructed}}$ and $I^{\text{reference}}$ are both normalised quantities.

6.6 Results

The outcomes of the simulations for the previously stated objectives are organized in the following sections.

6.6.1 Prior estimate incorporation in PBCS

Fig. 6.12 summarizes the outcome of the simulation as described in Section 6.5.1. In Fig. 6.12.(a), the image reconstructed from the full data sets is shown as a reference. The boxed region in the reference image (indicated in Fig. 6.12.(a)) extracted from the four different reconstructions are shown in Fig. 6.12.(b)-(e) : (b) CS reconstruction with a uniform density sampling mask; (c) CS reconstruction with a uniform density sampling mask and fully sampled k-space centre; (d) PBCS reconstruction with a sorting order obtained from low resolution image estimate; (e) CS reconstruction with an additional regularizing term.

As seen in Fig. 6.12.(b), at an acceleration factor of 4, conventional CS image recovery with a uniform density sampling function leads to reconstruction with a loss of image contrast and details, which is due to the lack of low frequency components measurements. In Fig. 6.12.(c), the fully sampled k-space centre ensures the capture of low frequency components, and it leads to a much improved reconstruction compared that in Fig. 6.12.(b). In the PBCS reconstruction (Fig. 6.12.(d)), although the low frequency components are not directly measured, the low resolution image approximation that was incorporated in the reconstruction via data sorting compensated for the missing low frequency information. As a result, a reconstruction with good image fidelity is obtained. In Fig. 6.12.(e), it is seen that although using the low resolution approximation as a regularizing term also achieved an improved outcome compared to Fig. 6.12.(b), it still lacks image details due to the low quality image prior estimate used as the regularizing term.

It is interesting to compare the reconstruction outcome using CS with a fully sampled k-space centre and PBCS with a low resolution approximation used as the prior estimate (comparing Fig. 6.12.(c) and Fig. 6.12.(d)). In the former case, the low frequency information is directly included in the CS reconstruction, whereas in the latter case, the low frequency information is inherently incorporated in the reconstruction. It is surprising to see that the PBCS reconstruction led to an outcome with better image contrast and details as indicated by the arrows. This difference is conjectured to be due to the different forms of reconstruction artifacts the two methods encountered as discussed in Section 6.3.3, so that in the case of PBCS the reconstruction artifacts are reduced with the use of a TV constraint.

This effect is further investigated in the next section.

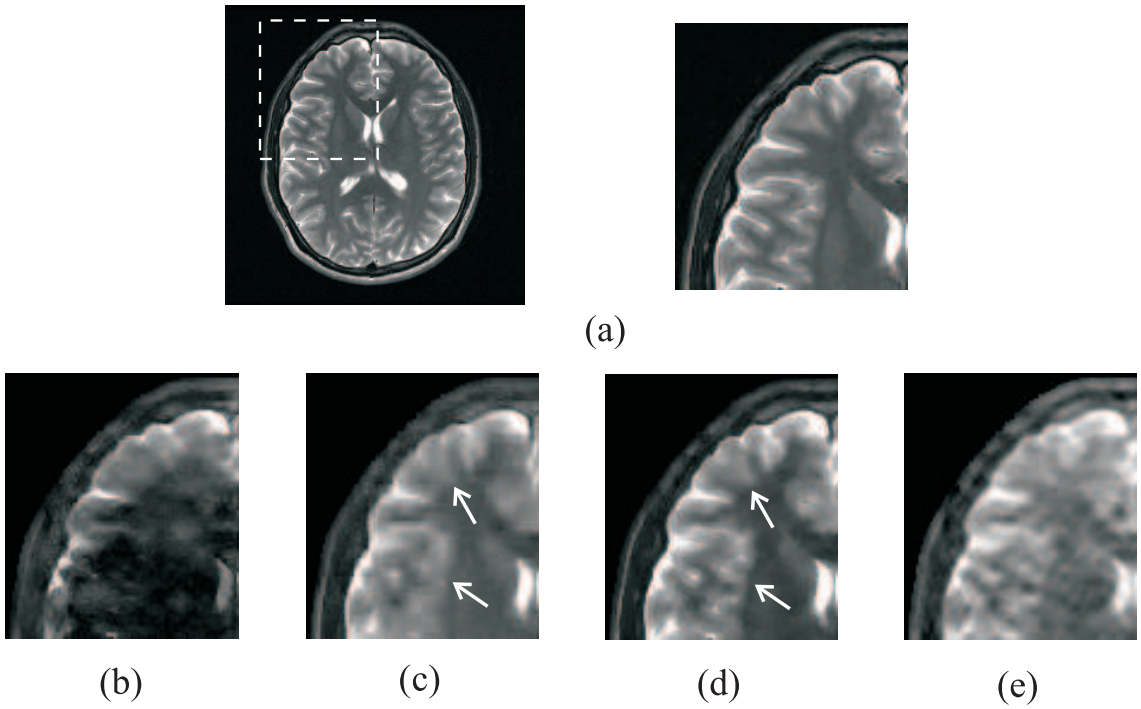

Figure 6.12 Reconstructions of an axial plane brain slice (a) using different methods, the boxed region as indicated in (a) is extracted from each reconstruction result and shown in (b-e). In (b), CS reconstruction is made with an uniform density sampling pattern at acceleration factor of 4 used. In (c), CS reconstruction is made with the same sampling pattern but the central 32 k-space lines are fully sampled. In (d), PBCS reconstruction is made and the prior image estimate used is a low resolution image constructed only from the 32 central k-space lines. In (e), an additional regularizing term that enforces the similarity between the reconstruction and the low resolution approximation is included in the CS reconstruction. The arrows indicate the regions where the reconstruction in (d) shows better recovery than (c).

6.6.2 Significance of sorting order in PBCS

Fig. 6.13 summarizes the outcome of the simulations as described in Section 6.5.2. In Fig. 6.13.(a), the image reconstructed from the full data set is shown as a reference. The boxed region in the reference image (indicated in Fig. 6.13.(a)) extracted from the different reconstruction methods as stated in Section 6.5.2 are shown in Fig. 6.13.(b-e) : (b) PBCS with no sorting order applied; (c) PBCS with a random sorting order; (d) PBCS with a sorting order obtained using a low resolution image estimate; (e) PBCS with a sorting order obtained using a full resolution image estimate.

Firstly, compare the reconstruction outcome when a TV constraint is used in the reconstruction (bottom row in Fig. 6.13.(b)-(e)). Intuitively, applying a random sorting order in PBCS reconstruction does not help in improving the reconstruction, it also led to increased level of reconstruction artifacts (compare Fig. 6.13.(b) and Fig. 6.13.(c)). In Fig. 6.13.(d)

and Fig. 6.13.(e), it is seen that data sorting based on appropriate prior estimates lead to improved reconstructions. Especially in Fig. 6.13.(e), although a non-preferable sampling pattern (a sampling pattern with a uniform density) is used, knowledge of an accurate sorting order allows an almost perfect reconstruction to be achieved. This is because using such a sorting order allows an accurate image estimate to be incorporated in the reconstruction.

The nature of the reconstruction artifacts incurred in each case can be studied by comparing the reconstruction outcome with (lower row) and without a TV (upper row) constraint applied. It is seen that in a conventional CS reconstruction where no data sorting was carried out, the reconstruction artifacts are seen as a loss of image details and contrast (upper row in Fig. 6.13.(b)), hence the TV constraint is not effective in reducing such artifacts (lower row in Fig. 6.13.(b)) and a heavy TV penalty term may further destroy the underlying image details. In contrast, in upper row of Fig. 6.13.(c-e), where image reconstructions are made with an additional sorting applied, the reconstruction artifacts are seen to have rapid variations. Especially in Fig. 6.13.(c), the artifacts have a almost additive noise-like appearance. Such rapid varying artifacts can be effectively reduced by applying a TV constraint as seen in the bottom row of Fig. 6.13.(c-e).

6.6.3 SENSECS

Fig. 6.14 summarizes the outcome of the simulations as described in Section 6.5.3, and Table 6.1 presents the NRMSs calculated for each type of reconstruction. In Fig. 6.14.(a), the image reconstructed from the full data set is shown as a reference. The boxed region in the reference image (indicated in Fig. 6.14.(a)) extracted from the different reconstruction methods are shown in Fig. 6.14.(b)-(e): (b) SENSE reconstruction; (c) CS reconstruction; (d) SENSECS reconstruction; (e) SENSE reconstruction with wavelet shrinkage denoising. The actual acceleration factors used are shown at the left top corner of each image.

Firstly compare the reconstruction outcome using SENSE (Fig. 6.14.(b)) and CS (Fig. 6.14.(c)) at various acceleration factors. It is seen that the noise level in SENSE reconstructions increases significantly as the acceleration factor increases, also shown by the corresponding NRMS values. Especially at high acceleration factors, the central region of the images are severely corrupted by reconstruction noise due to the high g-factor [PWSB99]. In contrast to the SENSE reconstructions, CS reconstructions show little noise corruption but show blurred image details and reduced image contrast, which is due to the failure of recovering some of the transform coefficients conveying the fine scale features. Also, the quality of CS reconstructions seem to degrade more gradually (as seen the gradually increasing NRMS values) compared to the cases of SENSE as the acceleration factor level increases.

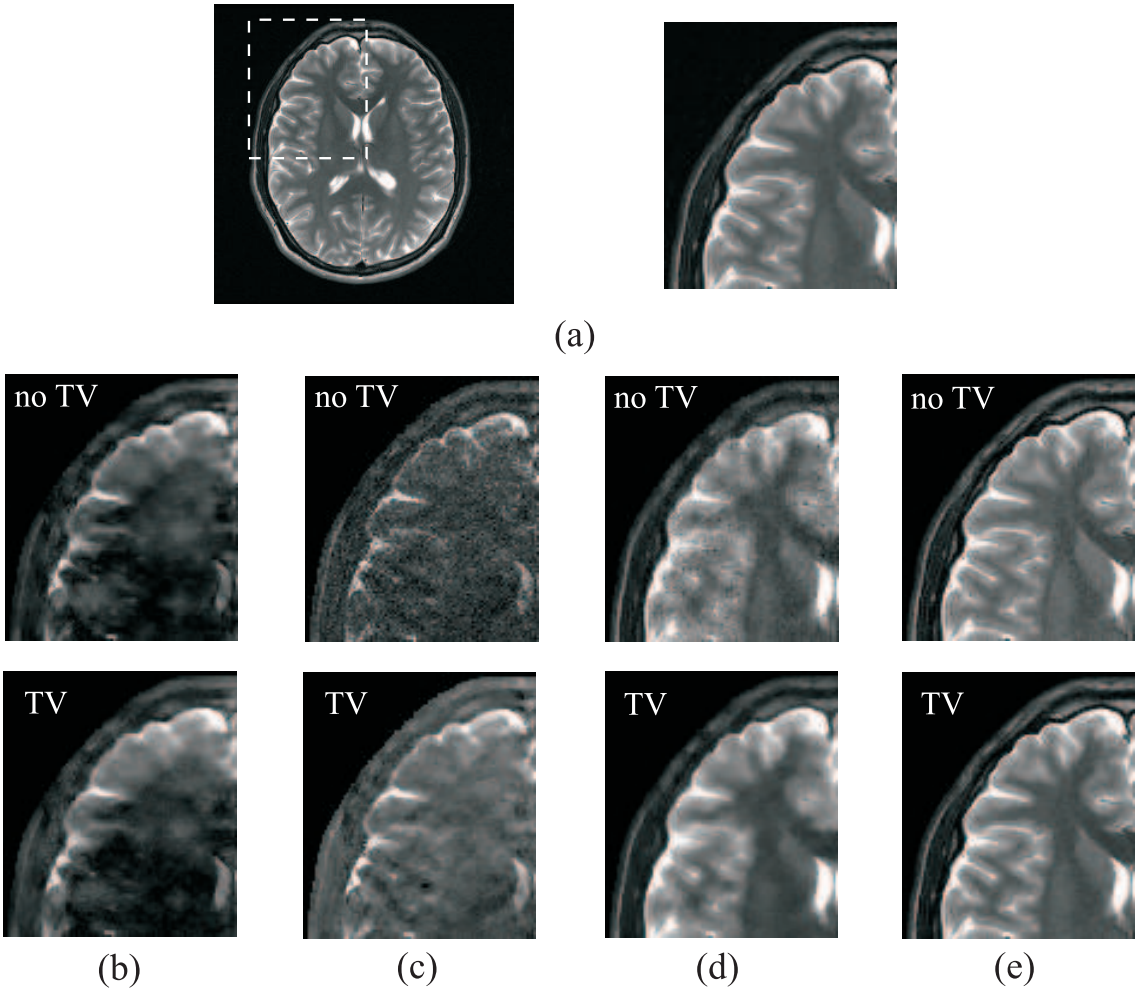

Figure 6.13 Reconstructions of an axial brain slice shown in (a) using PBCS with different sorting orders applied: (b) no sorting; (c) a random sorting order; (d) sorting order obtained by sorting a low resolution image prior estimate; (e) sorting order obtained by sorting a full resolution image prior estimate. The upper row shows reconstructions without a total variation constraint applied, and the lower row shows reconstruction results when a total variation constraint is included. From the reconstructions, it is seen that the accuracy of the data sorting order has a large influence on the quality of image reconstructions. In the conventional CS reconstruction (b), the reconstruction artifacts are smoothly varying; whereas in the PBCS reconstructions (c-e) where a data sorting is applied, the reconstruction artifacts have rapid variations that have been effectively reduced by using a TV constraint.

Secondly, compare the reconstructions using SENSECS (Fig. 6.14.(d)) to those using SENSE and CS alone. Comparing the reconstructions, it is seen that SENSECS leads to image reconstructions with sharp image details as well as low noise levels; comparing the NRMSs, it is seen that SENSECS outperforms SENSE and CS at all the acceleration factors investigated. At high acceleration factor (AF = 7.4), SENSECS exhibits slight aliasing and also a loss of image features in certain regions (as indicated by the arrow 1). This is because these regions in the SENSE reconstruction in Fig. 6.14.(a) (the prior image estimate) were so severely corrupted that they convey little information of the actual underlying image, and the following PBCS reconstruction can not fully recover the discrepancies between the SENSE reconstruction and the actual underling image. In comparison, those regions in the SENSE reconstruction that were less severely corrupted are still recovered with good fidelity in SENSECS (as indicated by arrow 2). The above observations further confirm that the SENSE reconstruction is used as a prior estimate in the second stage PBCS reconstruction.

Lastly, consider the use a of wavelet filter as a means of noise reduction of the SENSE reconstructions (Fig. 6.14.(e)). In general, it is seen that the wavelet shrinkage is not successful as the reconstruction noise in SENSE has a non-uniform profile. Hence it can be concluded that the second stage PBCS reconstruction in SENSECS is not merely a filtering process.

Table 6.1 NRMS for different reconstructions.

Acceleration factor	SENSE	CS	SENSECS	SENSE with filtering
5.8	0.38	0.23	0.10	0.27
6.5	0.45	0.25	0.12	0.37
7.4	0.61	0.28	0.22	0.46

6.7 Discussion

Compressed sensing (CS) is a relatively new approach in signal recovery from incomplete information which exploits the inherent sparsity (explicit and implicit) of the underlying signal to be recovered. Its application in MRI has great practical benefits and has been demonstrated to be successful [LDP07]. The success of CS recovery is fundamentally limited by the sparsity level of the underlying image. Prior estimate based compressed sensing (PBCS) is proposed as an approach that attempts to increase the sparsity of the signal to be

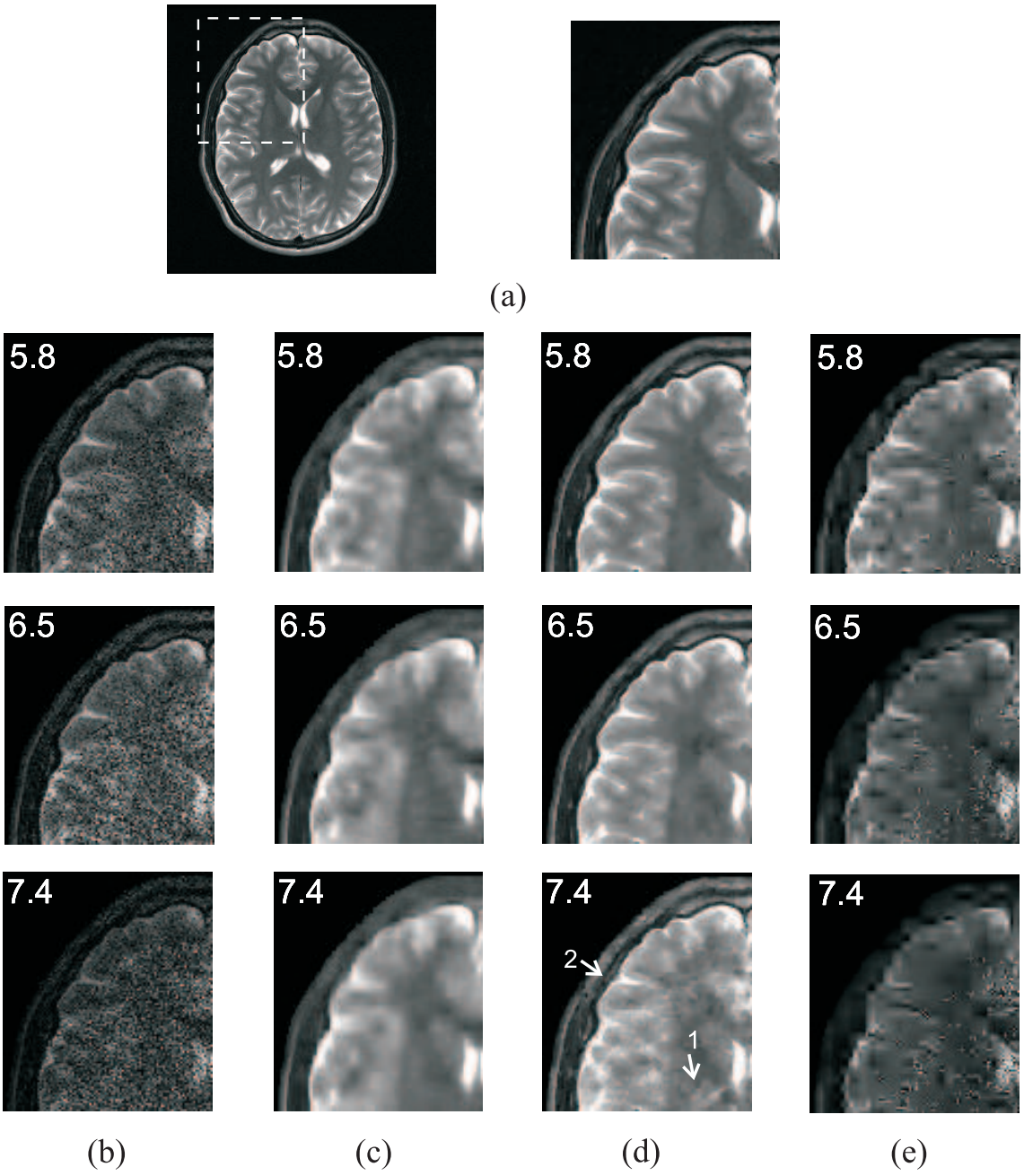

Figure 6.14 Reconstruction of an axial brain slice (a) using different methods at various acceleration factors. The boxed region as indicated in (a) extracted from the reconstruction results using different methods are shown in (b-e): (b) SENSE; (c) CS; (d) SENSECS; (e) SENSE reconstruction with wavelet shrinkage denoising. The various acceleration factors are shown on the left top corner. At moderate acceleration factors (5.8 and 6.5), SENSECS gives the best reconstruction results. In SENSECS reconstruction at a high acceleration factor (7.4), regions that were severely corrupted in the SENSE reconstruction bears slight residual aliasing artifacts (as indicated by arrow 1) and regions that were less severely corrupted by the reconstruction noise are relatively well recovered (as indicated by arrow 2). Also wavelet filtering is seen to be ineffective in these cases due to the non-uniform noise profiles in the SENSE reconstructions.

recovered by incorporating prior knowledge of the image to be recovered. Based on a data sorting on the prior image estimate, the elements in the underlying image are rearranged into a form that features a higher level of sparsity for a given transform, which could potentially lead to improved image recovery. It has been demonstrated that using a sorting order that is obtained by sorting a prior image estimate in PBCS effectively incorporates that prior estimate in the reconstruction. PBCS differs from the conventional approach of incorporating image prior knowledge (such as an additional regularising term as in Eq. (6.17)) in which the image estimate is used as a soft constraint, i.e. no presumption of the underlying image is made; so that errors in the prior image estimate will not propagate through to the reconstruction results. An additional benefit of PBCS is the modification of the form of reconstruction artifacts. In conventional CS reconstructions, the reconstruction artifacts are often dependent on the underlying image features, and hence are difficult compensate for. In PBCS, as a result of data sorting, the reconstruction artifacts also undergo a reverse sorting process, which modifies their original form. In case of a wavelet or DCT transform is used, the modified reconstruction artifacts often have rapid variations and can be more easily compensated for.

PBCS presents a new approach to utilize image prior knowledge in CS reconstructions via data sorting. In the current implementation of PBCS, only the magnitude information in the prior image estimate is utilised in the sorting process. However, in practice the underlying image is often considered to be a complex quantity. Hence it is possibly beneficial to take into account the image phase information in the sorting process, for instance performing a sorting process on the real and imaginary part separately as considered in [AD08]. However, image phase information is usually more difficult to obtain in practice. Apart from an image prior estimate as discussed in this work, other types of image prior knowledge can also be used. For instance the knowledge of object support can be used in the sorting process if the boundary information is of particular interest, such as in contrast enhanced MR angiography. The use of different sparse models (to which data sorting is attempted to resemble) is an interesting topic to investigate. In this work, the sparse models considered were monotonical variations (1D or 2D) that feature sparse representations when a standard wavelet/DCT transform is used. Another sparse model that could be used is a basis function (or combination of a few basis functions) of the sparsifying transform. For instance, a low harmonic cosine function when a DCT transform used. Moreover, as the sparsifying transform is not limited to standard transforms, other customized transforms may also be used, such as a principle component based sparsifying transform as discussed in [DSB+09]. In this case, the sparse model would be a 'standard' image with specific image features.

SENSECS is an application of PBCS in parallel MRI aiming to exploit both the image sparsity and coil sensibility encoding. It exploits the interesting complementary characteristics

of SENSE reconstruction and CS reconstruction, hence it combines the advantages of the two methods in an attempt to overcome their respective shortcomings. From the reconstruction results, it is seen that SENSECS is more advantageous than either SENSE or CS alone. It requires no prior information about the image to be recovered. The only trade-off for this method is the increased computational complexity compared to using each method alone. The composite sampling pattern used in SENSECS consists of two parts: regularly sampled k-space and an additional acquisition at the k-space centre, which is respectively favoured by SENSE and PBCS reconstruction. A systematic sampling pattern design could potentially achieve more optimum balance between SENSE reconstruction and PBCS reconstruction, and is to be further investigated. For instance at high acceleration factors when the SENSE reconstructions (the prior estimate) are severely corrupted, should relatively more samples be acquired to favour the SENSE reconstruction to reduce the reconstruction noise level, or should relatively more samples be acquired to favor PBCS reconstruction so that better compensation for the reconstruction artifacts can be made? Also in the current implementation of SENSECS, only the standard SENSE and CS reconstruction were performed in each stage; various types of additional image constraints can be incorporated in either stage of the reconstruction to further improve the overall reconstruction outcome. For instance, a Tikhonov regularization in the SENSE will lead to reduced level of reconstruction noise and hence a more accurate prior estimate for the following PBCS reconstruction. Compared to other similar approaches which carry out image reconstructions in separate pMRI and CS reconstruction steps as in [LLY08, BKM$^+$09], a distinctive advantage of SENSECS is that errors that occur the SENSE reconstruction will not necessarily propagate through to the final reconstruction results.

Chapter 7

GUISE and PBCS in contrast enhanced MR angiography

In this chapter, the implementations of the previously developed GUISE and PBCS methods in contrast enhanced magnetic resonance angiography (CE-MRA) are presented and discussed. They are well suited for this application and share similarities that both methods exploit the high sparsity in the contrast enhanced angiogram and could take advantage of the image prior knowledge embedded in a composite data set. A distinctive feature of these new methods is retrospective selection of acceleration factors at reconstruction, and hence to achieve a more optimum trade-off between temporal resolution and image quality. Firstly, a brief overview of contrast enhanced magnetic resonance angiography (CE MRA) is given, followed by the discussion of different methods in performing time-resolved CE-MRA. Then the implementations of GUISE and PBCS in time-resolved CE-MRA are presented. Their performance and characteristics are investigated using phantom and volunteer studies.

7.1 Magnetic resonance angiography (MRA)

In magnetic resonance angiography (MRA), the aim is to visualise the blood flow and pathology of the blood flow by producing image contrast between the blood in the vessels and its surrounding tissues. In contrast to the general MRI, data acquisition in MRA is tuned to produce flow-sensitive images rather than morphological images (with anatomical details). MRA is widely used for examining various types of arterial and venous diseases, and also is used for scout imaging for many surgical operations.

The principle of MRA imaging is to alter the magnetization properties of the blood flow

with respect to the surrounding stationary tissues. The existing MRA imaging methods can be put into two categories: flow-dependent MRA [1] and contrast enhanced MRA. As the name suggests, the former group of methods relies on the intrinsic blood flow to produce flow-dependent changes in the magnetization properties; such change is achieved by an injection of contrast agent in the latter case. Although the flow-dependent methods are less invasive than the contrast enhanced MRA which requires an injection, they can only produce good contrast in regions with rapid blood flow and have other limitations caused by the intrinsic speed of the blood flow [WRT05]. On the other hand, the performance of contrast enhanced MRA is not dependent on the blood flow and is widely accepted in clinical practice for its ability to provide safe and accurate angiography [ZMP07, SMH05].

7.2 Contrast enhanced MRA

In general, MR contrast enhancement agents change the T1 and/or T2 relaxation time of the tissues. Coupled with imaging sequence with suitable parameters a contrast difference can be introduced between the tissues containing the agent and surrounding tissues. They are widely used in detecting vascular diseases, tumors, infection, etc. in various regions in the body.

The most widely employed contrast agent in angiography is gadolinium (Gd) [2], which significantly shortens the T1 time of the blood, so that it is significantly less than the T1 of most surrounding tissues. Coupled with an appropriate T1 imaging sequence, vascular regions containing the contrast appear bright whereas the surrounding tissues appear dark. The administration of gadolinium is safe in the majority of patients, although evidence of renal problems precludes its use in some cases. Administration of Gd is usually made in the form of intravascular injection, although oral administration is also possible [YQR+95].

7.2.1 Data acquisition considerations in CE MRA

3D data acquisition is generally preferred in CE-MRA due to its intrinsically high SNR and also the thin contiguous imaging slices achievable allow angiograms to be produced in various forms that are easy for radiologists to interpret. Usually a fast 3D spoiled gradient echo sequence is employed due to its short T1 and TR times, however other types of non-cartesian trajectories are also used for exploiting some of their intrinsicically nice properties including fast imaging and insensitivity to flow motion [ZMP07].

In practice, the aim is to image the first arterial pass of the contrast in order to produce an

[1] the most commonly practised methods are time of flight imaging [MMR89] and phase contrast imaging [DSWW89]

[2] a type of heavy metal (lanthanide) that has seven unpaired protons, and hence allows rapid exchange with water protons [WRT05]

image without background venous enhancement. Acquisition of the k-space volume occurring during the arterial peak yields maximum arterial signal with minimal venous signal. However the distribution of energy in k-space is concentrated near the centre. Therefore acquiring the k-space center too early will lead to degraded signal to noise ratio (SNR) and contrast to noise ratio (CNR); on the other hand acquisition of the k-space centre too late is likely to introduce contrast venous phase contrast enhancement. Furthermore, not acquiring the k-space center when the contrast peaks may lead to k-space inconsistency and hence various types of artifacts depending on the nature of data acquisition sequence.

7.2.2 Imaging Techniques in CE MRA

Several methods have been developed to achieve the synchronization of the k-space center and the arrival of contrast agent in the arteries. Firstly, a best guess of the contrast travel time, defined as the time it takes for contrast to travel from the injection site (usually at the upper extremities) to the vascular region of interest, can be made by an experienced MR angiographer taking account of the factors such as injection site, age, cardiac output, and vascular anatomy [ZMP07]. Alternatively, a more educated guess of the contrast travel time can be obtained based on a test bolus run in which a small Gd contrast dose is injected at the same rate as planned for the actual experiment. However, due to the contrast agent dilution at the leading and trailing edges of the bolus, as well as different transit times through different portions of the pulmonary circulation, the travel time of the contrast agent is highly variable for different patients [ZMP07]. Hence timing of the contrast is very prone to error. Other methods that attempt to minimize the timing error of the contrast travel time are the use of auto triggering or rapid imaging. In the former case, a sequence is used to monitor the contrast arrival and automatically trigger the data acquisition. In the latter case, very rapid imaging techniques such as MR fluoroscopy can be employed to allow the operator to continually watch for the arrival of the contrast agent for the arrival of contrast agent and hence to manually activate the scan.

Since the timing of the contrast arrival is difficult and critical, time resolved imaging is preferred in many cases. In time resolved imaging, a time series of images are continuously acquired after the contrast injection, and chosen to cover a sufficiently long time period of interest. In the post-processing, images that correspond different stages of the dynamic contrast are formed, such as the pure arterial phase, and the mixed arterial and venous phase. The operator can then select the preferred image afterwards. Since time resolved imaging is able to track the temporal contrast variations, the need for contrast arrival timing is completely eliminated. Time resolved timing is described in more detail in the next section.

7.2.3 Time resolved imaging

Both high spatial resolution and high temporal resolution are sought in time resolved imaging. High spatial resolution is required in order to visualize the fine vascular details, whereas high temporal resolution in the repeatedly acquired temporal images is desirable to reveal the blood flow dynamics that helps to identify the pathology of the angiogram. In general, high spatial resolution means intrinsically longer data acquisition that lowers the obtainable temporal resolution, hence high spatial resolution and high temporal resolution are two competing requirements. Several methods have been developed to allow both high spatial and temporal resolution to be achieved.

In addition to choosing pulse sequences to shorten the TR and TE and thereby achieving a shorter image acquisition time interval, improving temporal resolution while maintaining the spatial resolution can be achieved by updating each time frame image by acquiring less than the full k-space data set defined by the Nyquist sampling rate. The current approaches can be put into two categories: rapid imaging and sliding window reconstruction. In the former case [SML+00, WPK+00, HMK+06, PKG+00, VPGB00, MWV+06, HW07, OWJF08], various types of constraints are exploited to allow direct image reconstructions from incomplete k-space data sets. In the latter case [TKC+96, NKF01, VCP07], missing k-space samples are estimated to form composite data sets using which image reconstructions are made. The two types of methods can also be used conjointly to achieve further improvement of the temporal resolution [VPGB00].

Rapid imaging in CE MRA

Parallel imaging has been successfully implemented in time resolved CE MRA to improve the temporal resolution [WPK+00, HMK+06, SML+00, ZVB+06]. The intrinsically high SNR available in CE MRA makes the application of SENSE-like pMRI methods especially attractive [WHW+04]. It is illustrated in [Sod00] that sensitivity encoding in two phase encoding directions can offer increased temporal and/or spatial resolution. Combination of the 2D SENSE with the partial Fourier technique has also been investigated in [HMK+06]. The implementation of k-space parallel imaging methods such as SMASH and GRAPPA have also been respectively reported in [SML+00, ZVB+06].

The intrinsically high image sparsity in CE MRA makes it an attractive field of application for compressed sensing (CS) [LDP07, FBB+08, LJ08, WB08, KG09]. As initially reported by Lustig, etl. in [LDP07], a high acceleration factor could be achieved in reconstructing the contrast enhanced angiogram without the use of an additional sparsifying transform. In [FBB+08, LJ08, WB08], an additional mask subtraction is incorporated prior to the CS reconstruction (discussed in more details later), so that the subtracted data set is

only attributed to the temporal difference between the two data sets and hence features a higher level of image sparsity, which in turn allows more successful CS reconstruction to be achieved. In [KG09], the CS reconstruction is directly made to estimate a final maximum intensity projection (MIP, explained in detail later) image to receive increased level of sparsity compared to applying compressed sensing in reconstructing each individual image slice in a 3D image volume.

Another group of methods that are particularly promising employ a radial k-space trajectory [PKG+00, VPGB00, MWV+06, HW07, OWJF08]. Recent hardware advances allow a high quality image to be reconstructed from radially sampled k-space using projection reconstructions (PR) [PKG+00, VPGB00]. Since the image spatial resolution in PR is determined by the readout resolution rather than the number of projections, high spatial resolution images can be potentially obtained very rapidly (only using a few projections). Moreover, the streaking artifacts resulting from the projection reconstruction are more tolerable for interpretation than the wrapping around artifacts in Cartesian sampling. Hence the use of radial trajectory in CE MRA has received much attention. The next advance of projection reconstruction in CE MRA is the highly constrained projection reconstruction (HYPR) [MWV+06] and its variations [HW07, OWJF08]. Based on a composite image formed using data obtained throughout the time resolved data acquisitions, projection reconstruction is limited to the vascular regions only. An acceleration factor up to 75 has been reported using HYPR [MWV+06].

Sliding window reconstruction

The main distinction between the conventional time resolving reconstruction and the sliding window (SW) reconstruction is that data sets used for producing different time frame images in conventional time resolved methods are temporally independent whereas SW reconstructions utilise k-space data sharing. As illustrated in Fig. 7.1, 'sliding window reconstruction' means a method whereby data from a short temporal interval (window) is utilised to reconstruct an image, then a later interval, overlapping with the previous, is used to form another image and so on. In SW reconstructions, only a portion of the k-space data is updated for reconstructing the next time frame, hence the resulting time frames are temporally correlated. The temporal footprint refers to the time span of an individual reconstruction, whereas the temporal frame rate refers to the time span of the updated data in producing the next reconstruction. At the same acceleration factor, SW reconstruction and conventional time resolved imaging have the same temporal footprint, but SW reconstruction offers high temporal frame rate (determined by the amount of window shift) without sacrificing other image reconstruction quality. Hence SW is widely used in cases where rapidly varying dynamic events need to be captured.

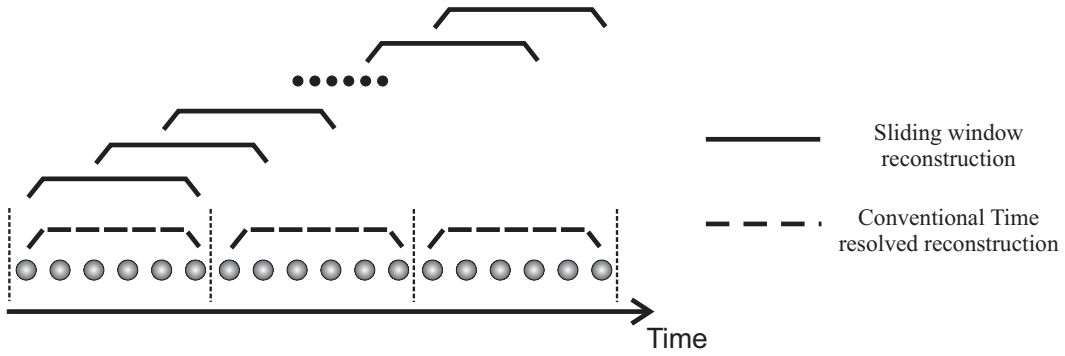

Figure 7.1 Comparison of sliding window (SW) reconstruction and conventional time resolved reconstruction. Subsets of k-space (as represented by the filled dots), each of which may represent a single or a group of FE lines on Cartesian grid or radial projections in radial trajectory or interleaves in spiral trajectory, are acquired sequentially. Image reconstructions are made using the consecutively acquired k-space subsets within a time interval (as indicated by the time windows). In conventional time resolved imaging, data sets corresponding to different intervals are used to produce different time frames, whereas the time intervals used in neighboring SW reconstructions overlap. In the diagram with a window shift amount of 2 data subsets while an individual reconstruction requires 6 data subsets, SW offers an improvement of the temporal frame rate by a factor of 3. However the temporal footprint, which is determined by the amount of data acquisition used for image reconstruction, is unchanged in SW reconstruction.

In Cartesian imaging, two commonly used SW reconstruction methods that allow improvement of temporal resolution by k-space view sharing are the keyhole [VBD+93] and time-resolved imaging of contrast kinetics (TRICKS) [TKC+96]. In both methods, asymmetric k-space acquisition along the temporal axis is used to exploit the fact that the k-space central region conveys much more contrast information than the peripheral regions. In the keyhole technique [VBD+93], a complete k-space volume is first acquired and then only the central k-space region is updated over time. Composite k-space data sets can be then formed using the newly acquired k-space center and the peripheral region acquired at the start. In many applications the keyhole assumption that the high spatial frequencies never evolve over time is not valid. In the TRICKS technique [TKC+96], the k-space volume is divided into different subsections that are all updated over time but with different frequencies. Then composite k-space data sets are formed combining the newly acquired k-space central region with the closest matching k-space peripheral regions along the temporal axis (Fig. 7.2). K-space interpolation of the acquired data sets can also be incorporated to improve the temporal fidelity [TKC+96]. Hence the temporal fidelity of the TRICK method is improved over that of the keyhole. TRICKS offers moderate improvement of temporal resolution without additional SNR loss [TKC+96], and has been applied in various types of vascular imaging [NKF01, VCP07]. More sophiscated versions of the TRICK methods, such TWIST [VEL+07], etc., have also been developed and reported to achieve better spatial-temporal domain reconstruction fidelity.

It is also possible to apply the TRICKS-like data sharing in SENSE and PR type reconstruc-

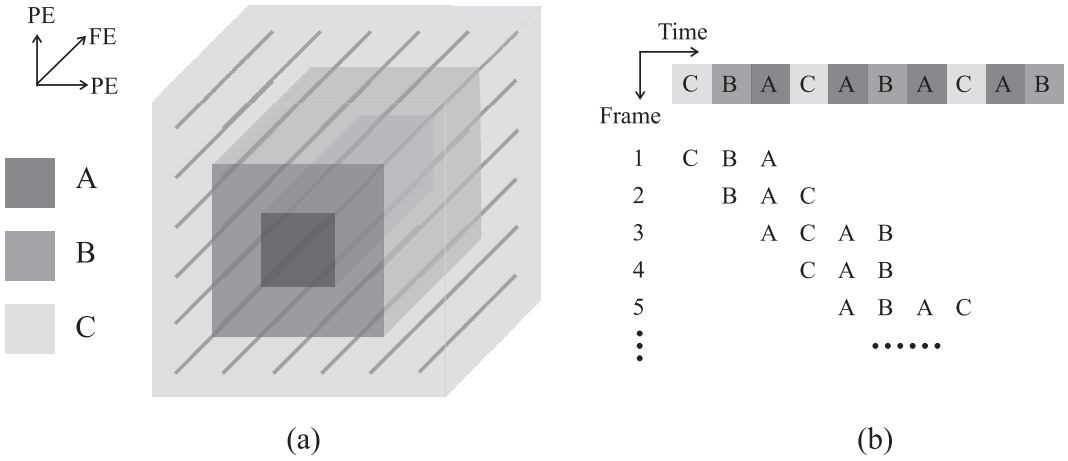

Figure 7.2 In TRICKS technique, the 3D k-space volume is divided into several sections (in this example, 3 sections) according to k-space positions (labeled as A,B,C) as shown in (a), the FE lines on Cartesian grids are acquired at different frequencies according to the k-space section they reside. The central k-space region is updated much more often than the peripheral regions, and each newly acquired k-space center is combined with the nearest peripheral regions on the temporal axis to form a composite full k-space volume. In case there are multiple acquisitions of the same region (as the case of time frame 5), k-space data interpolation of the duplicated k-space regions is made.

tion to further improve the temporal resolution as illustrated in Fig. 7.3. Fig. 7.3.(a), it is seen that the 3D k-space is first regularly under-sampled, then the regularly positioned FE lines are acquired at a rate that is determined by their position within the 3D k-space. Similarly, in Fig. 7.3.(b), where half of a fan-shaped 3D k-space radial trajectory is depicted, the radial lines are updated at different frequencies determined by their positions in k-space [VPGB00].

7.2.4 Image formation in CE MRA

The way a 3D image data set is reformatted and displayed plays an important role in interpretation of the imaged anatomy. In CE MRA, usually a relatively large FOV coverage is made for ease of visualizing the vascular pathology. A routinely used method is the maximum intensity projection (MIP), in which the entire 3D image volume is projected along a particular direction onto a 2D plane. As illustrated in Fig. 7.4, a projection ray is passed through the 3D volume, and the projection result is the maximum signal intensity found along the ray. In MIP images of CE MRA, the high intensity signal in blood vessel lumens containing contrast are likely to be received in the ray projection, and hence the projection tends to enhances the vascular contrast. MIP is computationally efficient, and projections can be made along any axis to display the image at different viewing angle.

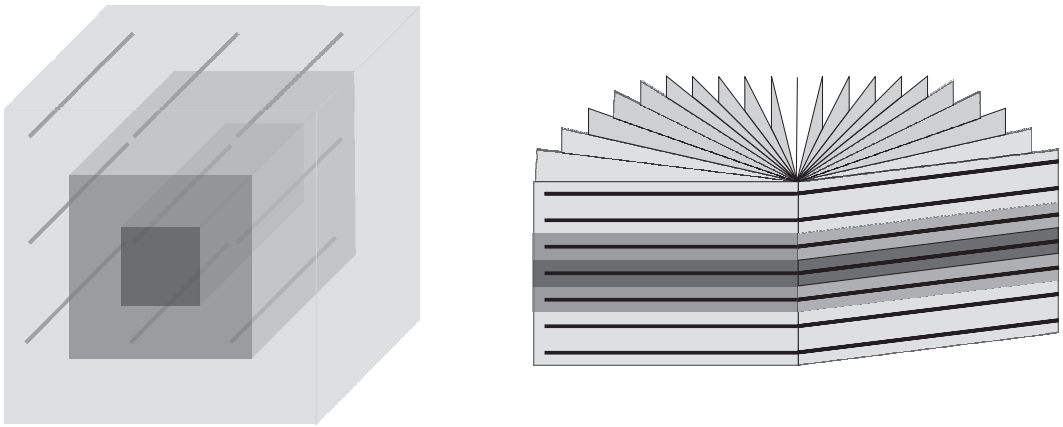

Figure 7.3 Combining TRICKS type view sharing with SENSE type parallel imaging (a) and projection reconstruction (b) to achieve higher temporal resolution. The same colour band as in Fig. 7.2 is used for different k-space sections. In (a), 2D SENSE reconstruction is made by using incomplete composite k-space data sets in which the phase encoding lines are acquired with different frequencies according the region they reside. Similarly, composite sets of radial lines as shown in (b) are formed by radial lines acquired at different frequencies and used for time resolved projection reconstructions.

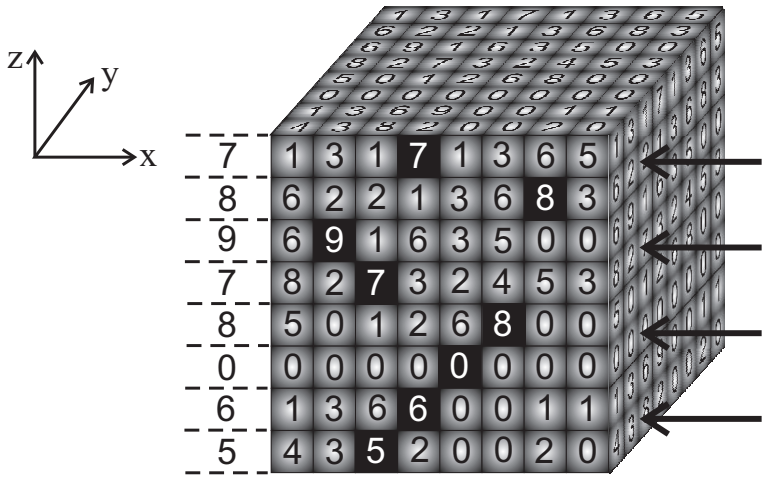

Figure 7.4 Maximum intensity projection of a 3D volume. In the diagram, projection along the x direction of a coronal plane is illustrated, where the highest intensity value in the x direction is shown on the left. Projection of the entire 3D volume results in a 2D sagittal plane MIP. In principle, projection ray can be made along any axis.

7.3 Implementation of GUISE and PBCS in CE MRA

Both high temporal frame rate and narrow footprint are desirable in SW reconstructions. The high temporal frame rate requires the ability to update a small portion of the k-space data set for the next image reconstruction, whereas the narrow footprint requires high image reconstruction acceleration factors. Existing SW methods on Cartesian grids [VBD+93, TKC+96, DCR+02] have limitations in both temporal frame rate and temporal footprint. TRICKS [TKC+96] and its variation [DCR+02] as introduced above require the entire k-space central region to be updated in each time frame, which limits the maximum temporal frame rate achievable. The limited improvement of temporal footprint is gained by sacrificing of the high spatial frequencies, which may lead to ringing artifacts.

In this section, two new Cartesian sampling SW methods that are based on the generalized unailasing using support and sensitivity encoding (GUISE) and prior estimate based compressed sensing (PBCS) reconstructions are presented. FE lines on Cartesian grids are sequentially acquired and then combined to allow SW reconstruction with high temporal frame rate to be made. The sparsity of the contrast enhanced angiograms and image prior information are exploited in reconstructions to allow a high acceleration factor to be achieved.

A fundamental trade-off in image construction is between the acceleration factor and the level of reconstruction artifacts. In the existing methods, the acceleration factor (or the temporal footprint) is determined prior to the actual scan, i.e., prospectively. However, in practice due to the varying contrast dynamics from patient to patient, the preset acceleration factor often does not reflect the optimal trade-off between the temporal footprint and the reconstruction artifacts. In the new methods, the acceleration factor can be selected retrospectively based on an estimation of the contrast flow dynamics. A more optimum trade-off can thereby be achieved. Also the retrospective reconstruction allows a reconstruction at a low temporal resolution to be first made, which can provide image prior information for reconstructing images at higher temporal resolution.

7.3.1 GUISE method

Recall that a key feature in GUISE is that the partial k-space data set used for image reconstruction corresponds to a periodic sampling pattern to achieve the computational efficiency. Fig. 7.5 illustrates its application in CE-MRA. The Cartesian 3D k-space volume is divided into equally sized regions, each of which contains the same number of FE lines to be acquired. After the initialization of the scan, samples within each block are acquired sequentially in a predefined order (Fig. 7.5). In this manner, the 3D k-space volume is essentially decomposed into a series of subsets each of which consists of FE lines at the same

position in all the repeating blocks. The number of subsets is equal to the number of elements of the repeating block. After the complete acquisition of the k-space, the same data acquisition is repeated to make multiple acquisitions of the k-space until the time interval of interest is sufficiently covered.

The sequentially acquired data set contains the temporal contrast level variation over the time interval. After reassembling the k-space subsets in the order in which they were acquired on the time axis (see Fig. 7.5), SW reconstructions can be made using the consecutively acquired samples to reveal the temporal information. Different lengths of the temporal window reflect the trade-off between the temporal footprint and the reconstruction SNR (Fig. 7.5). Mathematically, image reconstructions in GUISE are made by performing direct inversion of the encoding matrix $\mathbf{E}[\rho]$:

$$\tilde{\mathbf{f}} \;=\; \mathbf{E}[\rho]\,\mathbf{f}[\rho]\;,\;\; \mathbf{E} \;=\; \begin{bmatrix} \mathbf{W}^{-1}\,\mathrm{diag}(\mathbf{h})\,\mathbf{W}\,\mathrm{diag}(\mathbf{c}_1) \\ \mathbf{W}^{-1}\,\mathrm{diag}(\mathbf{h})\,\mathbf{W}\,\mathrm{diag}(\mathbf{c}_2) \\ \cdots \\ \mathbf{W}^{-1}\,\mathrm{diag}(\mathbf{h})\,\mathbf{W}\,\mathrm{diag}(\mathbf{c}_M) \end{bmatrix},\;\; \tilde{\mathbf{f}} \;=\; \begin{bmatrix} \tilde{\mathbf{f}}_1 \\ \tilde{\mathbf{f}}_2 \\ \cdots \\ \tilde{\mathbf{f}}_M \end{bmatrix}, \tag{7.1}$$

where $\tilde{\mathbf{f}}$ and $\mathbf{f}$ are the aliased image due to under-sampling and the underlying image, $[\rho]$ denotes the ROS region as discussed in Section 5.3, and $\mathbf{h}$ is the binary sampling mask that represents the positions of the samples used for image reconstruction. Since each k-space subset corresponds to a periodic sampling pattern, the combination of multiple subsets also form a periodic sampling mask $\mathbf{h}$, which allows computational efficiency to be achieved in the reconstruction.

Elimination of the stationary background

Recall that the use of an object region of support (ROS) allows the image elements that are known to contain zero signals to be eliminated from the image reconstruction and hence leads to improved reconstruction SNR as well as a higher acceleration factors as discussed in Section 5.3. In CE-MRA, the acquired k-space data set contains signal from both the blood vessels containing contrast as well as the anatomical background. In practice, radiologists usually tend to fit a tight FOV frame around the imaged region to minimize the necessary data acquisition (occasionally, wrapping around artifacts are tolerated if it is known that the vascular regions are not affected). As a result, the inherent ROS of the anatomy occupies a large portion of the FOV. However, it is usually only the blood vessels that contain dynamic contrast change over time that are of interest, and hence it is sufficient to only reconstruct those vessels. The ROS can be reduced to include only the vessels containing contrast change over time by suppressing the anatomical background background as illustrated by an example in Fig. 7.6. On the left, the axial plane slice shows the anatomy

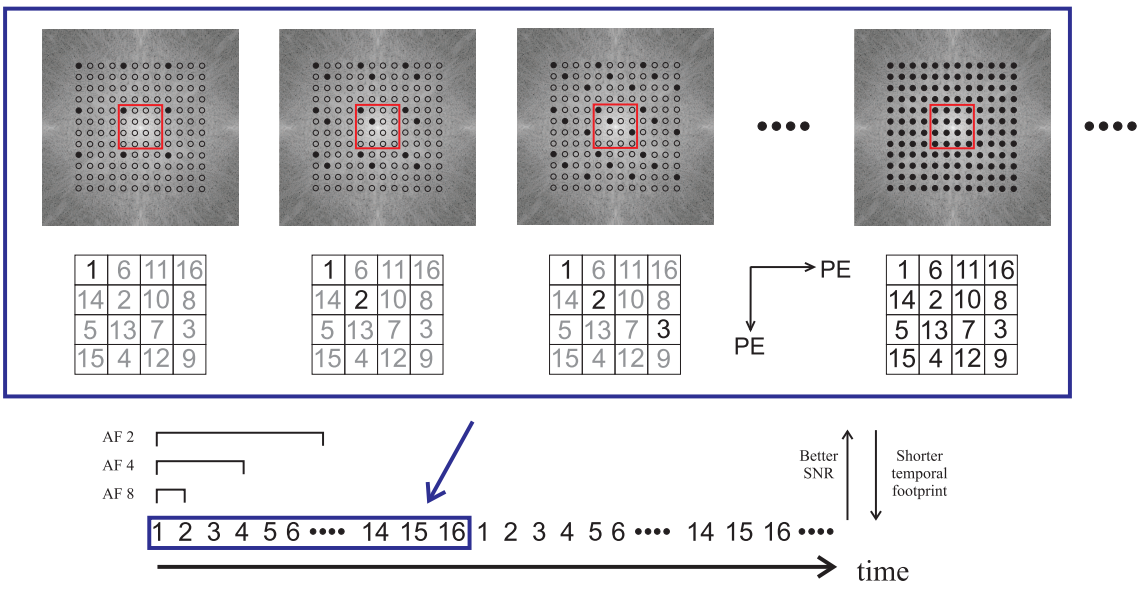

Figure 7.5 Diagram illustrating the data acquisition scheme in the proposed SW method based on GUISE. A repeating block size of 4×4 gives 16 k-space subsets that are to be acquired sequentially in a pre-defined order. The filled and empty dots represent the acquired and not yet acquired FE lines respectively. The same acquisition order is repeated to acquire multiple instances of the k-space data. In the post-processing, SW reconstructions can be made using the consecutively acquired k-space subsets with the freedom of choosing the temporal window length. In this example, using 2, 4 and 8 k-space subsets (out of 16) correspond to improvement factors of the temporal footprint of 8, 4 and 2 respectively. As the acceleration factor goes up, the reconstructions feature a deteriorating SNR.

of the knee region, with the presence of contrast seen as the bright regions, which occupies almost the entire FOV. Then an image of the same region, without the presence of contrast, is subtracted from the previous image as shown in the middle column. In the subtraction result, the anatomical background is completely eliminated, leaving an image only containing the contrast and hence features a much smaller ROS. In general, a k-space data set that is acquired without the presence of the contrast is subtracted from the k-space data set acquired with the contrast present. This way the stationary background is eliminated. Background elimination has been employed for some years in MR digital subtraction angiography (DSA) [KFGM96, FGK96] to improve the resulting image contrast. In this case, as the vascular region usually only take a very tiny portion of the FOV, the background subtraction results in significant reduction of the ROS and hence improvement of the reconstruction SNR as well as the potential to increase the acceleration factor.

Estimation of the vascular support

In considering conventional MR imaging, it was discussed that a loose object region of support can be obtained from a low resolution pre-scan. In case of CE MRA, the ROS

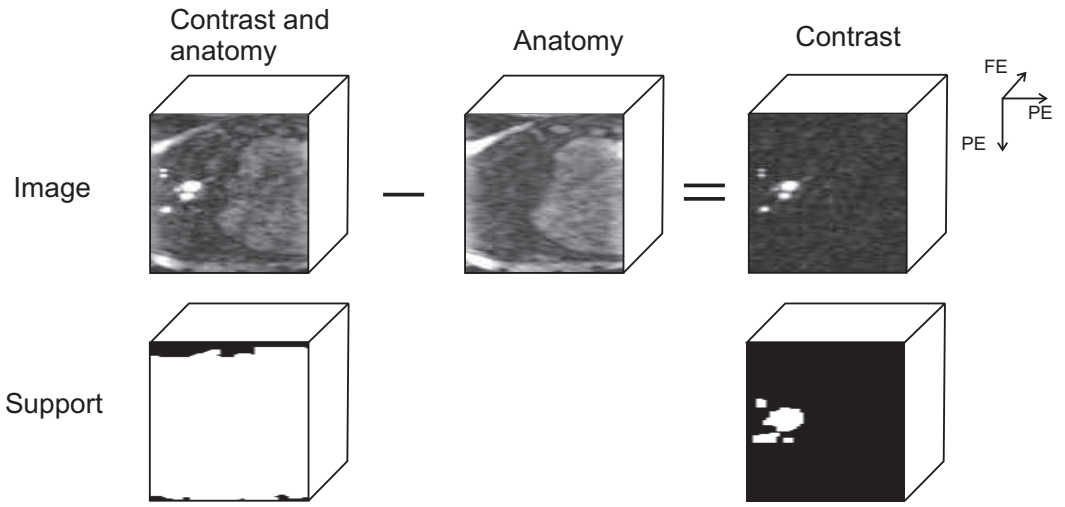

Figure 7.6 Reduction of the ROS in angiogram by background subtraction. The directly acquired k-space data contains signal from both the contrast and the anatomy (image on the left, shown in the axial plane that is consists of two FE directions), and hence has a large ROS. Subtracting a data set contains no contrast signal (image in the middle, usually acquired prior to the contrast arrival) gives a subtracted data set containing only contrast (on the right), which has a much smaller ROS defined only by the vascular regions.

of the blood vessels is difficult to estimate without the presence of contrast [3] and hence cannot be estimated prior to the actual scan. Rather, the ROS of the blood vessels can be estimated in the post-processing using the multiple k-space acquisitions made with the presence of contrast. Elimination of the anatomical background results in fully sampled k-space containing only the contrast, and Fourier transform produces contrast-only images. Hence a support mask of the vascular regions can be obtained by separating the contrast region from the free air region.

Due to the different contrast arrival time in various vascular regions, the ROS of vascular regions containing contrast are time dependent. As a result, the choice of the composite k-space data set determines the definition of the ROS of the vascular regions. For instance, a composite k-space that only contains contrast agent within the arteries will have a considerably smaller ROS compared to that of a mixed phase (arterial and venous). Two types of k-space composite data are considered for obtaining the vascular ROS. Firstly, a static composite is formed by combining all the k-space repetitions that contain contrast, which will include both the arterial and venous regions that contained contrast over the imaging time interval. Alternatively, a sliding composite can be formed by using a complete k-space data set that is determined by the current position of the sliding window on the time axis (Fig. 7.7). In the sliding composite case, the region of support (ROS) of contrast region is determined by the contrast status within the specific time interval. Similar forms

[3]The use of a time of flight image may be possible, but that method only works well in regions with rapid blood flow.

of composite data set were also considered in the use of HYPR [JCH+09].

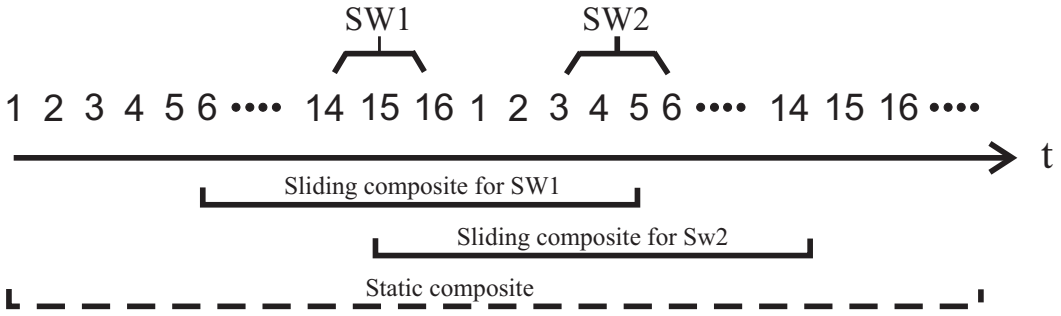

Figure 7.7 Illustration of static and sliding composite for obtaining the vascular ROS, the same k-space acquisition pattern as in Fig. 7.5 is used. The static composite is formed by combining all the k-space subsets that contain vascular contrast. The sliding composites are formed by taking only one complete k-space acquisition that covers the current sliding window using which an image reconstruction is to be made as well as the preceding and following subsets as illustrated for the case for SW1 and SW2. The use of sliding composite allows tighter vascular ROS to be obtained.

Due to the complicated vascular structures (particularly the veins), ROS estimation by direct thresholding of a 3D image volume has a risk of under-estimating the true vascular region. A new method that is based on maximum intensity projection (MIP) images has been developed (Fig. 7.8). Firstly, anatomical background-free MIP images are formed for three orthogonal planes: coronal, axial and sagittal, displayed as three columns in Fig. 7.8. The high contrast to noise ratio allows a loose support mask to be straightforwardly obtained for each of the MIP image by thresholding and morphological operations [WBMW08b]. Then for each support mask of the MIP, a 3D support mask of the same size as the 3D image volume is obtained by back-projecting the 2D mask along the 3rd direction. For instance, for a 3D image of size $256 \times 128 \times 32$, the support mask of the axial plane MIP (128×32) is replicated along the superior-inferior (SI) direction 256 times to give a support volume of $256 \times 128 \times 32$. Then the intersection of the three volume masks is taken as an estimate of the actual support mask as shown in Fig. 7.8. This method has a similar nature to the back projection reconstruction method commonly used in computed tomography (CT), in which a series of back projections of a 3D volume are made for image estimation. A drawback of this method is the potential redundancy in the estimated support region, i.e. regions outside the vessels might also be included in the mask due to the insufficient number of projection made (as illustrated in Fig. 7.9). On the other hand, this method has a higher level of safety in ensuring a voxel that is within the vascular region is included in the support mask comparing to direct thresholding. Such redundancy can be reduced by applying a tighter support for each MIP image and/or using a larger number of back-projections based on the MIP images formed at different angles.

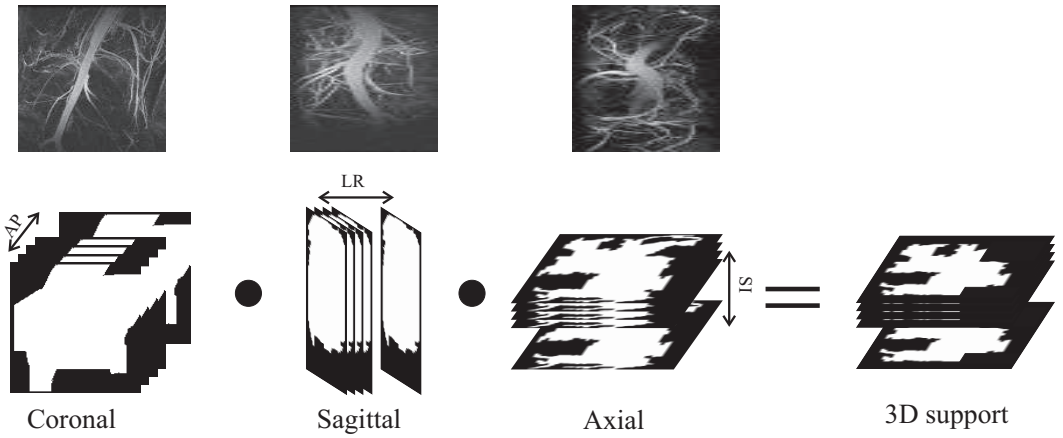

Figure 7.8 3D support mask estimation based on MIP images at orthogonal planes (coronal, axial and sagittal). A loose support mask is first obtained for each of the three MIP image. The resulting masks are then back projected along the anterior-posterior(AP), left-right(LR) and superior-interior(SI) direction respectively to form 3D masks. The intersection of the resulting 3D masks is taken as the support. The results are shown on the right with respect to the axial plane in which reconstructions were computed, slice-by-slice.

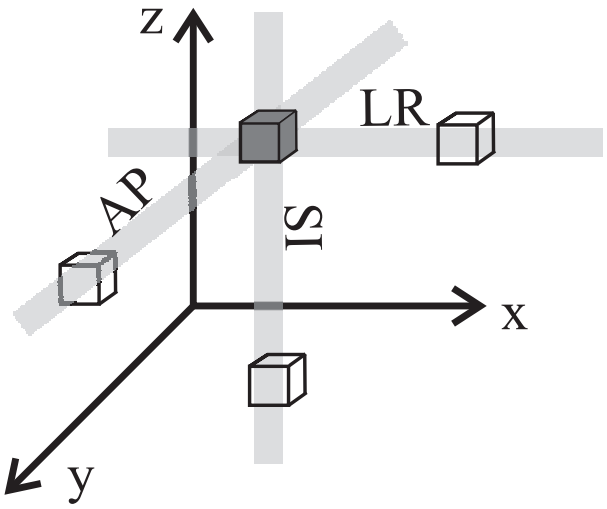

Figure 7.9 Estimation of vascular ROS using the proposed method may contains redundancy. In the diagram, the three voxels that are respectively within the ROS of the MIP image in the coronal, axial and sagittal plane each lead to a ray along the anterior-posterior(AP), left-right(LR) and superior-interior(SI) direction in the back projection. The intersection of the three rays as shown in gray represents a voxel that is mistakenly considered to be within the vascular ROS and hence causes redundancy in the resulting estimation. Reduction of the redundancy could be achieved by taking more back projections at different angles.

Overall GUISE method

The flow chart in Fig. 7.10 summarizes the application of the GUISE method in reconstructing a single slice: Firstly a composite image is formed by using all the k-space acquisitions; then a ROS mask is obtained from the composite image, which is then applied in reconstructing individual time frames using a sub-group of the k-space data acquisition. It is seen that a composite image has different temporal information than the reconstructed image time frame.

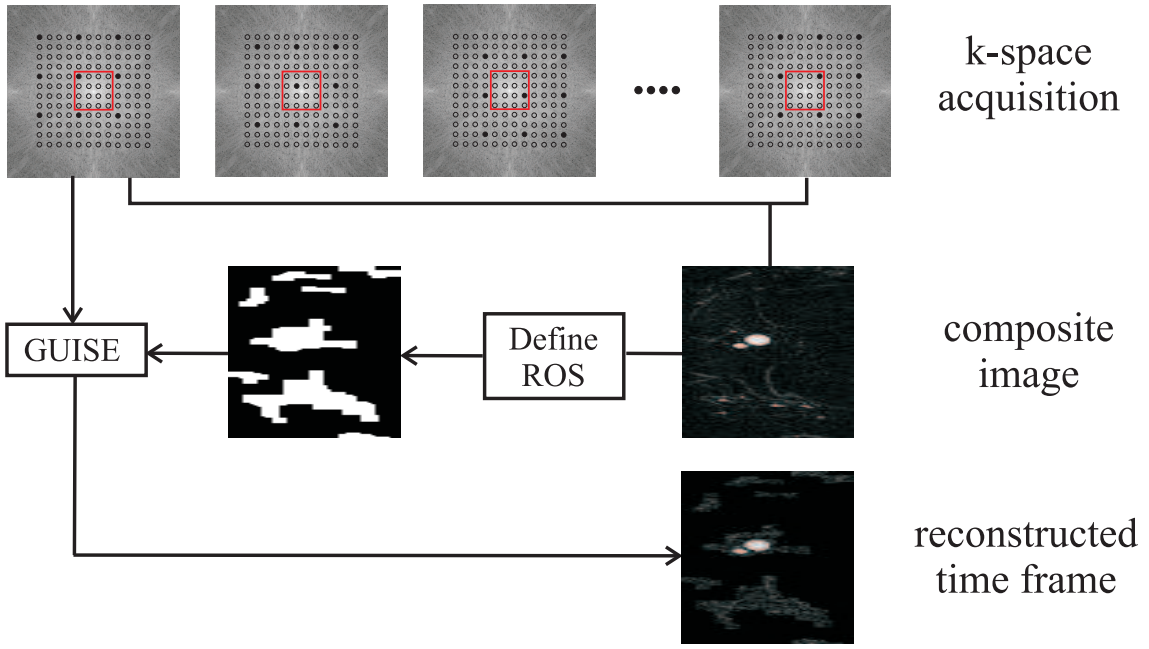

Figure 7.10 Flow chart summarizing the overall GUISE method (presuming that the anatomical background has been eliminated via a subtraction). The top row represents the k-space subsets that are acquired sequentially over time in a periodic fashion. Combining all these subsets gives a full k-space data set that corresponds to a composite image containing the contrast variation over the entire data acquisition time inverval, from which a ROS of the blood vessels can be obtained. Then the ROS obtained can be applied in reconstructing images using subsets of k-space data.

Sequential acquisition order for GUISE method

The data acquisition order determines which subsets of k-space are to be consecutively acquired and used for image reconstruction; in turn it determines the sampling mask that has a large influence on the conditioning of the matrix inversions. Given the periodic nature of the k-space subsets, the data acquisition can be determined by first choosing the the size of the repeating block and then deciding the sequential order in which the elements within the block are to be acquired.

Repeating block size

The size of the repeating block determines which elements are to be aliased together and affects the conditioning of the matrix inversion as discussed in Section 5.5.1. In this case, it also determines temporal frame rate achievable in SW reconstruction. As a single k-space subset is the smallest possible temporal window shift, it is the upper limit of the achievable temporal frame rate. For instance, with a block size of 4×4, shifting the temporal window by one k-space subset allows a temporal frame rate improvement factor of 16, where a block size of 16×16 potentially allows a temporal frame rate improvement factor of 256.

Acquisition order of sample elements within the repeated blocks

A difficulty arises in designing the actual acquisition order of sample elements within the repeated blocks to precondition the matrix inversions at reconstruction. In contrast to conventional MR imaging, where a specific sampling mask at a fixed acceleration factor is to be used, in CE MRA both the sampling mask (the position of the temporal window) and the acceleration factor (the length of the temporal window) are subject to change in the reconstruction. Hence it is infeasible to design an 'optimal' data acquisition order to cover all the possible temporal windows. The sequential forward selection (SFS) method as discussed in Section 5.5.2 is a nice fit in this scenario: rather than designing a sampling mask at a fixed acceleration factor, samples are sequentially picked to progressively minimize the overall cost function; together with the previously acquired samples each newly acquired sample forms a sub-optimal sample set for image reconstruction. In this way, SFS achieves sub-optimal sampling patterns for all the image reconstructions using the consecutively acquired samples. It is hence proposed to use the order in which samples are selected in the SFS method as the the sequential acquisition order for the samples. In addition, SFS is computationally cheap which is important for application in practice.

7.3.2 PBCS method

PBCS formulation in CE MRA

With reference to Section 6.2.3, CS image recovery in CE MRA can be formulated as:

$$\check{\mathbf{f}} = \arg\min_{\mathbf{f}} \ (\|\mathbf{F} - \mathrm{E}\mathbf{f}\|_2 + \alpha\|\mathbf{f}\|_1 + \beta TV(\mathbf{f})),$$

$$\mathbf{E} = \begin{bmatrix} \mathrm{diag}(\mathbf{h})\,\mathbf{W}\,\mathrm{diag}(\mathbf{c}_1) \\ \mathrm{diag}(\mathbf{h})\,\mathbf{W}\,\mathrm{diag}(\mathbf{c}_2) \\ \cdots \\ \mathrm{diag}(\mathbf{h})\,\mathbf{W}\,\mathrm{diag}(\mathbf{c}_M) \end{bmatrix}, \quad \mathbf{F} = \begin{bmatrix} \mathrm{diag}(\mathbf{h})\,\mathbf{F}_1 \\ \mathrm{diag}(\mathbf{h})\,\mathbf{F}_2 \\ \cdots \\ \mathrm{diag}(\mathbf{h})\,\mathbf{F}_M \end{bmatrix}, \tag{7.2}$$

where $\mathbf{f}$ and $\mathbf{F}$ are the underlying image and the partial k-space acquisition respectively; $\mathbf{h}$ is the mask that represents the positions of the FE lines used for image reconstruction in a specific temporal window, and $\mathbf{E}$ is the corresponding pMRI encoding matrix. Recall that CS recovery relies on the sparsity of the underlying image to be recovered. In conventional MR imaging, an additional sparsifying transform is usually required to achieve high level of sparsity. In CE MRA, due to the tiny portion of the vascular region within the FOV, sparisity in the angiogram can be achieved by eliminating the anatomical background by the k-space subtraction technique described previously. Hence in Eq. (7.2) above, the data set $\mathbf{F}$ is a subtracted k-space set, where the underlying image $\mathbf{f}$ is an image free of anatomical background. Due to the high level of sparsity and uniformity in the angiogram to be recovered, the total variation (TV) is useful in suppressing the background noise.

As the success of CS recovery above is fundamentally determined by the sparsity of the contrast enhanced image $\mathbf{f}$ [LDP07]; in PBCS, the elements of the underlying image $\mathbf{f}$ are rearranged based on the knowledge of a prior image estimate $\mathbf{f}'$, so that the sorted image $\mathbf{g}$ possesses higher level of sparsity for a given transform. PBCS reconstruction can be written as:

$$\hat{\mathbf{g}} = \arg\min_{\mathbf{g}} \ (\|\mathbf{F} - \mathbf{E}_R\,\mathbf{g}\|_2 + \alpha\|\Phi\mathbf{g}\|_1 + \beta TV(\mathbf{f})), \quad \hat{\mathbf{g}} \xrightarrow{R^{-1}} \hat{\mathbf{f}} \tag{7.3}$$

where $\hat{\mathbf{g}}$ is the estimate of the sorted image and $\hat{\mathbf{f}}$ is the final reconstructed image after unsorting; $\mathbf{E}_R$ denotes the column-changed encoding matrix according to sorting order R, which is obtained by sorting the image elements a reference image.

In time resolved CE MRA, the multiple acquisitions of the k-space data over the period that contrast agent is present allow a composite image to be straightforwardly formed that serves as a reference image in reconstructing individual image time frames. In contrast to PBCS in conventional MR imaging, in which the image prior estimate usually contain incomplete spatial domain information (lower spatial resolution, noise corruption, etc.), the prior estimate in this case contains full spatial resolution but incomplete temporal information. For instance, a composite image that contains both arterial and venous contrast phase offers insufficient temporal information for reconstructing a pure arterial phase image.

Data acquisition order in PBCS

PBCS has the same data sampling requirements as conventional compressed sensing (CS). As discussed in Section 6.2, the two requirements for a sampling pattern to achieve a successful CS reconstruction are achieving incoherent aliasing artifacts and using a non-uniform sampling density function that has more samples in the k-space central high energy level region. As discussed in the previous section in the case of GUISE, the data

acquisition order determines which samples will be consecutively acquired and hence determines the sampling patterns faced by individual sliding window reconstructions; and it is infeasible to explicitly design a sequential order taking considerations of all the possible sliding window reconstructions.

Instead, an acquisition design order is made as follows: firstly a sampling pattern mask (with a non-uniform sampling density function) is created at a given acceleration factor, then the acquisition order of the individual samples is decided by randomly picking the samples with an uniform weighting function (each sample has the same chance to be selected) until all the samples are picked. In this way, the sampling mask corresponding to the entire sample ensemble has the desired characteristic for CS recovery. The sampling masks corresponding to the sub-sets of the sample ensemble also have the desired characteristic with high probability: an incoherent PSF as the consecutively acquired samples are non-regularly positioned and a non-uniform sample density function as the sample ensemble from which the samples are randomly picked features a non-uniform density function.

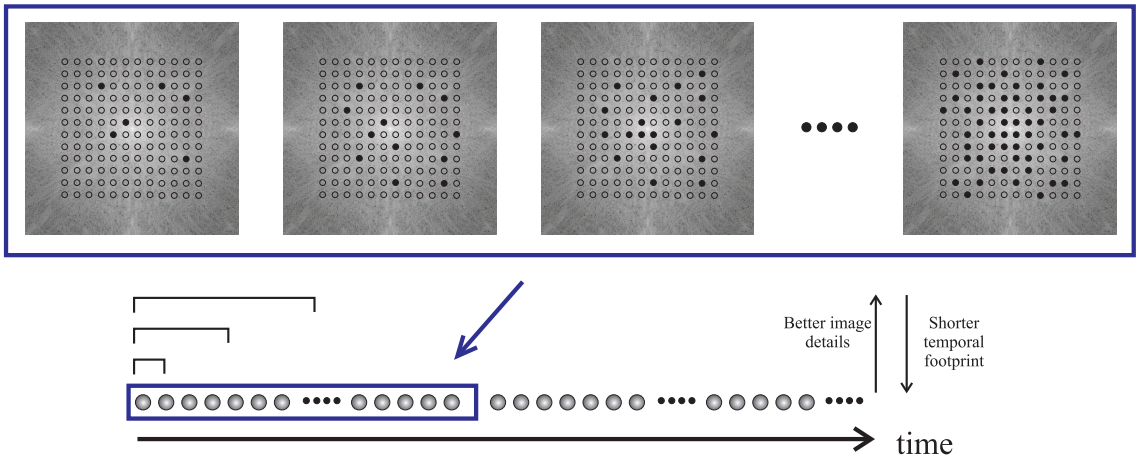

Figure 7.11 Diagram illustrating the data acquisition scheme for PBCS method. A sampling mask that features incoherent aliasing artifacts and a non-uniform density function is first formed (shown as the rightmost diagram on the top). Then the acquisition of the individual samples defined by the mask are made in a random order until all the samples defined by the mask are acquired. Image reconstructions can be made using consecutively acquired samples at different acceleration factors.

Overall PBCS reconstruction

The overall procedure of PBCS reconstruction is illustrated in Fig. 7.12. Firstly, sequentially acquired k-space samples are combined to form a composite data set, which gives an image corresponding to the entire data acquisition time period. This composite image is then sorted to form a 2D monotonical function (which has a sparse representation using a 2D DCT or wavelet transform) with a sorting order R. Then this sorting order R is used in reconstructing individual time frames using k-space subsets. In this case the prior estimate

is an image with low temporal resolution, and the discrepancies between the prior estimate and the underlying image is the different temporal information contained in the composite data set and that contained in the data subsets. The composite image (the prior estimate) contains information of the vascular regions over the entire time interval, whereas the data subsets used in individual reconstructions distinguish the presence of contrast for a specific time interval. The individual reconstructions can be formulated as PBCS:

$$\hat{\mathbf{g}} = \arg\min_{\mathbf{g}} \ (\|\mathbf{F} - \mathrm{diag}(\mathbf{h})\,\mathbf{W}_R\,\mathbf{g}\|_2 + \alpha\|\Phi\mathbf{g}\|_1), \quad \hat{\mathbf{g}} \xrightarrow{R^{-1}} \hat{\mathbf{f}} \tag{7.4}$$

where $\mathbf{g}$ is the composite image that provides the sorting order for recovering the underlying image $\mathbf{f}$.

As in the case of GUISE, two types of composite data sets can to be used to form a reference image: a static composite and a sliding composite. They are defined in the same way as in Fig. 7.7: either a static composite that is formed using all the k-space acquisitions or a sliding composite that is formed only using the k-space acquisition (one complete acquisition of all the samples defined by the sampling mask) that contains the data subset used in image reconstruction can be used. A reference image can then be obtained from the composite data either by inversely Fourier transforming the zero-filled k-space data or it can be obtained from a normal CS reconstruction procedure. The former often suffices as the artifacts of under-sampling have a low-level random noise appearance (such as shown in the example used in Fig. 7.12).

7.4 Experimental verification

A phantom study and a human volunteer study were carried out to investigate the performance of the proposed methods. The phantom study was carried out as an initial feasibility study to investigate the proposed retrospective reconstructions. Subsequently, on the confirmation of the phantom study outcome, experiments using human subjects were carried out. Both experiments were carried out using a 1.5T GE scanner equipped with an 8-channel receiver channel coil, in which the individual receiver channels are symmetrically placed around the cylindrical coil. A T1-weighted 3D spoiled gradient recalled (SPGR) sequence was used, and the two PE directions were set to left-right (LR) and anterior-posterior (AP). The data acquisition order in the SPGR sequence was altered to achieve the desired sequential data acquisition order in each case.

7.4.1 Phantom feasibility study

A simple phantom to represent blood flow in an artery was used for the study (Fig. 7.13). It was constructed entirely from plastic making it safe for use in an MR environment. The

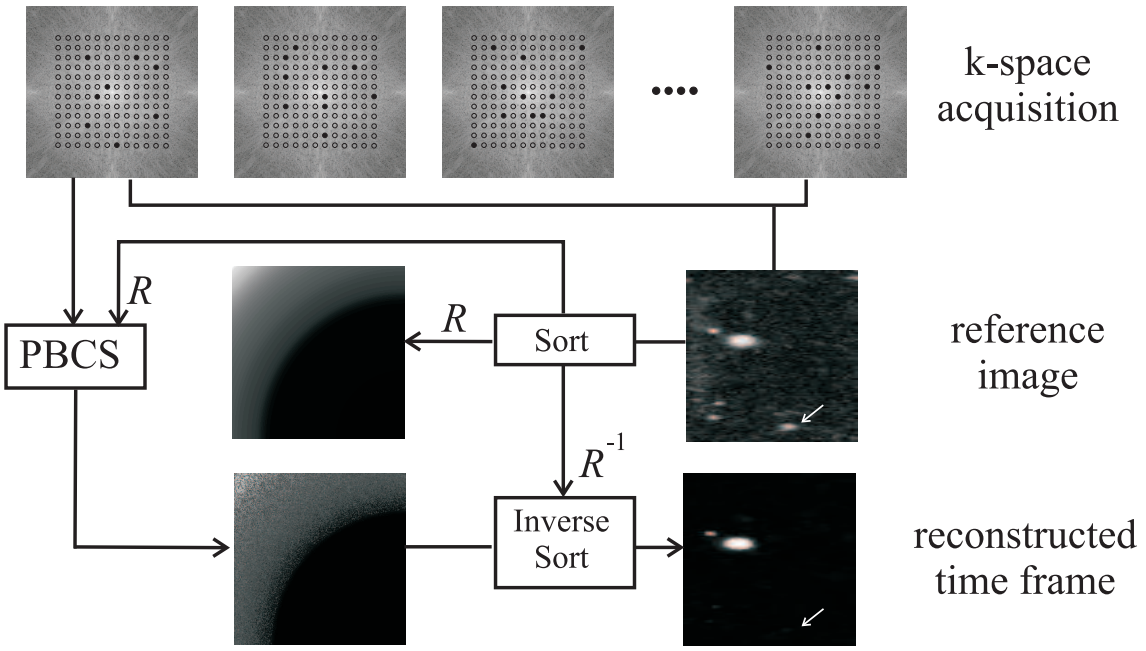

Figure 7.12 Flow chart summarizing the overall PBCS method (presuming the anatomical background has been eliminated via a subtraction). The FE lines within the designed sampling mask are sequentially acquired. Combining all the samples allows a reference image to be formed either by inverse Fourier transform or a CS reconstruction (in this case an inverse Fourier transform is used). A sorting order R is then obtained by sorting this composite image to achieve a monotonical curve that has a sparse representation under 2D DCT/wavelet transform. This sorting order R is then used in the PBCS to reconstruct images using subsets of the k-space, giving a reconstruction in a sorted form. The reconstruction is then subjected to an inverse sorting operation that restores the reconstructed time frame. The arrowed region indicates the different temporal contrast information contained in the composite image and the reconstructed time frame.

imaged object was a 1.5 L water-filled plastic bottle containing an internal loop and an external loop of clear plastic tube as shown. Three different tube thicknesses were joined to form the internal loop with internal diameters of 4 mm, 6 mm and 8 mm; the external loop was formed by wrapping the plastic bottle with the tube with a internal diameter of 4 mm and connecting it to the internal loop. A 4 L plastic container provided an approximately constant flow of water under the action of gravity through the tube inside the plastic bottle and into a second container placed on the floor of the scanner room. The flow rate was controlled using tap A. By operating taps B and C, copper sulfate ($CuSO_4$) solution could either be drawn into the syringe from a flask or injected into the flow of water. The addition of $CuSO_4$ to water greatly decreases its $T1$ and $T2$ relaxation times. The injection of the solution therefore simulated the introduction of contrast agent into the blood flow.

One GUISE-type acquisition and two PBCS-type acquisitions were made in the phantom study. In the GUISE-type acquisition, a repeating block size of 8×8 was used, and the order in which the samples were acquired was determined using sequential forward selection (SFS) as described in Section 7.3.1. In the first type of PBCS acquisition, all the FE lines

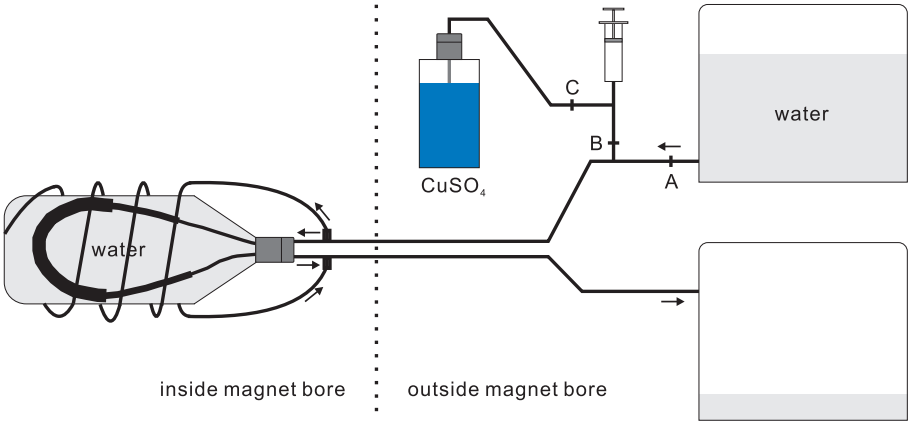

Figure 7.13 The custom-made phantom used for this experiment. Water flowed from the top tank through the phantom and into the bottom tank. The direction of the flow in the internal and external plastic loop is shown. The flow rate is controlled using tap A. Contrast agent (copper sulfate solution) was introduced into the stream of fluid using the syringe and taps B and C.

were sequentially acquired in a predetermined order to give complete k-space data sets; in the second PBCS acquisition, only FE lines that were defined by a sampling mask (at an acceleration factor of 8) were acquired in a predetermined order to give multiple instances of partial k-space data sets. The sampling mask was designed to have an inconsistent PSF and a variable PDF with more samples acquired at the k-space center. The pseudo-random acquisition order in each case is determined as described in Section 7.3.2. In each of the three acquisitions, a complete data set was first taken with water flow only for obtaining the coil sensitivity map, as well as to allow k-space subtraction to be performed to eliminate the background signal.

7.4.2 Volunteer study

Volunteer studies were carried out in imaging the knee region of two healthy adult volunteers. Ethical approval was obtained from the Upper South A Regional Ethics Committee (Ministry of Health, NZ) to make a single injection of gadolinium contrast into a number of healthy adult male volunteers. All volunteers were required to sign a consent form prior to the scan. Since a non-uniform sampling density is necessary for successful CS recoveries, PBCS data acquisition is constrained to a sampling mask that has a non-uniform sampling density.

The following scan parameters were used in the GUISE type acquisition: TR = 5.4 ms, TE = 1.6 ms, flip angle = 45°. A matrix size of $196 \times 128 \times 48$ was used to obtain a spatial resolution of $0.9 \times 0.9 \times 1$ mm. 20 ml of Gd-BOPTA (Multihance®) was injected as a bolus. A repeating block size of 16×16 was used and the acquisition order was determined using sequential forward selection. A complete acquisition of the 3D k-space volume took 30 s, and 5 repetitions were made.

The following scan parameters were used in the PBCS type acquisition: TR = 4.8 ms, TE = 1.8 ms, flip angle = 45°. A matrix size of $196 \times 128 \times 48$ was used to obtain a spatial resolution of $1 \times 1 \times 1$ mm. 20 ml of Gd-BOPTA (Multihance®) was injected as a bolus. Sample acquisitions were constrained to those defined by a sampling mask at acceleration factor of 4, and 20 instances of the partial k-space data sets were obtained to cover the same time period as the GUISE acquisition.

In both cases, a data acquisition without the presence of contrast is made; that data was used for estimating the coil sensitivity profile and subtracted from the following repetitions to eliminate the stationary background.

7.5 Results

7.5.1 Phantom feasibility study

Retrospective reconstructions in the phantom studies demonstrate the trade-off between the temporal footprint and the reconstruction artifacts. To demonstrate such trade-off, reconstructed coronal plane MIP images are organized in breakdown charts showing the temporal footprint doubled at each step down in the chart. For instance, the time interval covered by a single reconstruction at an acceleration factor of 2 is equivalently covered by two consecutive reconstructions at an acceleration factor of 4, at a doubled temporal footprint. Only the region occupied by the bottle phantom within the FOV is shown for illustration clarity.

GUISE acquisition

The outcome of the phantom study using GUISE type acquisition is summarized in the breakdown chart in Fig. 7.14, the temporal footprint of the reconstructions at each level is shown on the bottom right corner. Firstly, improving the temporal footprint better reveals the dynamic flow of the $CuSO_4$ solution, such as the contrast filling in the arrowed region in Fig. 7.14. The other benefit of improving the temporal footprint is the reduction of motion artifacts. It is seen that reconstruction at the acceleration factor 2 (Fig. 7.14.(a)) contains a considerable level of regular ghosting artifacts due to the change of $CuSO_4$ concentration within the time interval covered (about 15 s). In comparison, reconstructions at the acceleration factor 4 (Fig. 7.14.(b) and (c)) contain a lower level of ghosting artifacts due to the reduced level of motion within the shorter time interval 7.5 s. Especially the second reconstruction (Fig. 7.14.(c)) where the flow is almost steady, the ghosting artifacts are hardly visible.

The drawback of increasing the temporal footprint in GUISE reconstruction is the loss of

SNR. It is seen that although image reconstructions at acceleration factor of 8 reveal the dynamic flow of the contrast at an even finer time step (as arrowed) there is a noticeable drop of SNR in the reconstruction. Also the ill-conditioned matrix inversions led to residual aliasing artifacts in the reconstruction results.

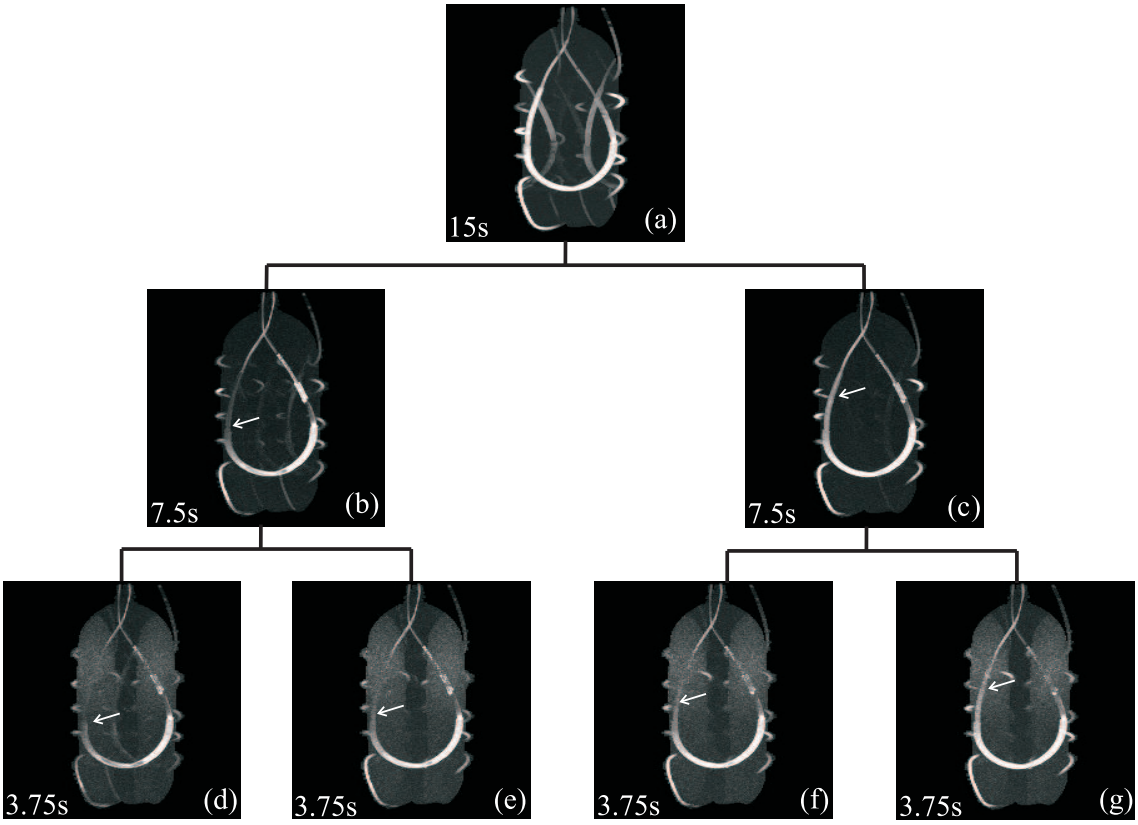

Figure 7.14 Reconstructed coronal plane MIP images from phantom study with GUISE type acquisitions at acceleration factors of 2(a), 4(b,c) and 8(d-g). The contrast solution flow within the plastic tube is imaged. The breakdown chart shows that reconstructions at lower temporal footprint are decomposed into two consecutive reconstructions at doubled temporal footprint. The arrows indicate regions where the concentration of the contrast change over time.

PBCS acquisition

The outcome of phantom study using the two PBCS type acquisitions are summarized in Fig. 7.15 (no prior image estimate is incorporated in the image reconstructions, hence conventional CS reconstructions were performed). The reconstructions from the first PBCS acquisition (with a uniform sampling density) is displayed in a breakdown chart that is same as that used in Fig. 7.14; the reconstructions from the second CS acquisition (with a non-uniform sampling density mask at acceleration factor of 8) are displayed underneath the bottom level of the breakdown chart for comparison, as they feature the same temporal footprint.

Similar to the observations made in GUISE reconstructions, it is seen that improving the temporal footprint by reconstructing from less data reveals the contrast temporal variations at a finer step. For example, comparing the upper tube region as indicated by the arrow in reconstruction at acceleration factors of 2 and 4. It is seen that there is an obvious trade-off between the temporal footprint and the level of reconstruction artifacts. Reconstructions at acceleration factor 4 contain a considerably higher level of reconstruction artifacts compared to those at acceleration factor 2. At acceleration factor 8, some tube regions containing contrast in reconstructed MIP images are overwhelmed by the reconstruction artifacts making the reconstruction little use (as indicated by the arrows in Fig. 7.14.(d)-(g)).

The advantage of employing a non-uniform density sampling mask can be seen by comparing Fig. 7.15.(d-g) to Fig. 7.15.(h-k). In the latter case, only samples that are defined by the sampling mask (shown on the left top corner) are collected and used for reconstructions. This type of data acquisition strategy results in much more successful reconstructions in revealing the contrast information. At the acceleration factor of 8, some of the reconstructed tube regions are overwhelmed by reconstruction artifacts in Fig. 7.14.(d-g) (as indicated by the arrows) when an uniform sampling density was used; on the other hand, all the tube regions containing contrast were well recovered in Fig. 7.14.(h-k) where a non-uniform density sampling mask was used.

Different data acquisition strategies in GUISE and PBCS methods lead to different forms of motion artifacts. In the former case regular ghosting of the tube region (where the motion of contrast material takes place) is received due to the regular block-wise sampling pattern, whereas the motion artifacts in PBCS acquisitions have a rather noise-like appearance due to the randomized sampling strategy. The noise-like motion artifacts are usually much less visually distracting than the regular ghost motion artifacts.

7.5.2 Volunteer study

The outcomes of the volunteer study are organised in three parts. The first two parts demonstrate the utilities of the proposed methods: sliding window reconstruction and retrospective selection of acceleration factor, and no prior knowledge is incorporated in the image reconstructions. The third part investigates the uses of the image ROS in GUISE reconstruction and the prior image estimate in PBCS reconstruction. It is important to note that ethical considerations prevented repeat studies in any of the volunteers. As a result, difference observed between methods may be in part attributable to the difference in anatomy and circulatory dynamics between volunteers.

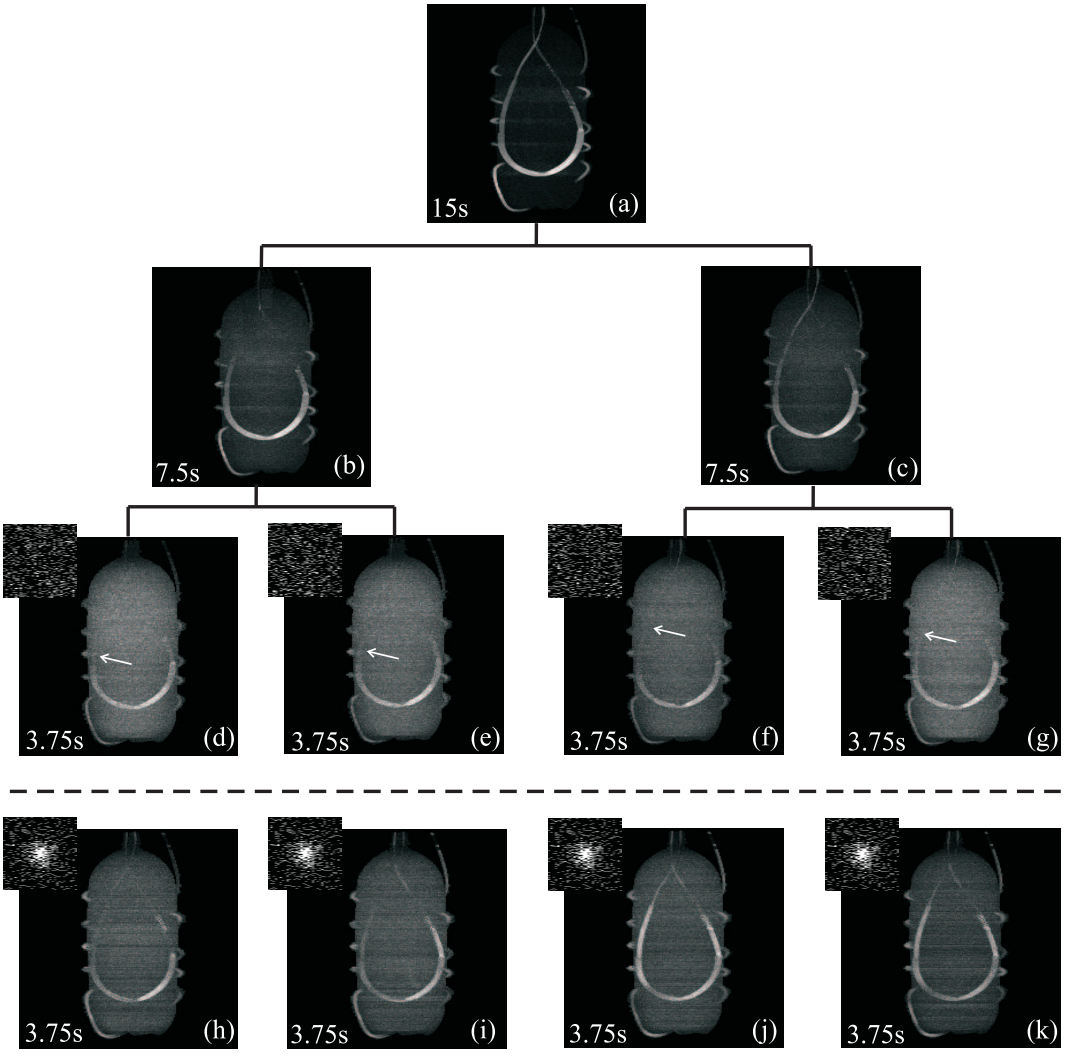

Figure 7.15 Reconstructed coronal plane MIP images from the phantom study with two PBCS type acquisitions at acceleration factors of 2(a), 4(b,c) and 8(d-k). The temporal footprint of each reconstruction is shown on the bottom left corner. The breakdown chart shows that reconstructions at lower temporal resolution are decomposed into two consecutive reconstructions at doubled temporal resolution. The reconstructions in (a-g) are made from an acquisition in which all the samples are sequentially acquired and hence allows reconstructions at various acceleration factors to be made; the reconstructions in (h-k) are made using samples acquired according to a fixed sampling mask at acceleration factor of 8 (compare the different sampling patterns used in each reconstruction as shown on the top left corner). The arrows indicate the contrast regions that failed to be recovered when an uniform sampling density is used.

Sliding window reconstruction

Sliding window (SW) reconstructions from the GUISE acquisition and PBCS acquisition are shown in Fig. 7.16. Reconstructions were made with a temporal footprint of 7.5 s (acceleration factor of 4) and a temporal frame rate of about 1 s. The four time frames are selected to correspond to similar time intervals in each of two acquisitions with respect to the injection of the contrast, and show contrast arrival in the first arterial pass.

Comparing the reconstruction results from GUISE type acquisition (Fig. 7.16.(a)) to those of PBCS type acquisition (Fig. 7.16.(b)), similar observations as in the phantom study are made: slight ghosting artifacts due to the flow motion of the contrast agent are present in the former case as regular superimpositions of the blood vessels (as indicated by the arrow in Fig. 7.16.(a)), whereas such artifacts are not visible in the PBCS reconstruction. As discussed previously, motion artifacts in PBCS reconstructions have a noise-like appearance and could be effectively reduced by imposing a total variation (TV) constraint. It is seen that the PBCS method leads to reconstructions with better contrast to background ratio due to the noise suppression offered by the 1st norm regularization and TV constraint. However, it is seen that in the PBCS reconstructions (Fig. 7.16.(b)), the amount of reconstruction artifacts tend to vary along the longitudinal direction, slices in the middle are generally better reconstructed that the slices at both edges. This is because the receiver coils used have a relatively short longitudinal axis, so that the the coil sensitivities fade away rapidly at both edges. However, GUISE reconstruction seemed to be less affected by this defect, which is an interesting observation could be further investigated.

Retrospective image reconstruction

In practice, often a particular view of the contrast temporal variations is desired, which requires the most appropriate chunk of data to be used for image reconstruction. Traditional SW methods allow time windows starting at different time points to be selected. However, the length of the time windows is fixed by the acquisition sequence and may not be optimal. In retrospective image reconstruction, both the time window length (acceleration factor) and the relative timing of each reconstruction could be chosen, such as illustrated in Fig. 7.17. The left column in Fig. 7.17 shows the time intensity curves (TIC) that depict the image intensity variations over the data acquisition time period of 150 s of selected arterial and venous regions (as indicated in the figure). The TICs were constructed from sliding window reconstructions with a frame rate of 0.5 s and a temporal footprint of 7.5 s (acceleration factor of 4).

Notice the constructed TICs are impaired with local variations that are attributed to reconstruction artifacts. However, it is seen that the TIC in the GUISE acquisition (Fig. 7.17.(a))

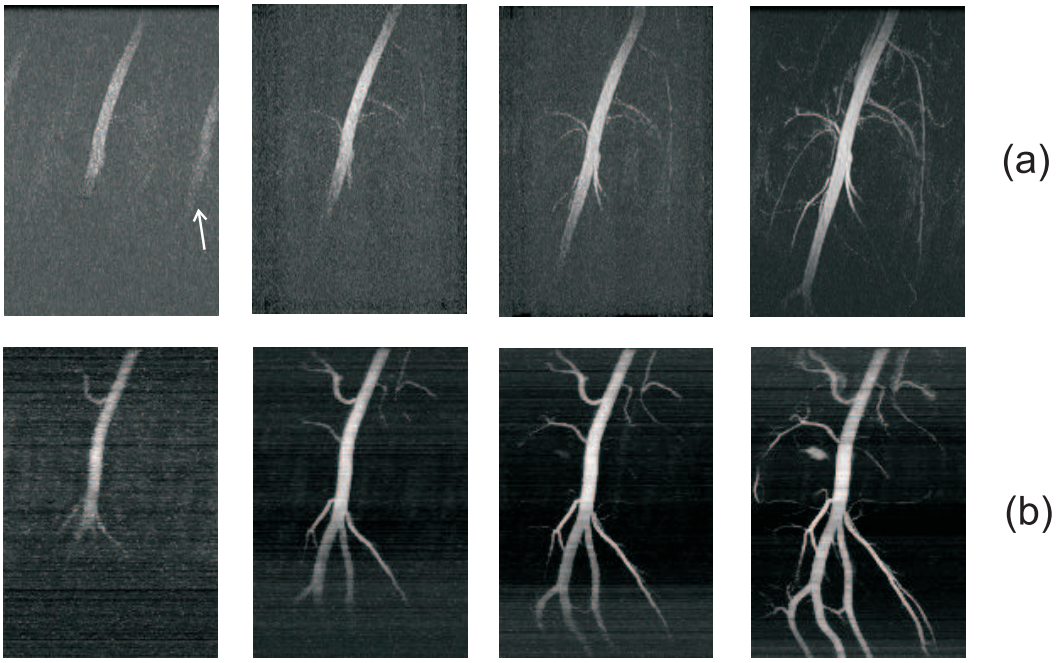

Figure 7.16 Sliding window reconstructions (coronal plane MIP) in volunteer studies at a temporal footprint of 7.5 s and temporal frame rate of 1 s from: (a) GUISE type acquisition; (b) PBCS type acquisition. The selected time frames correspond to similar time intervals within the total data acquisition period and show the rapid contrast filling in the main arteries.

features a substantially higher level of local variations comparing to that of the PBCS acquisition (Fig. 7.17.(c)), and also the variations appear to have some periodic content. This is due to the fact that different time frame reconstructions are made from different portions of the k-space data and face different sampling patterns, which give rise to two sources of variations in the reconstruction results. Firstly, since k-space has a very non-uniform energy distribution, the data subsets used for different reconstructions have different levels of energy which lead to non-uniform amplitudes at reconstruction. Secondly, the different sampling patterns used in different reconstructions lead to different levels of reconstruction artifacts. Both of the two sources of variations have a periodicity of 30 s, which is the time interval for a complete k-space acquisition. On the other hand, the TIC corresponding to the PBCS acquisition (Fig. 7.17.(b)) feature no such periodic variations, as each reconstruction is made with the same portion of the k-space data and also the same sampling mask. The only cause for variation in this case is the noise that can be largely eliminated by averaging a large enough group of voxels.

To demonstrate the retrospective selection of acceleration factor, image reconstructions using time windows with different lengths and different temporal positions are made based on the TIC curves on the left. In each case time window 1 is selected to produce a pure arterial view image, with a narrow temporal footprint (acceleration factor of 8). Time window 2 is selected to contain both arterial and venous views and also has a broader temporal

footprint (acceleration factor of 4). From the reconstruction results shown on the right, it is seen that the reconstruction corresponding to time window 2 is more superior than that of time window 1 in GUISE reconstruction as seen by the reduced level of reconstruction noise; however such difference is not obvious in the PBCS reconstructions. Hence trade-off between the temporal footprint and image quality is better tolerated in PBCS due to the nature of CS type reconstructions [LDP07].

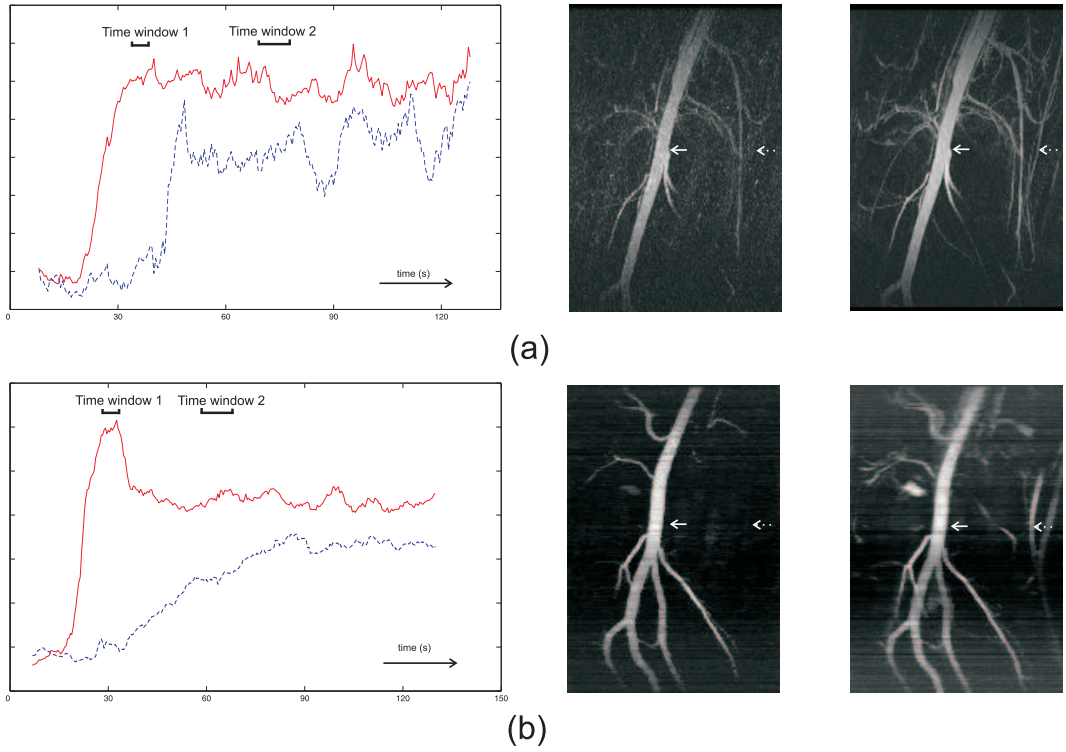

Figure 7.17 Retrospective reconstruction based on the TIC of voxels in selected arterial and venous regions that are respectively pointed by solid and dashed arrow (the average intensity of 9 voxels in these regions is taken): (a) GUISE acquisition; (b) PBCS acquisition. Two reconstructions using time window 1 and 2 are made, and the resulting coronal plane MIP images are shown on the right. Time window 1 is placed to give a pure arterial view of the contrast with a narrow temporal footprint. Time window 2 is placed to cover both arterial and venous phases, and also features a boarder temporal footprint.

Construction of a TIC from sliding window reconstructions requires two parameters to be set: the temporal frame rate (the shift amount of the time window) and the temporal footprint (reconstruction acceleration factor). The effects of the former factor are easy to comprehend in that a higher temporal frame rate leads to better resolution of the TIC curves, and vice versa. Due to the fact that the contrast level variations are expected to be intrinsically smooth over time, a relatively low frame rate should suffice to reveal the underlying contrast dynamics. The effects of the second factor are less obviously seen, and are demonstrated using TICs formed with acceleration factors with 2, 4 and 8 from the GUISE acquisitions as shown in Fig. 7.18.

The first observation of the TICs constructed with different acceleration factors is the different levels of local variations on the TICs due to reconstruction artifacts. As the reconstruction acceleration factor increases, the reconstruction artifacts increase substantially. The effects of sliding window reconstructions can be compared to those of a moving averaging filter. As the latter is essentially a low pass filter, sliding window reconstruction tends to underestimate the high frequency information in the underlying data. By the intrinsic characteristics of the blood flow, the relevant high frequency information is the rapid flow-in and wash-out actions of the contrast. Hence constructing the TICs at a higher acceleration factor allows the dynamics of the contrast to be more accurately depicted (such as a sharper rising/fall edge of the TIC, as indicated by the arrows in Fig. 7.18). In turn, it allows the desired time window to be more accurately placed on the time axis. However in practice, such benefits are often overwhelmed by the significantly increased level of reconstruction artifacts as demonstrated in Fig. 7.18. Another effect of lengthening the time window is the delayed response, i.e. the TIC with a long time window starts later and terminate earlier comparing to that with a shorter time window. But as the useful information is generally neither at the beginning nor the finish of the time period, such delay is acceptable. Thus to conclude, in practice a moderately low acceleration factor is suggested for constructing the time intensity curves.

Prior knowledge based image reconstruction

As demonstrated in Fig. 7.10 and Fig. 7.12 respectively, prior knowledge of the image can be obtained from a composite data set with broad temporal footprint and incorporated in GUISE and PBCS reconstructions. In the following, the uses of ROS in GUISE method and a image prior estimate in PBCS method are investigated. For the clarity of illustration, reconstructed MIP images as well as axial plane slices are shown.

Image reconstructions in GUISE method with and without the use of ROS constraints at acceleration factor of 8 and 12 are presented in Fig. 7.19. Firstly, the use of ROS allows acceleration factor higher than the number of receiver coils to be achieved, as demonstrated in Fig. 7.19.(d) and Fig. 7.19.(e). Secondly, as discussed in [WBMW09, PWSB99], use of a ROS leads to more stable matrix inversion and hence achieves a lower reconstruction noise level. A numerical comparison of the noise levels is made to demonstrate this: assuming in the ideal case the that a large artery filled with contrast agent should have an uniform intensity level, the variance of the voxel intensities in the artery is then used as a measure of the noise level and shown on the right bottom in each reconstruction. It is seen that as the size of the ROS reduces, the noise variance drops as expected. Furthermore, it is seen at acceleration factor 12, some vascular regions with low contrast level are overwhelmed by reconstruction noise when a loose ROS constraint is used, whereas they are still visible in the reconstruction when a tight support is used (see the arrowed regions in Fig. 7.19.(d-e)).

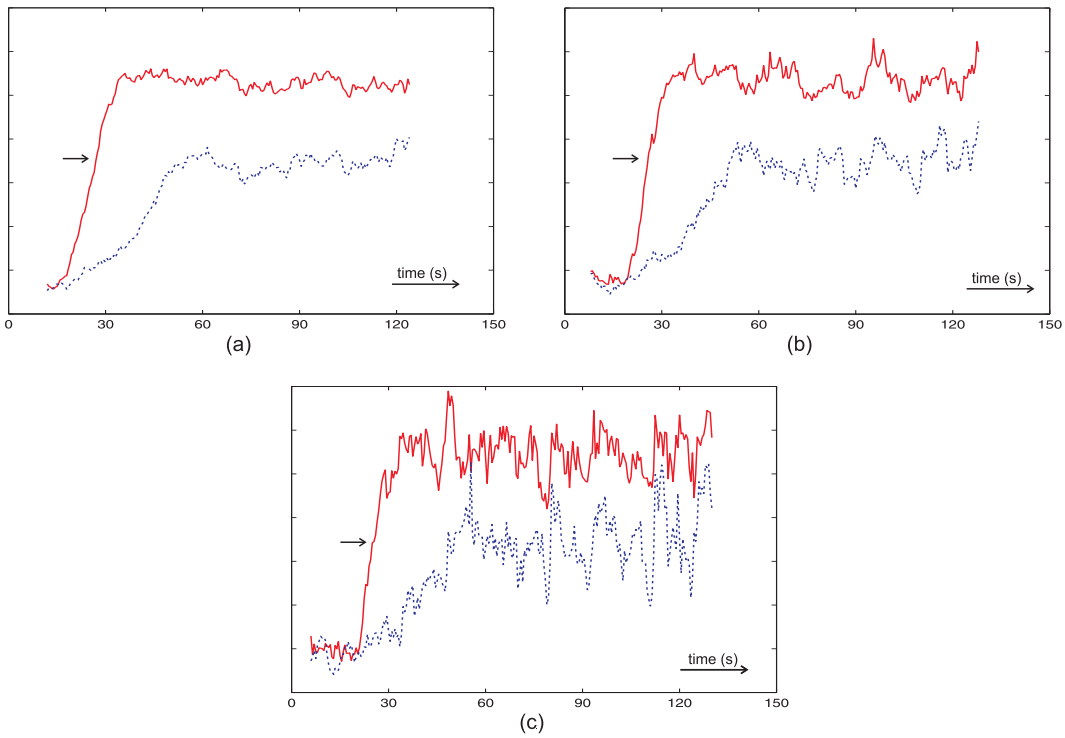

Figure 7.18 Time intensity curves (TIC) constructed from GUISE acquisition using different acceleration factors (based on the same voxels as those in Fig. 7.17.(a)) : (a) 2, (b) 4, (c) 8. TICs constructed at higher acceleration factors have the potential to reveal the contrast temporal variation more accurately. However in practice such benefit is often overshadowed by the increased level of reconstruction artifacts as demonstrated here. The arrow shows that using at a higher acceleration factor leads to a sharper rising edge in the resulting TIC.

PBCS reconstructions with and without the use of prior image estimate at various acceleration factors are compared in Fig. 7.20. Two types image prior estimate were used as shown in Fig. 7.20.(a) and Fig. 7.20.(b): reference image 1 was reconstructed from a k-space acquisition that the reconstruction data resides in; reference image 2 is reconstructed from a composite k-space data set that cover the entire data acquisition time interval. Reference image 2 is selected to study the case where the reference image contains different temporal information than the underlying image. The two types of reference image are also respectively referred as sliding composite and static composite in [JCH+09]. Both reference images were constructed by directly inverse Fourier transform the under-sampled k-space data sets, and hence feature noise like reconstruction artifacts. Then PBCS reconstructions were made in the following scenarios: without the use of prior image estimate; using reference image 1 as the prior image estimate; using reference image 2 as the prior image estimate.

It is seen that at acceleration factor of 12, all three approaches led to reasonably good reconstructions; however at higher acceleration factors (24 and 48), PBCS without a prior image estimate (conventional CS) led to poorer reconstructions compared to the cases where a

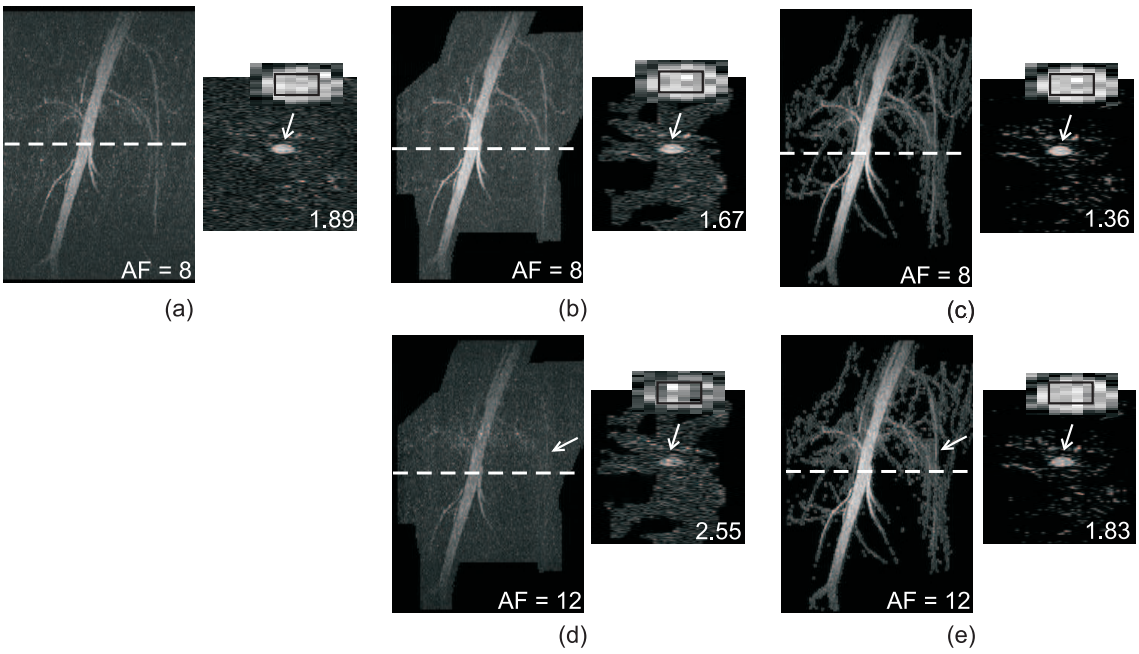

Figure 7.19 Comparing GUISE image reconstructions with and without the use of a ROS constraint at acceleration factors of : (a-c) 8, (d-e) 12. The three columns respectively display the GUISE reconstructions without the use of ROS (left), with the use of a loose ROS obtained from the MIPs of the composite image as discussed in Section 7.3.1(middle), with the use of a tight ROS that is obtained from the 3D image composite image volume (right). The use of ROS constraint allows image reconstructions at acceleration factor of 12 to be made as seen in (d) and (e), which is otherwise infeasible when 8 receiver coils are used. The variance of voxel intensity levels within the arterial region (based on the voxels within the boxed region shown in the enhanced views) in each case are calculated and displayed on the right bottom corner, which serve as a measure for the reconstruction noise level. The arrows show the vascular regions that are overwhelmed by reconstruction noise at high acceleration factor when a loose support is used.

prior image estimate was incorporated: a higher level of reconstruction artifacts was observed that degraded the image contrast and some vascular regions with low contrast level were failed to be recovered as indicated by the arrows in Fig. 7.20.(f-k). Comparing the PBCS reconstruction outcome with the use of different image prior estimates, it is seen that the use of reference image 1 led to better image reconstructions. This is because reference image 1 is highly correlated to the underlying image, based on which an accurate sorting order for sorting the underlying image can be obtained. Applying this sorting order in PBCS reconstruction leads to high sparsity in the sorted image which in turn leads to an accurate image reconstruction. In comparison, the venous enhancement in reference 2 misled the sorting of the image elements in the underlying image, and hence lowers the level of sparsity in the sorted image. However, it is seen that the reconstruction artifacts caused by the inaccurate image estimate (inaccurate sorting) are not correlated with the image estimate itself, i.e. no image feature from the prior estimate has been transplanted to the image reconstruction, which is a beneficial feature in prior estimate based image recovery methods.

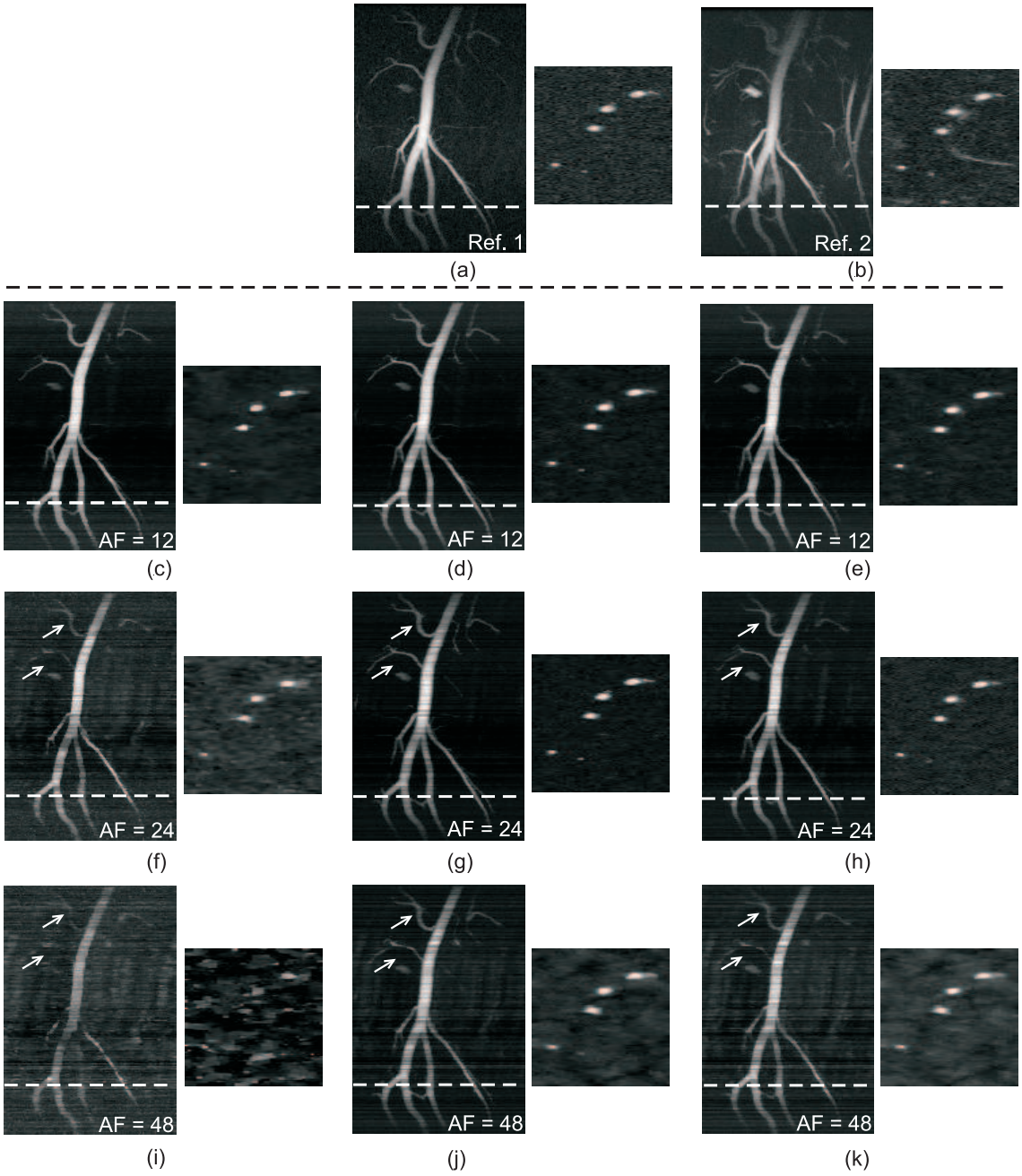

Figure 7.20 PBCS reconstructions with the uses of different prior image estimates at various acceleration factors : (c-e) 12; (f-h) 24; (i-k) 48. Reference image 1 (a) and reference image 2 (b) are respectively obtained from a sliding composite data set and a static composite data set, and feature different temporal information. The three columns in (c-k) respectively display the PBCS reconstructions without the use of image prior estimate (left), using reference image 1 as the image prior estimate (middle), using reference image 2 as the image prior estimate (right). It is seen that PBCS reconstructions with reference image 1 as prior image estimate led to the the best reconstruction results. The arrows indicate vascular regions with low contrast level that were poorly recovered in some cases.

7.6 Discussion

In this chapter, two new Cartesian based sliding window methods based on GUISE and PBCS are proposed and compared. The two methods offer similar functionalities but are based on distinctive principles: conventional parallel imaging and compressed sensing in parallel imaging, hence comparison of the two is an interesting investigation that could reveal the general pros and cons in applying the two categories of methods in CE MRA. From the phantom study and volunteer study conducted, it is concluded that the PBCS method is more advantageous than the GUISE method in satisfying the two conflicting requirements in CE MRA: high temporal resolution and high spatial resolution.

The PBCS method offers better SW image reconstructions. Firstly, the PBCS method offers a higher level of temporal frame rate, as it is not constrained by the sampling pattern periodicity as is the case in GUISE. Also the design of the sequential data acquisition order in PBCS is more computationally efficient compared to that proposed for GUISE. An improvement of the implementation of PBCS is to employ a more sophiscated sampling mask that satisfies the sampling requirements for both compressed sensing and parallel imaging, such as that discussed in [LAV+09]. Although constraining data acquisition to a sampling mask in PBCS limits the trade-off between the acceleration factor and image quality, i.e. it is infeasible to construct images using full k-space data set, such a limitation is acceptable as there is little degradation of reconstruction quality at low acceleration factors compared to that received at full k-space data set. In addition, a bonus of employing a fixed sampling mask in PBCS data acquisition is the ability to produce a low-artifact TIC, which is helpful in retrospective reconstruction.

The PBCS method leads to better image recovery at high acceleration factors. Without the incorporation of image prior knowledge, GUISE takes the conventional SENSE-like image recovery approach that obtains an image estimate by exploiting the distinctive coil sensitivity encoding, whereas PBCS takes the CS approach that exploits the additional constraint of image sparsity, and hence achieves better image recovery [WBMW08a]. In GUISE and PBCS, image prior knowledge is respectively incorporated in the form of ROS and the relative magnitudes of image elements, hence more information from the composite data set is incorporated in the PBCS reconstruction that leads to a more successful outcome. Also, it is observed that the image quality degrades much more mildly in PBCS reconstructions compared to those of GUISE as the acceleration factor goes up.

Incorporating prior knowledge in image reconstructions is demonstrated to be effective in both methods. In GUISE reconstruction, it is seen that a tighter ROS leads to improved reconstruction SNR and allows a higher acceleration factor to be achieved. However, defining a tight ROS is usually not a straightforward task and there is a potential risk of omitting

vascular regions with low contrast level. A safer method would be an iterative approach in which a loose support is first applied to obtain an initial reconstruction, based on which a tighter support can be estimated and reapplied in the reconstruction. In PBCS, the use of a prior image estimate is demonstrated to be very beneficial as a reference image with high temporal correlation with the underlying image can be readily obtained. With use of a prior image estimate, PBCS achieves an acceleration factor level that is comparable to that offered by the highly constrained back projection (HYPR) method, and is unprecedented by existing Cartesian methods. Both PBCS and HYPR take the spatial information of a reference image as prior knowledge while attempting to recover the missing temporal information. Compared to HYPR, the performance of PBCS is not dependent on the complexity of the vascular structures as is the case with HYPR; also the reference image is not directly involved in the image reconstruction as it is in HYPR, rather only the knowledge of relative magnitude of the image elements is used to sort the underlying image, hence no presumption of the actual underlying image is made based on the prior image estimate as demonstrated by the experimental results.

In the retrospective image reconstructions demonstrated, a time intensity curve (TIC) is used as the indicator of the arterial and venous contrast status in selected regions. It allows time windows to be selected based on an estimation of the contrast dynamics. In practice, the TIC curves are subject to reconstruction artifacts, particularly in cases where the sliding window reconstructions are subjected to periodically varying sampling patterns. Such variations can be largely reduced by using a low acceleration factor at little expense of practical utilities. Alternatively the periodic artifacts can potentially be reduced by exploiting knowledge of its periodicity and also the explicit sampling patterns used. Constructing the TICs based on a single image slice may potentially lead to bias due to the time difference of contrast arrival at different regions in the longitudinal vessels; such bias can be reduced by constructing the TICs based on several regions along the longitudinal vessels.

Overall, CE MRA is one instance of dynamic imaging that could benefit from the proposed methods. Other fields such as cardiac imaging also share a similar nature: sparse data set can be obtained by exploiting the temporal redundancy among consecutive data acquisitions. The simplicity of data acquisition sequence design allows the proposed methods to be readily implemented on the commercial scanners.

Chapter 8

Conclusions and future work

This chapter summarises the major findings of the research reported in this thesis, building on the more detailed conclusions that can be found at the end of the Chapter 5, 6 and 7. Suggestions for potential future work are also made.

8.1 Conclusions

Parallel MRI has received wide acceptance due to the high level of sampling acceleration achievable. However parallel MRI techniques lead to degraded image quality as a trade-off for reduced sample acquisitions. This thesis considers utilising additional prior knowledge of the underlying image to improve the image reconstruction in parallel MRI. Specifically, the sparsity of the underlying image is considered. Image sparsity exists in different forms. In the image domain, the sparsity refers to the fact that the imaged object is only supported within certain regions of the FOV; the image sparsity also exists in the transform domain, which means there is a high level of energy concentration in the image transform, so that only some of the most significant transform coefficients need to be recovered.

GUISE exploits the image domain sparsity in parallel MRI. The GUISE formulation naturally incorporates the object ROS, it also accommodates different sampling patterns and hence allows an adaptive sampling pattern design to be used. In order to achieve computational efficiency in both image reconstruction and sampling pattern design, the sampling patterns are restricted to those consisting of repeated blocks. A sampling pattern design method that incorporates knowledge of the coil sensitivity profiles and the object ROS is proposed. This adaptive sampling pattern design is shown to offer advantages over the fixed sampling patterns employed by other similar methods.

PBCS (SENSECS) exploits the transform domain sparsity in parallel MRI. PBCS is an in-

teresting extension of CS: based on a prior image estimate, the elements in the underlying image are rearranged so that the image can be recovered in an alternative form that features a much higher level of sparsity, which leads to improved image recoveries; then the prior image estimate is essentially incorporated in the image reconstruction when this sorted image is recovered via compressed sensing. SENSECS considers the application of PBCS in parallel imaging. In order to bypass the issue of sampling pattern design conflict in applying CS recovery in parallel imaging, the coil sensitivity encoding and image sparsity are respectively exploited in the SENSE and PBCS reconstruction stages. Due to the the complementary characteristics of SENSE type and CS type reconstructions, SENSECS achieves significantly improved reconstruction results compared to those by SENSE and CS alone.

GUISE and PBCS shares the common ground of exploiting the high sparsity of the contrast enhanced angiogram (after background subtraction) in their applications in CE MRA. Data acquisition schemes are designed so that retrospective image reconstructions can be made to achieve an optimum trade-off between temporal resolution and image quality. Also the retrospective image reconstruction allows an image with low temporal resolution to be first made, and prior knowledge can be obtained from this low temporal resolution reconstruction to aid reconstructing images at a higher temporal resolution: the ROS and prior image estimate used in GUISE and PBCS respectively. Application of PBCS reconstruction in CE MRA is particularly attractive as very high acceleration factor can be achieved.

8.2 Future work

In the following sections, possible future work related to each of the three novel contributions are respectively suggested.

8.2.1 GUISE

The current sampling pattern design in GUISE is solely based on the RMS error of the image reconstruction. However, RMS is not necessarily the best judge of the reconstruction quality in terms of human perception. Hence other types of error measure may be more useful in judging the suitability of a sampling pattern. Also, the current design of the sampling pattern has not taken into consideration the other sources of error that are likely to be present. For instance, the sensitivity to error in knowledge of coil sensitivity profile can be taken into account in the sampling pattern design process.

Image reconstruction in GUISE involves a direct inversion of the known encoding matrix. As discussed in Section 5.8, the use of iterative algorithms could achieve conditioning of the inverse problem by terminating the iterations at an early stage. The effects of the choice of sampling pattern in an iterative reconstruction are interesting to consider. For instance,

as the iterative approaches tend to recover the largest singular values first, the focus of sampling pattern design may then shift from an overall measure of the singular values (such as the IT metric) to the distribution of the singular values, aiming to achieve a higher level of energy concentration in a few of the largest singular values.

GUISE is an image plane pMRI approach in which a complete data set is directly estimated. As discussed in Section 4.4.1, k-space reconstruction methods such as GRAPPA achieve intrinsic conditioning of the inverse problem by only incorporating the neighboring sample measurements in estimating the missing k-space samples. Hence a hybrid reconstruction method in which some of the missing samples are first estimated as in GRAPPA, followed by a GUISE reconstruction using the resulting composite data set (containing measured and estimated samples), is intuitively beneficial. The consequential questions are : how should sampling strategies be designed and which samples should be estimated?

8.2.2 PBCS and SENSECS

In the current implementation of PBCS, only the magnitude information of the prior image estimate is utilised in the sorting process. However, in practice the underlying image in parallel MRI is considered to be a complex quantity due to the weighting of the complex coil sensitivity profile. Hence it is intuitively beneficial to take into account the image phase information in the sorting process, for instance performing a sorting process on the real and imaginary parts separately. However, it is usually difficult to obtain the phase information from an image approximation, such as a low resolution approximation or a SENSE reconstruction. Instead, it may be possible to derive the phase information using knowledge of the complex coil sensitivity profiles.

As mentioned in Section 6.7, the sparse model that can be used in PBCS is by no means constrained to monotonical variations as considered so far. In considering other sparse models, there are a few questions to be answered. How sparse is the representation of the sparse model for a given transform? As only an approximate sorting order is available, do some sparse models tolerate the inaccurate sorting order better than others? For instance, although both monotonical variations and high order sinusoidal curves have a sparse representation given a DCT transform, monotonical variation intuitively tolerates the inaccurate sampling order better. As the sorting process modifies the form of reconstruction artifacts, would it be possible to take into account of the least dissruptive reconstruction artifacts (such as in the form of random noise) when selecting the sparse model?

SENSECS is a promising approach in image reconstruction from multiple receiver coil data sets. It can be further improved if a systematic sampling pattern design method is adopted rather than the heuristic sampling used in this work as discussed in Section 6.7. The success

of SENSECS triggers a series of interesting questions to be considered. Rather than using SENSE reconstruction to gain an image estimate in the first step, would the use of other types of reconstruction be superior, such as GRAPPA? Is it in general benificial to first obtain an image estimate and use it in a following PBCS reconstruction rather than directly applying a CS reconstruction? What is the significance of different sparse models and sparsifying transforms used in PBCS? Would an improvement be received if the PBCS process is iterated, i.e. using the reconstruction result from one PBCS reconstruction as a prior image estimate for another PBCS reconstruction, given different sparsity models and/or sparsifying transforms are used? To investigate these questions, a reliable metric that could quantitatively evaluate the performance of the different approaches is required, noting that RMS is not a suitable metric for this purpose.

8.2.3 GUISE and PBCS in CE MRA

The estimate of ROS of the region containing contrast in GUISE has a large impact on the quality of the reconstruction outcome. The the MIP images based method as used in this work leads to a fairly loose estimate of the ROS and hence leads reconstruction with a lower level of SNR compared to what could be achieved with a tighter ROS mask. However, direct thresholding of the 3D reference image has the potential risk of under-estimating the ROS, which will severely degrade the diagnostic value of the reconstructed images. Another colleague Ph.D. student is currently investigating a new approach to estimate the ROS based on the statistics of the voxel intensities along different projection rays and has obtained some promising preliminary results. Also the continuity of the ROS of the vascular regions in the 3D image volume is an useful constraint to be incorporated in the ROS estimation.

A SENSECS type reconstruction may be applied as an extension of the current GUISE method, i.e. the reconstruction of GUISE can be used as a prior estimate for a second stage PBCS reconstruction. As discussed in Section 6.4.3, the second stage PBCS reconstruction in SENSECS leads to reduced level of reconstruction noise from the SENSE reconstructions. In the application in CE MRA, this approach is especially effective as the regions containing contrast ideally have uniform intensity value, hence a total variation penalty would be very effective in removing the rapid variations. One difficulty in practical implementation of this approach is the data acquisition scheme design. As for the operation of PBCS, it is preferable to acquire additional samples near the k-space centre, which means repeated acquisitions of the k-space centre need be fitted into the sequential GUISE sample acquisition sequence.

The concept of time intensity curve (TIC) based retrospective reconstruction can be further extended. In the current implementation, the TIC is only used to aid selecting the data

sets for image reconstruction, however the actual temporal contrast variations depicted by the TIC could also be incorporated in the image reconstructions. So far reconstructions of different temporal images have been treated as independent, however there is an intrinsic correlation among the temporal images in a time series due to the smooth variation of the contrast level over time. Hence the estimated contrast variation from the TIC can be incorporated in constructing a time series of images, for instance in a post-processing image correction to reduce the level of reconstruction artifacts.

References

[AB04] N. Aggarwal and Y. Bresler. "Accelerated parallel magnetic resonance imaging by adaptive k-space sampling," in *Proceedings of 2nd IEEE International Symposium on Biomedical Imaging*, Arlington, USA, 2004.

[AD08] G. Adluru and E.V. DiBella. "Data reordering for improved constrained reconstruction from undersampled k-space data," in *Proceedings of the 16th Annual Meeting of ISMRM*, Toronto, Canada, 2008.

[ATPA05] K. Arfanakis, A.A. Tamhane, J.G. Pipe, and M.A. Anastasio. "K-space undersampling in PROPELLER imaging," *Magnetic Resonance in Medicine*, vol. 53, no. 3, pp. 675–683, 2005.

[BACB01] P.J. Bones, N. Alwesh, T.J. Connolly, and N.D. Blakeley. "Recovery of limited-extent images aliased because of spectral undersampling," *Journal of the Optical Society of America A*, vol. 18, pp. 2079–2088, 2001.

[Bar07] B. Baraniuk. "Compressive sensing," *IEEE Signal Processing Magazine*, vol. 24, pp. 118–121, 2007.

[BBHM05] F.A. Breuer, M. Blaimer, R.B. Heidemann, and M.F. Mueller. "Controlled aliasing in parallel imaging results in higher acceleration (CAIPIRINHA) for multi-slice imaging," *Magnetic Resonance in Medicine*, vol. 53, pp. 684–691, 2005.

[BBM+04] M. Blaimer, F.A. Breuer, M. Mueller, R.M. Heidemann, M.A. Griswold, and P.M. Jakob. " SMASH, SENSE, PILS, GRAPPA: How to choose the optimal method ," *Topics in Magnetic Resonance Imaging*, vol. 15, pp. 223–236, 2004.

[BBM+06a] M. Blaimer, F.A. Breuer, M. Mueller, N. Seiberlich, D. Ebel, R.M. Heidemann, M.A. Griswold, and P.M. Jakob. " 2D-GRAPPA-Operator for faster 3D parallel MRI ," *Magnetic Resonance Imaging*, vol. 56, pp. 1359–1364, 2006.

[BBM+06b] F.A. Breuer, M. Blaimer, M.F. Mueller, N. Seiberlich, Heidemann R.M., Griswold M.A., and Jakob P.M. " Controlled aliasing in volumetric parallel imag-

ing (2D CAIPIRINHA)," *Magnetic Resonance in Medicine*, vol. 55, pp. 459–456, 2006.

[BBMR03] N.D. Blakeley, P.J. Bones, R.P. Millane, and P. Renaud. "Efficient frequency domain sample selection for recovering limited-support images," *Journal of the Optical Society of America A*, vol. 20, pp. 67–77, 2003.

[BKM+09] P.J. Beatty, K.F. King, L. Marinelli, C.J. Hardy, and M. Lustig. "Sequential application of parallel imaging and compressed sensing," in *Proceedings of the 17th Annual Meeting of ISMRM*, Honolulu, USA, 2009.

[BLH01] M. Bydder, D.J. Larkman, and J.V. Hajnal. "Generalized SMASH imaging," *Magnetic Resonance in Medicine*, vol. 47, pp. 160–170, 2001.

[BR05] M. Bydder and M.D. Robson. "Partial Fourier partially parallel imaging," *Magnetic Resonance in Medcine*, vol. 53, pp. 1393–1401, 2005.

[Can06] E. Candes. "Compressive sampling," in *Proceedings of the International Congress of Mathematicians*, Madrid, Spain, 2006.

[CDS99] S.S. Chen, D.L. Donoho, and M.A. Saunders. "Atomic decomposition by basis pursuit," *SIAM Journal of Science and Computing*, vol. 20, pp. 31–61, 1999.

[CM90] K.F. Cheung and R.J. Mark. "Imaging sampling below the Nyquist density without aliasing," *Journal of the Optical Society of America A*, vol. 7, pp. 92–105, 1990.

[CM93] J.W. Carlson and T. Minemura. "Imaging time reduction through multiple receiver coil data acquistiion and image reconstruction," *Magnetic Resonance in Medicine*, vol. 29, pp. 681–687, 1993.

[CRT06] E. Candes, J. Romberg, and T. Tao. "Robust uncertainty principles: Exact signal reconstruction from highly incomplete frequency information," *IEEE Trans. on Information Theory*, vol. 52, pp. 489–509, 2006.

[DCR+02] J.A. D'Arcy, D.J. Collins, I.J. Rowland, A.R. Padhani, and M.O. Leach. "Applications of sliding window reconstruction with cartesian sampling for dynamic contrast enhanced MRI," *Nuclear Magnetic Resonance in Biomedicine*, vol. 15, pp. 174–193, 2002.

[DG09] M.E. Davies and R. Gribonval. "Restricted isometry constants where ell-p sparse recovery can fail for $0 < p <= 1$," *IEEE Trans. on Information Theory*, vol. 55, pp. 2203–2214, 2009.

[Don06] D. Donoho. "Compresssed sensing," *IEEE Trans. on Information Theory*, vol. 52, pp. 1289 – 1306, 2006.

[DRT95] D. Donoho, J. Romberg, and T. Tao. "De-noising by soft thresholding," *IEEE Trans. on Information Theory*, vol. 38, pp. 613–627, 1995.

[DSB+09] M. Doneva, J. Sebegas, P. Bornert, H. Eggers, and A. Mertins. "Accelerated MR parameter mapping using compressed sensing with model-based sparsifying transform," in *Proceedings of the 17th Annual Meeting of ISMRM*, Honolulu, USA, 2009.

[DSWW89] C.L. Dumoulin, S.P. Souza, M.F. Walker, and W. Wagle. "Threedimensional phase contrast angiography," *Radiology*, vol. 9, pp. 139–149, 1989.

[FBB+08] A. Fischer, F. Breuer, M. Blaimer, N. Seiberlich, and P.M. Jakob. "Accelerated dynamic imaging by reconstructing sparse differences using compressed sensing.," in *Proceedings of the 16th Annual Meeting of ISMRM*, Toronto, Canada, 2008.

[FGK96] R. Frayne, T.M. Grist, and F.R. Korosec. "MR angiography with threedimensional MR digital subtraction angiography," *Topics in Magnetic Resonance Imaging*, vol. 8, pp. 366–388, 1996.

[FL09] S. Foucart and M.J. Lai. "Sparsest solutions of underdetermined linear systems via ell-q minimization for $0 < q <= 1$," *Journal of Concrete and Applicable Mathematics*, vol. 52, pp. 395–407, 2009.

[FSPC97] T. K. Foo, M. Saranathan, M.R. Prince, and T.L. Chenevert. "Automated detection of bolus arrival and initiation of data acquisition in fast, three-dimensional, gadolinium-enhanced MR angiography," *Radiology*, vol. 203, pp. 275–280, 1997.

[GJH+02] M.A. Griswold, P.M. Jakob, R.M. Heidemann, M. Nittka, and A. Haase. "Generalized autocalibrating partially parallel acquisitions (GRAPPA)," *Magnetic Resonance in Medicine*, vol. 47, pp. 1202–1210, 2002.

[GR00] Y. Gao and S.J. Reeves. "Optimal k-space sampling in MRSI for images with a limited region of support," *IEEE Trans. on Medical Imaging*, vol. 19, pp. 1168–1178, 2000.

[GR01] Y. Gao and S.J. Reeves. "Fast k-space sample selection in MRSI with a limited region of support," *IEEE Trans. on Medical Imaging*, vol. 20, pp. 868–876, 2001.

[HB06] W.S. Hoge and D.H. Brooks. "On the complimentarity of SENSE and GRAPPA in parallel MR imaging,," in *Proceedings of 28th Conference of IEEE Engineering Medical and Biology Society*, New York, 2006, pp. 755–758.

[HBV99] E. M. Haacke, M.R. Brown, and R. Venkatesan. *Magnetic Resonance Imaging: Physical Principles and Sequence Design*. J. Wiley and Sons, New York, 1999.

[HMK+06] H.H. Hu, A.J. Madhuranthakam, D.G. Kruger, J.F. Glockner, and S.J. Riederer. "Combination of 2D sensitivity encoding and 2D partial fourier techniques for improved acceleration in 3D contrast-enhanced MR angiography," *Magnetic Resonance in Medcine*, vol. 55, pp. 16–22, 2006.

[HNF86] J. Hennig, A. Nauerth, and H. Friedburg. "RARE imaging: A fast imaging method for clinical MR," *Magnetic Resonance in Medicine*, vol. 3, no. 6, pp. 823–833, 1986.

[HS52] M.R. Hestenes and E. Stiefel. "Methods of conjugate gradients for solving linear systems," *Journal of Research of the National Bureau of Standards*, vol. 49, pp. 409–436, 1952.

[HU88] M. Hutchinson and Raff U. "Fast MRI data acquisition using multiple detectors," *Magnetic Resonance in Medicine*, vol. 13, pp. 87–91, 1988.

[HW07] Y. Huang and G.A. Wright. "Time-resolved MR angiography with limited projections," *Magnetic Resonance in Medicine*, vol. 58, pp. 316–325, 2007.

[JCH+09] H.J. Jeong, T.A. Cashen, M.C. Hurley, C. Eddleman, C. Getch, H.H. Batjer, and T.J. Carroll. "Radial sliding-window magnetic resonance angiography (MRA) with highly-constrained projection reconstruction (HYPR)," *Magnetic Resonance in Medicine*, vol. 61, pp. 1103 – 1113, 2009.

[JGES98] P.M. Jakob, M.A. Grisowld, R.R. Edelman, and D.K. Sodickson. "AUTO-SMASH: A self-calibrating technique for SMASH imaging," *Magnetic Resonance Materials in Physics, Biology and Medicine*, vol. 7, pp. 42–54, 1998.

[JJS07] X. Jim, B.S. Jong, and D.R. Swati. " PULSAR: A Matlab toolbox for parallel magnetic resonance imaging using array coils and multiple channel receivers," *Concepts in Magnetic Resonance*, vol. 31B, pp. 24–36, 2007.

[JW05] X.J. Ji and S.M. Wright. "Parallel MR imaging with accelerations beyond the number of receiver channels using real image reconstruction," in *IEEE International Conference of the Engineering in Medicine and Biology Security*, 2005, pp. 735–738.

[KA00] K.F. King and L. Angelos. "SENSE with partial Fourier homodyne reconstruction," in *Proceedings of the 9th Annual Meeting of ISMRM*, Denver, Colorando, USA, 2000.

[KEN91] D. Kwiat, S. Einav, and G. Navon. "A decoupled coil detector array for fast image acquisition in magnetic resonance imaging," *Medical Physics*, vol. 18, pp. 251–265, 1991.

[KFGM96] F.R. Korosec, R. Frayne, T.M. Grist, and C.A. Mistretta. "Time-resolved contrast-enhanced 3D MR angiography," *Magnetic Resonance in Medicine*, vol. 36, pp. 345–351, 1996.

[KG09] D.H. Kim and S.M. Gho. "Compressed sensing reconstruction based on maximum intensity projection images," in *Proceedings of the 17th Annual Meeting of ISMRM*, Honolulu, USA, 2009.

[KLK00] W.E. Kyriakos, Panych L.P., and D.F. Kacher. "Sensitivity profiles from an array of coils for encoding and reconstruction in parallel (SPACE RIP)," *Magnetic Resonance in Medicine*, vol. 44, pp. 301–308, 2000.

[KMW89] J.R. Kelton, R.L. Magin, and S.M. Wright. "An algorithm for rapid image acquisition using multiple receiver coils," in *Proceedings of the 8th Annual Meeting of SMRM*, Netherlands, 1989, p. 1172.

[KS06] D.A. Koff and H. Shulman. "An overview of digital compression of medical images: can we use lossy compression in radiology?," *Cardiology*, vol. 4, pp. 211–217, 2006.

[Lan67] H.J. Landau. "Necessary density conditions for sampling and interpolation of certain entire functions," *Acta Mathematica*, vol. 117, pp. 37–52, 1967.

[Lau73] P.C. Lauterbur. "Image formation by induced local interactions: Examples employing nuclear magnetic resonance," *Nature*, vol. 242, no. 5394, pp. 190–191, 1973.

[LAV+09] M. Lustig, M. Alley, S.S. Vasanawala, D.L. Donoho, and J.M. Pauly. "L1 SPIRIT: Autocalibrating parallel imaging compressed sensing," in *Proceedings of the 17th Annual Meeting of ISMRM*, Honolulu, USA, 2009.

[LBB+85] P. Lanzer, C. Barta, E. H. Botvinick, H. U. Wiesendanger, G. Modin, and C. B. Higgins. "ECG-synchronized cardiac MR imaging: method and evaluation," *Radiology*, vol. 155, no. 3, pp. 681–686, 1985.

[LDP07] M. Lustig, D.L. Donoho, and J.M. Pauly. "Sparse MRI: The application of compressed sensing for rapid MR imaging," *Magnetic Resonance in Medicine*, vol. 58, pp. 1182–1195, 2007.

[LJ08] T. Lang and J. Ji. "Accelerating dynamic contrast-enhanced MRI using compressed sensing.," in *Proceedings of the 16th Annual Meeting of ISMRM*, Toronto, Canada, 2008.

[LKBW04] F.H. Lin, K.K. Kwong, J.W. Belliveau, and L.L. Wald. "Parallel imaging reconstruction using automatic regularization," *Magnetic Resonance in Medcine*, vol. 51, pp. 559–567, 2004.

[LKC+01] F.H. Lin, K. Kwong, Y. Chen, Haase A., and Jakob P.M. "Reconstruction of sensitivity encoded images using regulariztion and discrete time wavelet transform estimates of the coil maps," in *Proceedings of the 10th Annual Meeting of ISMRM*, Glasgow, Scotland, 2001.

[LLY08] D. Liang, B. Liu, and L. Ying. "Accelerating sensitivity encoding using compressed sensing," in *Proceedings of annual International Conference of the IEEE Engineering in Medicine and Biology Society*, Vancouver, Canada, 2008.

[LPC+07] C. Lew, A.R. Pineda, D. Clayton, D. Spielman, F. Chan, and R. Bammer. "SENSE phase-constrained magnitude reconstruction with iterative phase refinement," *Magnetic Resonance in Medcine*, vol. 58, pp. 638–651, 2007.

[LPS05] L. Landini, V. Positano, and M.F. Santarelli. *Advanced image processing in Magnetic resonance imaging*. Taylor and Francis, Florida, 2005.

[LWA+05] F.H. Lin, F.N. Wang, S.P. Ahlfors, M.S. Hamalainen, and Belliveau J.W. "Parallel MRI reconstruction using variance partitioning regularization," *Magnetic Resonance in Medcine*, vol. 58, pp. 735–744, 2005.

[Mac07] J.R. Maclaren. *Motion detection and correction in magnetic resonance imaging*. PhD Thesis, University of Canterbury, New Zealand, 2007.

[Man77] P. Mansfield. "Multi-planar image-formation using NMR spin echoes," *Journal of Physics C - Solid State Physics*, vol. 10, no. 3, pp. 55–58, 1977.

[Mar86] R.J. Mark. " Multidimensional-signal sample dependency at Nyquist densities ," *Journal of the Optical Society of America A*, vol. 3, pp. 268–273, 1986.

[MBMW07] J. Maclaren, P. Bones, R. Millane, and R. Watts. " MRI with TRELLIS: a novel approach to motion correction ," *Magnetic Resonance Imaging*, vol. 26, pp. 474–483, 2007.

[McR03] Donald W. McRobbie. *MRI from Picture to Proton*. Cambridge University Press, Cambridge, UK ; New York, 2003.

[MMR89] T.J. Masaryk, M.T. Modic, and P.M. Ruggieri. "Three-dimensional (volume) gradient-echo imaging of the carotid bifurcation: preliminary clinical experience," *Radiology*, vol. 171, pp. 801–806, 1989.

[MVN95] S.E. Moyher, D.B. Vigneron, and S.J. Nelson. "MRI phased array," *Journal of Magnetic Resonance Imaging*, vol. 5, pp. 139–144, 1995.

[MWV+06] C.A. Mistretta, O. Wieben, J. Velikina, W.F. Block, Y. Wu, and K. Johnson. "Highly constrained backprojection for time-resolved MRI," *Magnetic Resonance in Medicine*, vol. 55, pp. 30–40, 2006.

[Nis96] D.G. Nishimura. *Principles of Magnetic Resonance Imaging*. Stanford University, USA, 1996.

[NKF01] S. Naganawa, T. Koshikawa, and H. Fukatsu. "MR angiography of the carotid artery using 3D time-resolved imaging of contrast kinetics: comparison with real-time fluoroscopic triggered 3D-elliptical centric view ordering," *Radiation Medicine*, vol. 12, pp. 175–181, 2001.

[OSB99] A. V. Oppenheim, R. W. Schafer, and J. R. Buck. *Discrete-Time Signal Processing*. Prentice-Hall, New Jersey, 2nd edition, 1999.

[OWJF08] R.L. OHalloran, Z. Wen, H.H. James, and S.B. Fain. "Iterative projection reconstruction of time-resolved images using highly-constrained backprojection (HYPR)," *Magnetic Resonance in Medicine*, vol. 59, pp. 132–139, 2008.

[Pip99] J.G. Pipe. " Motion correction with PROPELLER MRI: Application to head motion and free-breathing cardiac imaging," *Magnetic Resonance in Medicine*, vol. 42, pp. 963–969, 1999.

[PKG+00] D.C. Peters, F.R. Korosec, T.M. Grist, K.K. Vigen, and J.E. Holden. "Undersampled projection reconstruction applied to MR angiography," *Magnetic Resonance in Medicine*, vol. 43, pp. 91–101, 2000.

[PWBB01] K.P. Pruessmann, M. Weiger, P. Bornert, and P. Boesiger. "Advances in sensitivity encoding with arbitrary k-space trajectories," *Magnetic Resonance in Medcine*, vol. 46, pp. 638–651, 2001.

[PWSB99] K.P. Pruessmann, M. Weiger, M.B. Scheidegger, and P. Boesiger. "SENSE: Sensitivity encoding for fast MRI," *Magnetic Resonance in Medicine*, vol. 42, pp. 952–962, 1999.

[QZZ+05] P. Qu, K. Zhong, B. Zhang, J. Wang, and G.X. Shen. "Convergence behavior of iterative SENSE reconstruction with non-Cartesian trajectories," *Magnetic Resonance in Medcine*, vol. 54, pp. 1040–1045, 2005.

[REH+90] P.B. Roemer, W.A. Edelstein, C.E. Hayes, S.P. Souza, and Muller O.M. "The NMR phased array," *Magnetic Resonance in Medicine*, vol. 16, pp. 192–225, 1990.

[RH95] S.J. Reeves and L.P. Heck. "Selection of observations in signal reconstruction," *IEEE Trans. on Signal Processing*, vol. 43, pp. 788–791, 1995.

[ROF92] L.I. Rudin, S. Osher, and E. Fatemi. "Nonlinear total variation based noise removal algorithms," *Physica D*, vol. 60, pp. 259–268, 1992.

[RR91] J.B. Ra and C.Y. Rim. "Fast imaging method using multiple reeiver coils with subencoding data set," in *Proceedings of the 10th Annual Meeting of SMRM*, San Francissco, 1991.

[RZ99] S.J. Reeves and Z Zhao. "Sequential algorithms for observation selection," *IEEE Trans. on Signal Processing*, vol. 47, pp. 123–132, 1999.

[SB06] B. Sharif and Y. Bresler. "Optimal multi-channel time sequential acquisition in dynamic MRI with parallel coils," in *3rd IEEE International Symposium on Biomedical imaging*, Virginia, USA, 2006, pp. 45–48.

[SB07] B. Sharif and Y. Bresler. "Adaptive real-time cardiac MRI using paradise: validation by the physiological improved phantom," in *4th IEEE International Symposium on Biomedical imaging*, New York, USA, 2007, pp. 1020–1023.

[Sha49] C.E. Shannon. "Communication in the presence of noise," in *Proceedings of the IRE*, 1949, p. 1021.

[SKPJ04] A.A. Samsonov, E.G. Kholmovski, D.L. Parker, and C.R. Johnson. "POCSENSE: POCS-based reconstruction for sensitivity encoded magnetic resonance imaging," *Magnetic Resonance in Medcine*, vol. 52, pp. 1397–1406, 2004.

[SMH05] G. Schneider, J.F.M. Meaney, and V.B. Ho. *Magnetic Resonance Angiography: Techniques, Indications and Practical Applications*. Springer, Milan, 2005.

[SML+00] D.K. Sodickson, C.A. McKenzie, W. Li, W.J. Manning, and E.R. Edelman. "Contrast-enhanced 3D MR angiography with simultaneous acquisition of spatial harmonics: A pilot study," *Radiology*, vol. 127, pp. 284–289, 2000.

[Sny05] Jan A. Snyman. *Practical Mathematical Optimization: An Introduction to Basic Optimization Theory and Classical and New Gradient-Based Algorithms*. Springer Publishing, New York, USA, 2005.

[Sod00] D.K. Sodickson. " Tailored SMASH image reconstructions for robust in vivo parallel MR imaging," *Magnetic Resonance in Medicine*, vol. 44, pp. 243–251, 2000.

[Str88] G Strang. *Linear Algebra and its Applications*. Harcourt Brace Jovanovich College Publishers, Florida, USA, 1988.

[SW71] E. M. Stein and G. Weiss. *Introduction to Fourier Analysis on Euclidean Spaces*. Princeton University Press, 1971.

[SW97] D.K. Sodickson and Manning W.J. "Simultaneous acquisition of spatial harmonics (SMASH): fast imaging with radiofrequency coil arrays," *Magnetic Resonance in Medicine*, vol. 38, pp. 591–603, 1997.

[TBP03] J. Tsao, P. Boesiger, and K.P. Pruessmann. "k-t BLAST and k-t SENSE: Dynamic MRI with high frame rate exploiting spatiotemporal correlations," *Magnetic Resonance in Medicine*, vol. 50, pp. 1031–1042, 2003.

[TKC+96] P.A. Turski, F.R. Korosec, T.J. Carroll, D.S. Willig, T.M. Grist, and C.A. Mistretta. "Contrast-enhanced magnetic resonance angiography of the carotid bifurcation using the time-resolved imaging of contrast kinetics (TRICKS) technique," *Topics in Magnetic Resonance Imaging*, vol. 12, pp. 175–181, 1996.

[TM02] D.S. Taubman and W.M. Marcellin. "JPEG 2000: image compression fundamentals, standards and practice," *Kluwer International Series in Engineering and Computer Science*, 2002.

[VBD+93] V.J. Vaals, M. Brummer, W. Dixon, D.S. Willig, T.M. Grist, and C.A. Mistretta. "Keyhole method for accelerating imaging of contrast agent uptake," *Journal of Magnetic Resonance Imaging*, vol. 3, pp. 671–675, 1993.

[VCP07] S. Vattoth, J. Cherian, and T. Pandey. "Magnetic resonance angiographic demonstration of carotid-cavernous fistula using elliptical centric time resolved imaging of contrast kinetics (EC-TRICKS)," *Magnetic Resonance Imaging*, vol. 25, pp. 1227–1231, 2007.

[VEL+07] F.M. Vogt, H. Eggebrecht, G. Laub, R. Kroeker, M. Schmidt, and J. Barkhausen. "High spatial and temporal resolution MRA (TWIST) in acute aortic dissection," in *Proceedings of the 15th Annual Meeting of ISMRM*, Berlin, Germany, 2007.

[VPGB00] K.K. Vigen, D.C. Peters, T.M. Grist, and W.F. Block. "Undersampled projection-reconstruction imaging for time-resolved contrast-enhanced imaging," *Magnetic Resonance in Medicine*, vol. 43, pp. 170–176, 2000.

[WB08] H. Wu and W.F. Block. "HYPR-constrained compressed sensing reconstruction for accelerated time resolved imaging," in *Proceedings of the 16th Annual Meeting of ISMRM*, Toronto, Canada, 2008.

[WBMW08a] B. Wu, P. Bones, R. Millane, and R. Watts. "Applying compressed sensing (CS) in parallel MRI," in *Proceedings of the 16th Annual Meeting of ISMRM*, Toronto, Canada, 2008.

[WBMW08b] B. Wu, P. Bones, R. Millane, and R. Watts. "Ordered k-space data acquisition in contrast enhanced magnetic resonance angiography (CE-MRA)," in *Proceedings of SPIE Medical Imaging*, San Diego, 2008, pp. 284–296.

[WBMW09] B. Wu, Philip J. Bones, Rick P. Millane, and Richard. Watts. "Improved matrix inversion in image plane parallel MRI," *Magnetic Resonance Imaging*, vol. 27, no. 7, pp. 942–953, 2009.

[WHW+04] G.J. Wilson, R.M. Hoogeveen, W.A. Willinek, R. Muthupillai, and J.H. Maki. "Parallel imaging in MR angiography," *Topics in Magnetic Resonance Imaging*, vol. 15, pp. 169–185, 2004.

[WPK+00] M. Weiger, K.P. Pruessmann, A. Kassner, S. Wolff, G. Roditi, T. Lawton, and A. Reid. "Contrast-Enhanced 3D MRA Using SENSE," *Journal of Magnetic Resonance Imaging*, vol. 12, pp. 671–677, 2000.

[WRT05] C. Westbrook, C.K. Roth, and J. Talbot. *MRI in practice*. Blackwell, Oxford, 3rd edition, 2005.

[XYL04] D. Xu, L. Ying, and Z.P. Liang. "SENSE reconstruction with inaccurate sensitivity functions: effects and remedies," in *26th Annual International Conference of the IEEE Engineering in Medicine and Biology Society*, 2004.

[YMOS05] E.N. Yeh, C.A. McKenzie, M.A. Ohliger, and D.K. Sodickson. "Parallel magnetic resonance imaging with adaptive radius in k-Space (PARS): constrained image reconstruction using k-space locality in radiofrequency coil encoded data," *Magnetic Resonance in Medicine*, vol. 53, pp. 1383–1392, 2005.

[YQR+95] S.W. Young, F. Qing, D. Rubin, K.J. Balkus Jr., J.S. Engel, J. Lang, W.C. Dow, J.D. Mutch, and R.A. Miller. "Gadolinium zeolite as an oral contrast agent for magnetic resonance imaging," *Journal of Magnetic Resonance Imaging*, vol. 5, pp. 499–508, 1995.

[YW82] D.C. Youla and H. Webb. "Image restoration by the method of convex projections," *IEEE Trans. on Medical Imaging*, vol. 1, pp. 81–94, 1982.

[ZMP07] H. Zhang, J.H. Maki, and M.R. Prince. "3D contrast-enhanced MR angiography," *Journal of Magnetic Resonance Imaging*, vol. 25, pp. 13–25, 2007.

[ZVB+06] M.O. Zenge, F.M. Vogt, K. Brauck, M. Jokel, J. Barkhausen, S. Kannengiesser, M.E. Ladd, and H.H. Quick. "High-resolution continuously acquired peripheral MR angiography featuring partial parallel imaging GRAPPA," *Magenatic Resonance in Medicine*, vol. 56, pp. 859–865, 2006.